Universidade de São Paulo
Instituto de Astronomia, Geofísica e Ciências Atmosféricas
Departamento de Astronomia

Cosmic ray acceleration and non-thermal radiative losses around black holes: the effects of magnetic reconnection

Aceleração de raios cósmicos e perdas radiativas não-térmicas em torno de buracos negros: efeitos da reconexão magnética

Behrouz Khiali

Orientadora: Profa. Dra. Elisabete M. de Gouveia Dal Pino

São Paulo
2015

Behrouz Khiali

Cosmic ray acceleration and non-thermal radiative losses around black holes: the effects of magnetic reconnection

Aceleração de raios cósmicos e perdas radiativas não-térmicas em torno de buracos negros efeitos da reconexão magnética

Tese apresentada ao Departamento de Astronomia do Instituto de Astronomia, Geofísica e Ciências Atmosféricas da Universidade de São Paulo como requisito parcial obtenção do título de **Doutor em Ciências**.

Sub-área de concentração: Astrofísica.

Orientadora: Profa. Dra. Elisabete M. de Gouveia Dal Pino

São Paulo
2015

Dedicated to my love

Zahra

Acknowledgments

The vocabulary of pages that follow is made up of formulas, graphics, and specialized jargon. Writing down the results of the work of four years using those tools has been, however, easier than putting down in everyday words my gratitude to whom accompanied me in the process. These paragraphs are my unsatisfactory attempt.

To Prof. de Gouveia Dal Pino, my advisor, who always guided me with a lot of disposal, optimism, and patience. For always caring about my career (and that of all your students) in spite of your tiredness and your other obligations; your unlimited commitment is for me a great example. I am deeply indebted with all her help and encouragement. *Thanks for all the knowledge and enthusiasm you transmitted me!*

To the professors of the Astronomy Department, in special the ones who participated directly of my scientific formation through their courses and advises: Silvia Rossi, Elisabete de Gouveia Dal Pino, Gasto Bierrenbach, Laerte Sodre, Roberto Costa, Jorge Horwath, Alex Carciofi, Rodrigo Nemmen.

To the staff of the Astronomy Department for all their support, in special: Aparecida Neusa (Cida), Conceio, Marina Freitas, Regina Iacovelli, Ulisses Manzo, who were always so attentive, flexible, and nice with me.

To the staff of the IAG, in special the very efficient secretaries of the Graduation Office: Ana Carolina, Lilian and Marcel Yoshio.

To FAPESP and CAPES for the financial support which made possible the development of this work.

To my group colleagues for discussing my work, sharing their knowledge, their incentive and friendship: Reinaldo Santos-Lima, Cláudio Melioli, Grzegorz Kowal, Gustavo Guerrero, Gustavo Rocha, Luis Kadowaki, Márcia Leão, Chandra Singh, and María Victoria.

Thanks to Grzegorz Kowal for sharing his numerical code, which was used in the numerical simulations of this thesis.

Thanks to all the friends and colleagues I made in IAG during the last years, specially the ones I spent more time together: Bruno Dias, Bruno Mota, Carlos Augusto Braga, Cyril Escolano, Douglas Barros, Edgar Ramirez, Felipe Oliveira, Fellipy Silva, Juan Carlos Pineda, Marcio Avellar, Thiago Junqueira, Tiago Ricci, Paulo Jakson, Pedro Beaklini, Juliana Motter, Daniel Moser, Leandro Rimulo, Graziela Rodrigues, Loic Le Tiran.

I am enormously grateful to my lovely wife Zahra Sadre Momtaz for all her love, comprehension, and the enormous help during the thesis. *Thank you for being by my side in all the situations!*

I acknowledge my parents Rahim and Fatemeh, For letting me choose my future freely, and for teaching me that the only way to achieve what I wish is through work and effort. To my grandparents, because their love and the memories of my childhood have definitely shaped my nature. Those of them who cannot see me today, I guess would be proud of me.

I acknowledge all my family, for their invaluable support and love: my father-in-law Nasser, my mother-in-law Shahnaz, my sisters Behnaz and Samira, my brother Nima and my brothers-in-law Amir Hossein and Ali.

Abstract

Cosmic Ray (CR) acceleration is still challenging in high energy astrophysics. The first-order Fermi mechanism within magnetic reconnection layers has been demonstrated to be a powerful CR accelerator in recent studies. In this work we have investigated this acceleration process in the nuclear region of radio-galaxies and microquasars, considering fast magnetic reconnection events in the coronal region between the field lines of the black hole (BH) magnetosphere and the lines arising from the inner accretion disk. We found that specially the very high energy gamma-ray emission, whose location is still not well determined from current observations of these sources, may be originated through this mechanism in the nuclear region around the black hole. We employed both leponic and hadronic models to interpret the observed non-thermal emission from radio to gamma-rays resulting from interactions of the accelerated particles by magnetic reconnection with the surrounding matter, radiation and magnetic fields. We compared the calculated acceleration rate from numerical simulations with the proper radiative cooling rates obtaining the maximum particle energy and then reconstructed the spectral energy distribution (SED) for a few microquasars and radio galaxies for which there is emission detected up to TeV energies, namely, the microquasars Cyg X-1 and Cyg X-3, and the radiogalaxies Cen A, Per A, M87 and IC310. We found that the calculated SEDs are consistent with the observations. We have shown that the TeV emission is produced by the photo-meson process in both class of sources.

We have also considered the same acceleration model occurring in the core region of low luminosity AGNs in general to investigate the origin of the recently detected high energy extragalactic neutrinos by the IceCube experiment. We found that the decay of charged pions produced by photo-meson process using the accelerated protons via magnetic reconnection around the black holes of these sources located between redshifts $z = 0$ and 5 can explain the observed diffuse neutrino flux.

The results of this study on cosmic ray acceleration and non-thermal radiative processes strengthen recent findings that suggest that the VHE emission in microquasars and low luminosity AGNs in general may be originated in the core of these sources. Furthermore, these results may help to constrain particle acceleration, emission processes and space distribution models for comparison with high resolution observations of the coming new instruments, specially the gamma-ray observatory Cherenkov Telescope Array (CTA) which will be built around 2020 and will have 10 times more sensitivity at the very high energies than the current gamma-ray detectors.

Resumo

Aceleração dos raios cósmicos (RC) ainda é um desafio em astrofísica de altas energias. O mecanismo de Fermi de primeira-ordem em camadas de reconexão magnética vem sendo reconhecido como um potente acelerador de RC em estudos recentes. Nesta tese investigamos este processo de aceleração na região nuclear de rádio-galáxias e microquasares, considerando eventos rápidos de reconexão magnética na região coronal entre as linhas de campo da magnetosfera do buraco negro (BN) e as linhas que se erguem do disco de acreção na região mais próxima do BN. Verificamos que especialmente a emissão de energia muito alta de raios gama, cuja localização ainda não está bem determinada a partir de observações correntes dessas fontes, pode ser originada por esse mecanismo na região nuclear em torno do buraco negro. Empregamos modelos leptônicos e hadrônicos para interpretar a emissão não-térmica observada do rádio aos raios gama resultante de interações das partículas aceleradas por reconexão magnética com a matéria circundante, a radiação e os campos magnéticos. Nós comparamos a taxa de aceleração calculada a partir de simulações numéricas com as taxas de resfriamento radiativo adequadas para obter a energia máxima das partículas. Em seguida, reconstruímos a distribuição de energia espectral (em inglês SED) para alguns microquasars e rádiogaláxias para os quais há emissão detectada até energias de TeV, isto é, os microquasars Cyg X-1 e Cyg X-3, e as rádiogaláxias Cen A, Per A, M87 e IC 310. Verificamos que os SEDs calculados são consistentes com as observações. Mostrámos que a emissão TeV é produzida pelo processo de foto-mésons em ambas as classes de fontes.

Também consideramos o mesmo modelo de aceleração ocorrendo na região central de AGNs de baixa luminosidade em geral para investigar a origem dos neutrionos extragalácticos de alta energia recentemente detectados pelo experimento IceCube. Verificamos que o decaimento dos píons carregados produzidos pelo processo de foto-mésons a partir dos prótons acelerados via reconexão magnética em torno dos buracos negros dessas fontes, localizadas entre redshifts $z = 0$ e 5, pode explicar o fluxo difuso de neutrinos observado.

Os resultados deste estudo sobre a aceleração dos raios cósmicos e suas perdas radiativas não térmicas fortalecem descobertas recentes que sugerem que a emissão de altas energias em microquasares e AGNs de baixa luminosidade, podem ser originadas no núcleo dessas fontes. Além disso, estes resultados podem ajudar a restringir os processos de aceleração, de emissão e também os modelos de distribuição espacial das partículas para comparação com as observações de alta resolução dos futuros instrumentos, especialmente o observatório de raios-gama o Cherenkov Telescope Array (CTA), que será construído em torno de 2020 e terá 10 vezes mais sensibilidade nas energias mais altas do que os detectores atuais.

And He it is who has made the stars for you that you may follow the right direction with their help amid the deep darkness of the land and the sea. We have explained the signs in details for a people who posses knowledge.
"Holy Quran, An'am-98"

Look at the stars,
Look how they shine for you!
"Yellow", Cold party.

Contents

Acknowledgments **vii**

Abstract **x**

Resumo **xiii**

1 What is this thesis about? **1**

1.1 The cosmic ray acceleration mechanisms uncovered by high energy observations . . . 1

1.2 Objectives of this thesis: What we want to understand . . . 8

1.3 Guidelines: How is this thesis constructed? . . . 9

2 Particle acceleration by magnetic reconnection and application to the surrounds of BH sources **12**

2.1 What we want to know . . . 12

2.2 CR acceleration by magnetic reconnection . . . 13

2.2.1 Models of fast magnetic reconnection . . . 13

2.2.2 First order Fermi acceleration in magnetic reconnection sites . . . 17

2.3 Conditions for fast magnetic reconnection and particle acceleration around BH sources . . . 23

2.3.1 The accretion disk and magnetic field configuration around the BH source 23
2.3.2 Fast magnetic reconnection condition in the surrounds of the BH source 26
2.4 What we have learned 30

3 Relevant non-thermal radiative processes 31
3.1 What we want to know 31
3.2 Relativistic particle cooling mechanisms 32
3.2.1 Relativist particle interactions with the magnetic field 32
3.2.2 Relativistic particle interactions with matter 34
3.2.3 Relativistic particle interactions with the radiation field 38
3.3 Photon absorption processes 42
3.3.1 Photon-photon ($\gamma\gamma$) annihilation 42
3.3.2 Absorption of low-energy photons by photo-ionization (γN interactions) 44
3.4 Energy distribution of the accelerated particles 45
3.5 An overview 47
3.6 What we have learned 48

4 The magnetic reconnection acceleration model applied to microquasars 50
4.1 What we want to know 51
4.2 Black Hole Binaries 51
4.3 Application of the magnetic reconnection acceleration model to Cygnus X-1 55
4.4 Application of the magnetic reconnection acceleration model to Cygnus X-3 61
4.5 gamma-ray absorption in microquasars 66
4.6 Comparison with other models 68
4.7 What we have learned 70

5 Application of the magnetic reconnection model to LLAGNs 74
5.1 What we want to know 76
5.2 LLAGNs 76
5.3 Cen A 78
5.4 IC 310 85
5.5 Per A 89
5.6 M87 92
5.7 Photon absorption in LLAGNs 96
  5.7.1 gamma-ray absorption by photon-photon ($\gamma\gamma$) annihilation 96
  5.7.2 Photon-neutral (γN) interactions 97
5.8 Comparison with other models 102
  5.8.1 Cen A 102
  5.8.2 Per A 102
  5.8.3 M87 103
  5.8.4 IC310 105
5.9 What we have learned 106

6 The origin of high energy neutrino emission from the core of LLAGNs 109
6.1 What we want to know 110
6.2 High energy neutrinos detected by the IceCube 110
6.3 Neutrino production via hadronic processes 113
  6.3.1 Neutrino production out of *pp* collisions 113
  6.3.2 Neutrino production out of $p\gamma$ interactions 115
6.4 Neutrino emission and diffuse intensity 116
6.5 Comparison with other models 121
6.6 What we have learned 123

7 Conclusions and perspectives 127
7.1 What we have learned 127
7.2 Perspectives and looking forward 130
7.2.1 Stochastic acceleration mechanism in time evolved pure turbulent plasmas 131
7.2.2 CR diffusion in turbulent plasmas 134

Bibliography 140

A How to find the magnetic reconnection acceleration rate from the numerical simulations? 161

B A magnetic reconnection model for explaining the multiwavelength emission of the microquasars Cyg X-1 and Cyg X-3 168

C Particle Acceleration and gamma-ray emission due to magnetic reconnection around the core region of radio galaxies 184

D High energy neutrino emission from the core of low luminosity AGNs triggered by magnetic reconnection acceleration 201

List of Figures

1.1 Scheme of diffusive shock acceleration. The shaded vertical region is the shock front, the circular blobs denote idealized scattering centers, and the solid line with arrows denotes the path of an idealized fast particle (adapted from Melrose 2009). 3

1.2 Two dimensional cut of a numerical simulation of the trajectory of a test proton approaching a three-dimensional reconnection layer. Topology of the longitudinal magnetic field represented as a gray texture in opposite directions for the fluxes on both sides of the reconnection layer. The particle energy increases from red to yellow and then finally to white when the particle reaches the current sheet (adapted from Kowal et al. 2011). . . . 5

1.3 Turbulent driven magnetic reconnection power (see §. 2.3) versus BH source mass, compared to the observed core radio and gamma-ray emissions of 233 LLAGNs (including radio galaxies, seyferts and liners; red diamonds) and nine microquasars (or galactic black holes, GBHs; green diamonds), including also the gamma-ray emission from blazars (represented in blue circles) and GRBs (represented in orange circles) (extracted from Kadowaki et al. 2015). 7

2.1 Schematic configuration of the Sweet-Parker magnetic reconnection model. Two magnetic flux tubes of opposite polarity encounter in a surface and reconnect under finite magnetic resistivity. This region defines a magnetic discontinuity also named current sheet (adapted from de Gouveia Dal Pino & Kowal 2015). 14

2.2 Schematic configuration of Petschek magnetic reconnection model (adapted from de Gouveia Dal Pino & Kowal 2015). 15

2.3 Schematic configuration of turbulent magnetic reconnection model (adapted from Lazarian et al. 2015). 17

2.4 A single test particle is injected in a three-dimensional current sheet and undergoes a first-order Fermi acceleration while bouncing back and forth between the two-converging magnetic fluxes of opposite polarity (see Figure 1.2). This figure shows the resulting change of the particle kinetic energy with the X coordinate and in the detail the kinetic energy exponential increase with time (from Kowal et al. 2011) 18

2.5 *Left panel*: Particle kinetic energy evolution and distribution for 10,000 test particles injected in a current sheet with turbulence embedded in order to make magnetic reconnection fast. The colors indicate which velocity component is accelerated (red or blue for parallel or perpendicular component to the local magnetic field, respectively). The energy is normalized by the rest proton mass. Subplots show the particle energy distributions at $t = 5.0t_A$, where the Alfvén time (t_A) is the typical length scale of reconnection layer divided by the Alfvén speed. *Right column*: XY cross section of 3D MHD simulation of the reconnection sheet with embedded turbulence where the particles were injected. It shows the current density distribution in the current sheet and the arrows depict the magnetic field orientation on both sides of the current sheet (Kowal et al. 2012) 20

2.6 Scheme of magnetic reconnection between the lines rising from the accretion disk and the lines around the BH horizon. Reconnection is made fast by the presence of embedded turbulence in the reconnection zone (see text for more details). Particle acceleration may occur in the magnetic reconnection zone by a first-order Fermi process (adapted from GL05). 24

3.1 Synchrotron radiation of a charged particle spiralling around a magnetic field line (Credit: James Schombert, University of Oregon) 33
3.2 Bremsstrahlung radiation of an electron accelerating around the nucleus of an ionised atom (Credit: Sarah H.R. Bank, Towson University) 34
3.3 Proton-proton inelastic interactions (Credit: Greg Vance, University of Wisconsin) 36
3.4 Cross section of the production of neutral pions in proton-proton collision σ_{pp}, as a function of E_p (Cerutti 2013) 37
3.5 Inverse Compton (Credit: Jeff Stanger, University of Sydney) 39
3.6 γ-ray production due to $p\gamma$ interaction 41
3.7 Pair production. 43
3.8 Cross section for photo-ionization process (Reynoso et al. 2011) 45

4.1 A schematic of microquasars containing central compact object, accretion disk, jets and companion star (Credit: Arne Rau, MPE Garching) 52
4.2 A schematic representation of the black hole binary system showing the location of the emission region in red around the BH. This emission region encompasses the reconnection acceleration region of Figure 2.6 which is not shown here. 54
4.3 Acceleration and cooling rates for electrons in the nuclear region of Cyg X-1. 57
4.4 Sketch of microquasar-star binary sytem (Adapted from Cerutti 2013) . . . 58

4.5 Acceleration and cooling rates for protons in the nuclear region of Cyg X-1. 59

4.6 Calculated spectral energy distribution for Cyg X-1 using the magnetic reconnection acceleration model compared with observations. The data depicted in the radio range is from Fender et al. 2000, the IR fluxes are from Persi et al. 1980; Mirabel et al. 1996, the hard X-ray data above 20 *keV* are from INTEGRAL (Zdziarski et al. 2012), the soft X-ray data below 20 *keV* are from BeppoSAX (Di Salvo et al. 2001), the soft gamma-ray data are from COMPTEL (McConnell et al. 2000, 2002), the data in the range 40 MeV- 40 GeV are measurements and upper limits from the *Fermi* LAT (Malyshev et al. 2013), and the data in the range 40 GeV- 3 TeV are upper limits from MAGIC (with 95% confidence level; Albert et al. 2007). The red and black stars correspond to emission from the companion star and the accretion disk, respectively, and are not investigated in the present model (see more details in the text.) 60

4.7 Acceleration and cooling rates for electrons in the core region of Cyg X-3. . 63

4.8 Acceleration and cooling rates for protons in the core region of Cyg X-3. . 64

4.9 Spectral energy distribution for Cyg X-3. The observed radio emission is taken from AMI-LA and RATAN (Piano et al., 2012); the data in the range 50MeV to 3GeV are from AGILE-GRID (Piano et al., 2012); and the data in the range $0.2 - 3.155$TeV are from MAGIC differential flux upper limits (95% C.L.). 65

4.10 Annihilation of produced gamma-ray via interacting with photon field of the companion star. 66

4.11 Geometry for Gamma-ray absorption at a location P due to interaction with a photon produced at point S. The interaction leads to e^+e^- pair production (Extracted from Dubus 2006). 67

4.12 Spectrum of Gamma-ray absorption around the companion star in Cyg X-1 and Cyg X-3 (*a* and *b* panels, respectively). 68

5.1 Schematic representation of the emission region which encompasses the reconnection region around the BH depicted in Figure 2.6 (not shown here) in the core of LLAGNs 75

5.2 Sketch of an AGN (Credit: Aurore Simonnet, Sonoma State University). . . 77

5.3 Acceleration and cooling rates for electrons (top) and protons (bottom) in the nuclear region of Cen A. 83

5.4 Calculated spectral energy distribution (SED) for Cen A using the magnetic reconnection acceleration model in a lepton-hadronic scenario compared with observations. The data depicted in the radio to optical energy range (10^{-5}eV$-$1eV) are from SCUBA at 800 μm (Hawarden et al. 1993), ISO & SCUBA at 450 μm and 850 μm (Mirabel et al. 1999); the data in the hard x-rays range is from *Swift-BAT* (Ajello et al. 2009) and *Suzaku* (Markowitz et al. 2006). We also include data from *OSSE* (Kinzer et al. 1995) and *COMPTEL* (Steinle et al. 1998) in the range of $5 \times 10^5 - 10^7$eV. The data observed in the energies $10^8 - 10^{10}$eV are taken by *EGRET* (Sreekumar et al. 1999; Hartman et al. 1999) and in the energies $10^8 - 10^{10}$eV by *Fermi-LAT* (Abdo et al. 2009b, 2010). The TeV data are taken by *HESS* (Aharonian et al. 2009). All data points showed here are corresponded to core emission. 84

5.5 Acceleration and cooling rates for electrons (top) and for protons (bottom) in the nuclear region of IC 310. See more details in the text. 87

5.6 A lepton-hadronic model of the SED of IC 310 compared with observations. The core radio data are obtained from Kadler et al. 2012; Dunn et al. 2010; Becker et al. 1991; White & Becker 1992; Condon et al. 2002; Douglas et al. 1996. The X-ray data are from XMM-Newton (Sato et al. 2005) and the VHE gamma-ray data are from *MAGIC* (Aleksić et al. 2014c). In the upper right side of the diagram it is depicted the detail of the modeling of the VHE branch. 88

5.7 Acceleration and cooling rates for electrons (top) and for protons (bottom) in the nuclear region of Per A (NGC 1275). 90

5.8 A leptonic model to reproduce the SED of Per A (NGC 1275) using the magnetic reconnection acceleration model. Data include *MOJAVE* (Lister et al. 2009), *Planck* (Ade et al. 2011), HST (Chiaberge et al. 1999), and HST FOS (Johnstone & Fabian 1995) for the radio to optical spectrum; data depicted in X-rays is from the XMM (Torresi 2012), *Swift*-BAT (Ajello et al. 2009), and BATSE (Harmon et al. 2004); and data depicted in the gamma-ray band is from *Fermi-LAT* (Abdo et al. 2009a; Ackermann et al. 2012) in the 100 MeV-100GeV energy range, and from *MAGIC* (Aleksić et al. 2010a,b, 2012a,b) in the VHE tail. We note that the error bars for the BATSE data (in the 10^5 eV range) were evaluated using Harmon et al. (2004); Soldi et al. (2014) and Wilson et al. (2012). 91

5.9 Acceleration and cooling rates for electrons (top) and for protons (bottom) in the nuclear region of M87. 93

5.10 A lepton-hadronic model of the SED of M87 compared with observations. The core radio data are obtained from MOJAVE VLBA (Kellermann et al. 2004) at 15 GHz, from (Biretta et al. 1991) at 1.5, 5 and 15 GHz, from IRAM (Despringre et al. 1996) at 89 GHz, from SMA at 230 GHz (Tan et al. 2008), from Spitzer at 21 and 7.2 GHz (Shi et al. 2007) and from Gemini (Perlman et al. 2001) at 3.2 GHz. Optical-UV emission from HST (Sparks et al. 1996). MeV/GeV gamma-ray data are from *Fermi-LAT* (Abdo et al. 2009c), and the low-state TeV spectrum (Aharonian et al. 2006) from *HESS*. 95

5.11 Sketch of an accretion disk formed around the BH in the center (point O). Source of energetic gamma rays lies above the disk as a hypothetical torus (see §. 3.2) which is seen at an angle Ψ by a distant observer. Produced gamma-rays and photons emitted from the unit surface of the disk dS (centred around point M) interact at the point P with an angle θ_0. The projection of point P in the disk plane is given by point Q. (Extracted from Cerutti et al. 2011). 98

5.12 Spectrum of gamma-ray absorption at selected heights z above the plane of the disk in Cen A, Per A, M87, and IC 310 (a, b, c, and d panels, respectively). 99

5.13 The transmitted flux $exp(-\tau)$ for different gamma-ray energies as function of the height z above the disk in Cen A, Per A, M87, and IC 310 (a, b, c, and d panels, respectively). 100

5.14 The γN optical depth ($\tau_{\gamma H}$) in Cen A, Per A, M87, and IC 310 (a, b, c, and d panels, respectively). 101

6.1 Acceleration and cooling rates for protons in the core regions of LLAGNs with a central black hole mass (a) $M = 10^7 M_\odot$ (Model 1), (b) $M = 10^8 M_\odot$ (Model 2), and (c) $M = 10^9 M_\odot$ (Model 3). 114

6.2 Calculated diffuse intensity of neutrinos from the cores of LLAGNs considering our magnetic reconnection acceleration model to produce the protons and gamma-ray photons for three different BH masses. The data are taken from IceCube measurements (Aartsen et al. 2014). 120

7.1 CR head-on and head-tail collisions with magnetized cloud moving with the velocity of u. 131
7.2 Acceleration times for injected test particles in turbulent MHD domain in different length sales (Resolution $N = 512$). 132
7.3 Pitch angle diffusion coefficients measured for different initial pitch angles in time-evolved turbulent plasma. 135
7.4 The same as Figure 7.3 but in steady-state turbulent plasma. 136

A.1 Particle kinetic energy evolution for 10,000 test particles injected in a current sheet with turbulence embedded in a large scale current sheet in order to make magnetic reconnection fast (Kowal et al. 2012). 162
A.2 Same as Fig A.1 but with vertical lines to highlight the region of exponential acceleration rate due to magnetic reconnection. 163

List of Tables

4.1 Model parameters for Cyg X-1 56
4.2 Model parameters for Cyg X-3 62

5.1 Model parameters for Cen A, Per A, M87 and IC 310. 80

6.1 Three sets of model parameters for LLAGNs. 116
6.2 Physical conditions around the LLAGNs represented by models 1, 2 and 3, obtained from Eqs. 2.10-2.12 and 2.14, using $r_x = 6$, $l = 20$, $l_X = 10$ and $\xi = 0.7$. 117

Chapter 1

What is this thesis about?

1.1 The cosmic ray acceleration mechanisms uncovered by high energy observations

Energetic relativistic particles, also denominated cosmic rays (CRs), strike continuously the top of the Earth atmosphere at a rate of $\sim 10^4 \mathrm{m}^{-2}\mathrm{s}^{-1}$. There are at least four different cosmic ray species: solar cosmic rays with energies around $10 - 10^9$eV, anomalous cosmic rays at the energy 10^6eV, Galactic cosmic rays in the range of $10^9 - 10^{15}$eV and extra-galactic/ultra-high energy cosmic rays with energies in $10^{15} - 10^{21}$eV range.

The exact composition depends on the part of the spectrum that is considered, but we can say that approximately 86% of these particles are protons, 11% are alpha articles, 1% consists of stable nuclei, up to Uranium, 2% are electrons and a non negligible fraction (about 1%) consists of antiparticles (positrons and antiprotons, Gaggero 2011).

The origin and the acceleration mechanism of these energetic particles are still highly debated questions and are related to many interesting astrophysical issues and most intriguing puzzles of modern physics, such as the nature of Dark Matter.

There are several mechanisms by which fast particles can be accelerated, and it is now recognized that the data require a rich variety of mechanisms operating under different conditions in different astrophysical accelerators. The most investigated mechanisms are stochastic acceleration and diffusive shock acceleration.

Fermi (1949) was the first author to propose stochastic acceleration as a model for production of CRs, whereby charged particles scattering in random collisions with moving magnetized clouds, e.g., in the interstellar medium, gain energy on average, mainly because head-on collisions (energy gaining) are more numerous than energy losing trailing ones (catch-up collisions) which is known as second-order Fermi process because the net particle energy gain is proportional to the second power of the ratio between the scattering velocity and the light speed.

Fermi (1954) realized however, that this process could not explain the commonly observed slope of the CR power law spectrum ($N(E) \sim E^{-2}$), producing a much steeper one. He then suggested that the acceleration would be more efficient if all collisions were head-on which is known as Fermi first-order mechanism since the particle energy gain is proportional to the first power of the ratio between the velocity of the scatterer and the light speed (Fermi 1954). It took almost 30 years for researchers to realize that this first-order Fermi process could operate in shock discontinuities, where trapped particles can be scattered by magnetic fluctuations on either side (in the upstream and downstream regions) of the shock front (Krimsky 1977; Bell 1978), as illustrated in figure 1.1.

This mechanism can explain particle acceleration in several astrophysical environments where strong shocks are present such as supernova remnants (Bell 2013), Galactic and extragalactic relativistic jets (that emerge from Galactic black hole binaries or microquasars, active galactic nuclei or AGNs, and gamma-ray bursts or GRBs; e.g., Bicknell & Melrose 1982; Meszaros & Rees 1992) and coronal mass ejections in the sun (e.g., Wild et al. 1963). This mechanism also can explain the nearly universal power law spectrum of the CRs (e.g., Bell 1978; Caprioli & Spitkovsky 2014) and the frequently observed radio emission in internal blobs and in the bow shock at the head of the Galactic and extra-

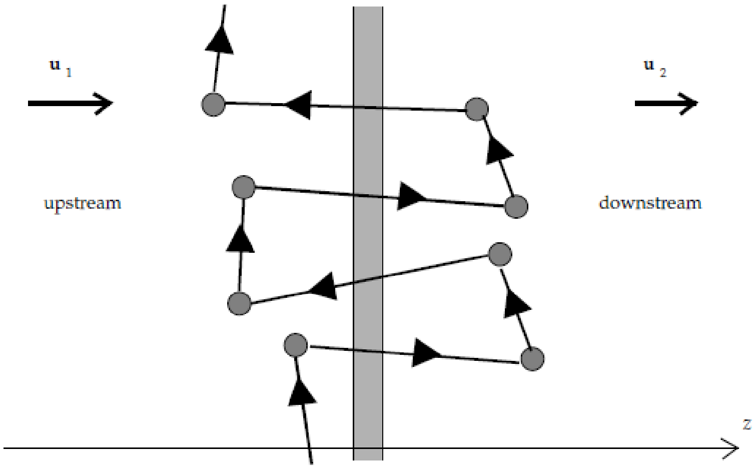

Figure 1.1: Scheme of diffusive shock acceleration. The shaded vertical region is the shock front, the circular blobs denote idealized scattering centers, and the solid line with arrows denotes the path of an idealized fast particle (adapted from Melrose 2009).

galactic relativistic jets. This emission is due to Synchrotron radiation and is generally attributed to shock acceleration since the observed flux $S_\nu \propto \nu^{-\beta}$, where $\beta \simeq p - 1/2$, ν is the radio frequency and p is the relativistic electron power law index ~ 2 predicted by first-order Fermi acceleration..

Another indirect way to detect cosmic rays is through the gamma-ray emission which may be produced in the relativistic shocks of sources like those mentioned above. This emission is generally attributed to inverse Compton emission of relativistic electrons, or pion decays due to relativistic proton interactions with soft photons or low energy protons.

Nevertheless, if the embedded magnetic field in a given source is strong enough, then shocks will be faint (since the magnetic field absorbs most of the kinetic energy of the impact, as it is well known from the Hankine-Hugoniot MHD conservation relations; e.g., Boyd & Sanderson 2005) and therefore, shock acceleration becomes inefficient. This requires alternative mechanisms for particle acceleration in such environments. This is the situation, for instance, in pulsars which are highly magnetized sources with large scale coherent dipolar fields. In these environments, particles are believed to be directly accelerated by the varying magnetic field, according to the Faraday law (e.g., Melrose 2009; de Gouveia Dal Pino, Kowal & Lazarian 2014).

Another possible mechanism for accelerating relativist particles in magnetically dominated environments, as for instance the solar corona or, as believed, the nuclear region of black hole (BH) sources e.g., (Blandford & Payne 1982) is related to magnetic reconnection (for reviews see e.g., Uzdensky 2011, 2015; de Gouveia Dal Pino, Kowal & Lazarian 2014; de Gouveia Dal Pino & Kowal 2015).

Magnetic reconnection occurs when two magnetic fluxes of opposite polarity get into contact. Under finite resistivity, these fluxes will partially annihilate at the contact discontinuity (also denominated current sheet[1]) and reconnect again releasing stored magnetic energy. de Gouveia Dal Pino & Lazarian (2005) proposed that a first-order Fermi process, similarly to what happens in shock discontinuities, could occur also in these magnetic discontinuities. According to their prediction, trapped particles within the reconnection layer will suffer head-on collisions with magnetic fluctuations while bouncing back and forth within the two converging fluxes, thereby undergoing a net energy gain directly proportional to the reconnection velocity divided by the light speed (see Figure 1.2). This acceleration mechanism has been also successfully tested numerically both in collisionless flows by means of two-dimensional (2D) pair plasma PIC simulations (e.g., Drake et al. 2006; Zenitani & Hoshino 2001; Zenitani et al. 2009; Drake et al. 2010; Cerutti et al. 2013, 2014; Sironi & Spitkovsky 2014) and collisional magnetic reconnection flows by means of 2D and 3D MHD simulations with test particles (Kowal et al. 2011, 2012). Furthermore, this process has been explored in depth in the natural laboratories of fast reconnection provided by solar flares (e.g., Drake et al., 2006; Lazarian & Opher, 2009; Drake et al., 2010; Gordovskyy et al., 2010; Gordovskyy & Browning, 2011; Zharkova et al., 2011) and the Earth magneto-tail (Deng & Matsumoto 2001; Su et al. 2013). For instance, Lazarian

---

[1] Because of the large value of the current density in the magnetic discontinuity

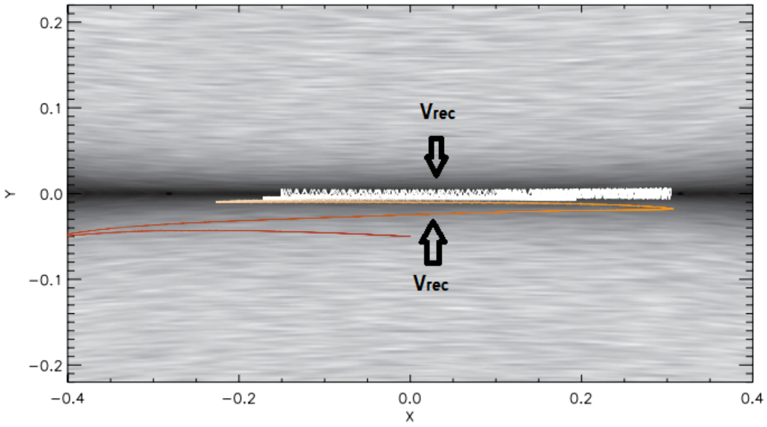

Figure 1.2: Two dimensional cut of a numerical simulation of the trajectory of a test proton approaching a three-dimensional reconnection layer. Topology of the longitudinal magnetic field represented as a gray texture in opposite directions for the fluxes on both sides of the reconnection layer. The particle energy increases from red to yellow and then finally to white when the particle reaches the current sheet (adapted from Kowal et al. 2011).

& Opher (2009) verified that the anomalous cosmic rays measured by Voyager seem to be indeed accelerated in the reconnection regions of the magneto-pause (see also Drake et al., 2010). In another study, Lazarian & Desiati (2010) invoked the same mechanism to explain the excess of cosmic rays in the sub-TeV and multi-TeV ranges in the wake produced as the Solar system moves through interstellar gas. Magnetic reconnection has been also invoked in the production of ultra high energy cosmic rays (e.g., Kotera & Olinto 2011 and references therein) and in particle acceleration in astrophysical jets and gamma-ray bursts (Giannios, 2010; del Valle et al., 2011; Zhang & Yan, 2011), and around compact sources near the jet basis (de Gouveia Dal Pino & Lazarian 2000; 2001; 2005; de Gouveia Dal Pino et al. 2010; Neronov & Aharonian 2007).

Lately, very high energy observations, specially at the TeV (i.e., 10^{12} eV) range with the Fermi and Swift satellites and ground based gamma ray observatories (HESS, VERI-

TAS and MAGIC) of AGNs and GRBs have been challenging the current particle acceleration theories which have to explain how particles are accelerated to very high energies in regions relatively small compared to the fiducial scale of their sources. This is particularly a difficulty related to non-blazars, or more specifically to low luminosity AGNs (LLAGNs), and microquasars. The observed VHE detections are surprising because, besides being highly under-luminous, the viewing angle of the jets of these sources with respect to the line of sight is of several degrees, therefore allowing for only moderate Doppler boosting. These characteristics make it difficult explaining the VHE of these sources adopting the same standard scenario of blazars (that is, shock acceleration along the jet). Furthermore, some LLAGNs are observed to be highly variable in the TeV range (e.g., M87 and IC 310). These short time variabilities corresponds to have an emission zone with length scales of the order of a few their Schwarzschild radius which it should be located in a compact zone in the core region of LLAGNs and the shock acceleration model along the jet have substantial problems to explain these TeV emissions.

In this work we will investigate this problem focusing on the acceleration of relativistic particles and their non-thermal energy emission in the surrounds of these black hole sources. We will consider the model proposed by de Gouveia Dal Pino and Lazarian (2005) where events of fast reconnection may take place between the magnetosphere of the BH and the magnetic field lines arising from the inner accretion disk (see Figure 2.6). Inspired by similar phenomena occurring in the solar corona (Deng & Matsumoto 2001; Su et al. 2013), they explored this process first in the framework of microquasars where they suggested that the observed radio outbursts and the formation of superluminal blobs could be due to these events. de Gouveia Dal Pino et al. (2010) extended this model to AGNs.

More recently, Kadowaki et al. (2015) and Singh et al. (2015) revisited this model exploring different processes to allow for fast magnetic reconnection around the BH sources and different accretion disk models. They calculated the total magnetic reconnection

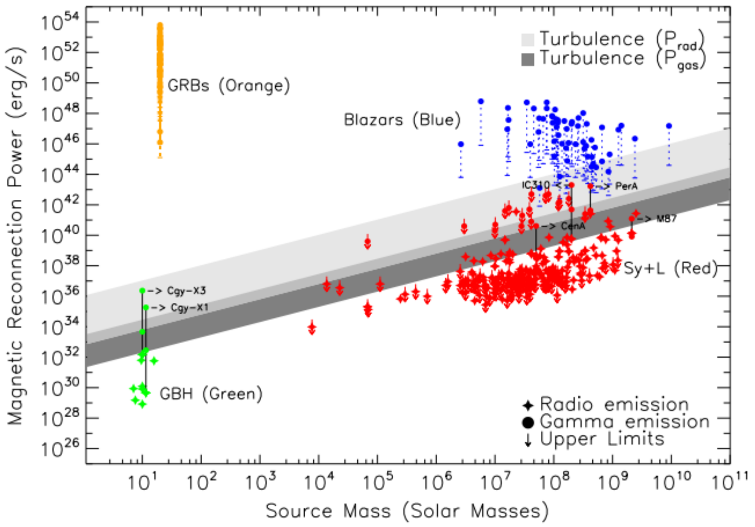

Figure 1.3: Turbulent driven magnetic reconnection power (see §. 2.3) versus BH source mass, compared to the observed core radio and gamma-ray emissions of 233 LLAGNs (including radio galaxies, seyferts and liners; red diamonds) and nine microquasars (or galactic black holes, GBHs; green diamonds), including also the gamma-ray emission from blazars (represented in blue circles) and GRBs (represented in orange circles) (extracted from Kadowaki et al. 2015).

power as a function of the the BH mass, the accretion disk rate, and the coronal parameters, and compared this power to the total observed (core) radio and gamma-ray luminosities of a sample of AGNs and microquasars containing more than 230 sources. They found that this power is more than sufficient to explain the core luminosities of microquasars and non-blazars AGNs or LLAGNs (see Figure 1.3). They also found that the magnetic reconnection power follows the same trend of the observed correlation between these luminosities and the BH masses of these sources spanning 10 orders of magnitude. They also found that the calculated reconnection power anti-correlates with the gamma-ray luminosities of blazars and GRBs, because in these cases the emission is generally expected to come from the jet that points to the line of sight and screens the core emission.

The results found above suggest that not only the radio but also the VHE emission whose origin is still uncertain, can be produced by magnetic reconnection in the surrounds of the BH of LLAGNs and microquasars. These results have motivated us to perform further tests to validate this model. In this thesis, we employ the magnetic reconnection acceleration model described above to reconstruct the entire spectral energy distribution (SED) of a few microquasars and LLAGNs for which there are detailed observations from radio to TeV energies, namely the microquasars Cyg X-1 and Cyg X-3 and the LLAGNs Cen A, Per A, M87, and IC 310. Furthermore, because the model above favours the acceleration of relativistic protons to very high energies, we also investigate here the production of neutrinos via the decay of charged pions produced by relativistic protons. We will calculate the expected flux of neutrinos in the core regions of LLAGNs and compare with the flux recently observed by the IceCube experiment (Ahlers & Murase 2014).

1.2 Objectives of this thesis: What we want to understand

The first part of this thesis is dedicated to the modelling of the high-energy radiation emitted by microquasars and LLAGNs and the reconstruction of the observed SEDs for a few examples of these classes. For this aim, we must take into account the particle acceleration as well as all the relevant non-thermal radiative and absorption processes. Furthermore, as stressed, we will also investigate the potential origin of the extragalactic diffuse high energy neutrino emission observed by the IceCube as due to the cores of LLAGNs, employing the same acceleration model. The ultimate goal of this thesis will be to answer the following questions:

1. How do particles gain energy by the magnetic reconnection mechanism?
2. Is magnetic reconnection a powerful CR accelerator comparable to shock acceleration?
3. What are the relevant acceleration and radiative processes in the surrounds of BH sources?
4. How does the pair production absorption influence the gamma-ray emission?
5. How does the short time variability can be explained by the reconnection scenario in the surrounds of BH sources?
6. What is the dominant cooling mechanism to produce TeV gamma-rays in LLAGNs and microquasars?
7. How are the high energy neutrinos produced in LLAGNs?
8. Can the magnetic reconnection model in the nuclear region of LLAGNs explain the origin of HE neutrinos and how are they produced in LLAGNs?

1.3 Guidelines: How is this thesis constructed?

The manuscript is divided into 7 chapters. Below, I give an overview of each part and indicate in which chapter the questions above will be answered. Chapter 2 introduces the magnetic reconnection model and shows how particles can be accelerated in current sheets (Question 1). The relevant non-thermal processes that may occur in the surrounds of BHs are discussed in Chapter 3 (Questions 3 and 4). Chapters 4 and 5 are dedicated to applications of the reconnection model to the reconstruction of the SED of microquasars and LLAGNs, respectively (Questions 2-7). The possibility of high energy neutrino production in the nuclear regions of LLAGNs and the calculation of the diffuse neutrino flux to compare with the observed flux by the IceCube is shown in Chapter 6 (Questions 6 and 7). In Chapter 7, it is briefly summarized the main results obtained in this thesis and presented the prospects for future studies, including preliminary results of a study of cosmic ray propagation in turbulent environments, like the intergalactic and interstellar media.

Chapter 2

Particle acceleration by magnetic reconnection and application to the surrounds of BH sources

In this chapter we describe the theory of particle acceleration by magnetic reconnection and discuss its applicability around black hole sources surrounded by an accretion disk and a magnetized corona.

2.1 What we want to know

- How the magnetic reconnection mechanism can accelerate particles to relativistic energies?

- What are the conditions for fast magnetic reconnection in the surrounds of BHs?

2.2 CR acceleration by magnetic reconnection

As stressed in Chapter 1, we will here explore a particle acceleration process that may be crucial in regions which are magnetically dominated and where shocks are expected to be weak, as in the case of the surrounds of black hole sources, below (or near) the jet launching basis. We will focus on particle acceleration due to magnetic reconnection. We present below a brief review of this process starting by defining magnetic reconnection and how it can become fast.

2.2.1 Models of fast magnetic reconnection

Magnetic reconnection occurs when two magnetic fluxes of opposite polarity encounter each other. In the presence of finite magnetic resistivity, the converging magnetic field lines annihilate at the discontinuity surface and a current sheet forms there (de Gouveia Dal Pino 1995).

The standard one-dimensional model of magnetic reconnection proposed separately by Sweet (1958) and Parker (1957), the so-called Sweet-Parker (S-P) model (Figure 2.1), using mass flux conservation predicts a reconnection velocity given by $V_R \sim v_A(\Delta/L) \sim v_A S^{-1/2} \ll 1$, where $S = Lv_A/\eta$ is the Lundquist number, with L being the large scale extension of the reconnection layer, Δ the thickness of the reconnection contact discontinuity and η the Ohmic resistivity which is generally very small in the typically high-conducting astrophysical plasmas. Besides, with the typical huge astrophysical sizes (L), S is very large for Ohmic diffusivity values (e.g., for the ISM $S \sim 10^{16}$) and therefore, the reconnection rate is much smaller than the Alfvén speed v_A. Direct observations of reconnection indicate that at least in some circumstances, as in the solar flares and the Earth magnetotail storms, reconnection is fast with rates V_R which are a substantial fraction of v_A (Deng & Matsumoto 2001; Su et al. 2013).

Petschek (1964) proposed a way to solve this difficulty by assuming a two-dimensional

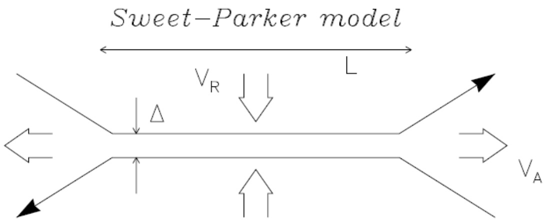

Figure 2.1: Schematic configuration of the Sweet-Parker magnetic reconnection model. Two magnetic flux tubes of opposite polarity encounter in a surface and reconnect under finite magnetic resistivity. This region defines a magnetic discontinuity also named current sheet (adapted from de Gouveia Dal Pino & Kowal 2015).

geometry and making $\Delta \sim L$ by focussing the reconnection process into a single point, the X-point, rather than over the entire large scale L of the magnetic fluxes (see Figure 2.2). Such a configuration indeed results a much faster reconnection speed $V_R \sim \pi/4(v_A lnS)$. However, it was later found to be unstable, rapidly collapsing to the Sweet-Parker configuration in magnetohydrodynamical (MHD) numerical simulations (Biskamp et al. 1997). Nevertheless, in a collisionless[1] pair (electron-positron or electron-ion) plasma with localized resistivity η, it was found that the Petcheck model could still be sustained making reconnection fast (de Gouveia Dal Pino, Kowal & Lazarian 2014; de Gouveia Dal Pino & Kowal 2015). In a collisionless two-fluid plasma, the particles mean free path is of the order of the large scale dimension of the system $L \sim \lambda_{mfp}$. Under such conditions, in an electron-ion plasma, for instance, the ion skin depth δ_{ion} (which can be viewed as the gyroradius of an ion moving at the Alfvén speed, i.e. $\delta_{ion} = \frac{v_A}{\omega_{ci}}$, where ω_{ci} is the ion cyclotron frequency) is comparable to the Sweet-Parker (S-P) diffusion scale, $\Delta = (\frac{L\eta}{v_A})^{0.5}$ (In the case of an electron-positron pair plasma, a similar condition is valid, but for the electron skin depth). But at these scales, the Hall effect given by the $\mathbf{J}\times\mathbf{B}$ term in Ohm's law [2] is important and able to sustain the Petschek X-point configuration. In a collisional plasma[3], on the other hand, the S-P thickness is larger than the micro-physical length scales relevant to collisionless reconnection, i.e., $\delta_{ion} \ll \Delta$ or $L \gg \lambda_{e,mfp}(m_i/m_e)^{0.5}$ and the Hall effect is no longer dominant (e.g., de Gouveia Dal Pino, Kowal & Lazarian 2014).

---

[1] A collisionless plasma is a plasma where the collisions between particles do not play an important role in the dynamics of the plasma. In a collisionless plasma, the mean free path between collisions is larger than or of the order of the characteristic length scale.

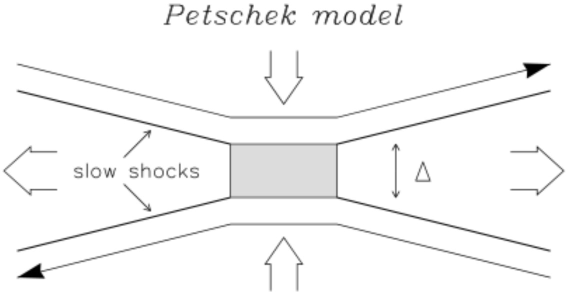

Figure 2.2: Schematic configuration of Petschek magnetic reconnection model (adapted from de Gouveia Dal Pino & Kowal 2015).

To overcome this problem, Lazarian & Vishniac (1999) proposed a model for fast reconnection in collisional fluids in the presence of when turbulence is present in the magnetic discontinuity (also denominated current sheet because of the large value of the current density in this interface). Given the fact that MHD turbulence is ubiquitous in astrophysical environments, this may be a universal trigger of fast reconnection. An important consequence of fast reconnection by turbulent magnetic fields is the formation

---

[2] MHD form of the Ohm's law is (Boyd & Sanderson 2005):

$$\mathbf{E} + \mathbf{u}\times\mathbf{B} - \mathbf{J}/\sigma = \frac{m_i}{Ze\rho}(\mathbf{J}\times\mathbf{B} - \nabla p_e) \tag{2.1}$$

where $\mathbf{u}$ and ρ are the plasma velocity and density, respectively. σ is the coefficient of electrical conductivity, m_i, the ion mass and p_e is the electron pressure

[3] In collisional plasma, the effective mean free path between particle interactions is much smaller than the characteristic scale length of the system.

of a thick volume filled with small scale multiple simultaneously reconnecting magnetic fluxes (see Figure 2.3). Lazarian & Vishniac (1999) showed that the reconnection velocity is given by

$$V_R \sim v_A min\left[\frac{l_{inj}}{L}, \frac{L}{l_{inj}}\right]^{0.5} (v_{inj}/v_A)^2 \tag{2.2}$$

where v_{inj} is the injection velocity of the turbulence and l_{inj} its injection scale. The predictions of this model have been tested successfully by numerical simulations (Kowal et al. 2009, 2012) which confirmed that the reconnection speed is of the order of the Alfvén speed and independent of resistivity.

Mass conservation ($\Delta/L = V_R/v_A$) and Equation 2.2 imply that the thickness of the magnetic reconnection layer is

$$\Delta = L min\left[\frac{l_{ing}}{L}, \frac{L}{l_{inj}}\right]^{0.5} (v_{inj}/v_A)^2. \tag{2.3}$$

It is easy to see that for $l_{inj} \sim L$ and $v_{inj} \sim v_A$, $V_R \sim v_A$ (which in the systems that we will consider here may be near the light speed) and therefore, reconnection is fast. Besides, we see that the presence of turbulence makes the reconnection layer thicker ($\Delta \sim l_{inj} \sim L$) and intrinsically three-dimensional since it applies to the entire volume of the current sheet. These two properties will be very important for allow for an efficient particle acceleration as we will describe in the next section.

This theory has been extensively investigated (e.g., Eyink et al. 2011; Lazarian et al. 2012) and confirmed numerically by means of 3D MHD simulations (Kowal et al. 2009, 2012). In particular, it has been shown (Eyink et al. 2011) that turbulent collisional fast reconnection prevails when the thickness of the current sheet is larger than the ion Larmor radius. As we will see later, for the systems we will study here this condition is naturally satisfied and we will adopt this model to derive the magnetic power released by fast reconnection. We should also notice that there has been direct evidences of turbulent reconnection in solar coronal events provided by observations with *Yohkoh* and *SOHO* satellites (e.g., Priest 2001) and also in the Earth magneto-tail (Retinò et al. 2007).

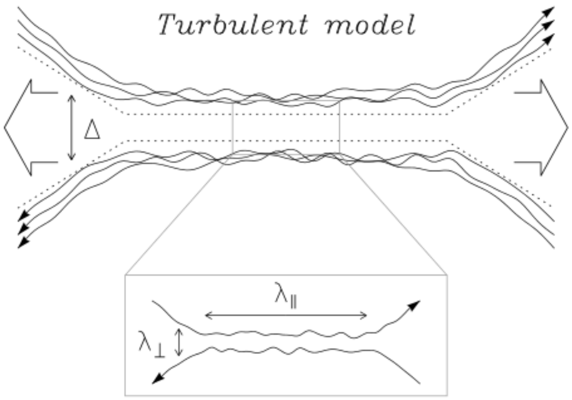

Figure 2.3: Schematic configuration of turbulent magnetic reconnection model (adapted from Lazarian et al. 2015).

2.2.2 First order Fermi acceleration in magnetic reconnection sites

As in shock acceleration where particles confined between the upstream and downstream flows of the velocity discontinuity undergo a first-order Fermi acceleration (see e.g., Blandford & Eichler 1987), de Gouveia Dal Pino & Lazarian (2005) proposed that a similar mechanism would occur when particles are trapped between the two converging magnetic flux tubes moving to each other in a current sheet with the reconnection velocity V_R. de Gouveia Dal Pino & Lazarian (2005) investigated this process analytically and showed that, as the particles bounce back and forth undergoing head-on collisions with magnetic fluctuations in the current sheet (see Figure 1.2 and Figure 2.4), their energy increases by $< \Delta E/E >\sim 8V_R/3c$ after each round trip, which therefore leads to an exponential energy growth after several round trips.

To demonstrate the relation above for $< \Delta E/E >$, we may consider the following process. The particles from the upper reconnection region will *see* the lower reconnection region moving towards them with the velocity $2V_R$ (see Figure 1.2). If a particle from the

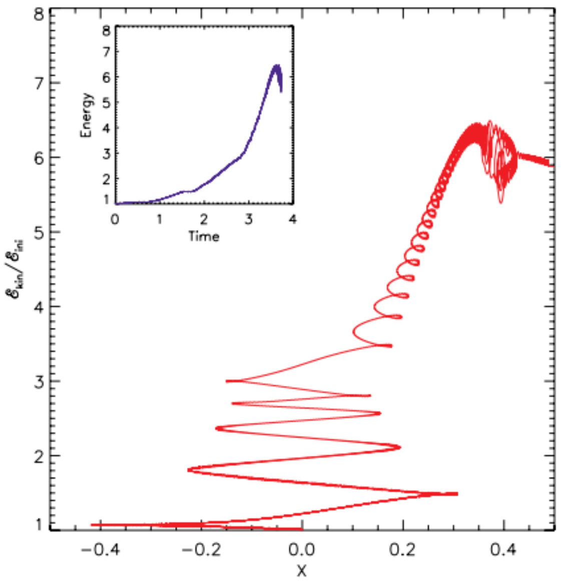

Figure 2.4: A single test particle is injected in a three-dimensional current sheet and undergoes a first-order Fermi acceleration while bouncing back and forth between the two-converging magnetic fluxes of opposite polarity (see Figure 1.2). This figure shows the resulting change of the particle kinetic energy with the X coordinate and in the detail the kinetic energy exponential increase with time (from Kowal et al. 2011)

upper region enters at an angle θ_p with respect to the direction of V_R into the lower region then the expected energy gain of the particle is $\Delta E/E = 2V_R \cos\theta_p/c$. For an isotropic distribution of particles their probability distribution function is $P(\theta_p) = 2\sin\theta_p \cos\theta_p d\theta_p$ and therefore the average energy gain per crossing of the reconnection region is (de Gouveia Dal Pino & Lazarian 2005)

$$< \frac{\Delta E}{E} >= \frac{V_R}{c}\int_0^{\pi/2} 2\cos^2\theta_p \sin\theta_p d\theta_p = 4/3\frac{V_R}{3} \tag{2.4}$$

Particles will complete a full acceleration cycle when they return back to the upper reconnection region. Similarly, if they are in the lower reconnection region they will see the upper reconnection region moving towards them with the speed $2V_R$. As a result, a full acceleration cycle provides an energy increase $< \Delta E/E >= 8/3\frac{V_R}{c}$

The relation above shows that in order to the process to be efficient, reconnection must be fast. As described in the previous section, this requires that V_R is of the order of the local Alfvén speed V_A.

This mechanism has been thoroughly tested by means of 2D and 3D MHD numerical simulations in which charged thermal particles have been accelerated to relativistic energies into collisional domains of fast magnetic reconnection (Kowal et al. 2011, 2012). Kowal et al. (2011) have demonstrated the equivalence between first-order Fermi particle acceleration involving 2D converging magnetic islands in current sheets (e.g., Drake et al. 2006, 2010), and the same process in 3D reconnection sites where the islands naturally break out into loops. Kowal et al. (2011) further demonstrated the importance of the presence of guide fields in 2D simulations to ensure equivalence with the results of more realistic 3D particle acceleration simulations, the presence of a guide field allows the particles to accelerate in the direction parallel to magnetic field as well (see more details in de Gouveia Dal Pino and Kowal 2015).

When considering embedded turbulence in the current sheet to make reconnection fast (as described by Lazarian & Vishniac 1999), Kowal et al. (2012) have verified the formation of a thick volume filled with small scale magnetic fluctuations in the reconnection layer. In order to test the acceleration of particles within such a domain, they introduced 10,000 protons and followed their trajectories. The left panel of Figure 2.5 shows the evolution of the kinetic energy of the particles in this case. After injection with a Maxwellian distribution, a large fraction of the test particles enter the current sheet and accelerate. Their kinetic energy grows exponentially which is in agreement with the prediction of the Fermi theory. The acceleration process is suggestive of a first order Fermi process (Kowal et al. 2012). In the sub-plot of the Figure 2.1, the particle spectrum shows the development of a power law index $\sim 1-2$ in the large energy tail. The evolution of the parallel and perpendicular components of the velocity with respect to the local mean magnetic field is shown in red and blue colors, respectively.

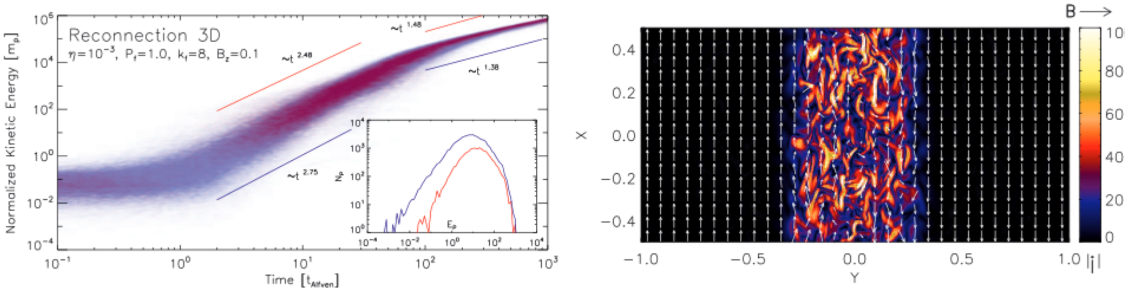

Figure 2.5: *Left panel*: Particle kinetic energy evolution and distribution for 10,000 test particles injected in a current sheet with turbulence embedded in order to make magnetic reconnection fast. The colors indicate which velocity component is accelerated (red or blue for parallel or perpendicular component to the local magnetic field, respectively). The energy is normalized by the rest proton mass. Subplots show the particle energy distributions at $t = 5.0t_A$, where the Alfvén time (t_A) is the typical length scale of reconnection layer divided by the Alfvén speed. *Right column*: XY cross section of 3D MHD simulation of the reconnection sheet with embedded turbulence where the particles were injected. It shows the current density distribution in the current sheet and the arrows depict the magnetic field orientation on both sides of the current sheet (Kowal et al. 2012)

We note also that tests performed in collisionless fluids, by means of 2D (e.g, Zenitani & Hoshino 2001; Zenitani et al. 2009; Drake et al. 2006, 2010; Cerutti et al. 2013, 2014; Sironi & Spitkovsky 2014), and 3D particle in cell (PIC) simulations (Sironi & Spitkovsky 2014) have generally achieved similar results to those of the collisional studies above with regard to the efficiency of the acceleration and the particle power law spectra, with the only difference that these can probe only the kinetic scales of the process (up to a few thousand particle skin depth), while the collisional MHD simulations probe the large MHD scales (Kowal et al. 2011, 2012).

Using the results of the 3D MHD numerical simulations of the acceleration of test particles in current sheets by Kowal et al. (2012) where reconnection was made fast by embedded turbulence (above Figure 2.5), we find that the acceleration rate for a proton is given by (Khiali et al. 2015a):

$$t^{-1}_{acc,rec,p} = 1.3 \times 10^5 \left(\frac{E}{E_0}\right)^{-0.4} t_0^{-1}(s), \tag{2.5}$$

where E is the energy of the accelerated proton, $E_0 = m_p c^2$, m_p is the proton rest mass, $t_0 = l_{acc}/v_A$ is the Alfvén time, and l_{acc} is the length scale of the acceleration region, for instance in this thesis, the width of current sheet is considered as l_{acc}. Although this result was found from numerical simulations employing protons as test particles, we can derive a similar expression for the electrons (Khiali et al. 2015a):

$$t^{-1}_{acc,rec,e} = 1.3 \times 10^5 \sqrt{\frac{m_p}{m_e}} \left(\frac{E}{E_0}\right)^{-0.4} t_0^{-1}(s), \tag{2.6}$$

where m_e is the electron rest mass. A detailed derivation of these two equations is presented in Appendix A.

The equations above will be used to compute the acceleration rates in our model as described in Chapters 4, 5 and 6.

As remarked above, the accelerated particles develop a power law energy distribution. An injected thermal particle distribution develops a power law tail at the highest energies as time goes by (see the details in Figure 2.5):

$$Q(E) \propto E^{-p}, \tag{2.7}$$

The analytical estimates of the first-order Fermi accelerated particle power law spectrum in current sheets predict power law indices $p \sim 1 - 2.5$ (e.g., de Gouveia Dal Pino & Lazarian 2005; Giannios 2010; Drury 2012), while the 3D MHD numerical simulations described above predict $p \sim 1$, which is also comparable with results obtained from 2D collisionless PIC simulations considering merging islands $p \sim 1.5$ (Drake et al. 2010), or X-type Petschek 2D configurations (e.g., Zenitani & Hoshino 2001), for which it has been obtained $p \sim 1$, or even with more recent 3D PIC simulations (Sironi & Spitkovsky 2014) which obtained $p < 2$. In summary, considering both analytical and numerical predictions $p \sim 1 - 2.5$. In this thesis, we will adopt values of p within this range of values. We note however that, at least in the case of the 3D MHD simulations, some caution is necessary with the derived spectral index $p \sim 1$, because in these simulations, particles are allowed to re-enter in the periodic boundaries of the computational domain and be further accelerated causing some deposition of particles in the very high energy tail of the spectrum after saturation of the acceleration which may induce some artificial increase in the slope (del Valle et al. 2016).

As stressed in de Gouveia Dal Pino & Lazarian (2005), though we are considering a magnetically dominated region, it is also possible that a diffusive shock may develop in the coronal region around the magnetic reconnection zone, due to the interaction of "coronal mass ejections", i.e. ejected plasma released by fast reconnection along the magnetic field lines, as observed in the solar corona when flares occur (see also Section 2.3 below). In this case, one should expect the shock velocity to be predominantly parallel to the magnetic field lines and the acceleration rate for a particle of energy E in a magnetic field B, would be approximately given by (e.g., Spruit 1988):

$$t^{-1}_{acc,shock} = \frac{\eta e c B}{E}, \tag{2.8}$$

where $0 < \eta \ll 1$ characterizes the efficiency of the shock acceleration. We fix $\eta = 10^{-2}$, which is appropriate for shocks with velocity $v_s \approx 0.1c$ commonly assumed in the Bohm regime (e.g., Romero et al. 2010b). In Chapters 4, 5 and 6, we will consider both acceleration mechanisms in the surrounds of the BH sources in order to evaluate the relative importance of both processes in the cores of these sources.

2.3 Conditions for fast magnetic reconnection and particle acceleration around BH sources

As remarked earlier, we will investigate here the acceleration of relativistic particles in the core of microquasars and LLAGNs, in the surrounds of the BH near the basis of the jet launching, as a result of events of fast magnetic reconnection and examine whether this process may reproduce the observed emission pattern specially at VHEs. This model has been described in detail by de Gouveia Dal Pino & Lazarian (2005); de Gouveia Dal Pino et al. (2010) and more recently by Kadowaki et al. (2015).

2.3.1 The accretion disk and magnetic field configuration around the BH source

Although there is still much speculation on what should be the strength and geometry of the magnetic fields in the surrounds of BHs, these are necessary ingredients in order to explain, e.g., the formation of narrow relativistic jets (e.g., Blandford 1976; Blandford and Payne 1982). As in de Gouveia Dal Pino & Lazarian (2005); de Gouveia Dal Pino et al. (2010) and Kadowaki et al. (2015), we employ a magnetized standard Shakura-Sunyaev (geometrically thin and optically thick) accretion disk around the BH [4] (Shakura & Sun-

---

[4] As stressed in Chapter 1, we note that the model here described also works when considering a magnetic ADAF accretion disk around the BH (see Singh et al. 2015).

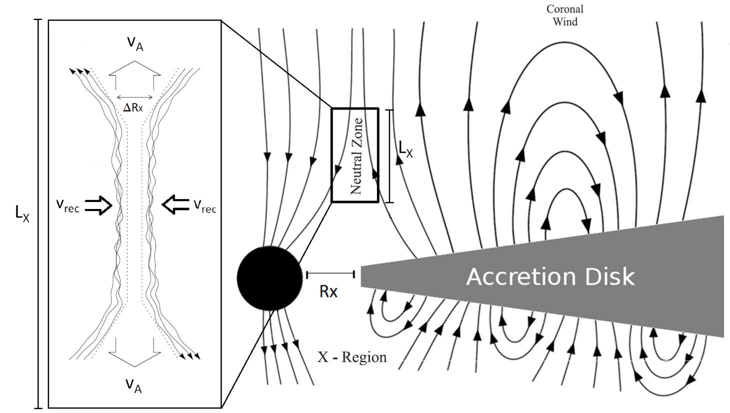

Figure 2.6: Scheme of magnetic reconnection between the lines rising from the accretion disk and the lines around the BH horizon. Reconnection is made fast by the presence of embedded turbulence in the reconnection zone (see text for more details). Particle acceleration may occur in the magnetic reconnection zone by a first-order Fermi process (adapted from GL05).

yaev 1973) (see the cartoon of Fig 2.6). Figure 2.6 presents a schematic representation of the possible magnetic field configuration around the BH.

The magnetosphere around the central BH can be built from the drag of magnetic field lines by the accretion disk (see de Gouveia Dal Pino & Lazarian 2005 and Kadowaki et al. 2015). The large-scale poloidal magnetic field in the disk corona can in turn be formed by the action of a dynamo inside the accretion disk or dragged from the surroundings. Under the action of disk differential rotation, this poloidal magnetic flux gives rise to a wind that partially removes angular momentum from the system and increases the accretion rate. This, in turn, increases the ram pressure of the accreting material that will press the magnetic lines in the inner disk region against the lines of the BH magnetosphere thus favouring the occurrence of reconnection (see Figure 2.6). We note that according to mean field dynamo theory, an inversion of the polarization of the magnetic lines is expected to occur every half of the dynamo cycle; when this happens a new flux of disk lines should reach the inner region with an inverted polarity with respect to the magnetic flux already sitting around the BH, therefore, favouring magnetic reconnection between the two fluxes. The advection of field lines from the outer regions also allows for periodic changes in the polarity (see more details in Kadowaki et al. 2015).

We note that the strongly magnetized and low dense coronal fluid of the systems we are considering in this work satisfies the condition $L > l_{mfp} > r_l$, where L is the typical large scale dimension of the system, l_{mfp} the ion mean free path $l_{mfp} = 1.44 \times 10^{17} \frac{T_i^2(eV)}{n_i ln\Lambda}$, where T_i and n_i are the ion temperature in eV and the number density, respectively, $ln\Lambda \sim 25$ is the Coulomb logarithm and r_l the ion Larmor radius ($r_l = \frac{E}{ceB}$). For such flows a weakly collisional or effectively collisional MHD description is more than appropriate and we will employ this approach here.

We further notice that we describe below the accreting and coronal flow around the BH adopting a nearly non-relativistic approximation. In Kadowaki et al. 2015, it is given quantitative arguments that indicate that this is a reasonable assumption. For instance, the evaluation of the magnetic reconnection power considering a pseudo-Newtonian gravitational potential to reproduce general relativistic effects, gives a value that is similar to the classical case. A kinematic relativistic approach for the accreting and coronal flows is not necessary either, since we are dealing with characteristic ion/electron temperatures smaller than or equal $\sim 10^9$K. Nevertheless, with regard to reconnection, the fact that v_A may approach the light speed (see below), may imply that relativistic effects can affect the turbulent driven fast reconnection. In particular, a recent study (Cho & Lazarian 2014; see also Lazarian, Kowal, Takamoto, de Gouveia Dal Pino and Cho 2015, in press) has demonstrated that relativistic collisional MHD turbulence behaves as in the non-relativistic case which indicates that Lazarian & Vishniac (1999) theory of fast reconnection can be also applicable in the nearly relativistic regime (see Section 2.3.2 below).

The magnetic field intensity in the inner disk and coronal region can be determined from the balancing between the magnetic pressure of the BH magnetosphere and the accretion ram and is given by (Kadowaki et al. 2015):

$$\frac{\dot{M}}{4\pi R_X^2}(\frac{2GM}{R_X})^{\frac{1}{2}} \sim \frac{B^2}{8\pi}, \tag{2.9}$$

so that

$$B \cong 9.96 \times 10^8 r_X^{-1.25} \xi^{0.5} m^{-0.5} \text{ G}, \tag{2.10}$$

where m is the BH mass in units of solar mass, ξ is the mass accretion disk rate in units of the Eddington rate [5] ($\xi = \dot{M}/\dot{M}_{Edd}$, with $\dot{M}_{Edd} = 1.45 \times 10^{18} m$ g s^{-1}), and $r_X = R_X/R_S$ is the inner radius of the accretion disk in units of the BH Schwarzchild radius ($R_S = \frac{2GM}{c^2}$). The last stable orbit around the BH is $r_X = 3$ and although physically possible, this condition leads to a singularity in the Shakura-Sunyaev disk solutions and, therefore, we adopt an inner radius $r_X = 6$, to avoid the singularity.

2.3.2 Fast magnetic reconnection condition in the surrounds of the BH source

As described in section 2.2, the presence of turbulence in the coronal flow and specially, the turbulence embedded in the current sheet formed by the encounter of the magnetic lines arising from the accretion disk and those of the BH magnetosphere can make reconnection very fast and cause the release of large amounts of magnetic energy power in the scenario described in Figure 2.6.

There is also another mechanism to induce fast magnetic reconnection based on anomalous resistivity (AR). This occurs in the presence of current driven instabilities that can enhance the microscopic Ohmic resistivity and speed up reconnection to rates much larger than that probed by the latter. However, AR results rates which are much smaller than reconnection driven by turbulence as it prevails only at very small scales of the fluid. In fact, as shown in Kadowaki et al. 2015, AR predicts a much thinner reconnection region and is unable to reproduce the observed emission for most of the sources they investigated. In particular, it has been demonstrated by Kadowaki et al. (2015) that magnetic power released by fast reconnection driven by AR cannot accelerate particles to energies larger than 10^{12} eV, because the calculated thickness of reconnection layer by AR is compatible with the Larmor radius corresponded to particle energies $\sim 10^{12}$eV.

---

[5] The maximum luminosity of an accreting source when there is balance between the force of radiation acting outward and the gravitational force acting inward is called Eddington limit. For accretion powered objects this limit implies a limit on the steady accretion rate, $\dot{M}_{Edd}$ (gs^{-1}) (Frank et al. 2002, page 2).

The employment of a fast magnetic reconnection model driven by turbulence, requires fiducial sources of turbulence. The fluids we are investigating here have large hydrodynamical and magnetic Reynolds numbers. The hydrodynamical Reynolds number for the LLAGNs and microquasars are $R_e = Lv/\nu \sim 10^{26}$ and $R_e \sim 10^{20}$, respectively. Where v corresponds to a characteristic velocity of the fluid and ν is the kinematic viscosity. For a magnetized fluid this is dominated by motions transverse to the magnetic field and is given by $\nu \sim 1.7 \times 10^{-2} n_c ln\Lambda/(T_c^{0.5} B^2)$ cm^{2}s^{-1}, where $ln\Lambda \sim 25$ is the Coulomb logarithm, while n_c and T_c are the coronal number density and temperature, respectively (see Eqs. 2.14 and 2.15 below).

Similarly, the magnetic Reynolds number is $R_{em} = Lv/\eta \sim 10^{24}$ for the LLAGNs and $R_{rm} \sim 10^{18}$ in the case of microquasars, where the magnetic diffusion coefficient η in the regime of strong magnetic fields is given by $\eta = 1.3 \times 10^{13} cm^2 s^{-1} Z ln\Lambda T^{-3/2}$ (Spitzer 1962), with Z being the ion charge number.

The high Reynolds numbers above imply that both the fluid and the magnetic field lines can be highly distorted and turbulent if there is turbulence triggering. In other words, any instability can naturally drive turbulence with characteristic velocities of the order of the particles thermal speed. Also, the occurrence of continuous magnetic reconnection during the building of the corona itself in the surrounds of the BH (Liu et al., 2003) will contribute to the onset of turbulence which will then be further fed by fast reconnection as in the Lazarian-Vishniac model (1999). Numerical simulations of coronal disk accretion also indicate the formation of a turbulent flow in the surrounds of the BH that may be triggered by magneto-rotational instability (see e.g, Tchekhovskoy et al., 2011; McKinney et al., 2012; Dexter et al., 2014). All these processes may ensure the presence of embedded turbulence in the magnetic discontinuity described in Figure 2.6.

The magnetic reconnection power released by turbulent driven fast reconnection in the magnetic discontinuity region (as sketched in Figure 2.6) has been derived in Kadowaki et al. (2015) and is given by:

$$W \simeq 1.66 \times 10^{35} \psi^{-0.5} r_X^{-0.62} l^{-0.25} l_X q^{-2} \xi^{0.75} m \;\; \text{erg s}^{-1}, \tag{2.11}$$

where $l = L/R_S$ is the height of the corona in units of R_S; $l_X = L_X/R_S$, $L_X \leq L$ is the extension of the magnetic reconnection zone (as shown in Figure 2.6), $q = [1-(3/r_X)^{0.5}]^{0.25}$ and $v_A = v_{A0}\psi$ is the relativistic form of the Alfvén velocity, with $v_{A0} = B/(4\pi\rho)^{1/2}$, B being the local magnetic field, $\rho \simeq n_c m_p$ the fluid density in the corona, n_c the coronal number density, m_p the proton mass, and $\psi = [1 + (\frac{v_{A0}}{c})^2]^{-1/2}$ Somov 2012.

In the work done by Kadowaki et al. (2015), a fiducial parametric space appropriate to BH sources was adopted considering $0.05 \leq \xi \leq 1$, $1 \leq l \leq 1$ and $0.06l \leq l_X \leq l$ (assuming $R_X = 6R_S$). In this work, we will consider values within this parametric space. As remarked in Chapter 1, they have shown that with this parametric space the calculated magnetic reconnection power according to Equation 2.11 is more than sufficient to explain the observed radio core and gamma-ray luminosities of LLAGNs and microquasars.

In Chapters 4 and 5, we will employ the equation above to model the acceleration of particles and the emission in the core of the microquasars Cyg X-1 & Cyg X-3 and LLAGNs Cen A, Per A, M87 and IC 310.

The acceleration region in our model corresponds to the cylindrical shell where magnetic reconnection takes place, as in Figure 2.6. This shell has a length l_X, with inner and outer radii given by R_X and $R_X + \Delta R_X$ respectively, where ΔR_X is the width of the shell corresponding to the current sheet which according to Eq. 2.3 is given by (Kadowaki et al. 2015):

$$\Delta R_X \cong 2.34 \times 10^4 \psi^{-0.31} r_X^{0.48} l^{-0.15} l_X q^{-0.75} \xi^{-0.15} m \text{ cm}. \tag{2.12}$$

The disk temperature in this model can be calculated from the standard disk model and is given by :

$$T_d \cong 3.71 \times 10^7 \alpha^{-0.25} r_X^{-0.37} m^{0.25} \text{ K}, \tag{2.13}$$

where $0.05 \leq \alpha < 1$ is the Shakura-Sunyaev disk viscosity parameter which we here assume to be of the order of 0.5. We will need this parameter in order to evaluate the black body radiation field of the accretion disk.

This model is able to provide the particle number density n_c in the coronal region in the surrounds of the BH, which is needed to model the acceleration mechanism and evaluate the cooling processes which is given by (Kadowaki et al. 2015):

$$n_c \cong 8.02 \times 10^{18} r_X^{-0.375} \psi^{0.5} l^{-0.75} q^{-2} \xi^{0.25} m^{-1} \text{ cm}^{-3}, \tag{2.14}$$

while the coronal temperature is

$$T_c \cong 2.73 \times 10^9 r_X^{-0.187} \psi^{0.25} l^{0.125} q^{-1} \xi^{0.125} \text{ K}. \tag{2.15}$$

The Eqs. 2.14 and 2.15 above were derived employing the model of Liu et al. (2002). As in the solar corona, this model assumes that gas evaporation at the foot point of a magnetic flux tube quickly builds up the density of the corona to a certain value and that the tube radiates the heating due to magnetic reconnection through Compton scattering.

We assume that the total power L_{tot} injected in relativistic particles is a fraction of the total released power by magnetic reconnection (W, see Eq. 2.11), so that we will have:

$$L_{tot} = f\ W \tag{2.16}$$

with $f < 1$. This power heats the surrounding gas and accelerates particles. We assume that approximately 50% ($f = 0.5$) of it is used to accelerate the particles. This is consistent with plasma laboratory experiments of particle acceleration in reconnection sheets (e.g., Yamada et al. 2014) and also with the observations of flares in the Sun (e.g., Lin & Hudsun 1971).

This power (L_{tot}) is shared between relativistic protons and electrons, we assume that half goes to the protons and half to the electrons.

2.4 What we have learned

We here described a first order Fermi particle acceleration model in magnetic reconnection sites based on de Gouveia Dal Pino & Lazarian 2005 model, showing its numerically tested efficiency (Kowal et al. 2011, 2012), specially when reconnection is made fast due to the presence of turbulence in the current sheet. Then, we described the applicability of this process in the coronal region around BH/accretion disk systems, calculating the total magnetic reconnection power that can be released as a function of the BH, accretion disk and coronal parameters. We also derived the corresponding acceleration rate for protons and electrons. These results will be applied to the construction of the SED of specific BH sources in Chapters 4 and 5.

In the next Chapter, we will describe how the accelerated particles in the surrounds of BH sources loose their energy and how their accelerated power law spectrum is modulated by these processes in the emission region around the acceleration zone.

Chapter 3

Relevant non-thermal radiative processes

Energetic charged particles in a flow cool down and radiate while interacting with magnetic, radiation and matter fields. In this chapter, the main non-thermal processes that involve highly relativistic electrons and protons are reviewed. We will present the main features of each interaction. The main purpose in this part is to single out what are the relevant processes occurring in the surrounds of the BHs. Also, we will show the cooling time-scale of each process as a function of the energy of the particles and the main equations that describe the high energy particle distribution.

In the second part of this Chapter, we will review the relevant absorption processes of the radiation produced by the relativistic particles in the surrounds of the BH sources.

These processes will be employed in Chapters 4 and 5 in the building of the spectral energy distribution of the cores of microquasars and low luminosity AGNs, respectively.

3.1 What we want to know

In summary, the main questions to be addressed in this Chapter are:

- What are the relevant non-thermal processes in the surrounds of BH?
- How to calculate the cooling time-scales of these processes and their fluxes for both hadronic and leptonic processes?
- How and what fraction of the produced radiation by the accelerated relativistic particles is absorbed locally in the core region of BH sources?

3.2 Relativistic particle cooling mechanisms

In this section we discuss briefly the relevant radiative loss processes for electrons and protons due to their interactions with the magnetic, matter and radiation fields to radiate.

3.2.1 Relativist particle interactions with the magnetic field

Charged particles with energy E, mass m and charge number Z spiralling in a magnetic field $\vec{B}$ emit synchrotron radiation at a rate (Rybicki & Lightman 1986)

$$t^{-1}_{synch}(E) = \frac{4}{3}\left(\frac{m_e}{m}\right)^3 \frac{\sigma_T B^2}{m_e c 8\pi}\frac{E}{mc^2}, \tag{3.1}$$

where m_e is the electron mass and σ_T is the Thompson cross section (see Fig. 3.1). The synchrotron spectrum radiated by a distribution of particles $N(E)$ as function of the scattered photon energy (E_γ) in units of power per unit area is (e.g., Villa & Aharonian 2009)

$$L_\gamma(E_\gamma) = \frac{E_\gamma V}{4\pi d^2}\frac{\sqrt{2}e^3 B}{hmc^2}\int_{E_{min}}^{E_{max}} dE N(E)\frac{E_\gamma}{E_c}\int_{\frac{E_\gamma}{E_c}}^{\infty} K_{5/3}(\xi)d\xi, \tag{3.2}$$

where V is the volume of the emission region, d is the distance of the source from us, h is the Planck constant, $K_{5/3}(\xi)$ is the modified Bessel function of 5/3 order, and the characteristic energy E_c is

$$E_c = \frac{3}{4\pi}\frac{ehB}{mc}\left(\frac{E}{mc^2}\right)^2. \tag{3.3}$$

In these calculations we assumed that the particle velocity is perpendicular to the local magnetic field in the emission region. To compute Eq. 3.2 we used the approximation

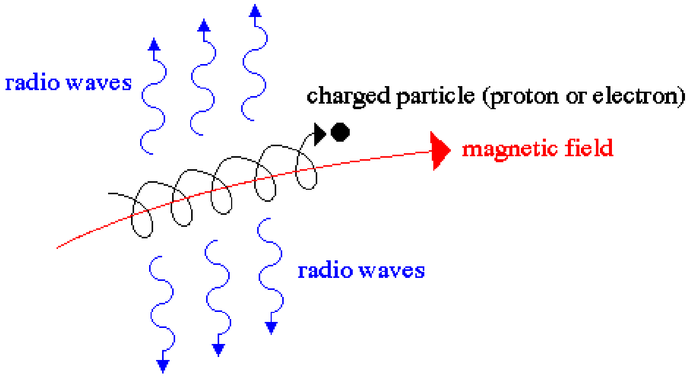

Figure 3.1: Synchrotron radiation of a charged particle spiralling around a magnetic field line (Credit: James Schombert, University of Oregon)

$$x\int_x^\infty K_5/3(\xi)d\xi \approx 1.85x^{1/3}e^{-x}. \tag{3.4}$$

where $x = E_\gamma/E_c$.

Practically, the synchrotron emission of the electrons dominates the low energy photon background which is a proper target for both inverse Compton (IC) and proton-photon ($p\gamma$) interactions (see below; see also e.g., Reynoso et al. 2011). The number density for multi-wavelength synchrotron scattered photons (in units of photons per energy per volume), has been approximated as (Zhang, Chen & Fang 2008)

$$n_{synch}(\epsilon) = \frac{L_\gamma(\epsilon)}{\epsilon^2 V}\frac{r}{c}4\pi d^2, \tag{3.5}$$

where r stands for the radius of the emission region and ϵ for the scattered synchrotron radiation energy. More precisely, ϵ corresponds to the photon energy of the multi-wavelength target radiation field for Synchrotron Self Compton (SSC) and $p\gamma$ interactions (see below).

3.2.2 Relativistic particle interactions with matter

Bremsstrahlung

When a relativistic electron accelerates in the presence of the electrostatic field of a charged particle or a nucleus of charge Ze, Bremsstrahlung radiation is produced (Fig. 3.2). For a fully ionized plasma with ion number density n_i, the Bremsstrahlung cooling rate is (Berezinskii 1990):

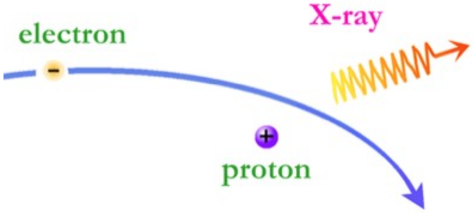

Figure 3.2: Bremsstrahlung radiation of an electron accelerating around the nucleus of an ionised atom (Credit: Sarah H.R. Bank, Towson University)

$$t_{Br}^{-1} = 4 n_i Z^2 r_0^2 \alpha_f c \left[\ln\left(\frac{2E_e}{m_e c^2}\right) - \frac{1}{3} \right], \tag{3.6}$$

where r_0 is the electron classical radius and α_f stands for the fine structure constant and E_e is the relativistic electron energy. The relativistic Bremsstrahlung spectrum (in units of power per unit area) is given by (Romero et al. 2010a)

$$L_\gamma(E_\gamma) = \frac{E_\gamma V}{4\pi d^2} \int_{E_\gamma}^{\infty} n \sigma_B(E_e, E_\gamma) \frac{c}{4\pi} N_e(E_e) dE_e, \tag{3.7}$$

where

$$\sigma_B(E_e, E_\gamma) = \frac{4\alpha_f r_0^2}{E_\gamma} \Phi(E_e, E_\gamma), \tag{3.8}$$

and

$$\Phi(E_e, E_\gamma) = \left[1 + \left(1 - \frac{E_\gamma}{E_e}\right)^2 - \frac{2}{3}\left(1 - \frac{E_\gamma}{E_e}\right) \right] \times \left[\ln \frac{2E_e(E_e - E_\gamma)}{m_e c^2 E_\gamma} - \frac{1}{2} \right]. \tag{3.9}$$

Proton-proton (pp) inelastic collision

One relevant gamma-ray production mechanism is the decay of neutral pions which can be created through inelastic collisions of the relativistic protons, for instance, with nuclei of the corona that surrounds the accretion disk by means of the following reactions (see Fig. 3.3, Atoyan & Dermer 2003; Becker 2008)

$$p + p \rightarrow n_1(\pi^+ + \pi^-) + n_2\pi^0 + p + p \tag{3.10}$$

where $\pi^\pm$ are charged pions, π^0 is neutral pion, n_1 and n_2 are multiplicities. π^0 will decay in gamma photons $\pi^0 \rightarrow \gamma + \gamma$ (Stecker 1970, 1971), carrying 33% of the accelerated proton energy. The charged pions $\pi^\pm$ also decay and produce neutrinos that will be discussed in Chapter 6 in more detail.

In this case the cooling rate is given by (Kelner 2006)

$$t_{pp}^{-1} = n_i c \sigma_{pp} k_{pp}, \tag{3.11}$$

where k_{pp} is the total in-elasticity of the process of value ~ 0.5. The corresponding cross section for inelastic pp interactions σ_{pp} can be approximately by (Kelner et al. 2009)

$$\sigma_{pp}(E_p) = \left(34.3 + 1.88L_\sigma + 0.25L_\sigma^2\right)\left[1 - \left(\frac{E_{th}}{E_p}\right)^4\right]^2 \text{mb}, \tag{3.12}$$

where mb stands for milli-barn, $L_\sigma = \ln\left(\frac{E_p}{1TeV}\right)$, and the proton threshold kinetic energy for neutral pion (π^0) production is $E_{th} = 2m_\pi c^2(1+\frac{m_\pi}{4m_p}) \approx 280$ MeV, where $m_\pi c^2 = 134.97$ MeV is the rest energy of π^0 (Villa & Aharonian 2009). This particle decays in two photons with a probability of 98.8%.

The spectrum can be calculated by

$$L_\gamma(E_\gamma) = \frac{E_\gamma^2 V}{4\pi d^2} q_\gamma(E_\gamma), \tag{3.13}$$

where $q_\gamma(E_\gamma)(\text{erg}^{-1}\text{cm}^{-3}\text{s}^{-1})$ is the gamma-ray emissivity.

For proton energies less than 0.1 TeV, $q_\gamma(E_\gamma)$ is

$$q_\gamma(E_\gamma) = 2\int_{E_{min}}^{\infty} \frac{q_\pi(E_\pi)}{\sqrt{E_\pi^2 - m_\pi^2 c^4}} dE_\pi, \tag{3.14}$$

where $E_{min} = E_\gamma + m_\pi^2 c^4/4E_\gamma$ and $q_\pi(E_\pi)$ is the pion emissivity. An approximate expression for $q_\pi(E_\pi)$ can be calculated using the δ-function (Aharonian & Atoyan 2000). For this purpose, a fraction k_π of the kinetic energy of the proton $E_{kin} = E_p - m_p c^2$ is taken by the neutral pion (Villa & Aharonian 2009). The neutral pion emissivity is then given by

$$\begin{aligned} q_\pi(E_\pi) &= c n_i \int \delta(E_\pi - k_\pi E_{kin}) \sigma_{pp}(E_p) N_p(E_p) dE_p \\ &= \frac{c n_i}{k_\pi} \sigma_{pp}(m_p c^2 + \frac{E_\pi}{k_\pi})\, N_p(m_p c^2 + \frac{E_\pi}{k_\pi}). \end{aligned} \tag{3.15}$$

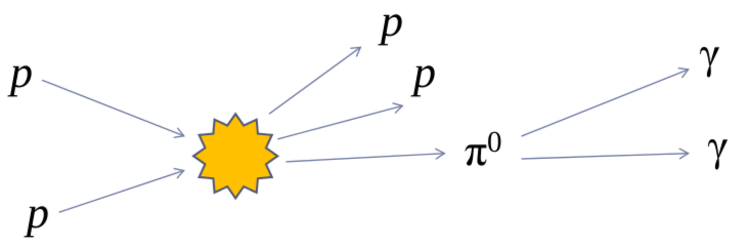

Figure 3.3: Proton-proton inelastic interactions (Credit: Greg Vance, University of Wisconsin)

The target ambient nuclei density is given by n_i and $N_p(E_p)$ stands for the energy distribution of the relativistic protons. For proton energies in the range GeV-TeV, $k_\pi \approx 0.17$ (Gaisser 1990), the total cross section $\sigma_{pp}(E_p)$ can be approximated by

$$\sigma_{pp}(E_p) \approx \begin{cases} 30\left[0.95 + 0.06 ln\left(\frac{E_{kin}}{1GeV}\right)\right] mb & E_{kin} \geq 1\text{GeV}, \\ 0 & E_{kin} < 1\text{GeV}. \end{cases} \tag{3.16}$$

The cross section increases slowly with energy (see Fig. 3.4).

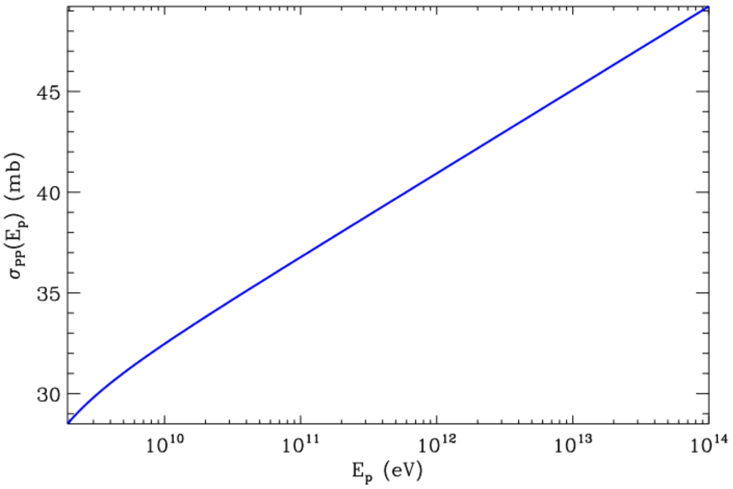

Figure 3.4: Cross section of the production of neutral pions in proton-proton collision σ_{pp}, as a function of E_p (Cerutti 2013)

For proton energies greater than 0.1 TeV, the gamma-ray emissivity is

$$\begin{aligned} q_\gamma(E_\gamma) &= cn_i \int_{E_\gamma}^{\infty} \sigma_{inel}(E_p) N_p(E_p) E_\gamma(\frac{E_\gamma}{E_p}, E_p) \frac{dE_p}{E_p} \\ &= cn_i \int_0^1 \sigma_{inel}(\frac{E_\gamma}{x}) N_p(\frac{E_\gamma}{x}) F_\gamma(x, \frac{E_\gamma}{x}) \frac{dx}{x}. \end{aligned} \tag{3.17}$$

The inelastic pp cross section is approximately given by

$$\sigma_{inel}(E_p) = (34.3 + 1.88 L_\sigma + 0.25 L_\sigma^2)[1 - (\frac{E_{th}}{E_p})^4]^2 mb, \tag{3.18}$$

Here $E_{th} = m_p + 2m_\pi + \frac{m_\pi^2}{2m_p} = 1.22$ GeV is the threshold energy of the proton to produce neutral pions π^0 and the number of photons whose energies are in the range of $(x, x+dx)$ where $x = E_\gamma/E_p$, caused per pp collision can be approximated by (Villa & Aharonian 2009)

$$F_\gamma(x, E_p) = B_\gamma \frac{lnx}{x} [\frac{1 - x^{\beta_\gamma}}{1 + k_\gamma x^{\beta_\gamma}(1 - x^{\beta_\gamma})}]^4 \times [\frac{1}{lnx} - \frac{4\beta_\gamma x^{\beta_\gamma}}{1 - x^{\beta_\gamma}} - \frac{4k_\gamma \beta_\gamma x^{\beta_\gamma}(1 - 2x^{\beta_\gamma})}{1 + k_\gamma x^{\beta_\gamma}(1 - x^{\beta_\gamma})}]. \tag{3.19}$$

The best least-squares fits to the numerical calculations yield:

$$B_\gamma = 1.30 + 0.14L_\sigma + 0.011L_\sigma^2, \tag{3.20}$$

$$\beta_\gamma = (1.79 + 0.11L_\sigma + 0.008L_\sigma^2)^{-1}, \tag{3.21}$$

$$k_\gamma = (0.801 + 0.049L_\sigma + 0.014L_\sigma^2)^{-1}. \tag{3.22}$$

Where $L_\sigma = ln(E_p/1TeV)$ and $0.001 \leq x \leq 0.1$ (for more details see Villa & Aharonian 2009).

3.2.3 Relativistic particle interactions with the radiation field

Energetic electrons transfer their energy to low energy photons causing them to radiate at high energies (inverse Compton process). On the other hand, when high energy protons interact with low energy photons ($p\gamma$ interactions) they produce pions and gamma-ray photons with energies larger than 10^8 eV in the so called photomeson process.

Inverse Compton

Cold photons can be boosted to high energies through inverse Compton (IC) scattering off relativistic electrons (See Fig. 3.5). The IC cooling rate for an electron in the wide energy range of target photon fields (from radio to gamma rays) is given by (Blumenthal & Gould 1970)

$$t_{IC}^{-1}(E_e) = \frac{1}{E_e}\int_{\epsilon_{min}}^{\epsilon_{max}}\int_{E_{ph}}^{\frac{\Gamma E_e}{1+\Gamma}}(E_\gamma - E_{ph})\frac{dN}{dtdE_\gamma}dE_\gamma. \tag{3.23}$$

Here E_{ph} and E_γ are the incident and scattered photon energies, respectively, and

$$\frac{dN}{dtdE_\gamma} = \frac{2\pi r_0^2 m_e^2 c^5}{E_e^2}\frac{n_{ph}(E_{ph})dE_{ph}}{E_{ph}}F(q), \tag{3.24}$$

where $n_{ph}(E_{ph})$ is the target photon density (in units of energy^{-1}volume^{-1}) and

$$F(q) = 2q\ln q + (1+2q)(1-q) + 0.5(1-q)\frac{(\Gamma q)^2}{1+\Gamma}, \tag{3.25}$$

$$\Gamma = 4E_{ph}E_e/(m_ec^2)^2, \tag{3.26}$$

$$q = \frac{E_\gamma}{[\Gamma(E_e - E_\gamma)]}. \tag{3.27}$$

Accelerated electrons around the BH may have interaction with photons produced by the synchrotron emission in the coronal region, in which case the process is SSC, or by photons emitted by the surface of the accretion disk. This photon field can be represented by a black body radiation and is given by

$$n_{bb}(E_{ph}) = \frac{1}{\pi^2\lambda_c^3 m_ec^2}(\frac{E_{ph}}{m_ec^2})^2[\frac{1}{\exp(\frac{E_{ph}}{kt}) - 1}]. \tag{3.28}$$

Here λ_c, t and k are the Compton wavelength ($\lambda_c = \frac{h}{mc}$, h stands for Planck constant and m for particle mass here in this case is m_e), disk temperature and Boltzmann constant, respectively.

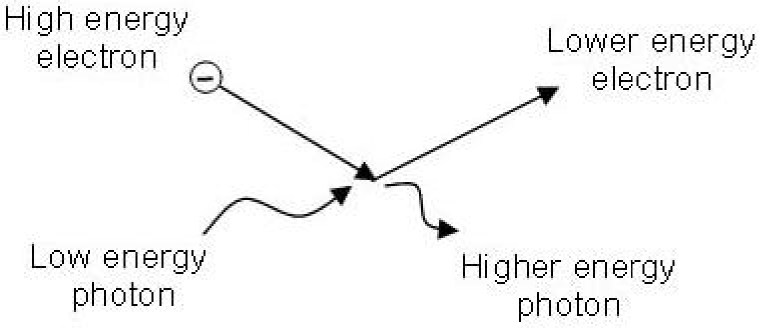

Figure 3.5: Inverse Compton (Credit: Jeff Stanger, University of Sydney)

Taking into account the Klein-Nishina effect[1] on the cross section, the total luminosity per unit area can be calculated from (Romero et al., 2010a)

$$L_{IC}(E_\gamma) = \frac{E_\gamma^2 V}{4\pi d^2}\int_{E_{min}}^{E_{max}} dE_e N_e(E_e) \times \int_{E_{ph,min}}^{E_{ph,max}} dE_{ph} P_{IC}(E_\gamma, E_{ph}, E_e), \tag{3.29}$$

---

[1] The Klein-Nishina formula gives the differential cross section of photons scattered from a single free electron in lowest order of quantum electrodynamics. At low frequencies (e.g., visible light) this is referred to as Thomson scattering; at higher frequencies (e.g., x-rays and gamma-rays) this is referred to as Compton scattering (see Blumenthal & Gould 1970 for more details).

where d is distance of source to us and $P_{IC}(E_\gamma, E_{ph}, E_e)$ is the spectrum of photons scattered by an electron of energy $E_e = \gamma_e m_e c^2$ in a target radiation field of density $n_{ph}(E_{ph})$. According to Blumenthal & Gould (1970), it is given by

$$P_{IC}(E_\gamma, E_{ph}, E_e) = \frac{3\sigma_t c(m_e c^2)^2}{4E_e^2}\frac{n_{ph}(E_{ph})}{E_{ph}}F(q), \tag{3.30}$$

and for the scattered photons in the range

$$E_{ph} \leq E_\gamma \leq \frac{\Gamma}{1+\Gamma}E_e. \tag{3.31}$$

Proton-photon ($p\gamma$) interactions

The photomeson production takes place for photon energies greater than $E_{th} \approx 145$MeV. A single neutral pion can be produced in an interaction near the threshold and then decay giving rise to gamma-rays via the channels (Atoyan & Dermer 2003):

$$p + \gamma \to p + \pi^0, \tag{3.32}$$

with $\pi^0 \to \gamma + \gamma$ carrying 20% of the accelerated proton energy and

$$p + \gamma \to p + \pi^+ + \pi^-, \tag{3.33}$$

where the charged pions will also decay producing neutrinos as described in Chapter 6.

In our model the appropriate photons come from the synchrotron radiation. The cooling rate for this mechanism in an isotropic photon field with density $n_{ph}(E_{ph})$ can be calculated by (Stecker 1968):

$$t_{p\gamma}^{-1}(E_p) = \frac{c}{2\gamma_p^2}\int_{\frac{E_{th}^{(\pi)}}{2\gamma_p}}^{\infty} dE_{ph}\frac{n_{ph}(E_{ph})}{E_{ph}^2} \times \int_{E_{th}^{(\pi)}}^{2E_{ph}\gamma_p} d\epsilon_r \sigma_{p\gamma}^{(\pi)}(\epsilon_r)K_{p\gamma}^{(\pi)}(\epsilon_r)\epsilon_r, \tag{3.34}$$

where $\gamma_p = \frac{E_p}{m_e c^2}$, ϵ_r is the photon energy in the rest frame of the proton and $K_{p\gamma}^{(\pi)}$ is the in-elasticity of the interaction. Atoyan & Dermer (2003) proposed a simplified approach to calculate the cross-section and the in-elasticity which are given, respectively, by

$$\sigma_{p\gamma}(\epsilon_r) \approx \begin{cases} 340\ \mu barn & 300\mathrm{MeV} \le \epsilon_r \le 500\mathrm{MeV} \\ 120\ \mu barn & \epsilon_r > 500\mathrm{MeV}, \end{cases} \tag{3.35}$$

and

$$\mathrm{K}\dot{}\mathrm{p}\gamma(\epsilon_r) \approx \begin{cases} 0.2 & 300\mathrm{MeV} \le \epsilon_r \le 500\mathrm{MeV} \\ 0.6 & \epsilon_r > 500\mathrm{MeV}. \end{cases} \tag{3.36}$$

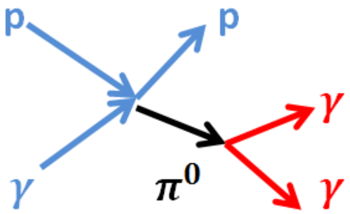

Figure 3.6: γ-ray production due to $p\gamma$ interaction

To find the luminosity from the decay of pions, we use the analytical approach proposed by Atoyan & Dermer (2003). Taking into account that each pion decays into two photons, the $p\gamma$ luminosity is

$$\begin{aligned} L_{p\gamma}(E_\gamma) &= 2\frac{E_\gamma^2 V}{4\pi d^2}\int Q_{\pi^0}^{(p\gamma)}(E_\pi)\delta(E_\gamma - 0.5E_\pi)dE_\pi \\ &= 20\frac{E_\gamma^2 V}{4\pi d^2}N_p(10E_\gamma)\omega_{p\gamma,\pi}(10E_\gamma)n_{\pi^0}(10E_\gamma), \end{aligned} \tag{3.37}$$

where $Q_{\pi^0}^{(p\gamma)}$ is the emissivity of the neutral pions given by

$$Q_{\pi^0}^{(p\gamma)} = 5N_p(5E_\pi)\omega_{p\gamma,\pi}(5E_\pi)n_{\pi^0}(5E_\pi), \tag{3.38}$$

$\omega_{p\gamma}$ stands for the collision rate which is

$$\omega_{p\gamma}(E_p) = \frac{m_p^2 c^5}{2E_p^2}\int_{\frac{E_{th}}{2\gamma_p}}^{\infty} dE_{ph}\frac{n_{ph}(E_{ph})}{E_{ph}^2}\int_{E_{th}}^{2E_{ph}\gamma_p} dE_r \sigma_{p\gamma}^{(\pi)}(E_r)E_r, \tag{3.39}$$

and n_{π^0} is the mean number of neutral pions produced per collision given by

$$n_{\pi^0}(E_p) = 1 - P(E_p)\xi_{pn}. \tag{3.40}$$

In the single-pion production channel, the probability for the conversion of a proton to a neutron with the emission of a $\pi^{\pm} meson$ is given by $\xi_{pn} \approx 0.5$. For photomeson interactions of a proton with energy E_p, the interaction probability is represented by $P(E_p)$, which is

$$P(E_p) = \frac{K_2 - \bar{K}_{p\gamma}(E_p)}{K_2 - K_1}. \tag{3.41}$$

The in-elasticity in the single-pion channel is approximated as $K_1 \approx 0.2$, whereas $K_2 \approx 0.6$. For energies above 500 MeV the mean inelasticity $\bar{K}_{p\gamma}$ is

$$\bar{K}_{p\gamma} = \frac{1}{t_{p\gamma}(\gamma_p)\omega_{p\gamma}(E_p)}. \tag{3.42}$$

where $t_{p\gamma}$ is the time of $p\gamma$ interactions (Eq. 3.34).

3.3 Photon absorption processes

3.3.1 Photon-photon ($\gamma\gamma$) annihilation

The photon-photon annihilation $\gamma + \gamma \to e^+ + e^-$ is the dominant absorption process for high-energy gamma rays produced by the radiative processes described above. They can be annihilated by the surrounding radiation field via electron-positron pair production.

This process is possible only above a kinematic energy threshold given by (Gould & Scheder 1967)

$$E_\gamma \epsilon (1 - \cos\theta) \geq 2m_e^2 c^4, \tag{3.43}$$

which in head-on collisions can be rewritten as

$$E_\gamma \epsilon > (m_e c^2)^2, \tag{3.44}$$

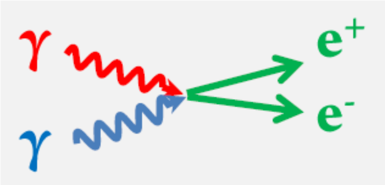

Figure 3.7: Pair production.

where E_γ and ϵ are the energies of the emitted gamma-ray and the ambient photons, respectively, and θ is the collision angle in the laboratory reference frame.

The attenuated luminosity $L_\gamma(E_\gamma)$ after the gamma-ray travels a distance l is (e.g., Romero & Christiansen 2005)

$$L_\gamma(E_\gamma) = L_\gamma^0(E_\gamma)e^{-\tau(l,E_\gamma)} \tag{3.45}$$

where L_γ^0 is the intrinsic coronal gamma-ray luminosity and $\tau(l, E_\gamma)$ is the optical depth. The differential optical depth is given by:

$$d\tau = (1-\mu)n_{ph}\sigma_{\gamma\gamma}d\epsilon d\Omega dl' \tag{3.46}$$

where $d\Omega$ is the solid angle of the target soft photons, μ is the cosine of the angle between the gamma-ray and the arriving soft photon, l' is the path along the gamma-ray emission and n_{ph} is the photon density (in cm^{-3}erg^{-1}sr^{-1}) of the surrounding field that we admit to be a black-body radiation field for the BH sources here investigated (see Chapters 4 and 5).

The $\gamma\gamma$ interaction cross-section $\sigma_{\gamma\gamma}$ is defined as (Gould & Scheder 1967)

$$\sigma_{\gamma\gamma}(\epsilon, E_\gamma) = \frac{\pi r_0^2}{2}(1-\beta^2)[2\beta(\beta^2-2) + (3-\beta^4)ln(\frac{1+\beta}{1-\beta})], \tag{3.47}$$

where r_0 is the classical radius of the electron and

$$\beta = [1 - \frac{(m_e c^2)^2}{\epsilon E_\gamma}]^{1/2}. \tag{3.48}$$

Since the gamma-ray absorption via photon-photon annihilation depends on the geometry of the systems, in Chapters 4 and 5, we will describe this effect in detail for both classes of astrophysical sources we are considering in this study, i.e., the black-hole binary systems (or microquasars) Cyg X-1 and Cyg X-3, and the LLAGNs or radio galaxy cores Cen A, Per A, M87, and IC 310, respectively.

3.3.2 Absorption of low-energy photons by photo-ionization (γN interactions)

The low energy photons produced in the nuclear emission region will propagate in the surrounding interstellar medium of the host galaxy filled mainly by hydrogen and helium gas. Photons with energies larger than the hydrogen Lyman threshold (13.6 eV) will be able to photo-ionize the neutral gas.

The optical depth resulting from these interactions is approximately given by

$$\tau_{\gamma H}(E_\gamma) = N_H \sigma_{\gamma N}(E_\gamma) \tag{3.49}$$

where N_H is the neutral hydrogen column density, and $\sigma_{\gamma N}$ is the absorption cross section. As in Reynoso et al. 2011, we take this from Ryter (1996) for $E_\gamma < 1$ keV considering that atomic hydrogen and galactic dust are the dominant components of the environment (Fig. 3.8). The values of N_H for each source investigated here are taken from the observations and are listed in Table 5.1.

It should be noted that as we see in Fig. 3.8, the maximum absorption edge corresponds to the hydrogen ionization energy ($\sim 10eV$), other three relevant absorption edges are corresponded to different ionization energies of helium, the K-shell electrons of oxygen, and the iron. Figure 3.8 shows the absorption edges corresponding to the different elements.

This γN absorption has been considered in the reconstruction of the SEDs of the four LLAGNs in Chapter 5. As we will see there, the photons produced in the optical-soft X-ray range are fully absorbed by these interactions.

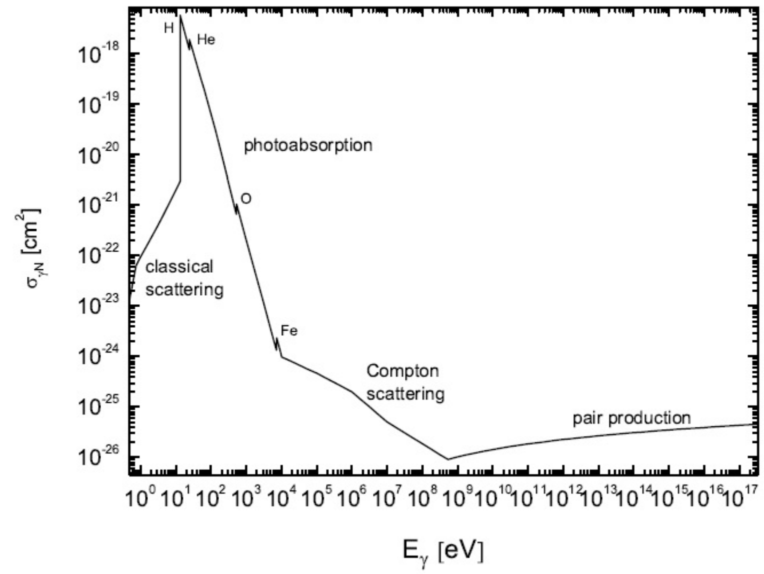

Figure 3.8: Cross section for photo-ionization process (Reynoso et al. 2011)

3.4 Energy distribution of the accelerated particles

As described in Chapter 2, the particles around the BH that are accelerated up to relativistic energies by the first-order Fermi process occurring in the magnetic reconnection site (Figure 2.6), will radiatively lose energy via the interactions described above with the surrounding magnetic field (producing synchrotron emission), the photon field (producing inverse Compton, synchrotron-self-Compton, and photo-mesons $p\gamma$), and with the surrounding matter (producing pp collisions and relativistic Bremsstrahlung radiation). The radiative cooling of the particles occurs mainly in the region around the reconnection site and we call it the *emission region* which can be assumed as a sphere or a torus encompassing the BH and the reconnection zone around it. This will characterize the emission volume V given in the equations in the previous sections.

We parametrize the injection spectrum of accelerated particles in the emission zone as (in units of erg^{-1}cm^{-3}s^{-1})

$$Q(E) = Q_0 E^{-p} exp[-E/E_{max}] \tag{3.50}$$

with $p > 0$ and E_{max} is the cut-off energy which can be calculated from the balance between the acceleration rates and the cooling rates due to the several processes described above. As stressed in section 2.2.2, we assume for the power law index p values between 1 and 2.5 for the sources here investigated.

The normalization constant Q_0 is calculated using Eq. 3.50 and the total power injected for each type of particle

$$L_{(e,p)} = \int_V d^3r \int_{E^{min}}^{E^{max}} dE\ E\ Q_{(e,p)}(E) \tag{3.51}$$

where V is the volume of the emission region and $L_{(e,p)}$ is the fraction of the magnetic reconnection power that accelerates the electrons and protons (see eq. 2.11).

The injection particle spectrum is modified in the emission region due to the radiative losses. We assume that the minimum energy of the particles is given by $E_{min} = (\gamma_{min} - 1)mc^2$, where m is the rest mass of the particles and γ_{min} is the minimum Lorentz factor. This is a free parameter of the model, but we find that it has very little influence on the results of the observed emission (Chapters 4 and 5).

The kinetic equation that describes the general evolution of the particle energy distribution $N(E,t)$ is the Fokker-Planck differential equation (Ginzburg & Syrovatskii, 1995). We here use a simplified form of this equation. We employ the one-zone approximation to find the particle distribution, assuming that the emission region is spatially thin enough, so that we can ignore spatial derivatives in the transport equation. Physically, this means that we are neglecting the contributions to $N(E)$ coming from other regions than the magnetic reconnection region in the inner coronal region around the BH. We consider a steady-state particle distribution which can be obtained by setting $\frac{\partial N}{\partial t} = 0$ in the Fokker-Planck differential equation, so that the particle distribution equation is

$$N(E) = |\frac{dE}{dt}|^{-1} \int_E^{\infty} Q(E) dE. \tag{3.52}$$

Here $-\frac{dE}{dt} \equiv E t_{cool}^{-1}$, where t_{cool}^{-1} is the total cooling rate that can be calculated assuming all the cooling mechanisms. It is interesting to note that if the energy losses are proportional to the particle energy ($\frac{dE}{dt} \propto E$), $N(E)$ does not change the injection spectrum and $N(E) \propto E^{-p}$, as in the *pp* inelastic collisions or Bremsstrahlung cooling processes. In loss mechanisms like the synchrotron and IC scattering in the Thomson regime, $N(E)$ is steeper because in these cases $\frac{dE}{dt} \propto E^2$ and $N(E) \propto E^{-(p+1)}$.

The spectrum will be harder if dE/dt is constant as for ionization losses, $N(E) \propto E^{-(p-1)}$. In the case of IC scattering in the Klein-Nishina limit, $\frac{dE}{dt} \propto E^{-1}$ and so, the spectrum is even harder and $N(E) \propto E^{-(p-2)}$.

3.5 An overview

Before proceeding to the applications, we briefly summarize the overall picture developed in this and the previous Chapter.

In the innermost region of accretion disk in microquasars and LLAGNs around the BH sources, magnetic field lines of the BH magnetosphere and of the corona of the accretion disk may reconnect and particles can gain energy due to magnetic reconnection acceleration. In three-dimensions, the reconnection layer around the BH describes cylindrical shell with thickness R_X. A torus or a sphere encompasses this region and all the relevant radiative processes can occur there. The injected accelerated particle spectrum of protons and electrons is a power-law in energy and is modified by radiative losses.These include the interactions of the protons and electrons with the magnetic field (through synchrotron radiation), the thermal particles (through *pp* inelastic collisions and relativistic Bremsstrahlung), and the radiation field (through $p\gamma$ collisions and inverse Compton scattering).The hadronic interactions results charged pions beside the neutral pions that produce the neutrinos also.

The final product of our calculations are broadband spectral energy distributions, duly corrected by $\gamma\gamma$ absorption. In the next chapters we present some general results and apply the model proposed here to reproduce the observational spectrum of specific sources of microquasars and LLAGNs, also making predictions for their gamma-ray emission.

We also construct the neutrino diffuse intensity in the context of LLAGNs and demonstrate that HE neutrinos may be originated from the nuclear region of these class of astrophysical sources via decays of charged pions produced through hadronic interactions.

3.6 What we have learned

In this chapter, we have presented the main non-thermal cooling processes of relativistic particles that may be relevant around BH/accretion disk/coronal systems. We have also presented the relevant photon absorption processes around these systems. In the next chapters 4 and 5, we will present the results of the applications of the theoretical grounds presented in this chapter and particle acceleration in Chapter 2 to reconstruct the observed emission structure of microquasars and LLAGNs, respectively.

Chapter 4

The magnetic reconnection acceleration model applied to microquasars

In this chapter, we apply the magnetic reconnection model described in the previous chapters to the innermost regions around the black hole, in order to reconstruct the observed spectral energy distribution (SED) from the radio to the gamma-ray emission of the microquasars Cyg X-1 and Cyg X-3. In particular, we find that the still controversial origin of the gamma-ray emission can be attributed to the core of these sources. The results of this Chapter have been also published (Khiali et al. 2015a) and the article is appended to this thesis (Appendix B).

In general lines, the procedure to calculate the SED of these sources begins with the determination of the total power released by fast magnetic reconnection within the acceleration region (Eq. 2.11), that is, in the cylindrical shell of height L_X and thickness ΔR_X (Eq. 2.12, see Figure 1). This power is then employed to compute the spectrum of accelerated electrons and protons (Eq. 3.50) that will be injected into the emission volume V, i.e., the sphere that encompasses the acceleration region.

The maximum energy that each particle spectrum can attain is obtained from the comparison of the acceleration rates, for both electrons and protons, with the relevant radiative loss processes (see Chapter 2). As we will see, the accelerated electrons will loose energy by synchrotron, IC and Bremsstrahlung mechanisms, with a dominance of the synchrotron process shaping their spectrum. The fluxes of these emission processes are then calculated and also the number density of the synchrotron photons that are partially self-scattered by the electrons (leading to SSC emission) and by protons (in $p\gamma$ interactions). Likewise, the energy distribution of the protons is also calculated taking into account the radiative cooling mechanisms due to synchrotron, pp and $p\gamma$ interactions that will shape the very high energy part of the SED.

4.1 What we want to know

- Is magnetic reconnection model able to accelerate the particles to ultra relativistic energies in the core region of microquasars?
- What is the maximum energies of electrons and protons in the nuclear region of microquasars?
- What are the main radiative processes responsible for each emission, especially in the gamma-ray band?
- How would be the effect of the companion star on the radiative absorption, specially at the gamma-rays?

4.2 Black Hole Binaries

Black hole binaries (BHBs, also denominated microquasars; Mirabel & Rodriquez 1994) are formed by a stellar-mass compact object, probably a black hole, and a non-collapsed star which is also called companion star or donor star because the matter lost by this star is accreting to the compact object. In microquasars, a fraction of this accreting matter is ejected from the system as two collimated jets (Paredes et al. 2006 and see the work by Villa 2012). Figure 4.1 shows an artistic representation of a microquasar.

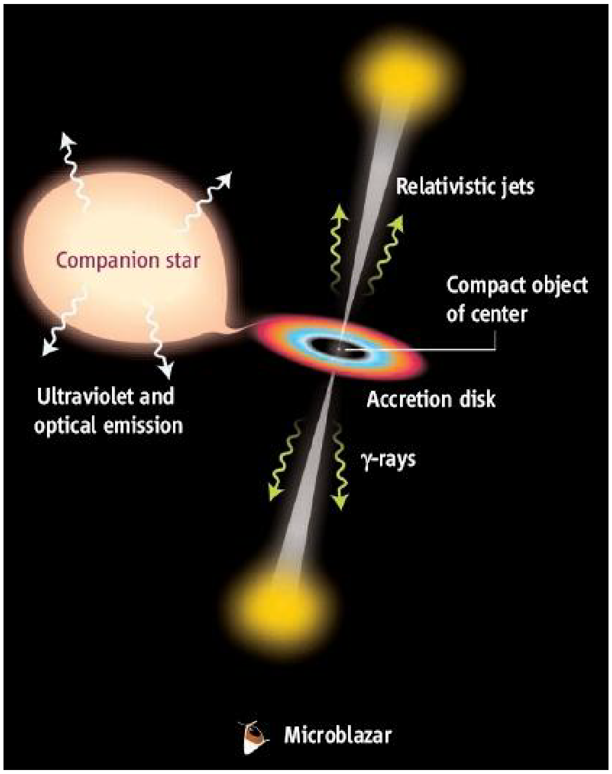
Relativistic jets
Companion star
Compact object
of center
Ultraviolet and
optical emission
Accretion disk
γ-rays
Microblazar

Figure 4.1: A schematic of microquasars containing central compact object, accretion disk, jets and companion star (Credit: Arne Rau, MPE Garching)

Detected non-thermal radio to gamma-ray emission from these systems (Figure 4.4), provide clear evidence of the production of relativistic particles in their jets and probably also in the innermost regions very close to the black hole (BH). Currently, more than a dozen microquasars have been detected in the Galaxy (Zhang 2013).

Generally, these sources are far from being stable and individual systems have often complex emission structure. Nevertheless, all classes of BHBs exhibit common features and show basically two major states when considering their X-ray emission (2-100 keV): a quiescent and an outburst state (e.g., Remillard & McClintock 2006). The former is characterized by low X-ray luminosities and hard non-thermal spectra. Usually, transient BHBs exhibit this state for long periods, which allows one to obtain typical physical parameters of the system. On the other hand, the outburst state corresponds to intense activity and emission, and can be sub-classified in three main active and many intermediary states. According to Remillard & McClintock 2006 (see also Zhang 2013), the three main active states are the thermal state (TS), the hard state (HS) and the steep power law state (SPLS). These states are usually explained as changes in the structure of the accretion flow, as remarked before. During the TS, the soft X-ray thermal emission is believed to come from the inner region of the thin accretion disk that extends until the last stable orbit around the black hole. On the other hand, during the HS the observed weak thermal component suggests that the disk has been truncated at a few hundreds/thousands gravitational radii. The hard X-ray emission measured during this state is dominated by a power-law (PL) component and is often attributed to inverse Compton scattering of soft photons from the outer disk by relativistic electrons from the hot inner region of the system (e.g., Remillard & McClintock 2006; Malzak et al. 2006). The SPLS is almost a combination of the above two states, but the PL is steeper.

The observed radio and infra-red (IR) emission in microquasars is normally interpreted as due to synchrotron radiation produced by relativistic particles in the jet outflow.

More recently a few microquasars have been also detected in the gamma-ray range with *AGILE* (Tavani et al., 2009; Bulgarelli et al., 2010; Sabatini et al., 2010a,b, 2013), *Fermi-LAT* (Atwood et al., 2009; Bodaghee, 2013) and *MAGIC* (Lorentz, 2004). For Cygnus X-1 (Cyg X-1), for instance, upper limits with 95% confidence level have been obtained in the range of ≥ 150 GeV (Albert et al., 2007), while in the case of Cygnus X-3 (Cyg X-3), upper limits of integrated gamma-ray flux above 250 GeV have been inferred by Aleksic et al. (2010). Upper limits in the 0.1-10 GeV range have been also suggested

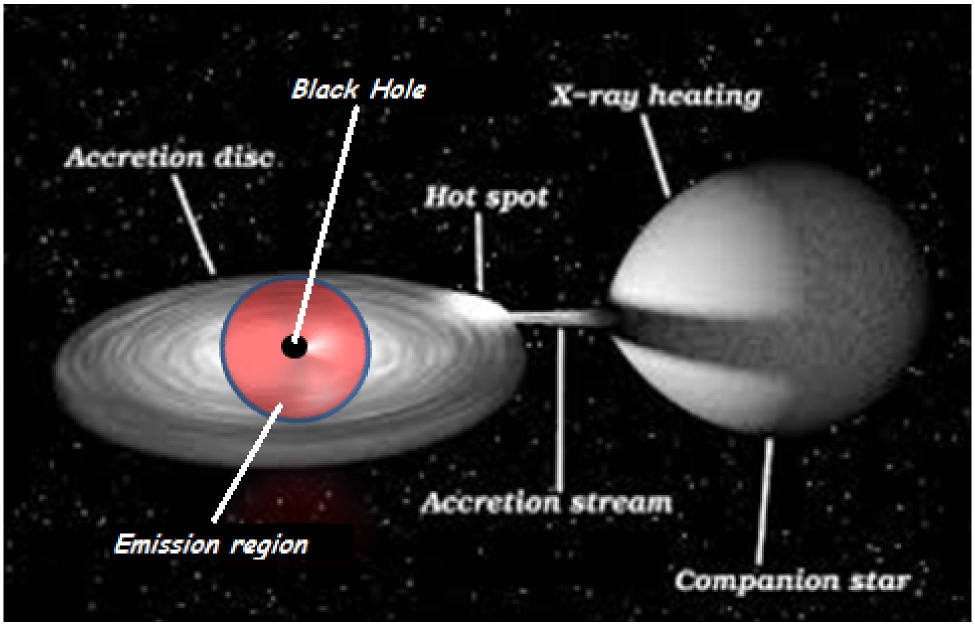

Figure 4.2: A schematic representation of the black hole binary system showing the location of the emission region in red around the BH. This emission region encompasses the reconnection acceleration region of Figure 2.6 which is not shown here.

for GRS 1915+105 and GX 339-4.

There is no definite mechanism yet to explain the origin of the very high energy (VHE) emission in microquasars. The main reason for this is that the current sensitivity of the gamma-ray instruments is too poor to establish the location of this emission in the source (e.g., Bodaghee 2013).

In the following sections, we will apply the fast magnetic reconnection model described in Chapter 2 to the black hole binaries Cyg X-1and Cyg X-3 to model their observed non-thermal radiation. These sources are the only ones for which it has been observed emission from radio to gamma-rays up to TeV energies (see Bodaghee 2013) and it has been found that the calculated reconnection power is more than enough to explain their luminosities (Kadowaki et al. 2015; Singh et al. 2015).

4.3 Application of the magnetic reconnection acceleration model to Cygnus X-1

Cyg X-1 is a widely studied black hole binary system (Malyshev et al. 2013) at a distance of 1.86-2.2 kpc (Reid et al. 2011; Ziolkowski 2005), which is accreting from a high mass companion star orbiting around the BH with a period is 5.6 days (Gies et al. 2008). The orbit inclination is between 25° and 35° (Gies & Bolton 1986) with an eccentricity of $\sim$0.018 (Orosz 2011), so that one can assume an approximate circular orbit with a radius r_{orb}.

The parameters employed used to calculate the reconnection acceleration (as described in Chapter 2) and the radiative losses (as described in Chapter 3) for this source are given in Table 4.1. We note that our model has actually only 7 free parameters (i.e., R_x, L_X, $L \leq L$, p, γ_{min}, ξ and α). The remaining quantities of Table 4.1 are obtained directly from these parameters through Eqs. 2.11 to 2.14 (i.e, B, W, ΔR_X, n_c and T_d), or from the observations (i.e, d and m). In order to calculate the extension L_X of the reconnection region (see Figure. 2.6), we consider the value $L_X \simeq 10R_S$ (GL05, de Gouveia Dal Pino et al. 2010; Kadowaki et al. 2015). The volume V of the emission region in Table 4.1 is calculated by considering the spherical region that encompasses the central BH and reconnection region in Figure 2.6. This volume has dimensions $V = 4/3\pi L^3$ (see also the very schematic representation in Figure 4.2).

The black hole mass has been taken from Orosz (2011). Figures 4.3 and 4.5 show the cooling rates for the different energy loss processes described in Chapter 3 (Eqs. 3.1, 3.6, 3.11, 3.23 and 3.34) for electrons and protons, respectively. These are compared with the acceleration rates due to first-order Fermi acceleration by magnetic reconnection (Eqs. 2.5 and 2.6) and to shock acceleration (Eq. 2.8) in the core region.

We notice that for both protons and electrons the acceleration is dominated by the first-order Fermi magnetic reconnection process. Besides, the main radiative cooling process

Table 4.1: Model parameters for Cyg X-1

B	Magnetic field (G)	2.3×10^7
n_c	Coronal particle number density (cm^{-3})	4.5×10^{16}
T_d	Disk temperature (K)	4.4×10^7
W	Reconnection power (erg/s)	3.6×10^{36}
ΔR_X	Width of the current sheet (cm)	1.1×10^7
R_x	Inner radius of disk (cm)	2.6×10^7
L_X	Height of reconnection region (cm)	4.3×10^7
V_{vol}	Volume of emission region (cm^3)	3.5×10^{23}
d	Distance (kpc)	2
M	Mass of BH ($M_\odot$)	14.8
p	Particle power index	1.8
$R_\star$	Stellar radius (cm)	1.5×10^{12}
$T_\star$	Stellar temperature (K)	3×10^4
r_{orb}	Orbital radius (cm)	3.4×10^{12}
θ	Viewing angle (rad)	$\pi/6$

for the electrons is synchrotron radiation, while for protons the photo-meson production ($p\gamma$ interactions) governs the loss mechanisms (Figure 4.5). In this case, the proper target radiation field are the photons from synchrotron emission. The intercept between the magnetic reconnection acceleration rate and the synchrotron rate in Figure 4.3 gives the maximum energy that the electrons can attain in this acceleration process, which is $\sim$ 10GeV. Protons on the other hand, do not cool as efficiently as the electrons and can attain energies as high as $\sim 4 \times 10^{15}$eV.

In order to reproduce the observed SED, we have calculated the non-thermal emission fluxes as described in Chapter 3 in the surrounds of the BH. Figure 4.6 shows the computed SED for Cyg X-1 compared with observed data.

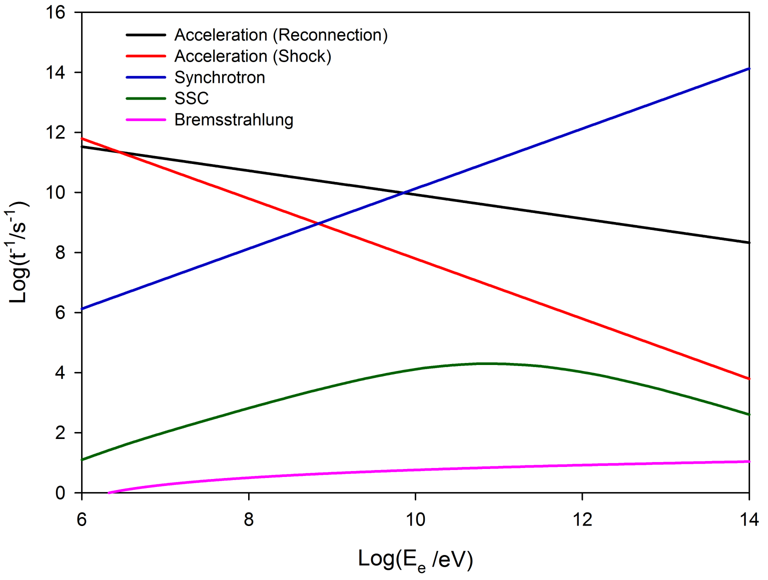

Figure 4.3: Acceleration and cooling rates for electrons in the nuclear region of Cyg X-1.

As remarked in §. 3.3, we have also considered the gamma-ray absorption due to electron-positron pair production resulting from interactions of the gamma-ray emission in the core with the surrounding radiation field. As stressed, our calculations indicate that this process is dominated by the radiation field of the companion star. As a result, the opacity depends on the phase of the orbital motion and on the viewing angle.

The parameters employed in the evaluation of this absorption are in the last four lines of Table 4.1, and have been taken from Romero et al. (2010a). It has been proposed from $MAGIC$ observations (Albert et al. 2007) that the gamma-ray production and absorption are maximized near the superior conjunction (Bodaghee 2013) at phase $\phi_b = 0.91$ (see Figure 4.4). In our calculations we considered this orbital phase for Cyg X-1.

The calculated opacity is described in detail in §. 4.5 below. It results in a very high energy gamma-ray absorption (see Figure 4.12). We find that the produced gamma-rays are fully absorbed in the energy range of 50 Gev-0.5 TeV which causes the energy gap

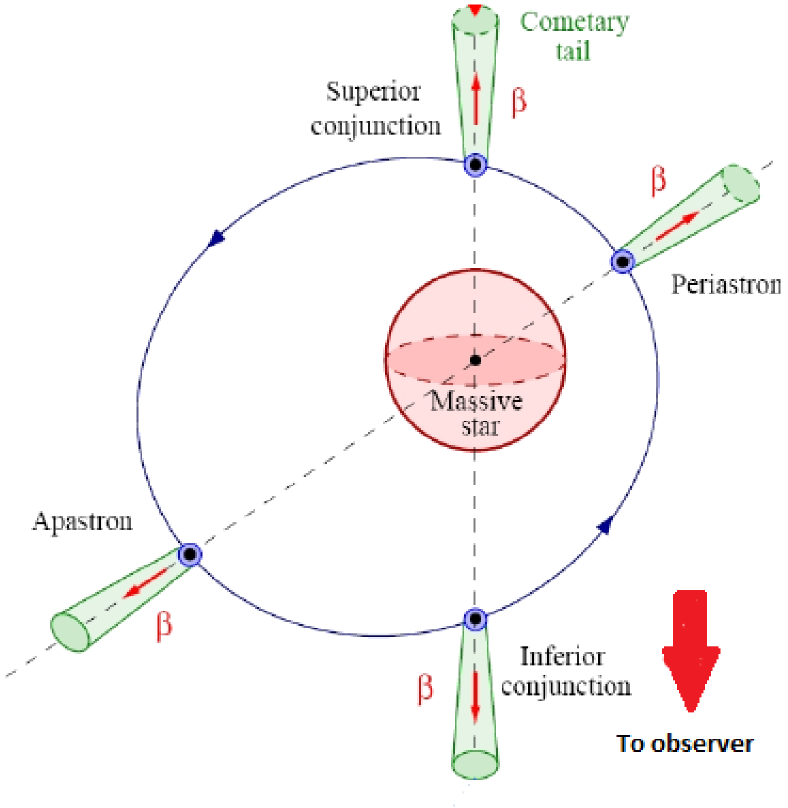
Cometary tail
Superior conjunction
β
β
Periastron
Massive star
Apastron
β
β
Inferior conjunction
To observer

Figure 4.4: Sketch of microquasar-star binary sytem (Adapted from Cerutti 2013)

seen in the calculated SED in Figure 4.6. The observed upper limits by MAGIC plotted in the diagram in this range are possibly originated outside the core, along the jet where gamma-ray absorption by the stellar radiation is not important (see also Romero et al. 2010a).

We note that in Figure 4.6 the observed flux in radio (10 μeV $-$ 0.1 eV) and soft gamma-ray ($10^5 - 10^8$ eV) are explained by leptonic synchrotron and SSC processes, respectively, according to the present model. In the range 10 MeV- 0.2 GeV, SSC is the main mechanism to produce the observed data as a result of interactions between the high energy electrons with synchrotron photons. At energies in the range 0.2 GeV - 3 TeV, neutral pion decays reproduce the observed gamma-rays. These neutral pions

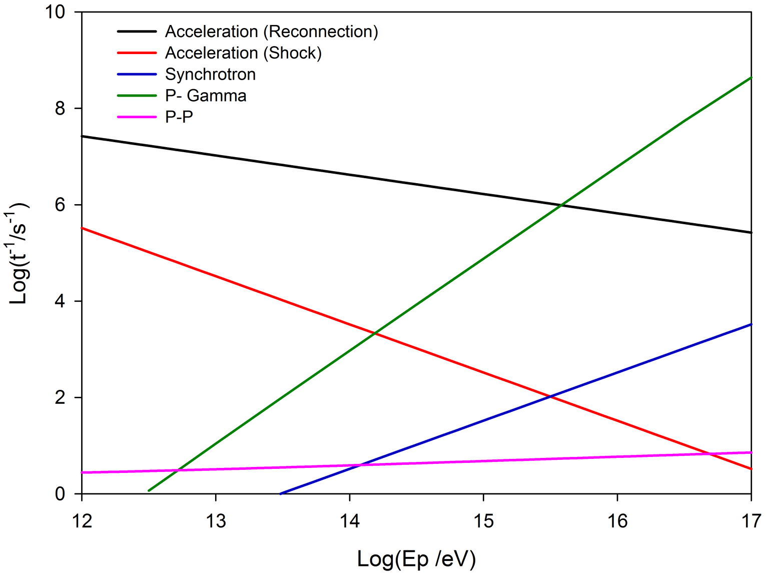

Figure 4.5: Acceleration and cooling rates for protons in the nuclear region of Cyg X-1.

result from *pp* and $p\gamma$ interactions. In the range of 0.3 GeV- 30 GeV, *pp* collisions are the dominant radiation mechanism, but in the very high energy gamma-rays, interactions of relativistic hadrons (mostly protons) with scattered photons from synchrotron radiation may produce the observed flux.

The observed emission in the near infrared (0.1 eV-10 eV), represented in Figure 4.6 by red stars is attributed to thermal blackbody radiation from the stellar companion, and the accretion X-ray emission (1 keV-0.1 MeV) also represented in Figure 4.6 by dark stars, is believed to be due to thermal Comptonization of the disk emission by the surrounding coronal plasma of temperature $\sim 10^7$ K (Di Salvo et al., 2001; Zdziarski et al., 2012). For this reason, these observed data are not fitted by the coronal non-thermal emission model investigated here.

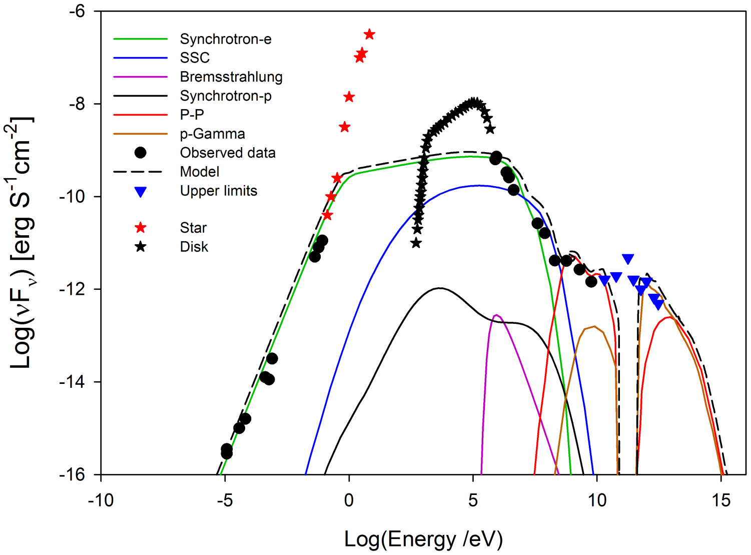

Figure 4.6: Calculated spectral energy distribution for Cyg X-1 using the magnetic reconnection acceleration model compared with observations. The data depicted in the radio range is from Fender et al. 2000, the IR fluxes are from Persi et al. 1980; Mirabel et al. 1996, the hard X-ray data above 20 keV are from INTEGRAL (Zdziarski et al. 2012), the soft X-ray data below 20 keV are from BeppoSAX (Di Salvo et al. 2001), the soft gamma-ray data are from COMPTEL (McConnell et al. 2000, 2002), the data in the range 40 MeV- 40 GeV are measurements and upper limits from the *Fermi* LAT (Malyshev et al. 2013), and the data in the range 40 GeV- 3 TeV are upper limits from MAGIC (with 95% confidence level; Albert et al. 2007). The red and black stars correspond to emission from the companion star and the accretion disk, respectively, and are not investigated in the present model (see more details in the text.)

4.4 Application of the magnetic reconnection acceleration model to Cygnus X-3

Cyg X-3 is also a high mass X-ray binary that possibly hosts a BH (Zdziarski & Mikolajewska 2013) and a Wolf-Rayet as a companion star (van Kerkwijk et al. 1992). The system is located at a distance of 7.2-9.3 kpc (Ling et al. 2009) and has an orbital period of 4.8 h and an orbital radius $\approx 3 \times 10^{11}$cm (Piano et al. 2012). Our model parameters for Cyg X-3 are given in Table 4.2. As in Cyg X-1, the values for the first five parameters were calculated from Eqs. 2.10-2.14, which describe the magnetic reconnection acceleration model in the core region. We have also used for the accretion disk inner radius the value $R_X = 6R_S$ and for the extension L_X of the reconnection region the value $L_X = 10R_S$ (de Gouveia Dal Pino & Lazarian 2005; Kadowaki et al. 2015; Khiali et al. 2015a). The BH mass has been taken from Schmutz et al. (1996).

The cooling and acceleration rates for electrons and protons are depicted in Figures 4.7 and 4.8, respectively. The maximum electron and proton energies in both diagrams are obtained from the intercept between the acceleration rate curve and the dominant radiative loss rate curve. As in Cyg X-1, it is clear from the diagrams that acceleration by magnetic reconnection is dominating over shock acceleration in the core region. Synchrotron emission is the main mechanism to cool the electrons which may reach energies as high as $\sim$ 10GeV, while the most important loss mechanism for protons is $p\gamma$ interactions with synchrotron photons. They can be accelerated up to $\sim 4 \times 10^{15}$eV.

In this system, the close proximity of the stellar companion ($R_d \approx 3{\times}10^{11}$cm), the large stellar surface temperature ($T_\star \sim 10^5$K), and the high stellar luminosity ($L_\star \sim 10^{39}$erg s^{-1}) of the companion star may result a considerable attenuation of the gamma-rays via $\gamma\gamma$ pair production (Bednarek 2010). The detection of TeV gamma-rays in Cyg X-3, therefore, relies on the competition between the production and the attenuation process above. This attenuation is shown in Figure 4.12.

Table 4.2: Model parameters for Cyg X-3

B	Magnetic field (G)	2.1×10^7
n_c	Coronal particle number density (cm^{-3})	3.9×10^{16}
T_d	Disk temperature (K)	4.5×10^7
W	Reconnection power (erg/s)	4.5×10^{36}
ΔR_X	Width of the current sheet (cm)	1.3×10^7
R_x	Inner radius of disk (cm)	3×10^7
L_X	Height of reconnection region (cm)	5×10^7
V_{vol}	Volume of emission region (cm^3)	5.3×10^{23}
d	Distance (kpc)	8
M	Mass of BH ($M_\odot$)	17
p	Particle power index	2.2
$R_\star$	Stellar radius (cm)	2×10^{11}
$T_\star$	Stellar temperature (K)	9×10^4
r_{orb}	Orbital radius (cm)	4.5×10^{11}
θ	Viewing angle (rad)	$\pi/6$

Figure 4.9 shows the calculated SED compared to the observed data for this source. The gamma-ray absorption was calculated from Eq. 3.45, employing the UV field of the companion star which is a more significant target than the radiation fields of the accretion disk and the corona (see the stellar parameters in the last four lines of Table 4.2 which were taken from Cherepashchuk & Moffat 1994). The orbital phase considered was $\phi_b = 0.9$, near the superior conjunction (Aleksic et al. 2010), as in Cyg X-1. The energy gap caused by this gamma-ray absorption is shown in Figure 4.9 in the $50\mathrm{GeV} - 0.4\mathrm{TeV}$.

The contributions of pp and $p\gamma$ interactions are the dominant ones in the high energy gamma-ray range. These processes become more relevant in the coronal region around the BH since the magnetic field there is strong and enhances the synchrotron radiation

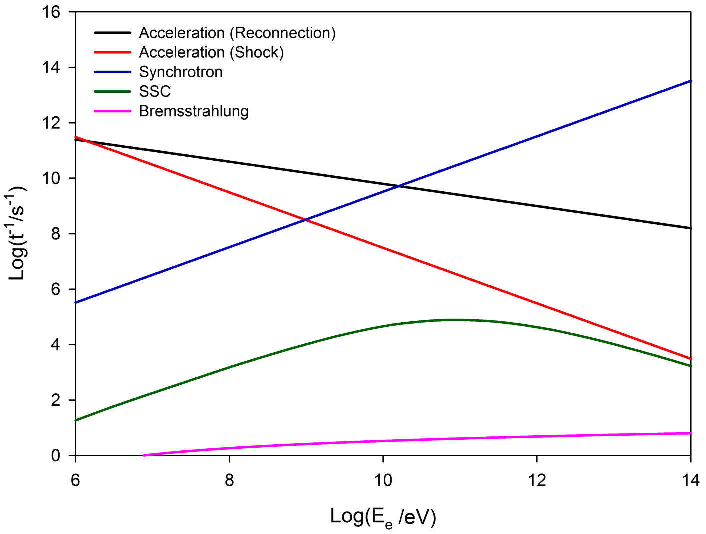

Figure 4.7: Acceleration and cooling rates for electrons in the core region of Cyg X-3.

of the electrons and protons. Also the matter and photon densities are large enough in the core region, providing dense targets for pp and $p\gamma$ collisions and SSC scattering. In the energy range 10MeV − 50Gev, the emission is dominated by the neutral pion decay resulting from pp inelastic collisions.

Also, the resulting interactions between accelerated protons and scattered photons from synchrotron emission produce neutral pions and the gamma ray emission from these pion decays results in the tail seen in the SED for energies $\geq$ 1TeV.

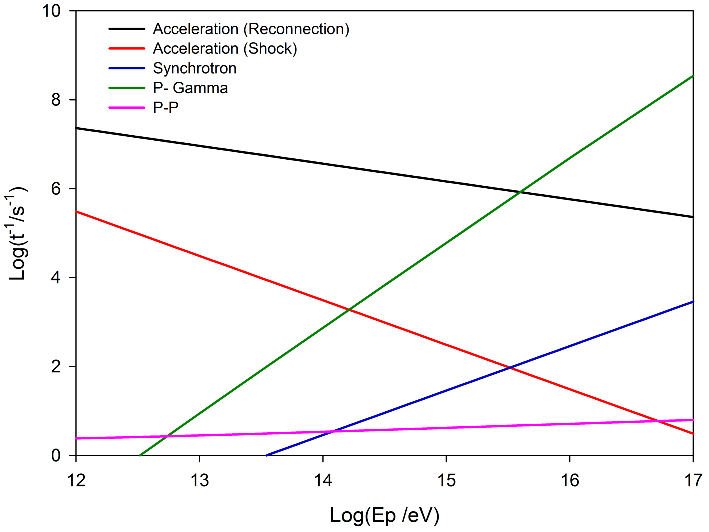

Figure 4.8: Acceleration and cooling rates for protons in the core region of Cyg X-3.

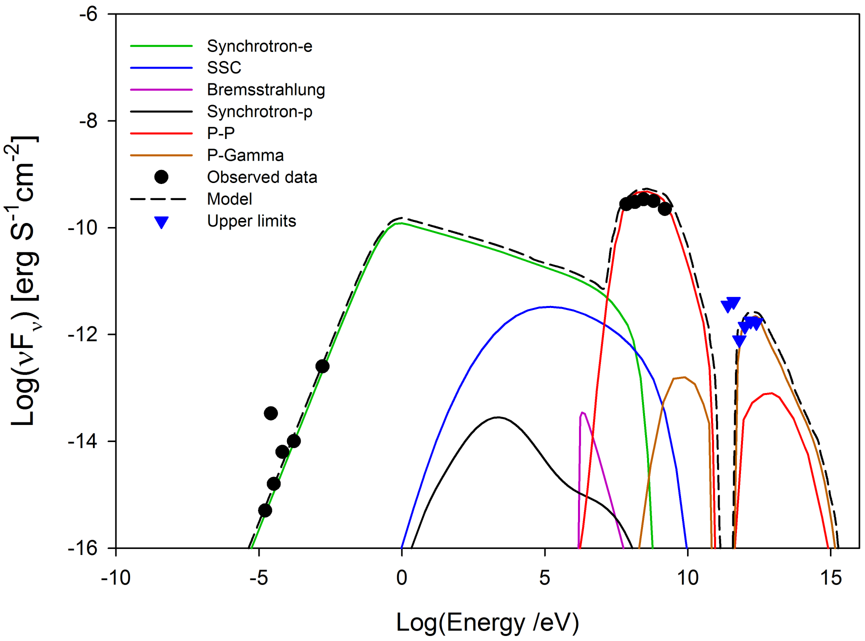

Figure 4.9: Spectral energy distribution for Cyg X-3. The observed radio emission is taken from AMI-LA and RATAN (Piano et al., 2012); the data in the range 50MeV to 3GeV are from AGILE-GRID (Piano et al., 2012); and the data in the range $0.2 - 3.155$TeV are from MAGIC differential flux upper limits (95% C.L.).

4.5 gamma-ray absorption in microquasars

As described in Chapter 3, Gamma-rays can be annihilated by the surrounding radiation field via electron-positron pair creation: $\gamma + \gamma \rightarrow e^{+} + e^{-}$. In microquasars, besides the radiation field of the tight companion star, coronal and accretion disk photons can also absorb Gamma-rays. It has been shown by Cerutti et al. (2011) that the absorption due to coronal photons is negligible compared with the contribution from the disk. Besides, adopting the same absorption model for the disk radiation field of these authors we find that the disk contribution to gamma-ray absorption is also less relevant than that of the stellar companion, generally a Wolf-Rayet star, which produces UV radiation (see Figure 4.10). To evaluate the optical depth due to this component, we have adopted the model described by Sierpowska-Bartosik & Torres (2008); (see also Dubus 2006; Zdziarski & Mikolajewska 2013).

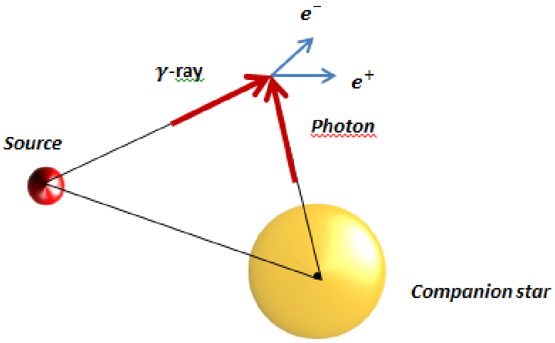

Figure 4.10: Annihilation of produced gamma-ray via interacting with photon field of the companion star.

The companion star with radius $R_\star$ and a black-body surface temperature $T_\star$ produces a photon density at a distance $d_\star$ from the star

$$n_{ph} = \frac{2\epsilon^2}{h^3 c^3} \frac{1}{\exp(\epsilon/kT_\star)} \frac{R_\star^2}{d_\star^2}. \tag{4.1}$$

In the absorption models proposed by Sierpowska-Bartosik & Torres (2008) and Dubus

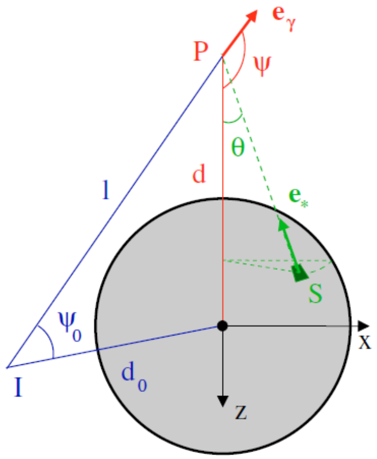

Figure 4.11: Geometry for Gamma-ray absorption at a location P due to interaction with a photon produced at point S. The interaction leads to e^+e^- pair production (Extracted from Dubus 2006).

(2006), the geometrical parameters $d_\star$, μ and l are strongly dependent on the viewing angle θ and the orbital phase ϕ_b. Figure 4.11 shows the geometry for absorption of a Gamma-ray at a location P with stellar photons emitted at S and producing e+ e- pairs. The Gamma-ray is emitted at I and l is the length of the Gamma-ray path to P. The (x, z) plane is defined by the star center and gamma-ray path. In the superior conjunction, the compact object is behind the star and the orbital phase is $\phi_b = 0$. We here consider the same orbital phase that has been observed during the high energy observations for Cyg X-1 and Cyg X-3. More details on the geometrical conditions of the binary systems and the integration extremes has been discussed in Sierpowska-Bartosik & Torres 2008 and Dubus 2006.

Fig. 4.12 shows our results for calculating the Gamma-ray absorption for the microquasars studied in this work. We plot the attenuated luminosity (Eq. 3.45) $e^{-\tau}$ as function of radiation energy around the companion star. We see that in the range of 4×10^{11}eV $- 5 \times 10^{12}$eV, the produced gamma-ray in the core region of these sources can

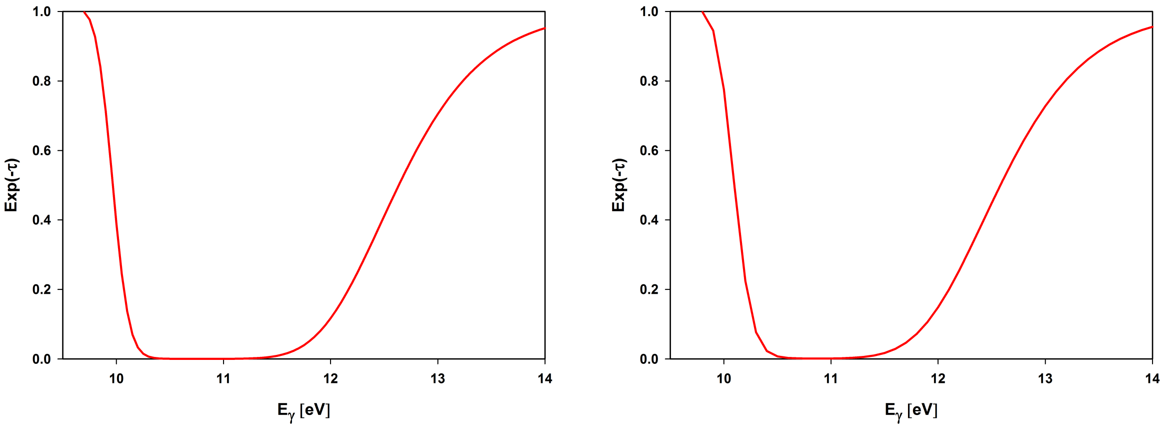

(a) Cyg X-1

(b) Cyg X-3

Figure 4.12: Spectrum of Gamma-ray absorption around the companion star in Cyg X-1 and Cyg X-3 (*a* and *b* panels, respectively).

be absorbed fully.

We note that the pairs produced by the absorbed gamma-rays may emit predominantly synchrotron emission in the surrounding magnetic fields (Bosch-Ramon et al. 2008), but their emission is expected to be negligible compared to the other synchrotron processes of the system. We thus neglected this effect in our treatment of pair absorption (see also Zdziarski et al. 2014) in the building of the SEDs in Figures 4.6 and 4.9 for Cyg X1 and Cyg X3, respectively.

4.6 Comparison with other models

Other authors have proposed alternative scenarios to the one discussed here for both Cyg X-1 and Cyg X-3. The models of Piano et al. (2012), for instance, which were based on particle acceleration near the compact object and on propagation along the jet, indicate that the observed gamma-ray $\leq$ 10 GeV in Cyg X-3 could be produced via leptonic (inverse Compton) and hadronic processes (*pp* interactions). However, they have no quantitative estimates for the origin of the VHE gamma-ray upper limits at $\geq$0.1 TeV obtained by *MAGIC*. Sahakyan et al. (2013), on the other hand, assumed that the jet of Cyg X-3 could accelerate both leptons and hadrons to high energies and the accelerated protons escaping from the jet would interact with the hadronic matter of the companion star producing gamma-rays and neutrinos. However, their model does not provide proper fitting in the TeV range either.

In the case of Cyg X-1, Zhang, Xu & Lu (2014) have employed a leptonic model to interpret recent Fermi LAT measurements also as due to synchrotron emission but produced along the jet and to Comptonization of photons of the stellar companion. The TeV emission in their model is attributed to interactions between relativistic electrons and stellar photons via inverse Compton scattering. According to them this process could also explain the *MAGIC* upper limits in the range of $50\text{GeV} - 0.5\text{TeV}$, i.e., the band gap in Figure 4.6. However, unlike the present work where we obtained a reasonable match due to $p\gamma$ interactions, their model is unable to explain the observed upper limits by *MAGIC* in the very high energy gamma-ray tail.

Also with regard to Cyg X-1, we should note that the detection of strong polarized signals in the high-energy range of 0.4-2 MeV by Laurent et al. (2011) and Jourdain et al. (2012) suggests that the optically thin synchrotron emission of relativistic electrons from the jet may produce soft gamma-rays. There are indeed some theoretical models that explain the emission in this range by using a jet model (Zdziarski et al., 2012; Malyshev et al., 2013; Zdziarski et al., 2014; Zhang, Xu & Lu, 2014). Nevertheless, contrary to this view, Romero, Vieyro & Chaty (2014) argue that the MeV polarized tail may be originated in the coronal region of the core without requiring the jet. This study is therefore, consistent with the present model as it supports the coronal nuclear region for the origin of the non-thermal emission.

We should also stress that there are two possible interpretations for the lack of clear evidence of detectable TeV emission in Cyg X-1 and Cyg X-3. On one hand, there may be a strong absorption of these photons by the ultraviolet (UV) radiation of the companion star (through the photon-photon process). On the other hand, the lack of emission may be due to the limited time of observation (Sahakyan et al., 2013). In our model, we verified that neutral pion decays due to $p\gamma$ interactions at the emission region close enough to the central black hole, near the jet basis, could produce TeV gamma-rays. Because of the high magnetic field near the black hole, a large density synchrotron radiation field produced there could be a target photon field for the photo-meson production. These results predict that a long enough observation time and higher sensitivity would allow to capture substantial TeV gamma-ray emission from these microquasars. This may be also probed by the forthcoming Cherenkov Telescope Array (CTA) (Actis et al., 2011; Acharya et al., 2013; Sol et al., 2013).

A final remark is in order. To derive the SEDs of the sources investigated here, we have assumed a nearly steady-state accelerated particle energy distribution at the emission zone. This assumption is valid as long as acceleration by fast magnetic reconnection is sustained in the inner disk region, or in other words, as long as a large enough disk accretion rate is sustained in order to approach the magnetic field lines rising from the accretion disk to those anchored into the BH embedded in turbulence. In microquasars, this should last no longer than the time the system remains in the outburst state, normally ranging from less than one day to several weeks.

4.7 What we have learned

We presented here the role of magnetic reconnection in accelerating particles in the innermost regions of μQSRs, applying this acceleration model to reconstruct the spectral energy distribution (SED) of the BHBs Cyg X-1 and Cyg X-3.

Considering all the relevant leptonic and hadronic radiative loss mechanisms due to the interactions of the accelerated particles with the surrounding matter, magnetic and radiation fields in the core regions of the BHBs Cyg X-1 and Cyg X-3, we compared the time scales of these losses with the acceleration time scales above and found larger energy cut-offs for particles being accelerated by magnetic reconnection than by a diffusive shock (see Figures 4.3 and 4.5 for Cyg X-1, and Figures 4.7 and 4.8 for Cyg X-3). These cut-offs have an important role in the determination of the energy distribution of the accelerated particles and therefore, in the resulting SED and stress the potential importance of magnetic reconnection as an acceleration mechanism in the core regions of BHBs and compact sources in general.

We have also shown that, under fiducial conditions, the acceleration model developed here is capable of explaining the multi-wavelength non-thermal SED of both microquasars Cyg X-1 and Cyg X-3. The radio emission may result from synchrotron process in both cases.

The observed soft gamma-rays from Cyg X-1 are due to synchrotron and IC processes. The target photons for the IC come mainly from synchrotron emission (SSC). Neutral Pion decay resulting from *pp* inelastic collisions may produce the high energy gamma rays in both systems, while the very high energy (VHE) gamma rays are the result of neutral pion decay due to photo-meson production ($p\gamma$) in the core of these sources.

The importance of the $\gamma\gamma$ absorption due to interactions with the photon field of the companion star for electron-positron pair production has been also addressed in our calculations. According to our results, the observed gamma-ray emission in Cyg X-1 in the range $5 \times 10^{10} - 5 \times 10^{11}$eV (see inverted blue triangles in Figure 4.6) cannot be produced in its core region (see also Romero et al. 2010a). In the case of Cyg X-3, we have found that the emission in the range of $50\text{GeV} - 0.4\text{TeV}$ (see inverted blue triangles in Figure 4.9) is also fully absorbed in the core region by the same process. This suggests that in both sources, this emission is produced outside the core, probably along the jet, since at larger distances from the core the gamma ray absorption by the stellar companion decreases substantially. In fact, this is what was verified by Zhang, Xu & Lu (2014) in the case of Cyg X-1.

In the next Chapter, we will investigate the application of the magnetic reconnection model to the core region of radio galaxies.

Chapter 5

Application of the magnetic reconnection model to LLAGNs

We describe here the results of the application of the magnetic reconnection acceleration model described in Chapter 2 to the core region of the only LLAGNs for which it has been observed emission up to TeV energies, namely, the radio galaxies Cen A, Per A, M87 and IC 310[1]. These radio galaxies have been observed at VHE by *FERMI-LAT, VERITAS* and *HESS* (e. g., Abdo et al. 2009c, 2010; Abramowski et al. 2012; Aleksić et al. 2014b).

As in Chapter 4, we will calculate here the SED of each of these sources using the Eqs. 2.11, 2.5 and 2.6 to compute the magnetic reconnection power and acceleration rates and the equations described in Chapter 3, to compute the radiative losses and radiation fluxes.

We take into account both leptonic and hadronic radiative loss mechanisms in the emission region which corresponds to the torus with volume V that encompasses the cylindrical shell where magnetic reconnection particle acceleration takes place in Figure 2.6 (see also Figure 5.1). Considering that the cylinder extends up to L in both hemispheres, then the small radius of the torus is $r = L/2$ and the large radius is R_X, so that the effective emission zone in our model has an approximate volume $V = \pi^2 L^2 R_X$.

---

[1] We note that very recently, another LLAGN has been also detected in the VHE range too, namely PKS 0625-354 (Dyrda et al. 2015).

We note that we have adopted a torus rather than a spherical emission region enveloping the reconnection acceleration zone as we did in the case of microquasars. The reason for adopting a torus geometry here is because very short time variable gamma rays emitted from some sources for instance M87 (1-2 days) or IC 310 (4.8 minutes) are originated from compact region with the length scales much more smaller than R_X as emission region and torus can fulfil this conditions. However for the sources without significant time variabilities such as Cen A and Per A, we employed the sphere model.

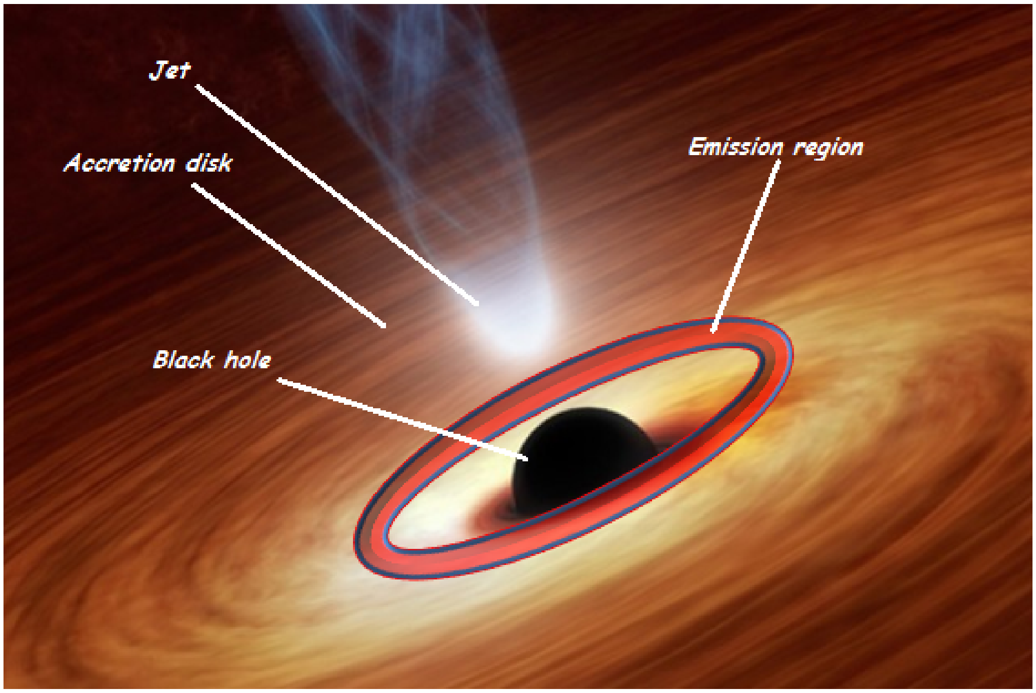

Figure 5.1: Schematic representation of the emission region which encompasses the reconnection region around the BH depicted in Figure 2.6 (not shown here) in the core of LLAGNs

The results of this Chapter have been described in a paper submitted to publication

(Khiali et al. 2015b). A copy of it is in Appendix C.

5.1 What we want to know

- What is the maximum energy of accelerated particles in the core region of LLAGNs?
- Are high energy gamma-rays originated from the innermost region of LLAGNs?
- Which cooling processes are relevant to interpret the observed emission, particularly in the controversial range of gamma-rays?
- How the gamma-ray short time variabilities can be explained by the magnetic reconnection model?
- What is the role of the galaxy host neutral gas and dust in the extinction of the produced radiation, particularly the optical to soft X-rays?
- Are the produced gamma-rays annihilated by pair production?

5.2 LLAGNs

The non-thermal multi-wavelength emission from active galactic nuclei (AGNs) has been broadly studied (e.g., Reynoso et al. 2011; Lenain et al. 2008).

Regarding the very high energy (VHE) emission, until recently only AGNs with highly beamed jets towards the line of sight, namely blazars, were detected by gamma-ray telescopes. More than a chance coincidence, these detections are consistent with the conventional scenario that attributes the VHE emission of these sources to particle acceleration along the jet being strongly Doppler boosted and producing apparently very high fluxes.

Lately, however, a few sources which belong to the branch of low luminosity AGNs (or simply LLAGNs) for having bolometric luminosities of only a few times the Eddington luminosity, L_{Edd} (Ho et al. 1997; Nagar et al. 2005) have been also detected at TeV energies by ground based gamma-ray observatories (see e.g., Sol et al. 2013 and references therein). As pointed out in Chapter 4, the angular resolution and sensitivity of these detectors are still so poor that it is hard to establish exactly the location of the emission, i.e. whether it comes from the jet or the core (e.g., Kachelriess et al. 2010).

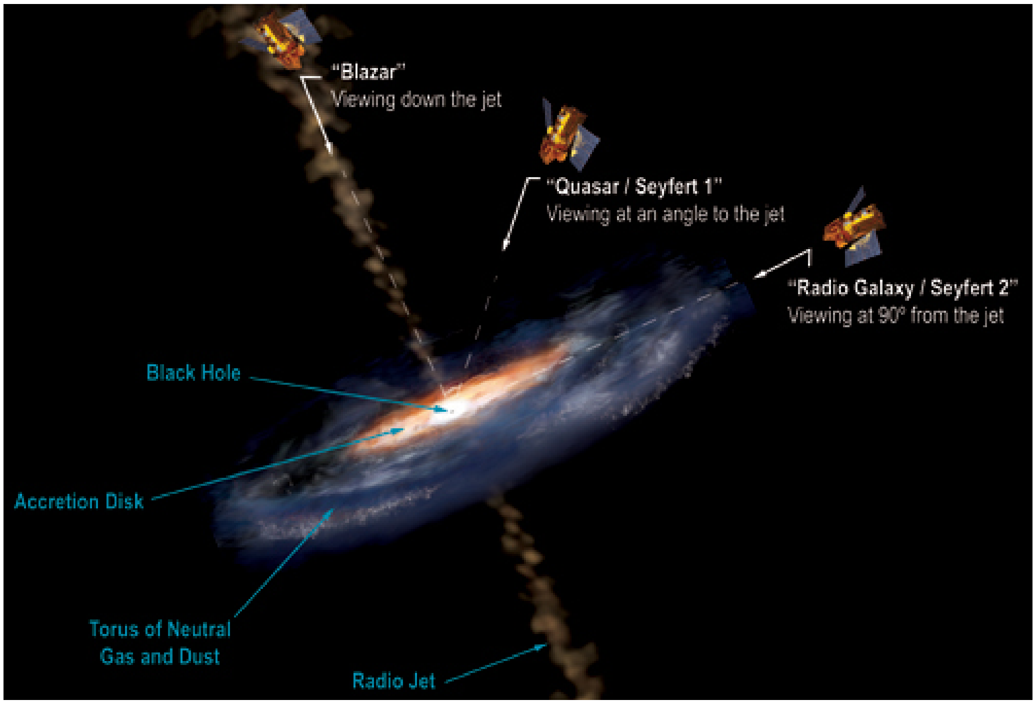
"Blazar"
Viewing down the jet
"Quasar / Seyfert 1"
Viewing at an angle to the jet
"Radio Galaxy / Seyfert 2"
Viewing at 90° from the jet
Black Hole
Accretion Disk
Torus of Neutral Gas and Dust
Radio Jet

Figure 5.2: Sketch of an AGN (Credit: Aurore Simonnet, Sonoma State University).

Among these sources, the radio galaxies M87, Cen A, Per A (or NGC1275) and IC 310 are probably the most striking cases. These VHE detections were surprising because, besides being highly underluminous, the viewing angle of the jets of these sources is of several degrees, therefore allowing for only moderate Doppler boosting. These characteristics make it difficult explaining the VHE of these sources adopting the same standard scenario of blazars. As we see in Figure 5.2, the viewing angle we have of the AGN determines how we perceive it. Since LLAGNs, like Seyfert and radio-galaxies, are viewd edge-on, there is this possibility for gamma-rays to be originated in the nuclear region, because in this case unlike the blazars, the relativistic jets cannot screen the core emission.

5.3 Cen A

The prominent radio galaxy Cen A (or NGC 5128) is the nearest FR I active radio galaxy[2] to Earth (z=0.0018, Graham 1978), at a distance of $\simeq$ 3.8 Mpc (Rejkuba 2004), making it uniquely observable among this class of objects and an excellent source for studying the physics of relativistic outflows as well as of the core region. Cen A is one of the best well known extragalactic objects over a wide range of frequencies and the photon emission from the nuclear region of the galaxy has been detected from the radio to the gamma-rays band. Cen A has been proposed as a possible source of UHE cosmic rays (with energies $\leq 6 \times 10^{19}$eV; Abraham et al. 2007) by the Pierre Auger collaboration. The super massive black hole (SMBH) mass inferred from kinematics of stars, as well as H_2 and ionized gas is estimated to be in the range of $\sim 10^7 - 10^8\ M_\odot$ (Marconi et al. 2006; Neumayer et al. 2007), and here we adopted the value $5 \times 10^7 M_\odot$. The viewing angle of the jet (θ) is still debatable, for instance at parsec scales it is $\theta \sim 50^\circ - 80^\circ$ (Tingay et al. 1995), whereas at the 100 pc scale $\theta \sim 15^\circ$ (Hardcastle et al. 2003).

In this section we show the results for Cen A obtained by applying the model described in Chapters 2 and 3, around the nuclear region, employing the set of parameters listed in Table 5.1.

The values for the first five parameters in Table 5.1 have been calculated from Eqs. 2.10-2.13 and 2.14. We take for the accretion disk inner radius the value $R_X = 6R_S$, for the extension L_X of the reconnection region (see Figure 2.6), we consider the value $L_X \simeq 10R_S$, and for the extension of the corona $L \simeq 20R_S$. These adopted values are compatible with the results of Kadowaki et al (2015) and ensure a sufficient magnetic these values a reconnection power to explain the observed emission and besides, the small size of emission region is compatible with high energy short time variability (see below). As remarked earlier, the volume V of the emission region in Table 1 was calculated by considering the torus that encompasses the reconnection region in Figure 2.6. The magnetic reconnection power W is evaluated from Eq. 2.11.

---

[2] Fanaroff-Riley I (FR I) sources are radio galaxies which often have symmetric radio jets whose intensity falls away from the nucleus (Fanarroff & Riley 1974)

Table 5.1: Model parameters for Cen A, Per A, M87 and IC 310.

	Parameters	Cen A	Per A	M 87	IC 310
B	Magnetic field (G)	1.25×10^4	4812	1620	8874
W	Magnetic reconnection power (erg/s)	1.2×10^{43}	8.2×10^{43}	5.25×10^{44}	4.5×10^{43}
ΔR_X	Width of the current sheet (cm)	3.6×10^{13}	2.4×10^{14}	1.35×10^{15}	3.2×10^{12}
n_c	Coronal particle number density (cm^{-3})	7.1×10^9	10^9	3.3×10^8	10^{11}
T_d	Temperature of the disk (K)	1.9×10^8	3×10^8	5.2×10^8	2.25×10^8
R_x	Inner radius of disk (cm)	8.8×10^{13}	6×10^{14}	5.3×10^{15}	1.7×10^{14}
L_X	Extension of the reconnection region (cm)	1.5×10^{14}	10^{15}	4.4×10^{15}	8.8×10^{12}
L	Extension of the corona (cm)	3×10^{14}	2×10^{15}	4.4×10^{15}	8.8×10^{12}
V	Volume of emission region (cm^3)	7.8×10^{43}	2.3×10^{46}	10^{48}	1.36×10^{41}
d	Distance of the source(Mpc)	3.8	75	16.7	78
m	Mass of BH ($M_\odot$)	5×10^7	3.4×10^8	3×10^9	10^8
p	Injection spectral index	2.4	2.15	2.4	1.7
γ_{min}	Particle minimum Lorentz factor	6	2	4	2
N_H*	Dust/neutral gas column density (cm^{-2})	10^{23}	4×10^{20}	2×10^{20}	1.2×10^{21}

* The observed values for N_H of Cen A, Per A, M87 and IC 310 are taken from Morganti et al. (2008); Canning et al. (2010); Lieu et al. (1996) and Kalberla et al. (2010), respectively.

Figure 5.3 shows the radiative cooling rates for the different energy loss processes for electrons and protons as described in Section 3.2. These are compared with the acceleration rates due to first-order Fermi acceleration both within the magnetic reconnection site (Eqs. 2.5 and 2.6) and behind a shock (Eq. 2.8). We notice that at high energies for both protons and electrons the acceleration is dominated by the first-order Fermi magnetic reconnection process in the core region. Besides, the main radiative cooling process for the electrons is synchrotron radiation (Figure 6.1(a)), while for protons the photo-meson production ($p\gamma$ interactions) governs the loss mechanisms (Figure 5.3(b)). For the $p\gamma$ interactions, we have found that the proper target radiation field is that of the photons from the electron synchrotron emission.

The intercept between the magnetic reconnection acceleration rate and the synchrotron rate in Figure 5.3(top) gives the maximum energy that the electrons can attain in this acceleration process, which is $\sim 3 \times 10^{11}$eV. As in the black hole binaries (Chapter 4), protons on the other hand, do not cool as efficiently as the electrons and can attain energies as high as $\sim 2.5 \times 10^{17}$eV.

We have constructed the SED for Cen A, using a lepton-hadronic model where particles are accelerated close to the central BH by magnetic reconnection and interact with the surrounding fields radiating in a spherical region of radius L. The SED is depicted in Figure 5.4.

In Figure 5.4, we considered injected accelerated particles with a power-law spectral index $p = 2.4$ (see Equation 3.50) which is consistent with theoretical predictions of particle acceleration within magnetic reconnection sites (see §. 2). We note that in order to fit the observed data in the radio to optical range, we had to assume a minimum energy for the injected electrons in the acceleration zone (Eq. 11 in KGV15), $E_{min} = \gamma_{min} m_e c^2$, with $\gamma_{min} = 6$. Though this injected value has no influence on the VHE tail of the SED, it is determinant in the match of the low energy branch. We have found that values of $\gamma_{min} < 6$ do not lead to the synchrotron match in the low energy range. Our calculations show that synchrotron radiation explains the observed emission in the radio to visible band, while SSC is the dominant mechanism to produce the observed hard ($X-$rays) and low energy gamma-rays as a result of interactions between energetic electrons with scattered synchrotron photons. Also in the Figure, neutral pion (π^0) decays can explain the observed gamma-rays at TeV energies, via pp and $p\gamma$ interactions which are the two main processes producing π^0.

As we will see in §. 5.7, the gamma-ray absorption due to pair production occurs according to Figures 5.12(a) and 5.13(a) very near the accretion disk at heights smaller than $\sim 0.001 R_S$, thus much smaller than the emission region that extends up to $\sim 20 R_S$ in our model, so that $exp(-\tau) \simeq 1$ and the absorption effect is not effective at the heights of interest.

On the other hand, since the dust column density of Cen A is significantly high ($N_H = 10^{23}\mathrm{cm}^{-2}$, Reynoso et al. 2011), we found that optical to soft X-ray emission is fully absorbed via γN absorption (see figure 5.4, Eq. 3.49).

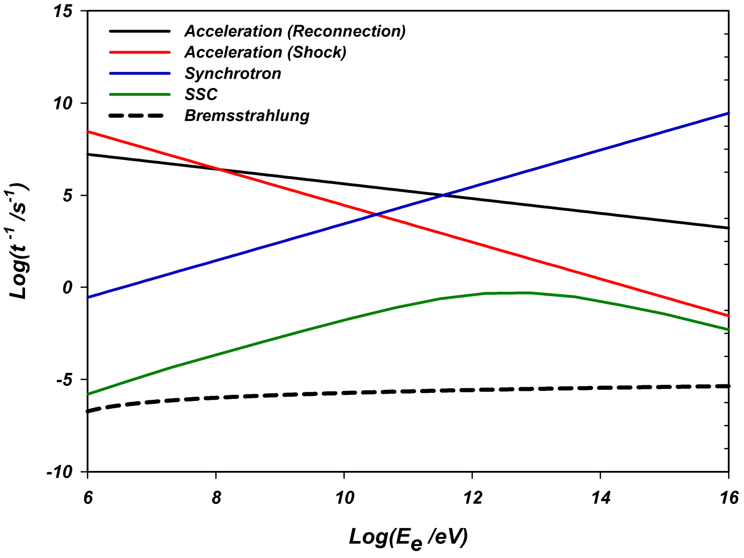

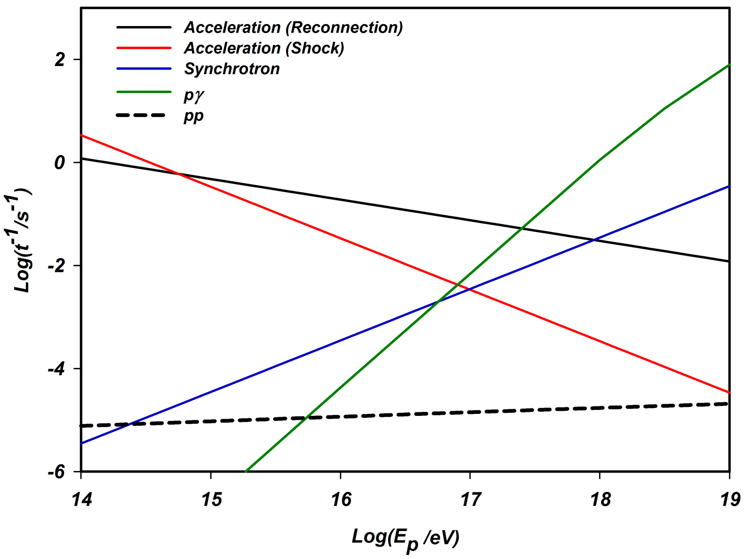

Figure 5.3: Acceleration and cooling rates for electrons (top) and protons (bottom) in the nuclear region of Cen A.

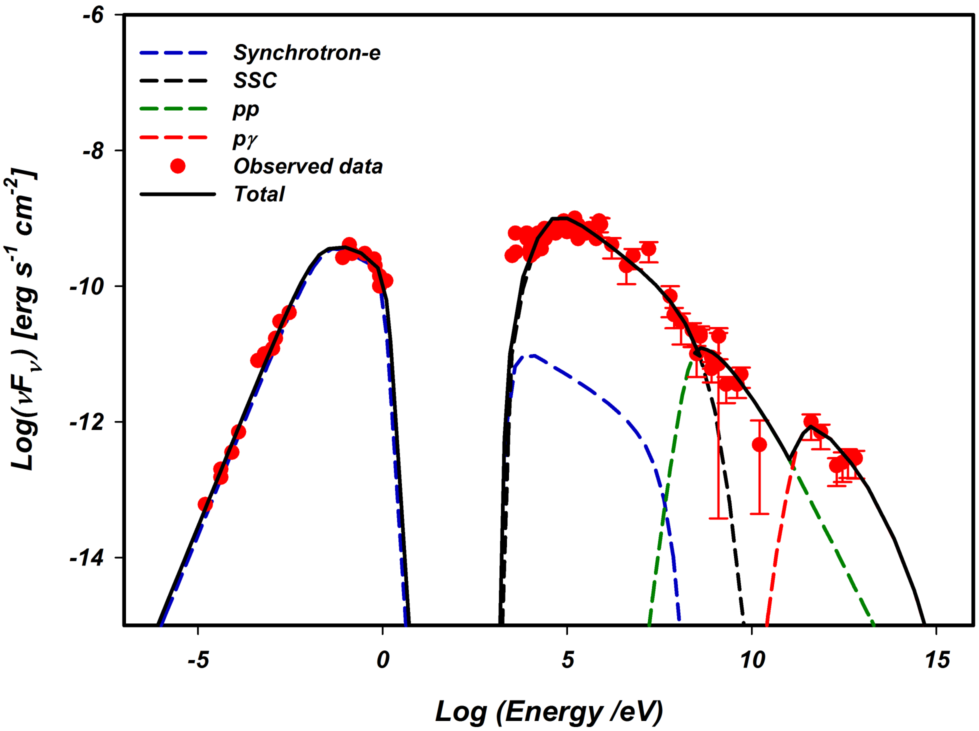

Figure 5.4: Calculated spectral energy distribution (SED) for Cen A using the magnetic reconnection acceleration model in a lepton-hadronic scenario compared with observations. The data depicted in the radio to optical energy range (10^{-5}eV − 1eV) are from SCUBA at 800 μm (Hawarden et al. 1993), ISO & SCUBA at 450 μm and 850 μm (Mirabel et al. 1999); the data in the hard x-rays range is from *Swift-BAT* (Ajello et al. 2009) and *Suzaku* (Markowitz et al. 2006). We also include data from *OSSE* (Kinzer et al. 1995) and *COMPTEL* (Steinle et al. 1998) in the range of $5 \times 10^5 - 10^7$eV. The data observed in the energies $10^8 - 10^{10}$eV are taken by *EGRET* (Sreekumar et al. 1999; Hartman et al. 1999) and in the energies $10^8 - 10^{10}$eV by *Fermi-LAT* (Abdo et al. 2009b, 2010). The TeV data are taken by *HESS* (Aharonian et al. 2009). All data points showed here are corresponded to core emission.

5.4 IC 310

The peculiar galaxy IC 310 (also named B0313+411 and J0316+4119 in observational reports) is one of the brightest objects which, as Per A, is also located in the Perseus galaxy cluster at a distance of 78 Mpc from Earth (Aleksić et al. 2014c) and harbours a supermassive BH with a mass of $\sim 10^8 M_\odot$ (Aleksić et al. 2014c). The redshift of this source is z=0.0189 (Bernardi et al. 2002) which makes it the fourth nearest AGN at VHE gamma-rays (Kadler et al. 2012), after Cen A with z=0.00183, M 87 with z=0.004 and Per A with z=0.017559.

IC 310 has been observed at energies E>100 GeV by MAGIC (Mariotti et al. 2010) and Fermi-LAT collaboration also reported the detection of photons above 30 GeV (Neronov et al. 2010). However the origin of the gamma-ray emission is not clear yet and both the jet and the core are considered as possible emission regions.

Recently, MAGIC collaboration has reported fast time variability for IC 310 on the VHE gamma-ray with time scales ∼4.8 min (Aleksić et al. 2014a,c) which constrains the size of the emission zone to 20% of its R_S.

The parameters we used to calculate the acceleration and cooling time scales and also to reconstruct the SED of this source are shown in Table 5.1.

The comparison between the acceleration and cooling rates is depicted in Figures 5.5(top) and 5.5(bottom) for electrons and protons, respectively. As in the other cases, we see that the calculated maximum energy for both electrons and protons reaches larger values for magnetic reconnection than for shock acceleration, so that magnetic reconnection should be the dominating mechanism to accelerate particles in the nuclear region of this source as well. The diagrams indicate that electrons can accelerate up to 8×10^{10} eV, while the protons up to 2×10^{17} eV. Also in this source synchrotron emission is the dominant loss mechanism for electrons and $p\gamma$ radiation is the dominant one for protons for energies larger than $\sim 10^{15}$ eV.

Figure 5.6 shows the calculated SED for IC 310. As in the other sources, the observed radio emission can be explained by synchrotron and the TeV gamma-rays by the *pp* and $p\gamma$ processes due to particles injected with a power law spectral index p=1.7.

The core opacity to this emission has been also calculated for IC 310 in figures 5.12 and 5.13 which indicate that the gamma-ray absorption is negligible in the emission length scales here considered $\sim 0.3R_S$.

At low energies ($10-10^2$eV), as we show in §. 5.7, the produced radiation is fully absorbed due to γN interactions (see Figures 5.6 and 5.14(d)).

As for M87, our model and the adopted parametrization can also naturally explain the fast variability of the VHE gamma-rays in 3C 310. The effective emission zone for this source has a size $L \simeq 0.3R_S$ according to our model (see Table 5.1), which is compatible with the scale inferred from the observed high variability in the gamma-ray emission, $\sim$ 4.8 min.

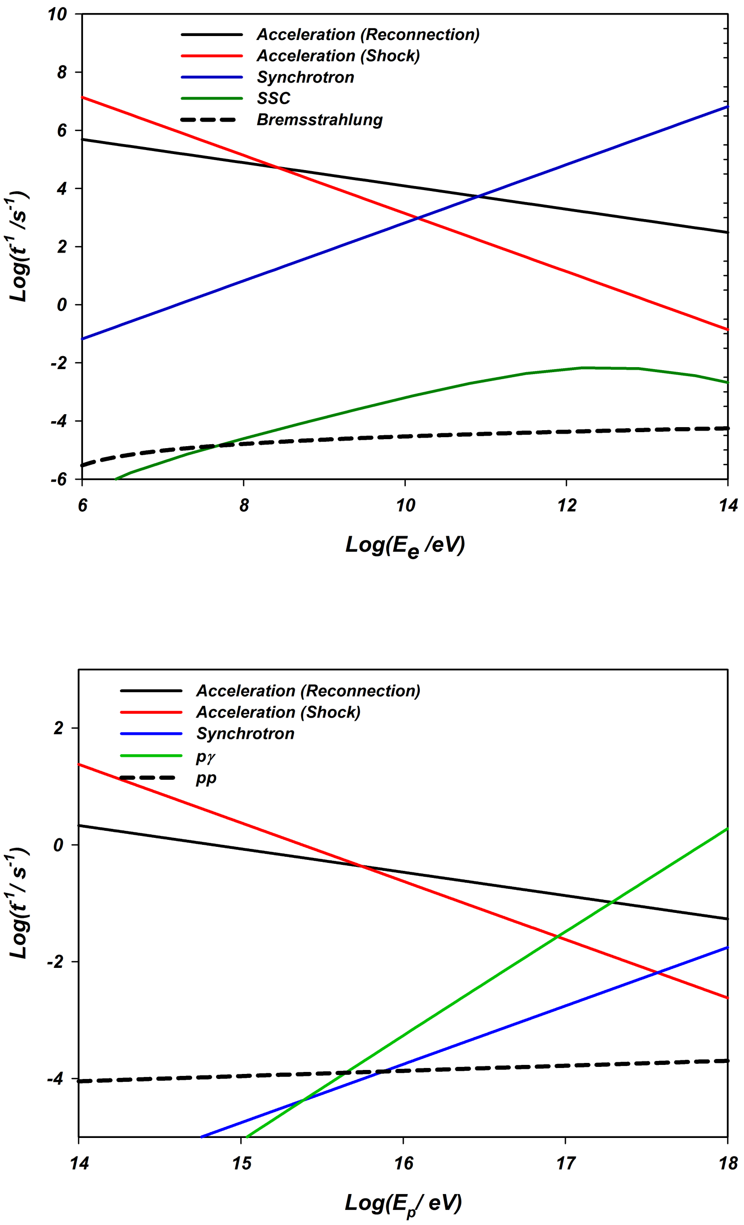

Figure 5.5: Acceleration and cooling rates for electrons (top) and for protons (bottom) in the nuclear region of IC 310. See more details in the text.

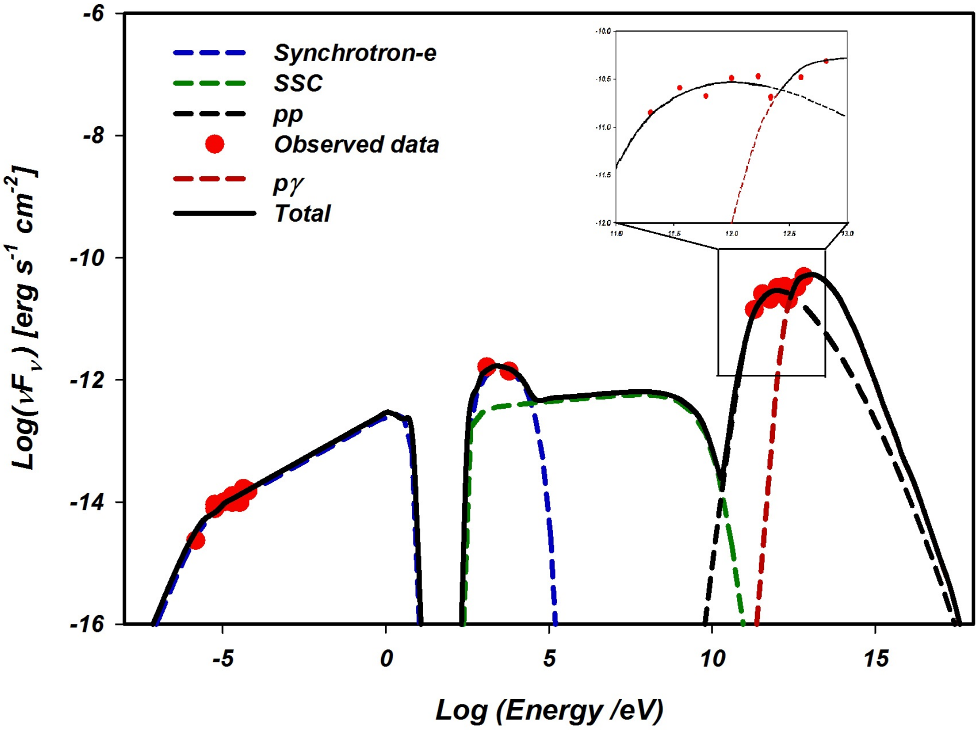

Figure 5.6: A lepton-hadronic model of the SED of IC 310 compared with observations. The core radio data are obtained from Kadler et al. 2012; Dunn et al. 2010; Becker et al. 1991; White & Becker 1992; Condon et al. 2002; Douglas et al. 1996. The X-ray data are from XMM-Newton (Sato et al. 2005) and the VHE gamma-ray data are from *MAGIC* (Aleksić et al. 2014c). In the upper right side of the diagram it is depicted the detail of the modeling of the VHE branch.

5.5 Per A

Perseus A (also known as NGC 1275 and 3C 84), is a nearby active galaxy located at the centre of the Perseus cluster and hosts a central SMBH mass of $\sim 3.4 \times 10^8 \mathrm{M}_\odot$ (Wilman et al. 1994). In fact, Per A is one of the closest gamma-ray emitting AGNs. Its distance to the Earth is 75 Mpc (Brown & Adams 2011) and is also of great interest, specially due to its proximity, also providing an excellent opportunity to study the physics of relativistic outflows. Per A also seems to exhibit jet precession with an orientation angle $\approx 30^\circ - 55^\circ$ (Walker et al. 1994; see also Falceta-Gonçalves et al. 2010), which may be an indication that Per A is the result of a merger between two galaxies (Liu and Chen 2007). It is a very bright radio galaxy showing an extended jet with FR I morphology (e.g., Vermeulen et al. 1994; Buttiglione et al. 2010) with asymmetric jets at both kpc (Pedlar et al. 1990) and pc scales (Asada et al. 2006).

The parameters of our model for producing the SED of Per A are tabulated in Table 1. As in Cen A, the first five parameters are calculated from Eqs. 2.10- 2.14. We have also used for the accretion disk inner radius the value $R_X = 6R_S$ and for the extension L_X of the reconnection region the values $L_X = 10R_S$ and $L \simeq 20R_S$ (see Table 5.1).

The radiative loss and acceleration rates for electrons and protons are compared in Figure 5.7. As in Cen A, magnetic reconnection is the dominant acceleration mechanism over shock acceleration at the high energy branch for both electrons and protons and determines the maximum energy that the particles can achieve before losing part of it radiatively. Electrons may be accelerated up to 3×10^{11}eV and the main process to cool them is synchrotron, while the maximum energy the protons can achieve is 10^{17}eV and *photo-meson* production ($p\gamma$) is the dominant mechanism to cool them. Similarly to Cen A, the dominant photon field interacting with the accelerated protons is the synchrotron radiation.

We have constructed the SED for this source employing a leptonic scenario (Fig-

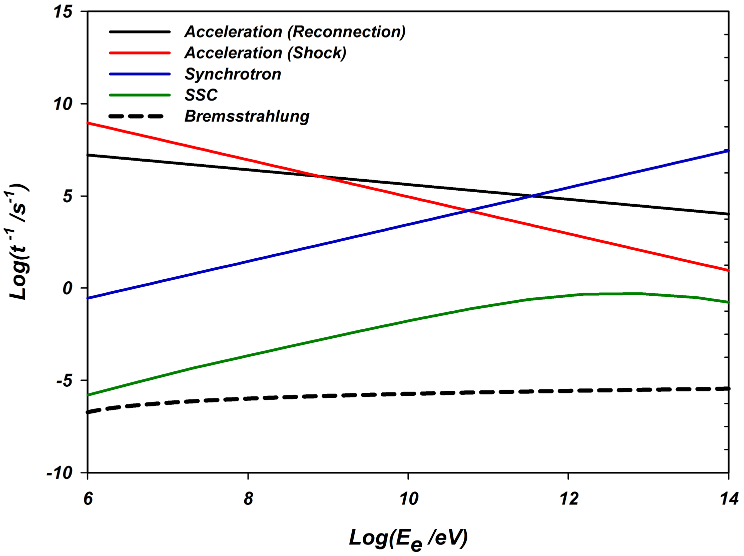

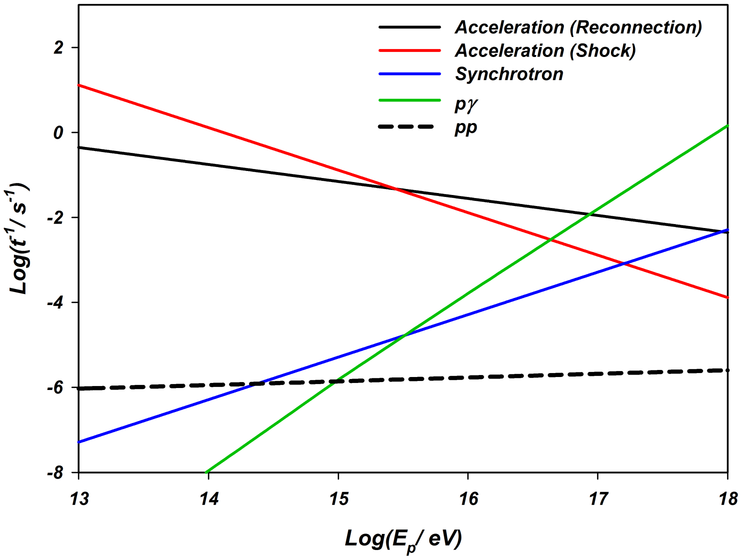

Figure 5.7: Acceleration and cooling rates for electrons (top) and for protons (bottom) in the nuclear region of Per A (NGC 1275).

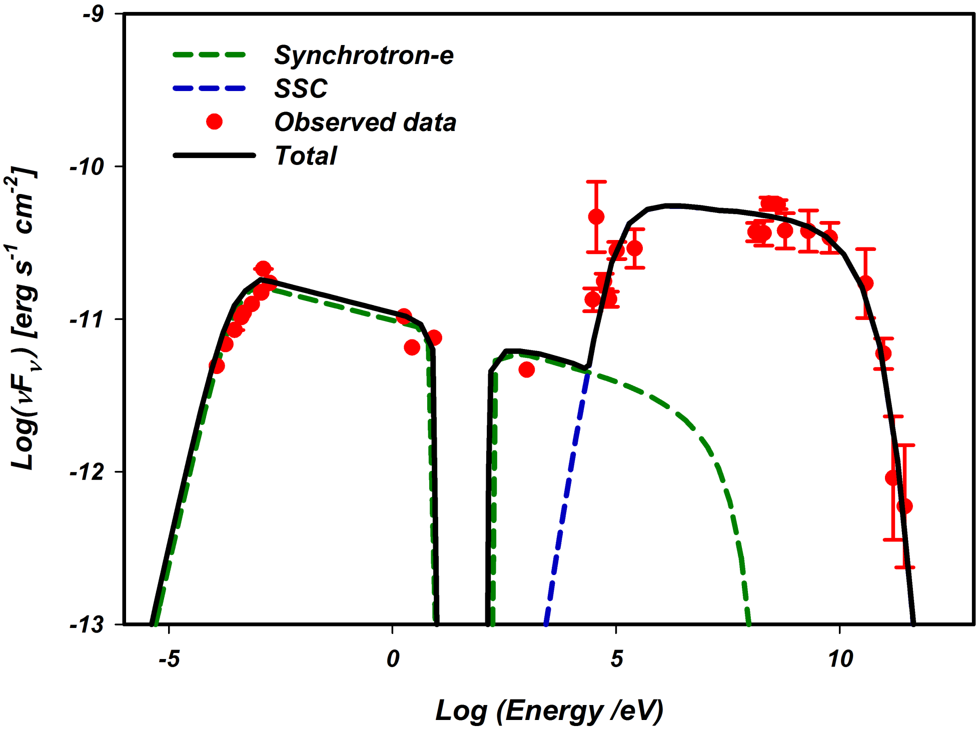

Figure 5.8: A leptonic model to reproduce the SED of Per A (NGC 1275) using the magnetic reconnection acceleration model. Data include *MOJAVE* (Lister et al. 2009), *Planck* (Ade et al. 2011), HST (Chiaberge et al. 1999), and HST FOS (Johnstone & Fabian 1995) for the radio to optical spectrum; data depicted in X-rays is from the XMM (Torresi 2012), *Swift*-BAT (Ajello et al. 2009), and BATSE (Harmon et al. 2004); and data depicted in the gamma-ray band is from *Fermi-LAT* (Abdo et al. 2009a; Ackermann et al. 2012) in the 100 MeV-100GeV energy range, and from *MAGIC* (Aleksić et al. 2010a,b, 2012a,b) in the VHE tail. We note that the error bars for the BATSE data (in the 10^5 eV range) were evaluated using Harmon et al. (2004); Soldi et al. (2014) and Wilson et al. (2012).

ure 5.8). In this case, the primary particles were injected with a power law spectral index $p = 2.15$ (Eq. 2.7). The radio spectrum is matched by electron synchrotron emission, with particles injected into the acceleration zone with rest mass energy (i.e., with $\gamma_{min} = 1$). The observed x-ray and gamma-ray emission is explained by SSC occurring in the nuclear region in a spherical region of radius $L \sim 20R_S$, as described in §. 3.2. The observations indicate that there is a high energy cut-off around $\sim 3 \times 10^{11}$eV in this source. In our scenario this is due to leptonic emission produced by interactions of high energy electrons with the radiation field produced by themselves and this cut-off is compatible with the maximum energy calculated from the comparison of the reconnection acceleration rate with the synchrotron loss rate in Fig. 5.7(top).

The optical depth for the produced gamma-rays was also taken into account in the construction of Figure 5.8 and is shown in Figures 5.12(b) and 5.13(b). We note that the 100 GeV gamma-rays may be fully absorbed due to pair production only very near the disk ($z < 0.001R_s$). These vertical distances from the disk compared to the length scale of the emission region are very small and we can ignore the absorption effect at the larger heights compatible with the extension of the emission region in our model. Nevertheless, the radiation produced in the range of $10 - 10^2$eV is entirely absorbed by the galaxy dust lane as we show in Fig. 5.8 (see §.3.3.2). The corresponding optical depth versus energy is plotted in Fig. 5.14(b).

5.6 M87

The FR I giant radiogalaxy M87 is another well-known nearby AGN located at 16.7 Mpc within the Virgo cluster which harbours a SMBH with a mass of $M_{BH} \sim 6 \times 10^9\ M_\odot$ (e. g., Gebhardt & Thomas 2009) which, along with Cen A and Per A, is known as a peculiar extragalactic laboratory to study high energy astrophysics and investigate the nonthermal mechanisms of VHE emission in AGNs. The observations indicate that its

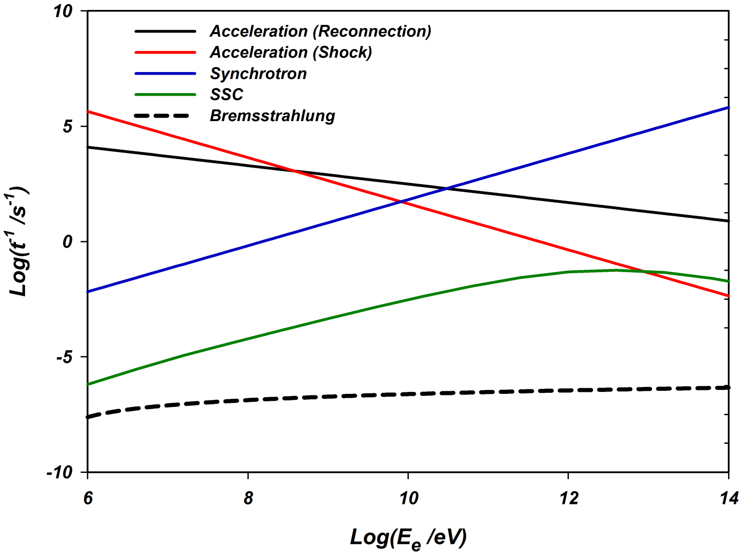

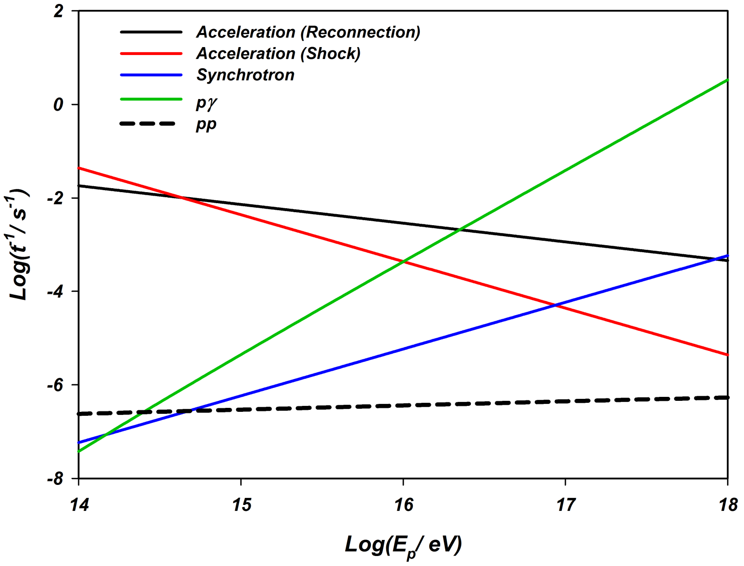

Figure 5.9: Acceleration and cooling rates for electrons (top) and for protons (bottom) in the nuclear region of M87.

jet is oriented within 20° of the line of sight (Biretta et al. 1999), so that as in the other cases, no significant Doppler boosting is expected for the gamma-ray flux.

The TeV gamma-ray signal from M87 was first reported by *HEGRA* (Aharonian et al. 2003) and then confirmed by *HESS* (Aharonian et al. 2006). The latter also revealed that this emission is strongly variable with time scales of 1-2 days and thus produced in a very compact region, as pointed out before.

Table 5.1 shows the parameters that we used to calculate the acceleration and cooling rates and also to reconstruct the SED of this source.

In Figures 5.9, we compare the rates of the radiative cooling processes with the rates of the acceleration mechanisms for electrons and protons. As in the other two sources, we find that the dominant energy loss mechanisms are the synchrotron and the $p\gamma$ interactions for electrons and protons, respectively, and the acceleration is dominated by the magnetic reconnection process which defines the energy cut off for both electrons and protons. Figure 5.9 indicates that this maximum energy is $\sim 4 \times 10^{10}$eV for electrons and $\sim 5 \times 10^{16}$eV for protons.

Figure 5.10 shows the calculated SED for M87 compared to the observations. It is also reproduced by a lepton-hadronic model in the core region as described in §. 2, where we assumed an injected particle energy distribution $\propto E^{-p}$ with a power index $p = 2.4$.

With an electron minimum energy $E_{min} = 4m_e c^2$, we can fit the observed core radio to visible spectrum by synchrotron emission.

The spectrum detected by the *Fermi-LAT* connects smoothly with the low-state TeV tail detected by HESS. In Figure 5.10, our model reproduces this connection effectively with gamma-ray emission produced by SSC and pp collisions. The observed TeV tail by *HESS* is fitted by the decay of neutral pions from $p\gamma$ interactions with photons coming from synchrotron radiation.

Figures 5.12(c) and 5.13(c) show the absorbed gamma-ray flux for M87. As in the other cases, this absorption is significant only at heights smaller than R_S and therefore, its

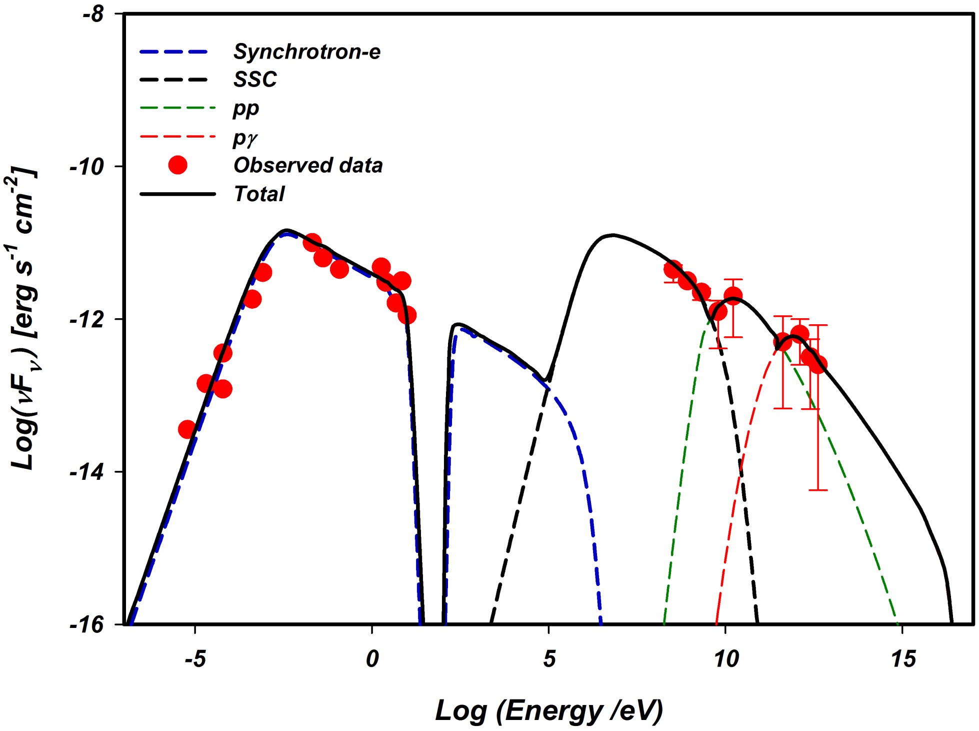

Figure 5.10: A lepton-hadronic model of the SED of M87 compared with observations. The core radio data are obtained from MOJAVE VLBA (Kellermann et al. 2004) at 15 GHz, from (Biretta et al. 1991) at 1.5, 5 and 15 GHz, from IRAM (Despringre et al. 1996) at 89 GHz, from SMA at 230 GHz (Tan et al. 2008), from Spitzer at 21 and 7.2 GHz (Shi et al. 2007) and from Gemini (Perlman et al. 2001) at 3.2 GHz. Optical-UV emission from HST (Sparks et al. 1996). MeV/GeV gamma-ray data are from *Fermi-LAT* (Abdo et al. 2009c), and the low-state TeV spectrum (Aharonian et al. 2006) from *HESS*.

effect can be neglected at the much larger emission scales considered here. However, the calculated optical depth in the low energies around $10^2 - 10^3$eV (Eq. 3.49) is significant and the emitted photons are absorbed by interactions with neutral gas and dust from the surrounding ISM (see Fig. 5.10).

We note that our model and the chosen parametrization is also consistent with the observed TeV rapid variability of M87 which is $\sim 1 - 2$ days (Abramowski et al. 2012) implying an extremely compact emission region (corresponding to scales of only a few R_S). As remarked in §3.2, the emission region in our model corresponds to the torus region that encompasses the cylindrical shell where magnetic reconnection particle acceleration takes place in Figure 2.6, i.e., the effective emission zone in our model has a thickness $\simeq L$. For this source $L \simeq 5R_S$ (see Table 5.1), which is of the order of the inferred scale from the observed variability.

5.7 Photon absorption in LLAGNs

We consider two main absorption processes of the photons produced by the accelerated particles in the nuclear region of the sources: the gamma-ray photon absorption due to $e^- e^+$ pair creation, and the absorption of optical and X-ray photons due to external interstellar neutral gas and dust (photon-neutral) absorption.

5.7.1 gamma-ray absorption by photon-photon ($\gamma\gamma$) annihilation

In our model the dominant radiation field for this process in the coronal region is due to the scattered photons from the accretion disk (see Figures 5.12 & 5.13). To evaluate the optical depth due to this process, we have adopted the model described in Cerutti et al. (2011), assuming that the gamma-rays are produced within a spherical region around the disk with radius extending up to $L \simeq 20R_S$. The attenuated gamma-ray luminosity $L_\gamma(E_\gamma)$ at a distance z above the disk is given by (Romero & Christiansen 2005)

$$L_\gamma(E_\gamma) = L^0_\gamma(E_\gamma)e^{-\tau(z,E_\gamma)} \tag{5.1}$$

where L^0_γ is the intrinsic coronal gamma-ray luminosity and $\tau(z, E_\gamma)$ is the optical depth which depends on the gamma-ray energy and the distance above the disk z. The total gamma-ray optical depth τ can be calculated by integration of Eq. 3.46 over the high energy photon path length l and disk photon density as target radiation field (Eq. 3.28, in $\mathrm{cm^{-3}erg^{-1}sr^{-1}}$) yields (Cerutti et al. 2011)

$$\tau = \int_0^{+\infty}\int_0^{\Omega_{disk}}\int_{\epsilon_{min}}^{+\infty} n_{ph}(1-\cos\theta_0)\sigma_{\gamma\gamma}d\epsilon d\Omega dl, \tag{5.2}$$

where Ω_{disk} is the total solid angle covered by the accretion disk seen from the gamma ray and θ_0 is the angle between the two photons. In order to calculate the explicit optical depth, a relevant geometrical sketch of the system is needed to be established and applied. Figure 5.11 shows the accretion disk/BH system and all the geometrical parameters. The details of geometrical relations are described in Cerutti et al. (2011).

Figures 5.12 and 5.13 depict the gamma-ray absorption spectrum for the sources investigated here, for different heights z. We see that in all cases at distances larger than $\sim 0.1R_S$ from the disk surface, the absorption of gamma-rays becomes negligible. Since we are adopting here an emission region with an extension $\simeq 0.6R_S$ to $\simeq 20R_S$, it is reasonable to exclude the absorption effect in our calculations of the SEDs, as described above.

5.7.2 Photon-neutral (γN) interactions

As we describe in §. 3.3.2, the low energy photons produced in the nuclear emission region (with energies larger than the hydrogen Lyman threshold) will photo-ionize the surrounding interstellar hydrogen and helium gas (see Eq. 3.49). Using the values of N_H

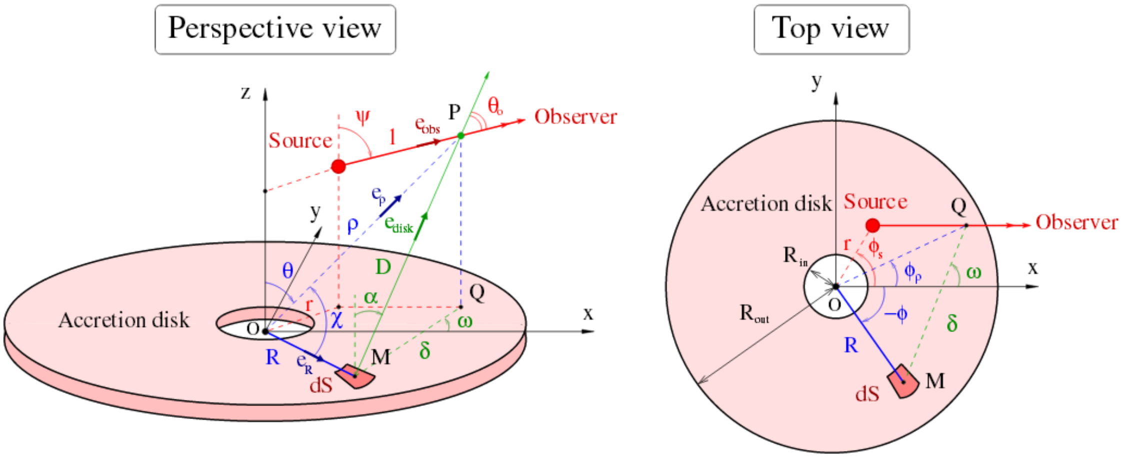
Perspective view
Top view
z
Source
ψ
l
e_{obs}
P
θ_0
Observer
y
e_ρ
ρ
e_{disk}
θ
D
r
α
Q
x
Accretion disk
O
χ
ω
R
e_R
M
δ
dS
y
Accretion disk
Source
Q
Observer
R_{in}
r
ϕ_s
ϕ_ρ
ω
x
O
R_{out}
−ϕ
δ
R
dS
M

Figure 5.11: Sketch of an accretion disk formed around the BH in the center (point O). Source of energetic gamma rays lies above the disk as a hypothetical torus (see §. 3.2) which is seen at an angle Ψ by a distant observer. Produced gamma-rays and photons emitted from the unit surface of the disk dS (centred around point M) interact at the point P with an angle θ_0. The projection of point P in the disk plane is given by point Q. (Extracted from Cerutti et al. 2011).

listed in Table 5.1, we calculated the γN optical depths due to these interactions for the LLAGNs studied in this work. The results are depicted in Figure 5.14. These results have been considered to reconstruct the SEDs of these sources.

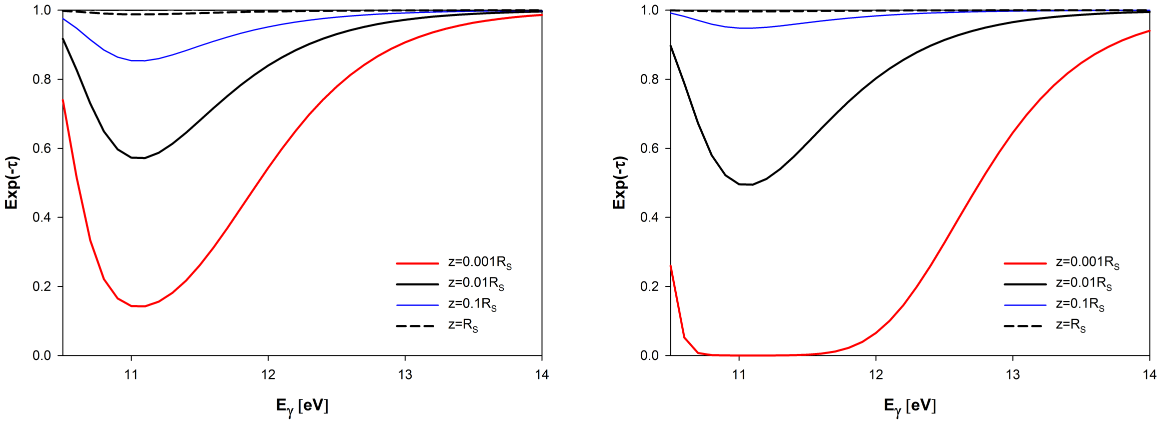

(a) Cen A

(b) Per A

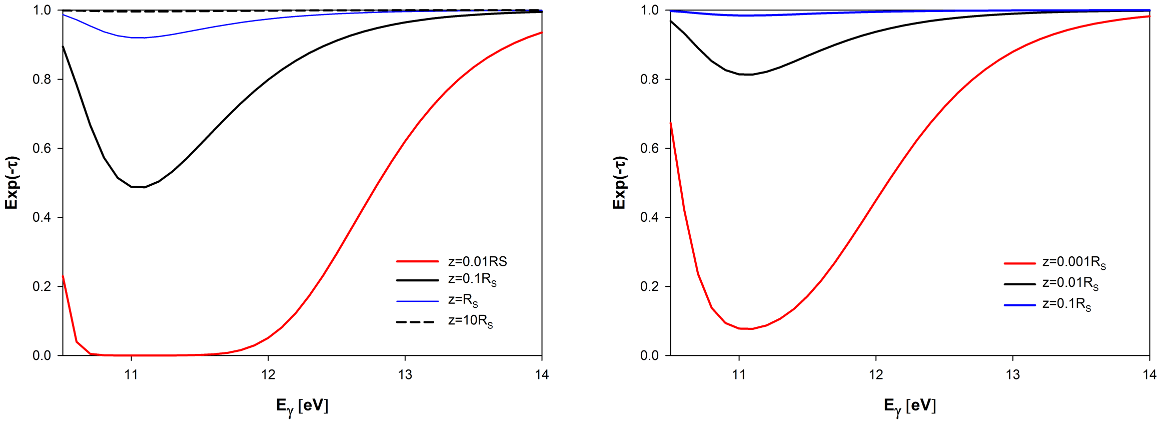

(c) M87

(d) IC 310

Figure 5.12: Spectrum of gamma-ray absorption at selected heights z above the plane of the disk in Cen A, Per A, M87, and IC 310 (a, b, c, and d panels, respectively).

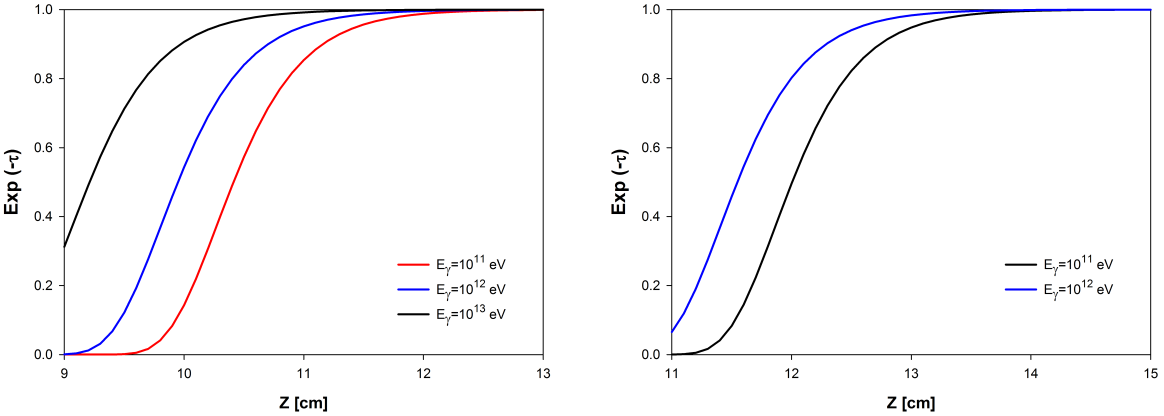

(a) Cen A

(b) Per A

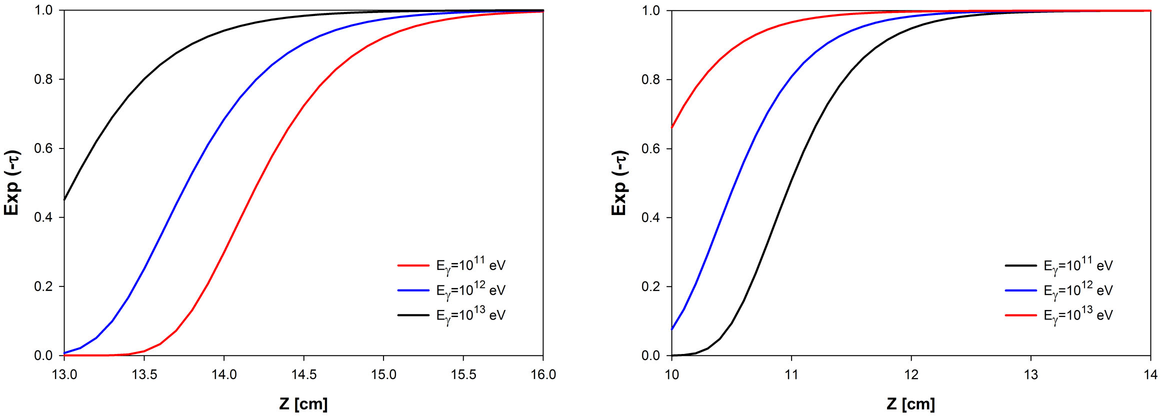

(c) M87

(d) IC 310

Figure 5.13: The transmitted flux $exp(-\tau)$ for different gamma-ray energies as function of the height z above the disk in Cen A, Per A, M87, and IC 310 (a, b, c, and d panels, respectively).

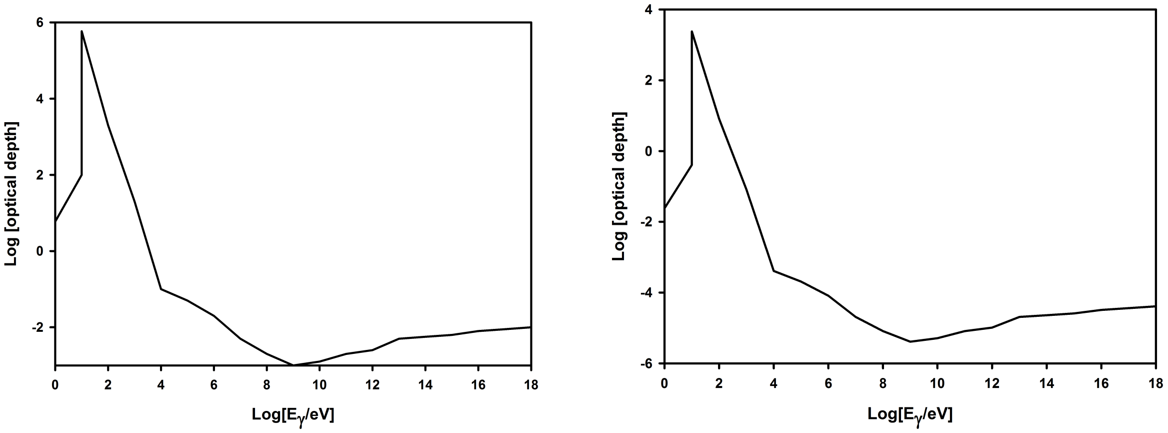

(a) Cen A

(b) Per A

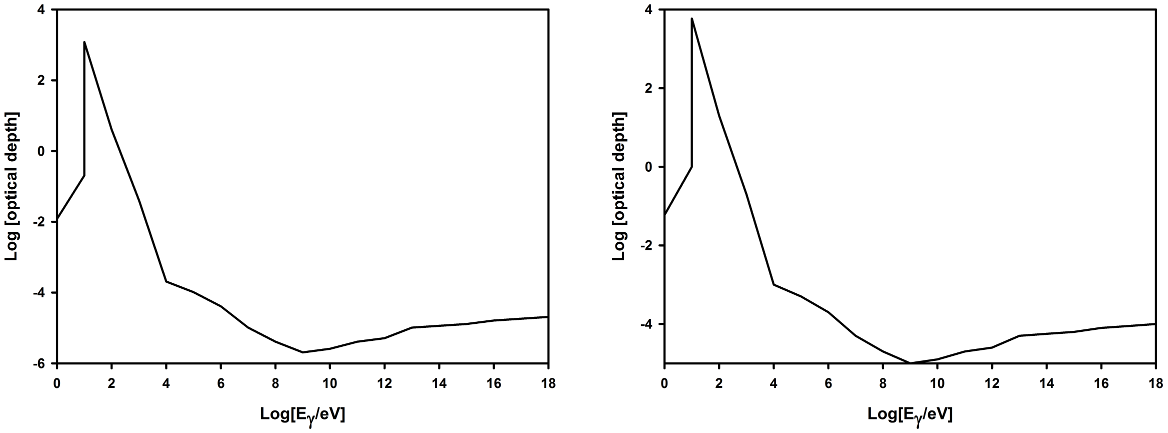

(c) M87

(d) IC 310

Figure 5.14: The γN optical depth ($\tau_{\gamma H}$) in Cen A, Per A, M87, and IC 310 (a, b, c, and d panels, respectively).

5.8 Comparison with other models

As stressed earlier, alternative models have tried to explain the observed emission structure and in particular the VHEs, of the sources here studied as mostly due to jet emission. We briefly discuss these models below and compare with ours.

5.8.1 Cen A

According to our results for Cen A, the observed hard X-rays and $Fermi-LAT$ gamma-ray data can be interpreted as due to SSC and pp interactions, respectively, with accelerated particles injected in the nuclear region (at scales $\sim 20R_S$) driven by magnetic reconnection with a distribution with power law index $p = 2.4$. The TeV radiation observed by $HESS$, on the other hand, is explained by neutral pion decays resulting from $p\gamma$ interactions.

In Sahu et al. 2012, the authors also showed that the TeV gamma-rays in Cen A could be explicated by $p\gamma$ interactions, but between relativistic protons accelerated by Fermi process in shocks along the jet with the monochromatic photons observed at 170keV. Another model (Reynoso et al. 2011) also proposed particle acceleration at the jet basis with the production of the hard X-rays by synchrotron emission, and the $Fermi - LAT$ and $HESS$ data by IC and pp mechanisms, respectively, along the jet. Kachelriess et al. (2010), on the other hand, argued against the production of the gamma-rays in Cen A by pp interactions along the jet because on leaving the source they would interact with the extragalactic background light (EBL) resulting in a flatter spectrum in the TeV range than the observed one by HESS (see also §. 1).

5.8.2 Per A

In the case of Per A, there is no relevant data yet in TeV energies, but our core model can nearly explain the observed $Fermi - LAT$ and $MAGIC$ data in the 0.1 GeV $-$ 650 GeV range with a leptonic scenario dominated by SSC. The synchrotron photons that are absorbed in SSC are produced by accelerated electrons by magnetic reconnection in the coronal nuclear region around the BH (within distances $\sim 20R_S$) having a distribution with a power law index $p = 2.15$.

An SSC model has been also proposed by Aleksić et al. (2014b), but they assumed that the Per A core could be a BL Lac blazar with the jet bending strongly at larger scales and the high energy non-thermal radiation could be originated in a sub-structure of the jet near the core pointing towards our line of sight. This bending still requires observational support and any evidence of jet precession (e.g., Walker et al. 1994; Falceta-Gonçalves et al. 2010) may favour this model. But our proposed model dismisses the necessity of such a strong bending and besides, is supported by the correlations with the observations found in Kadowaki et al. (2015); Singh et al. (2015) as discussed in Chapter 2.

5.8.3 M87

In the case of M87, we have applied the same magnetic reconnection model in the nuclear region around the BH (within a region of 5 R_S) considering the injection of the accelerated particles with a power law index $p = 2.4$. This has resulted a lepton-hadronic scenario for the SED with SSC emission and neutral pion decays from *pp* collisions explaining the $Fermi-LAT$ data. We also found that the decay of the neutral pions due $p\gamma$ interactions can explain the observed data by $HESS$ in the TeV range.

The suggested sites of TeV emission for this source in former works range from large scale structures of the kpc jet (Stawarz et al. 2005) to a compact peculiar hot spot (the so-called HST-1 knot) at a distance 100 pc along the jet (Stawarz et al. 2006) and inner (sub-parsec) parts of the sources. Reynoso et al. (2011) for instance, considered that this emission is produced in the nuclear jet, but reconstructed all the emission features, which are highly variable and possibly non-simultaneous, with a single *pp* mechanism.

Giannios et al. (2010), on the other hand, proposed that compact minijets induced by magnetic reconnection moving relativistically within the nuclear jet in different directions, some of which pointing to our line of sight, might explain the short-time variable TeV flares observed in M87. This model holds several similarities with ours as it proposes that the minijets are generated by reconnection events in the core region, and then move out with the jet flow up to scales of $\sim 100 R_S$. Our model also predicts the development of outbursts with the formation of reconnected features (plasmons) that may be carried out with the jet (see de Gouveia Dal Pino & Lazarian 2005) and might explain e.g., observed superluminal features near the jet basis (de Gouveia Dal Pino & Lazarian 2005; de Gouveia Dal Pino et al. 2010). However, Giannios et al. (2010) study provides no predictions for the SED structure of M87.

In addition, there is an extensive list of models that propose that the variable VHE emission of M87 can be originated in the inner jet. These span from leptonic models, such as the decelerating flow model (Georganopoulos et al. 2005), the spine-shear (Tavecchio & Ghisellini 2008), and the mini/multi-blob model (Lenain et al. 2008), to hadronic models with the emission due to proton interactions with synchrotron photons (Reimer et al. 2004), or *pp* interactions in a cloud-jet scenario (Barkov et al. 2012). However, the location of the very high emission region is still an unsolved problem.

Neronov & Aharonian (2007) also proposed a nuclear origin for the TeV emission of M87 coming directly from the magnetosphere of the black hole (see also Levinson 2000). They showed that accelerated electrons in the strong rotation-induced electric fields in vacuum gaps in the BH magnetosphere, similar to a pulsar magnetosphere, could lead to the observed TeV emission. Since the acceleration and emission mechanisms occurs in a very compact region close to the event horizon of the BH, it potentially can explain the observed variability of TeV gamma-ray emission from M87. Besides, as in our model, they also explain this emission as due to $p\gamma$ interactions with an IR compact target photon field produced by synchrotron emission. However, as stressed in §. 3, the attenuation of gamma-ray emission due to electron-positron pair production may be significant in distances smaller than or equal to $\sim R_S$ (see Figures 5.12 & 5.13), which may affect their results. In our model, the emission scales are larger ($\sim 5R_S$) making these attenuation effects negligible.

5.8.4 IC310

In the case of IC 310, according to our results also a lepton-hadronic model in the nuclear region is able to explain the observed SED features with protons and electrons accelerated by magnetic reconnection and injected in the emission region with a power law distribution with index $p = 1.7$. As remarked, the observed radio emission is well fitted by synchrotron and the VHE emission detected by *MAGIC* can be explained by decays of neutral pions resulting from pp and $p\gamma$ interactions.

Our model with an appropriate choice of parameters is also able to explain naturally the time variability detected in the sources here investigated. In particular, the very fast variability reported for the IC 310 gamma-ray emission of about ~ 4.8 min (Aleksić et al. 2014c) implies an emission region scale of $\simeq 0.3R_S$. To explain this variability and compactness of the emission region, Aleksić et al. (2014c) suggested that the particles could be accelerated by electric fields in the BH magnetosphere, as in pulsar models. Nevertheless, as demonstrated, our magnetic reconnection model reproduces the observed SED with an emission region with a similar size as expected above.

In summary, the construction of the SEDs of the sources discussed here (Cen A, Per A, M87 and IC 310) based on our magnetic reconnection model in the core region, have demonstrated that the observed emission at low energies (radio to optical) can be explained by synchrotron emission. SSC with target photons coming from electron synchrotron emission is the dominant (leptonic) mechanism to produce the observed hard X-rays and low energy gamma-rays, while neutral pion decays resulting from pp inelastic collisions and photo-meson interaction ($p\gamma$) are the dominant mechanisms to produce the very high energy (VHE) gamma-rays. Interestingly, in the case of the microquasars Cyg X1 and Cyg X3, we have also found that the core model could reproduce the full observed

SED including the low and high energy branches (Khiali et al. 2015a)[3].

5.9 What we have learned

In this chapter, we have employed the reconnection acceleration model to the core region of the low luminous radio galaxies Cen A, Per A, M87 and IC 310 and showed that it is able to reproduced very well their SEDs, from radio to gamma-rays up to TeV energies. Magnetic reconnection acceleration seems to provide a better efficiency in regions where magnetic activity is dominant in comparison with diffusive shock acceleration. Particles can gain energy up to a few times ~ 100 PeV due to magnetic reconnection acceleration.

The observed TeV gamma-ray emission may be originated via neutral pion decays in hadronic processes.

The fast magnetic reconnection acceleration model can also naturally explain the observed short time variability, specially of the high energy gamma-ray in M87 and IC 310.

We have found that the gamma-ray absorption via electron-positron pair production in the vicinity of the emission region in our model is negligible, but the radiation produced in the optical and X-ray range around 1keV is fully absorbed fully absorbed by the neutral gas and dust of the surrounding ISM of the host galaxy of these sources.

The observations and the comparison with recent works indicate the origin of the

---

[3] We should remark that the observed emission at low energies (radio to optical) from the core regions in the case of Cen A and M87 is fitted by the core model described here only if we assume that the minimum electron energy injected in the acceleration region is a few times the particle rest mass. If one considers instead, $\gamma_{min} = 1$ in the computation of the SEDs of these sources, the calculated synchrotron spectrum produced inside the core, mostly in the IR band, is fully absorbed by the energetic electrons and protons in order to produce the SSC and $p\gamma$ emissions, respectively, at the higher energies. Thus if this were the case, the observed radio to optical spectrum in these sources would be probably due to more evolved synchrotron radiation produced beyond the VHE emission region, probably in the jet basis, which would be compatible with jet-like models for the low energy range (e.g., Reynoso et al. 2011).

VHE emission in these sources is still debatable. A core origin, as the one suggested here arises as an interesting possibility as long as magnetic activity is significant in the surrounds of the BH. To remove the ambiguity between core and jet models, we will need substantially improved observations, specially in the gamma-ray range. With the much larger resolution, sensitivity and field of view expected for the forthcoming Cherenkov Telescope Array (CTA) observatory (Actis et al. 2011;Acharya et al. 2013; Sol et al. 2013) and with longer times of exposure of these nearby sources, we may collect higher resolution data and more significant information on variability that will allow to determine the real location of the emission region.

In the next Chapter, we will extend the study performed in this Chapter and apply the same magnetic reconnection acceleration model in the core region of LLAGNs to investigate the origin of the observed extragalactic neutrino emission.

Chapter 6

The origin of high energy neutrino emission from the core of LLAGNs

The detection of astrophysical very high energy (VHE) neutrinos in the range of TeV-PeV energies by the IceCube observatory (Ahlers & Murase 2014) has opened a new season in high energy astrophysics. Energies $\sim$PeV imply that the neutrinos are originated from sources where cosmic rays (CRs) can be accelerated up to $\sim 10^{17}$eV. In the previous Chapter, we have shown that the observed TeV gamma-rays from radio-galaxies may have a hadronic origin in their nuclear region and in such a case this could lead also to neutrino production. In this Chapter we will explore the possibility that relativistic protons accelerated by magnetic reconnection in the core region of these sources may produce VHE neutrinos via the decay of charged pions produced by photo-meson process. We will also calculate the diffuse flux of VHE neutrinos using this model and compare with the IceCube data. These results of this Chapter have been published in Khiali & de Gouveia Dal Pino (2015) and a copy of the article is in Appendix D in attachment.

6.1 What we want to know

- What would be the dominant mechanism to produce the high energy neutrinos?
- Are the HE neutrinos originated from LLAGNs?
- Can the magnetic reconnection model in the nuclear region of LLAGNs explain the origin of the HE neutrinos observed by the IceCube?

6.2 High energy neutrinos detected by the IceCube

Neutrino observations can provide unique information to understand their origin and can even lead to the discovery of new classes of astrophysical sources. The inherent isotropic nature of the detected neutrino flux by IceCube is compatible with an extragalactic origin and is supported by diffuse high energy gamma-ray data (Ahlers & Murase 2014). The observed neutrinos with energies $\sim PeV$ (i.e., 10^{15} eV) suggest that they are originated from a source where cosmic rays (CRs) can be accelerated up to $\sim 10^{17}$eV.

A potential mechanism to produce VHE neutrinos in the TeV-PeV range is through the decay of charged pions created in proton-proton (pp) or proton-photon ($p\gamma$) collisions in a variety of astrophysical sources which, in the framework of the IceCube observations, may include active galactic nuclei (AGNs) (Kasanas & Ellison 1986; Stecker et al. 1991; Atoyan & Dermer 2001; Neronov & Semikoz 2002) and gamma-ray bursts (GRBs) (Waxman & Bahcall 1997).

Hadronic mechanisms producing VHE neutrinos via the acceleration of cosmic rays (CRs) in AGNs have been suggested for more than three decades (Eichler 1979; Protheroe & Kasanas 1983; Mannheim 1995; Hazlen & Zas 1997; Mucke & Protheroe 2001; Kalashev et al. 2014; Marinelli & Fraija 2014b; Atoyan & Dermer 2003; Becker 2008). Currently, the detection of gamma-ray emission at TeV energies in AGNs, not only in high luminous blazars, but also in less luminous radio-galaxies, has strengthened the notion that they may be excellent cosmic ray accelerators and therefore, important potential neutrino emission candidates.

Several recent models have tried to describe the detected TeV neutrino emission as due to AGNs. For instance, Marinelli & Fraija (2014b) employed two different hadronic scenarios involving the interaction of accelerated protons at the AGN jet either with photons produced via synchrotron self-Compton (SSC) or with thermal particles in the giant lobes. They then derived the expected neutrino flux for LLAGNs, or more specifically, for radio galaxies for which they examined the origin of the observed TeV gamma-ray spectra as due to hadronic processes. Earlier work by Gupta (2008) had already introduced hadronic scenarios to explain the TeV emission in LLAGNs (e.g., Cen A). Also, Fraija (2014a,b) suggested neutral pion decays from pp and $p\gamma$ interactions in these sources as probable candidates to explain the high energy neutrinos. In another model, Kalashev et al. (2014) attempt to reproduce the IceCube data using the $p\gamma$ mechanism considering the radiation field produced by the accretion disk around the AGN central black hole (assuming a standard Shakura-Sunyaev accretion disk model). Alternatively, Kimura et al. (2014) calculated the neutrino spectra using the radiatively inefficient accretion flows (RIAF) model in the nuclei of LLAGNs considering both pp and $p\gamma$ mechanisms and stochastic proton acceleration in the RIAF turbulence.

The possibility of producing VHE neutrino emission has been also extensively explored in blazars - i.e., AGNs for which the relativistic jet points to the line of sight as remarked before (e.g., Atoyan & Dermer 2003; Becker 2008; Murase et al. 2014; Dermer et al. 2014). Dermer et al. (2014), in particular, revisited the previous studies assuming that the observed neutrinos could be produced in the inner jet of blazars and concluded that neither the flux nor the spectral shape suggested by the IceCube data could be reproduced by this scenario which predicts a rapid decline of the emission below 1 PeV. Tavecchio et al. 2014 and Tavecchio & Ghisellini 2014, on the other hand, considered the distribution of lower-power blazars, namely, BL Lac objects and, by employing a two-zone spine-sheath jet model to these sources concluded that they might be suitable for the production of the observed PeV neutrinos revealed by the IceCube.

Presently, it is very hard to define what should be the dominant process or the real sources that are producing the observed neutrino flux mainly due to the lack of more precise measurements. But while waiting for better measurements, we can explore further mechanisms and try to make reliable predictions in order to constrain the candidates.

The big challenge in models that rely on hadronic processes in the AGN nuclei is how to produce the relativistic protons that may lead to gamma-ray emission and the accompanying neutrino flux. Diffusive shock acceleration at the jet launching base was discussed by Begelman et al. (1990). Levinson (2000) and more recently, Vincent (2014) proposed that TeV gamma-ray emission might be produced in the BH magnetosphere by pulsar-like mechanisms, i.e., with particles being accelerated by the electric potential difference settled by non uniform magnetic field. As remarked above, Kimura et al. (2014) discussed stochastic acceleration in an accreting RIAF turbulent scenario, but currently none of these models can be regarded as dominant or disclaimed given the uncertainties from the observations regarding the location of the gamma-ray emission.

Here, we use the magnetic reconnection model described in the former chapters and specially in Chapter 5 to probe the origin of the HE neutrinos detected by the IceCube. We calculate the spectrum of neutrinos arising from the interactions of the accelerated protons by magnetic reconnection around the supermassive BHs of LLAGNs with the surrounding radiation and thermal particle fields. We have seen in Chapter 3 that these interactions produce weakly decaying π^0 and $\pi^{\pm}$ pions and the latter may generate high energy neutrinos. We will then evaluate the diffuse neutrino intensity that a whole population of LLAGNs may produce and compare with the IceCube data.

6.3 Neutrino production via hadronic processes

In Chapter 5, we have demonstrated that the core region of LLAGNs is able to accelerate protons up to energies of a few 10^{17}eV through the first-order Fermi magnetic reconnection mechanism described in section 2.2.2 (and Figure 2.6). This indicates that these sources could be powerful CR accelerators. As demonstrated in Chapter 5 (see also below), these protons can cool very efficiently via synchrotron, $p\gamma$ and pp interactions in the region that surrounds the BH of these sources. These hadronic interactions lead to the production of HE gamma-rays and VHE neutrinos via decays of neutral and charged pions, respectively. In Chapter 5 (see also Khiali et al. 2015b), we calculated the spectral energy distribution of HE gamma-ray emission for the LLAGNs for which this emission has been detected (i.e, Cen A, Per A, M87 and IC310). Below, we calculate the VHE neutrino emission from the nuclear region considering arbitrary sources of this class.

6.3.1 Neutrino production out of pp collisions

The charged pions can be created through inelastic collisions of the relativistic protons with particles (nuclei) of the corona that surrounds the BH and the accretion disk by means of the following reactions (Atoyan & Dermer 2003; Becker 2008)

$$p + p \to n_1(\pi^+ + \pi^-) + n_2\pi^0 + p + p \tag{6.1}$$

where n_1 and n_2 are multiplicities, $\pi^0 \to \gamma + \gamma$ (Stecker 1970, 1971), carrying 33% of the accelerated proton's energy. The charged pions $\pi^\pm$ then decay and produce neutrinos via $\pi^+ \to \nu_\mu + \bar{\nu}_\mu + \nu_e + e^+$ and $\pi^- \to \nu_\mu + \bar{\nu}_\mu + \bar{\nu}_e + e^-$, where ν_μ, $\bar{\nu}_\mu$, and ν_e are the muon neutrino, muon antineutrino, and electron neutrino, respectively (Margolis et al. 1978; Stecker 1979; Michalak et al. 1990). The pp cooling rate is almost independent of the proton energy which has been discussed in §. 3.2.2.

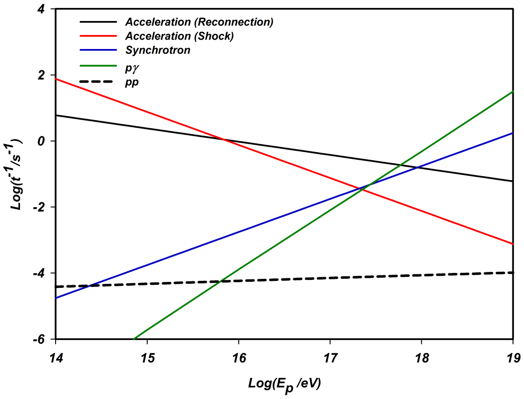

(a) *Model* 1

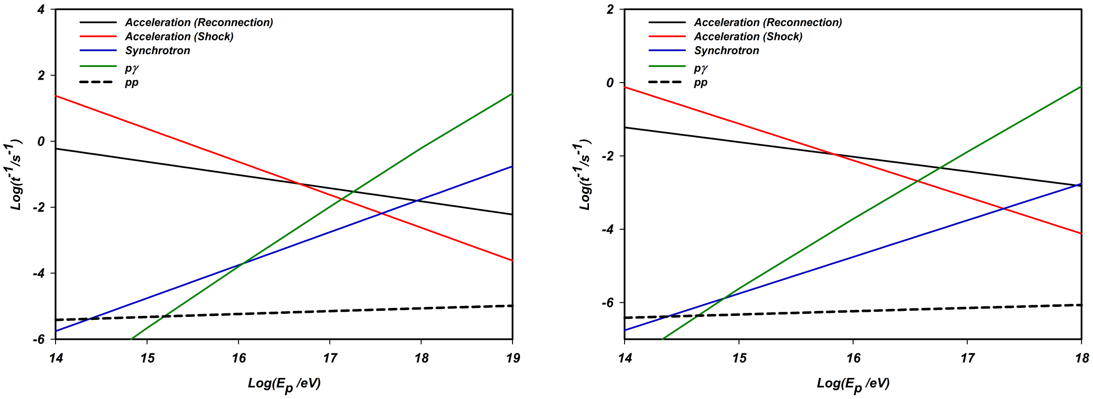

(b) *Model* 2

(c) *Model* 3

Figure 6.1: Acceleration and cooling rates for protons in the core regions of LLAGNs with a central black hole mass (*a*) $M = 10^7 M_\odot$ (Model 1), (*b*) $M = 10^8 M_\odot$ (Model 2), and (*c*) $M = 10^9 M_\odot$ (Model 3).

6.3.2 Neutrino production out of $p\gamma$ interactions

The photomeson ($p\gamma$) production takes place for photon energies greater than $E_{th} \approx 145$ MeV. Pions are also obtained from the $p\gamma$ interaction near the threshold via the channels (Atoyan & Dermer 2003)

$$p + \gamma \rightarrow p + \pi^0, \tag{6.2}$$

with $\pi^0 \rightarrow \gamma + \gamma$ carrying 20% of accelerated protons energy and

$$p + \gamma \rightarrow p + \pi^+ + \pi^-, \tag{6.3}$$

and the charged pions will also decay producing neutrinos as described in §. 3.2.3.

The radiative cooling rate for this mechanism in an isotropic photon field with density $n_{ph}(E_{ph})$ can be calculated by (Stecker 1968):

$$t_{p\gamma}^{-1}(E_p) = \frac{c}{2\gamma_p^2} \int_{\frac{E_{th}^{(\pi)}}{2\gamma_p}}^{\infty} dE_{ph} \frac{n_{ph}(E_{ph})}{E_{ph}^2} \times \int_{E_{th}^{(\pi)}}^{2E_{ph}\gamma_p} d\epsilon_r \sigma_{p\gamma}^{(\pi)}(\epsilon_r) K_{p\gamma}^{(\pi)}(\epsilon_r)\epsilon_r, \tag{6.4}$$

where in our model the appropriate photons come from the synchrotron radiation[1], $n_{ph}(E_{ph}) = n_{synch}(\epsilon)$, $\gamma_p = \frac{E_p}{m_e c^2}$, ϵ_r is the photon energy in the rest frame of the proton, $K_{p\gamma}^{(\pi)}$ is the inelasticity of the interaction , $E_{th}^{\pi} = m_\pi(1 + \frac{m_\pi}{2m_p})$ is the threshold energy for the production of pions which is equal to 145 MeV, and $\sigma_{p\gamma}^{(\pi)}$ is the cross section calculated by Eq. 3.35, . Atoyan & Dermer (2003) proposed a simplified approach to calculate the cross-section and the inelasticity which are given by

$$\sigma_{p\gamma}(\epsilon_r) \approx \begin{cases} 340\ \mu barn & 300 \text{ MeV} \leq \epsilon_r \leq 500 \text{ MeV} \\ 120\ \mu barn & \epsilon_r > 500 \text{ MeV}, \end{cases} \tag{6.5}$$

---

[1] We find that for photomeson production, the radiation from the accretion disk is irrelevant compared to the contribution from the coronal synchrotron emission above the disk (see Chapter 3 and Khiali et al. (2015a,b) for a detailed derivation of the synchrotron rate and its radiation field density).

Table 6.1: Three sets of model parameters for LLAGNs.

	Parameters	Model 1	Model 2	Model 3
m	BH mass ($M_\odot$)	10^7	10^8	10^9
p	Injection spectral index	1.9	1.7	2.2

and

$$K_{p\gamma}(\epsilon_r) \approx \begin{cases} 0.2 & 300 \text{ MeV} \leq \epsilon_r \leq 500 \text{ MeV} \\ 0.6 & \epsilon_r > 500 \text{ MeV}. \end{cases} \quad (6.6)$$

6.4 Neutrino emission and diffuse intensity

To calculate the neutrino emission from the nuclear region of an LLAGN, we consider a population of protons accelerated by magnetic reconnection in the surrounds of the BH according to the model described in Chapter 2.

We assume for these accelerated particles an isotropic power law spectrum (in units of erg^{-1}cm^{-3}s^{-1}) (see §. 3.4):

$$Q(E) = Q_0 E^{-p} exp[-E/E_{max}] \quad (6.7)$$

where $p > 0$ and E_{max} is the cut-off energy.

The normalization constant Q_0 above is calculated from the total power injected to accelerate the protons according to the relation:

$$L_p = \int_V d^3r \int_{E_{min}}^{E_{max}} dE \; E \; Q(E) \quad (6.8)$$

where V is the volume of the emission region around the magnetic reconnection zone and L_p corresponds to the magnetic reconnection power W given by Eq. 2.11. To calculate W

Table 6.2: Physical conditions around the LLAGNs represented by models 1, 2 and 3, obtained from Eqs. 2.10-2.12 and 2.14, using $r_x = 6$, $l = 20$, $l_X = 10$ and $\xi = 0.7$.

	Parameters	Model 1	Model 2	Model 3
B	Magnetic field (G)	2.8×10^4	8874	2806
W	Magnetic reconnection power (erg/s)	2.4×10^{42}	2.4×10^{43}	2.4×10^{44}
ΔR_X	Width of the current sheet (cm)	7.2×10^{12}	7.2×10^{13}	7.2×10^{14}
n_c	Coronal particle number density (cm^{-3})	3.6×10^{10}	3.6×10^{9}	3.6×10^{8}

we have adopted the following suitable set of parameters $\xi = 0.7$, $R_X = 6R_S$, $L_X = 10R_S$, and $L = 20R_S$.

The maximum energy of the accelerated particles E_{max} is derived from the balance between the magnetic reconnection acceleration rate and the radiative loss rates as given in Chapter 3. Figure 5.3 compares these rates for protons considering LLAGNs with three different BH masses 10^7, 10^8 and $10^9 M_\odot$. We have also considered different power-law indices (p) for the injected particle spectrum in each of these models (see Table 6.1) which as stressed in Chapter 5, are compatible with the values derived from analytical and numerical studies of first-order Fermi acceleration by magnetic reconnection and also with values inferred from the observations (see also Khiali et al. 2015b and references therein).

The calculated values of B, W, ΔR_X and n_c from Eqs. 2.10-2.12 and Eq. 2.14 for these three representative source models are listed in Table 6.2. For simplicity, the derived proton luminosities (which are $\sim 1/4\ W^2$) and emission properties of these three models

---

[2] The magnetic reconnection power (Eq. 2.11) will both heat the surrounding gas and accelerate particles. As in Kadowaki et al. (2015), we assume that approximately 50% of the reconnection power goes to accelerate the particles. This is consistent with plasma laboratory experiments of reconnection acceleration (Yamada et al. 2014) and also with the observations of solar flares (e.g., Lin & Hudsun 1971). We further assume that this power is equally shared between the protons and electrons/positrons, so that the proton luminosity will be 25% of the calculated value by Eq. 2.11.

will characterize the whole range of LLAGNs in the the calculation of the HE neutrino flux below. The adoption of this approach, rather than accounting for a whole range of BH mass sources allows us to avoid the introduction of further free parameters in the modelling.

In Figure 6.1, for comparison we have also calculated the proton acceleration rate due to a shock formed in the surrounds of the reconnection region (Eq. 2.8) for the same set of parameters as above. As in Khiali & de Gouveia Dal Pino (2015), we find that the maximum energy attained from magnetic reconnection acceleration is higher than that shock acceleration. It should be also remarked that protons with these calculated maximum energies have Larmor radii smaller than the thickness of the reconnection layer ΔR_X (Eq. 2.12), as required (see Chapter 2).

The neutrinos that are produced from pion decay will escape from the emission region without any absorption and their spectrum is given by (Tavecchio et al. 2014; Kimura et al. 2014):

$$E_\nu L_\nu(E_\nu) \simeq (0.5t_{pp}^{-1} + \frac{3}{8}t_{p\gamma}^{-1})\frac{L_X}{c}E_p L_p, \tag{6.9}$$

where E_ν is the neutrino energy and E_p the proton energy. Since Figure 5.3 demonstrates that the $p\gamma$ emission cools the protons faster than pp collisions, the dominant hadronic process in our model is the $p\gamma$ emission. Therefore, this mechanism will prevail in the production of the neutrinos and the first term of Eq. 6.9 can be neglected. In $p\gamma$ interactions, E_ν is related with the parent proton energy through the equation $E_\nu = 0.05E_p$ (Spurio 2015), because the average energy of the pion is ~ 0.2 of the parent proton energy and in the decay of the π^+ chain four leptons are produced (including one electron neutrino as remarked), each of which has roughly 1/4 of the pion energy. It has been also demonstrated in Spurio (2015) that the ratio of the neutrino luminosity to the photon luminosity from $p\gamma$ interactions is $\sim 1/3$.

In consistency with the statement above, the maximum energy of the produced neutrinos can be calculated from $E_{\nu,max} = 0.05E_{p,max}$ (Becker 2008; Hazlen 2007), which according to our model is $\sim 3 \times 10^{16}$eV for a source with a black hole mass $M_{BH} = 10^7 M_\odot$, $\sim 5 \times 10^{15}$eV for a source with $M_{BH} = 10^8 M_\odot$, and $\sim 2 \times 10^{15}$eV for a source with $M_{BH} = 10^9 M_\odot$.

The total diffuse neutrino intensity from the extragalactic sources we are considering here, i.e., LLAGNs may have contributions from different redshifts. Neglecting evolutionary effects in the core region of these sources, we can estimate the total intensity as (Murase et al. 2014):

$$\Phi_\nu = \frac{c}{4\pi H_0} \int_0^{z_{max}} dz \frac{1}{\sqrt{(1+z)^3 \Omega_m + \Omega_\Lambda}} \times \int_{L_{min}}^{L_{max}} dL_\gamma \;\; \rho_\gamma(L_\gamma, z) \frac{L_\nu(E_\nu)}{E_\nu}, \quad (6.10)$$

where L_γ is the gamma-ray luminosity, and $\rho_\gamma(L_\gamma, z)$ is the γ-ray luminosity function (GLF) of the core of the sources, defined as the number density of sources per unit comoving volume, per unit logarithmic luminosity between the redshifts $z = 0$ to $z = z_{max}$, being the latter the maximum observed redshift for radiogalaxies, $z_{max} \simeq 5.2$ (Klamer et al. 2005). GLF is integrated from L_{min} to L_{max} which are obtained from *Fermi*-LAT observations and are given by 10^{41} and 10^{44} erg/s, respectively (Di Mauro et al. 2014). The values for the cosmological parameters are assumed as: $H_0 = 70$ km s^{-1}Mpc^{-1}, $\Omega_M = 0.3$ and $\Omega_\Lambda = 0.7$.

Because of the large uncertainties in the determination of the location of the gamma-ray emission in the sources, we evaluate $\rho_\gamma(L_\gamma, z)$, as in (Di Mauro et al., 2014), from the estimated radio luminosity function (RLF) which for non-blazars is given by

$$\rho_\gamma(L_\gamma, z) = \rho_{r,tot}(L_{r,tot}^{5\mathrm{GHz}}(L_{r,core}^{5\mathrm{GHz}}(L_\gamma)), z) \times \frac{d \log L_{r,core}^{5\mathrm{GHz}}}{d \log L_\gamma} \; \frac{d \log L_{r,tot}^{5\mathrm{GHz}}}{d \log L_{r,core}^{5\mathrm{GHz}}}. \quad (6.11)$$

$d \log L_{r,core}^{5\mathrm{GHz}} / d \log L_\gamma$ and $d \log L_{r,tot}^{5\mathrm{GHz}} / d \log L_{r,core}^{5\mathrm{GHz}}$ can be calculated by (Di Mauro et al. 2014)

$$\log L_\gamma = 2.00 \pm 0.98 + (1.008 \pm 0.025) \log (L_{r,core}^{5\mathrm{GHz}}), \quad (6.12)$$

and

$$\log L_{r,core}^{5\mathrm{GHz}} = 4.2 \pm 2.1 + (0.77 \pm 0.08) \log (L_{r,tot}^{5\mathrm{GHz}}), \quad (6.13)$$

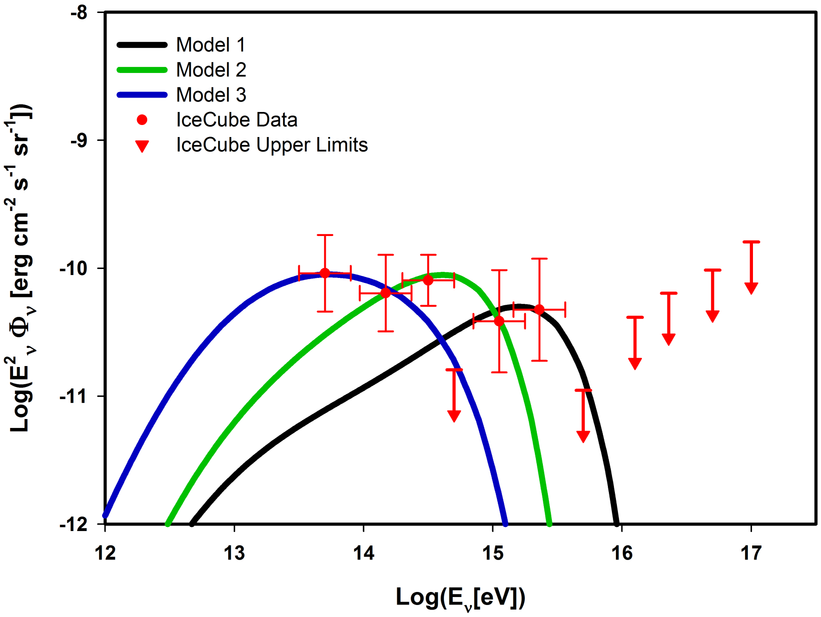

Figure 6.2: Calculated diffuse intensity of neutrinos from the cores of LLAGNs considering our magnetic reconnection acceleration model to produce the protons and gamma-ray photons for three different BH masses. The data are taken from IceCube measurements (Aartsen et al. 2014).

where $L^{5\mathrm{GHz}}_{r,tot}$ and $L^{5\mathrm{GHz}}_{r,core}$ are the radio total and core luminosities, respectively. The total RLF, $\rho_{r,tot}(L^{5\mathrm{GHz}}_{r,tot}(L^{5\mathrm{GHz}}_{r,core}(L_\gamma)), z)$, is found from interpolation of the observed data for radio-galaxies provided by Yuan & Wang (2012):

$$\begin{aligned}\rho_{r,tot}(L^{5\mathrm{GHz}}_{r,core}(L_\gamma), z) = (-1.1526 \pm 0.0411) \log L^{5\mathrm{GHz}}_{r,core} + (0.5947 \pm 0.1224) z \\ + 23.2943 \pm 1.0558 \ \mathrm{Mpc^{-3}(\log L^{5GHz}_{r,core})^{-1}}.\end{aligned} \tag{6.14}$$

The resulting neutrino flux is shown in Figure 6.2. It was calculated using eq. 6.10 above, considering the maximum neutrino energies obtained for sources with the three different BH masses (as in Figure 6.1).

Sources with $M_{BH} = 10^7 M_\odot$ result a spectrum that matches better with the observed most energetic part of the neutrino flux by the IceCube, at $\sim 3 \times 10^{15}$ to 10^{16} eV, while sources with BH masses of the order of $10^8 M_\odot$ produce a spectrum that nearly fits the observed neutrinos flux in the range of $10^{14} - 10^{15}$eV, and sources with mass $\sim 10^9 M_\odot$ fit the narrow energy band $5 \times 10^{13}\mathrm{eV} - 10^{14}\mathrm{eV}$ as well as the upper limit at 5×10^{14}eV.

6.5 Comparison with other models

As remarked in §. 6.2, other models have been proposed in the literature to explain the IceCube neutrino flux which cannot be discarded or confirmed, considering the current poorness of the data available.

Tavecchio et al. (2014) and Tavecchio & Ghisellini (2014), for instance, have proposed that the lower power blazar class of BL Lac objects could be promising candidates to produce the observed neutrino flux. In their two-zone jet model, the neutrinos are produced by photomeson interactions involving photons emitted in the slower, outer layer that envelopes the faster inner jet component. A limitation of this model is that the high-energy cut-off of the accelerated protons, as well as their injected power are free parameters, unlike in our model where both quantities are directly obtained from the magnetic reconnection acceleration mechanism. Besides, since the BL Lacs are a subclass of the blazars, another difficulty with this model is that it is not clear whether the remaining more powerful blazars, which are also TeV gamma-ray emitters, can or cannot produce neutrinos. According to the recent studies of Dermer et al. (2014) and Murase et al. (2014), which employed a single zone jet model, the powerful blazars would not be suitable candidates to explain the IceCube data. These analyses and the relatively large number of free parameters employed in the evaluation of the neutrino flux leave the question on whether or not blazars do contribute to the IceCube data opened.

Another model to explain the observed neutrino flux has been proposed by Kalashev et al. (2014) who studied photo-pion production on the anisotropic photon field of a Shakura-Sunyaev accretion disk in the vicinity of the BH in AGNs. But this model does not provide an acceleration mechanism either and therefore, the proton high energy cut-off is also a free parameter.

Recently, radio galaxies have been also discussed as possible sources of the observed HE neutrinos by Becker et al. (2014). They demonstrated that FR I radio galaxies would be more probable sources of this emission than FR II radio galaxies. In this work, as we considered the global diffuse contribution from LLAGNs spread over a range of z values, we cannot distinguish the relative contributions from both classes.

Finally, another recent study (Kimura et al. 2014) speculates that the protons responsible for the neutrino emission could be accelerated stochastically by the turbulence induced in a RIAF accretion disk in the core region of LLAGNs. This acceleration process should be essentially a second-order Fermi process and therefore, less efficient than a first-order Fermi process. Nevertheless, their analytically estimated acceleration rate $t_{acc}^{-1} \propto E^{-0.35}$ seems to be too large when compared to that predicted for first-order Fermi processes, as for instance in the present study where the acceleration rate has been extracted directly from 3D MHD simulations with test particles ($t_{acc}^{-1} \propto E^{-0.4}$; Kowal et al. 2012, see also Chapter 2 and Khiali et al. 2015a), or in shock acceleration (for which analytic predictions give $t_{acc}^{-1} \propto E^{-1}$ (Spruit 1988)). Furthermore, since the candidates to produce PeV neutrinos in this case are radio-galaxies, which are the observed gamma-ray emitters, it seems that the employment of the gamma-ray luminosity function (GLF; Di Mauro et al. 2014) to calculate the diffuse neutrino intensity as we did here seems to be more appropriate than the employment of the luminosity function in X-rays, as these authors considered.

In summary, in spite of its simplicity, the numerically tested acceleration model applied to the core region of LLAGNs here presented indicates that LLAGNs are very promising candidates to explain the IceCube VHE neutrinos.

6.6 What we have learned

In this work we have explored a model to describe the observed flux of extragalactic very high energy (VHE) neutrinos by the IceCube (Aartsen et al. 2014) in the framework of low luminosity AGNs (LLAGNs), or more specifically, of radio-galaxies. The recent detection of gamma-ray emission in the TeV range in these sources makes them also potential candidates of VHE neutrino emission via the decay of charged pions which can be produced by the interaction of accelerated relativistic protons with ambient lower energy photons and protons.

We have examined here a fast magnetic reconnection mechanism in the surrounds of the central BH occurring between the lines lifting from the accretion disk in the corona and those of the BH magnetosphere to accelerate particles to relativistic energies through a first-order Fermi process in the reconnection layer (see Chapter 2 and de Gouveia Dal Pino & Lazarian 2005; Kowal et al. 2012). Recently, it has been demonstrated that this model successfully reproduces the observed gamma-ray luminosity of hundreds of LLAGNs (Chapter 2 and Kadowaki et al. 2015; Singh et al. 2015) and also shapes the SEDs of several radio-galaxies, particularly reproducing their TeV gamma-ray energies mainly via photomeson (pγ) interactions (Chapter 5 and Khiali et al. 2015b).

Applying the same acceleration model as described above (see Chapter 2), considering three different LLAGN sources with representative BH masses, we have shown that also the observed VHE neutrino Icecube flux (Aartsen et al. 2014) can be obtained from the decay of charged pions produced in photomeson interactions involving the accelerated protons and Synchrotron photons in the core region of these sources.

Specifically, in Fig. 6.1, we compared the magnetic reconnection acceleration rate (derived from the numerical simulations of Kowal et al. 2012 and calculated for the source parameters) with the relevant hadronic cooling processes and obtained the maximum energy for the accelerated protons mainly constrained by the $p\gamma$ interactions. In Fig. 6.1, we also compared the magnetic reconnection with the shock acceleration rate in the surrounds of the BH for the same parametric space and demonstrated the higher efficiency of the first process in this region. According to our results in Fig. 6.1, protons are able to accelerate up to energies of the order of $\sim 10^{17}$eV and therefore, are suitable to produce 0.1-1 PeV neutrinos.

Fig. 6.2 indicates that the observed neutrino flux in the few PeV range can be matched by sources with $M_{BH} \sim 10^7 M_\odot$ (Model 1), while the flux in the energy range of 0.1PeV$<$ E_ν $<$1PeV can be matched by sources with $M_{BH} \sim 10^8 M_\odot$ (model 2), and that in the range $\leq$ 0.1PeV can be fitted by sources with $M_{BH} \sim 10^9$eV (model 3).

We note that, although the calculated neutrino flux was obtained from the integration of the contributions of LLAGNs over the redshifts between z=0 and 5.2 (Eq. 6.10) considering, for simplicity, sources with only three characteristic values of BH masses, one may naturally expect that a continuous integration considering the sources with all possible BH masses within the range $10^7 - 10^9 M_\odot$ should provide a similar fitting to the observed data. We also note that our model is unable to explain the IceCube upper limits at the $\sim$ 10 PeV range (also depicted in Fig. 6.2), which are probably due to other astrophysical compact source population.

Furthermore, we expect that with the 10-fold increased sensitivity at TeV energies, and the larger field of view and improved angular resolution of the forthcoming gamma-ray observatory CTA (Actis et al. 2011; Acharya et al. 2013), the list of LLAGNs with confirmed detection of gamma-ray emission at TeV energies (which currently has only four sources: Cen A, Per A, M87 and IC 310 as we have seen in Chapter 5), will increase substantially, allowing for a more precise evaluation of the contribution of individual sources for the IceCube neutrino flux.

Chapter 7

Conclusions and perspectives

7.1 What we have learned

We have presented in this thesis the results of our investigations on CR acceleration by magnetic reconnection mechanism in the surrounds of the black hole in microquasars and LLAGNs. We have also studied the origin of the non-thermal emission observed in these sources as well as the origin of the detected extragalactic high energy neutrinos by the IceCube.

In the first Chapter, we presented the theoretical and observational motivation for this thesis.

In Chapter two we discussed a magnetic reconnection acceleration model in the nuclear region of black hole (BH) sources. We described the physical conditions necessary to trigger fast magnetic reconnection driven by turbulence and particle acceleration in these sources. We further described how trapped particles between reconnection sheets can be accelerated by a first-order Fermi process and gain energy. Considering the results of the numerical simulations of particle acceleration in magnetic reconnection domains by Kowal et al. (2012), we obtained an expression to calculate the acceleration rate by the magnetic reconnection mechanism for both electrons and protons.

The accelerated particles in the vicinity of the BH sources will lose energy by interactions with the surrounding density, magnetic and radiation fields. All the relevant cooling mechanisms for both leptonic and hadronic processes were described in Chapter 3. Calculating the cooling rates and comparing them with the acceleration rates gives the maximum energy that an accelerated particle in the reconnection zone can retain after radiative cooling in the emission region around the acceleration region. In Chapter 3, we also described the absorption effects for low and high energies, i.e., the optical/IR photon-atom interactions (γN) and the gamma-gamma photon interactions ($\gamma\gamma$), respectively. The way to calculate the flux of the several radiative processes and the absorption mechanisms were also presented in Chapter 3.

In Chapters 4 and 5 we described most of the results of this thesis, namely, the application of the magnetic reconnection acceleration model and the non-thermal radiative cooling processes described in the previous chapters to the core regions of a few microquasars and LLAGNs in order to build their SEDs and compare with the observations. The main motivation for this work was the results found by de Gouveia Dal Pino et al. (2010); Kadowaki et al. (2015); Singh et al. (2015) showing that observed radio core and specially the VHE emission from LLAGNs and microquasars, can be produced by magnetic reconnection in the surrounds of the BHs of these sources.

The results we found in Chapter 4 indicate that protons and electrons in the vicinity of the BH in the sources Cyg X-1 and Cyg X-3, can be accelerated to energies $\sim 10^{16}$eV and $\sim 10^{11}$eV, respectively. We also showed that the observed TeV emission of these sources, can be produced by $p\gamma$ interactions (Khiali et al. 2015a). The results we found in Chapter 5 indicate that in the nuclear region of LLAGNs such as Cen A, Per A, M87 and IC 310, protons and electrons gain energies by magnetic reconnection acceleration to energies $\sim 10^{18}$ eV $\sim 10^{11}$ eV, respectively. In these sources the TeV emission can be generally explained by $p\gamma$ interactions too (Khiali et al. 2015b).

These results together strengthen the earlier results found by Kadowaki et al. (2015);

Singh et al. (2015) who demonstrated that the observed correlation between the (core) radio and gamma-ray luminosities of LLAGNs and microquasars with their BH mass can be explained by the magnetic reconnection power released in the core according to the model described here.

Gamma-ray astronomy is undoubtedly entering in the golden age where space and ground based telescopes cover the sky simultaneously covering over 6 orders of magnitude in energy range (from 100 MeV to a few TeV) with still poor sensitivity and angular resolution, but with perspectives of substantial improving in near future. We are facing a period in the history of high-energy astrophysics where the gamma-ray astronomy is becoming mature enough to make reliable and direct observations of the cosmic accelerators. More than a hundred sources have been detected by the third generation of Atmospheric Cherenkov telescopes such as HESS, MAGIC and VERITAS above 1 TeV. With the coming Cherenkov Telescope Array (CTA) the sensitivity and angular resolutions will increase to factors up to 10 in the highest energies and the energy range will extend to a few 100 TeV. This definitely will open exciting new windows, particularly allowing for the possibility of defining better the location of the gamma-ray emission in the sources investigated here (Actis et al. 2011; Acharya et al. 2013; Sol et al. 2013). Other instruments are coming into play like e.g., the HAWC (Abeysekara et al. 2014) to improve our ”vision” of the gamma-ray sky.

In Chapter 6, it is suggested that the nuclear region of LLAGNs can be the origin of the high energy neutrinos observed by the IceCube. We showed that the accelerated protons by magnetic reconnection in the nuclear region of these sources when interacting with the emitted synchrotron photons can produce charged pions which decay and produce neutrinos. Our calculations have demonstrated that the observed diffuse intensity of high energy neutrinos is fitted well by our model (Khiali & de Gouveia Dal Pino 2015).

Also, the comparison of the results above with alternative models in the literature that point to a jet origin for the VHE emission in these sources (see Chapters 4 5 and 6), have stressed the current uncertainties regarding the region where this emission is produced. This work has tried to shed some light on this debate proposing on a core model, at the jet basis, with a magnetically dominated environment surrounding the BH. But a definite answer to this question will be probably given by much higher resolution and sensitivity observations which may be achieved in near future, e.g., with the forthcoming CTA as remarked above.

7.2 Perspectives and looking forward

The results on particle acceleration around compact sources presented in this thesis have opened the room for new investigation on core processes near the jet launching basis in these sources. Magnetic reconnection arises as a potential alternative and efficient mechanism to accelerate relativistic particles, specially in magnetically dominated regions in these sources and even along their jets (e.g., Giannios 2010; Sironi and Spitkovsky 2014) and also in other classes of sources (e.g., Cerutti et al. 2014).

Another important process not discussed in this thesis is the propagation of these accelerated particles into the ambient medium, once they leave their sources of origin. The propagation of CRs is also a key process in the understanding of the high energy, non-thermal universe. They are produced everywhere in the cosmos: in compact sources, like pulsars, supernova remnants and black hole sources as discussed in this thesis, as well as in more diffuse media, like in shocked regions of the intracluster gas. Understanding how they are produced in these different environments and how they propagate through the intergalactic and intracluster turbulent magnetized medium is still under debate. When CRs propagate through the turbulent magnetic fields in the intergalactic (IGM) and interstellar medium (ISM) they are deflected and their directions are randomized making it hard to tell how they originated. This turbulent transport requires a model to describe the stochastic variations of the particles pitch-angle.

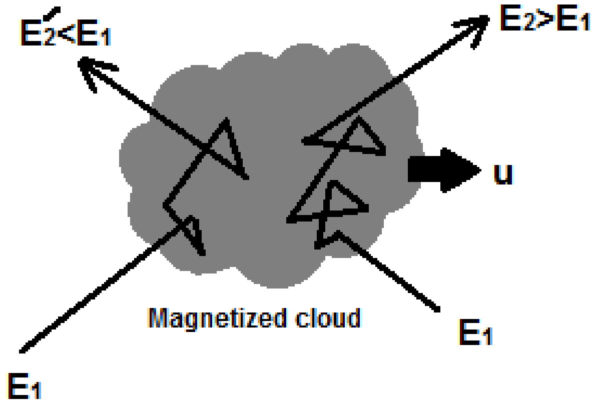

Figure 7.1: CR head-on and head-tail collisions with magnetized cloud moving with the velocity of u.

The presence of turbulent magnetic field leads to scattering of the CRs parallel and perpendicular scattering of the CRs in the background magnetic field. Charged particles experience momentum diffusion or in the other words stochastic acceleration. These scattering effects can be quantified by diffusion coefficients. Finding the diffusion coefficients is important for exploring acceleration of charged particles in diffuse turbulent media, behind shocks, in magnetic reconnection current sheets, as well as in particle transport (e.g., Fletcher1997) and in the lifetime of CRs (e.g., Jokipii and Parke 1969; Ptuskin 2001).

In the finalization of this PhD thesis project, we have started exploring numerically the effects of propagation of accelerated relativistic particles in turbulent environments. In the next sections we will briefly describe the preliminary results of this study and the prospects for forthcoming work.

7.2.1 Stochastic acceleration mechanism in time evolved pure turbulent plasmas

Kowal et al. (2012) besides testing particle acceleration within large scale current sheets that favor a first-order Fermi process, also tested the acceleration of particles in *pure* MHD turbulence, where particles suffer collisions both with approaching and receding magnetic irregularities (Figure 7.1). The acceleration rate in this case is more like a second-order Fermi process. Kowal et al. (2012) neglected in their simulations the time evolution of the MHD environment since this is generally much longer than the particle time scales. In fact, particles are accelerated by magnetic fluctuations in the turbulent field and interact resonantly with larger and larger structures as their energy increases due to the scatterings. In a steady state turbulent environment, as considered in Kowal et al. (2012), particles will see on average the same sort of fluctuation distribution, so that after several Alfvén times, one should expect no significant changes in the particle spectrum, simply because the particles dynamical time is much smaller than the turbulent dynamical time scales. This is certainly valid in first-order Fermi processes. Nonetheless, for second-order Fermi, as the energy gain is less efficient than in a first-order process, it

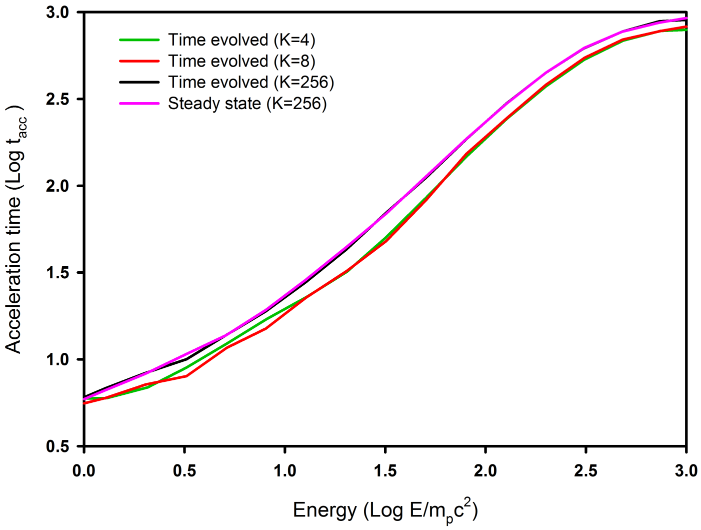

Figure 7.2: Acceleration times for injected test particles in turbulent MHD domain in different length sales (Resolution $N = 512$).

is possible that the $\delta B/\delta t$ term becomes relevant and then, time variations of the MHD turbulence should be considered in the evaluation of the spectrum of the accelerated particles (Kowal et al. 2012). Thus, this evolution may be important when calculating real spectra and loss effects (e.g., Lehe et al. 2009).

We tested numerically the inclusion of the $\delta B/\delta t$ term in the time evolved MHD domain on the particle acceleration (see Eqs. 1 and 2 of Kowal et al. 2012; see also Betatron acceleration process in Cho & Lazarian (2006)) by injecting a large number of test particles. We have found the acceleration time considering different turbulence length scales at injection (i.e., different wavenumbes, $k = 2\pi/l$) and compared the results with the case of steady state MHD turbulent domain. The largest scale of the system is the full box size L and corresponds to the wavenumber $k = 1$, while the smallest scale is given by the Nyquist wavenumber $k_{Nyq} = N/2 = 256$ and $k_{Nyq} = 128$ for linear numerical resolutions $N = 512$ and $N = 256$ grid cells, respectively.

In order to calculate the acceleration time for the injected particles in the turbulent MHD domain, we chose two different snapshots which have their own values for magnetic field and flow velocity. Then by linear interpolation of these values in time, we evaluated the temporal evolution of the mean magnetic field and the flow velocity.

Figure 7.2 shows the acceleration times for relativistic protons in different turbulent length scales considering a resolution $N = 512$. As we see, the acceleration in the case with time evolved plasma in the larger scales is more efficient than the steady state by approximately a factor two, as expected from analytical studies (e.g. Cho and Lazarian 2006). Furthermore, in time evolved environment the acceleration time increases with increasing wavenumber k. This because for large k (small l), l is smaller than the particles *Larmor* radius and therefore, the particles traverse many uncorrelated eddies during one gyro orbit.

7.2.2 CR diffusion in turbulent plasmas

As mentioned earlier, the presence of turbulent magnetic field leads to scattering of the CRs parallel and perpendicular to the background magnetic field. Charged particles experience momentum diffusion or in other words stochastic acceleration. These scattering effects can be quantified by diffusion coefficients and this requires the study of the physics of particles diffusion.

The diffusion coefficient can be defined as (Shalchi 2009):

$$D_{xx} = \lim_{t\to\infty} \frac{\langle(\Delta x)^2\rangle}{2t} \tag{7.1}$$

where $\langle(\Delta x)^2\rangle$ is the mean square displacement of the particles

$$\langle(\Delta x)^2\rangle = \langle(x(t) - x(0))^2\rangle. \tag{7.2}$$

The condition $t \to \infty$ means that $t \gg t_d$, where t_d is a characteristic time scale that is needed for the particles to reach the diffusive regime. A time dependent or *running diffusion coefficient* can be defined as

$$D_{xx}(t) = \frac{\langle(\Delta x)^2\rangle}{2t} \tag{7.3}$$

or, as (Shalchi 2009):

$$d_{xx} = \frac{1}{2}\frac{d}{dt}\langle(\Delta x)^2\rangle \equiv \frac{d}{dt}(tD_{xx}(t)) \tag{7.4}$$

If a charged particle moves through a partially turbulent magnetic system, during the scattering process, its pitch angle changes with time ($\dot{\mu} \neq 0$) where μ is the pitch angle cosine. By tracing the change of the pitch angle cosine ($\mu(t) - \mu(0)$) in a short time interval to keep the deviation of μ small (Beresnyak et al. 2011), we can obtain the pitch angle diffusion coefficient $D_{\mu\mu}$ using:

$$D_{\mu\mu} = \frac{\langle(\mu_t - \mu_0)^2\rangle}{2t} \tag{7.5}$$

These pitch-angle scattering effects cause parallel spatial diffusion. The parallel mean

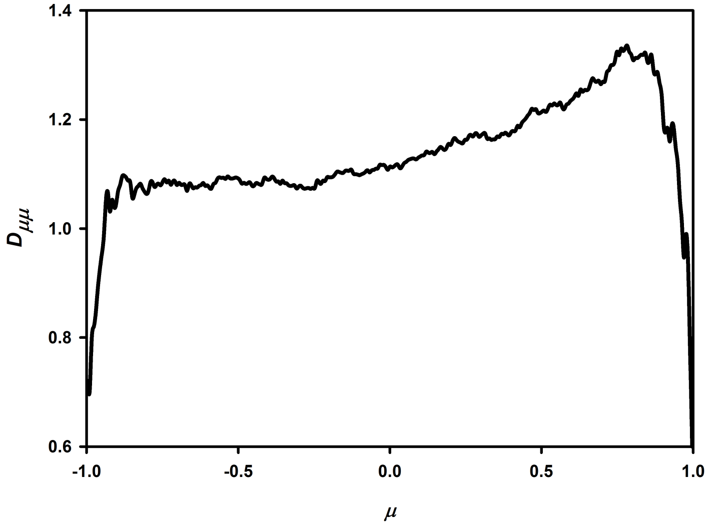

Figure 7.3: Pitch angle diffusion coefficients measured for different initial pitch angles in time-evolved turbulent plasma.

free path $\lambda_{\|}$ of CRs can be determined by pitch angle scattering via:

$$\lambda_{\|} = \frac{3}{4}\int_0^1 d\mu \frac{v(1-\mu^2)^2}{D_{\mu\mu}}, \tag{7.6}$$

where v is the particle velocity.

The main approach to derive $D_{\mu\mu}$ is the application of the perturbation theory or quasilinear theory (QLT, Jokipii 1966) which works well in the case of the parallel transport in turbulence with a Kolmogorov spectrum.

On the other hand, it should be noted that QLT does not provide reasonable results for pitch angle diffusion for $\mu \sim 0$. To solve this problem, non-linear theory has been developed. The other problem of QLT is in the context of the particle perpendicular transport which QLT is not able to describe it. In order to improve the description of perpendicular diffusion several solutions have been proposed such as the non-linear guiding center theory (Matthaeus et al. 2003).

Another way to obtain more understanding in these processes is through numerical

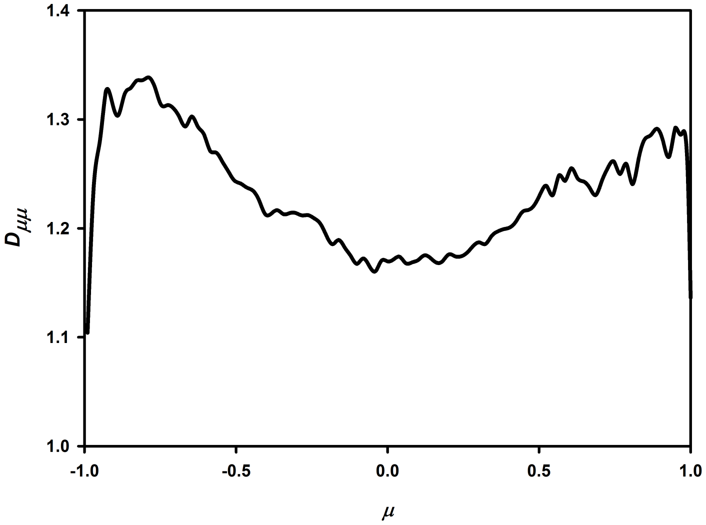

Figure 7.4: The same as Figure 7.3 but in steady-state turbulent plasma.

simulations. As preliminary results on CR diffusion in turbulent plasmas, Figures 7.3 and 7.4 display the measured $D_{\mu\mu}$ for particles with the same energy, Larmor radius $r_g = 0.8$ of the cube size and different μ_0 in time-evolved and steady-state pure turbulent plasmas, respectively, for different initial pitch angles. The calculated diffusion coefficient in the case of time-evolved turbulent is smaller than in the steady-state turbulent plasma. We are going to investigate the effect of this on the efficiency of CR acceleration in forthcoming work.

Finally, calculating the diffusion coefficient in the momentum space (D_p), gives us the possibility of finding the particle acceleration rate via (Dermer et al. 1996):

$$t_{acc}^{-1} = D_p/p^2, \tag{7.7}$$

where the momentum diffusion coefficient is defined as (Michalek & Ostrowski 2009):

$$D_p = \frac{\langle (p_t - p_0)^2 \rangle}{2t}. \tag{7.8}$$

Therefore, tracing the momentum diffusion enables us to find directly the particle acceleration rate and compare it with analytical and more empirical numerical methods as those described in this thesis (see Appendix A) in different astrophysical plasmas with turbulence, like the diffuse ISM or IGM where a second order Fermi process prevails, or behind shocks and magnetic reconnection discontinuities with embedded turbulence where a first-order Fermi process prevails.

In summary, there are several important issues to be explored in the context of the CR acceleration and propagation. These issues include:

- The investigation of the role of the dynamical time evolution of pure turbulent environments on the acceleration rate of test particles. As we have demonstrated above on preliminary basis, the time variations of the magnetic fields in such systems can increment by a factor two the rate of acceleration in a second-order Fermi process (see also Kowal, de Gouveia Dal Pino & Lazarian 2012; de Gouveia Dal Pino and Kowal 2015).

- To probe the different regimes of particle diffusion both in the parallel and perpendicular directions to the local magnetic field, in order to derive numerically the diffusion coefficients and the acceleration rates in pure turbulent MHD systems and also in systems with turbulence embedded in large scale magnetic reconnection discontinuities. This will help to understand the micro-physics of stochastic particle acceleration in diffuse media, as well as behind shocks (e.g., Kirk et al. 2000; Jokipii 1982) and within current sheets (e.g., de Gouveia Dal Pino and Lazarian 2005; Kowal et al. 2011, 2012).

- To compare the parallel and perpendicular diffusion coefficients in different turbulence regimes.

- To apply the turbulent reconnection and stochastic acceleration to different astrophysical sources and environments.

- To study test particle propagation in collisional and collisionless turbulent MHD systems by means of numerical simulations, aiming at establishing fiducial predictions for CR and magnetic field interactions in real systems, like the collisionless IGM (e.g. Santos-Lima et al. 2014) and the collisional ISM (e.g. Kowal et al. 2007).

Bibliography

Aartsen, M. G., Ackermann, M., Adams, J., et al. 2014, Physical Review Letters, 113, 101101

Abdo, A. A., et al. 2009a, ApJ, 699, 31

Abdo, A. A., et al. 2009b, ApJ, 700, 597

Abdo, A. A., et al. 2009c, ApJ, 707, 55

Abdo, A. A., et al. 2010, ApJ, 719, 1433

Abeysekara, A. U., et al. 2014, ApJ, 796, 108

Abraham, J., et al. 2007, Science, 318, 938

Abramowski, A., et al. 2012, ApJ, 746, 151

Acharya, B. S., Actis, M., Aghajani, T., et al. 2013, Astroparticle Physics, 43, 3

Ackermann, M., et al. 2012, ApJS, 203, 4

Actis, M., Agnetta, G., Aharonian, F., et al. 2011, Experimental Astronomy, 32, 193

Ade, P. A. R. et al. 2011, A& A, 536, 7

Aharonian, F. A., & Atoyan, A. M. 2000, A&A, 362, 937

Aharonian, F. A., Akhperjanian, A., Beilicke, M., et al. 2003, A&A, 403, L1

Aharonian, F. A., et al. 2006, Science, 314, 1424

Aharonian, F. A., et al. 2009, ApJL, 695, L40

Ahlers, M., & Murase, K. 2014, Phys. Rev. D, 90, 023010

Ajello, M., et al. 2009, ApJ, 690, 367

Albert, J., Aliu, E., Anderhub, H., et al. 2007, ApJ, 665, L51

Aleksić, J., Antonelli, L. A., Antoranz, P., et al. 2010, ApJ, 721, 843

Aleksić, J., et al. ApJ, 723, L207

Aleksić, J., et al. ApJ, 710, 634

Aleksić, J., et al. A&A, 539, L2

Aleksić, J., et al. A&A, 541, 99

Aleksić, J., Antonelli, L. A., et al. 2014a, A& A, 563, A91

Aleksić, J., Ansoldi, S., Antonelli, L. A., et al. 2014b, A& A, 564, AA5

Aleksić, J., Ansoldi, S., Antonelli, L. A., et al. 2014c, Science, 346, 1080

Amsler, C., Doser, M., Antonelli, M., et al. 2008, Physics Letters B, 667, 1

Asada, K., Kameno, S., Shen, Z. Q. et al. 2006, Publ. Astron. Soc. Japan, 58, 261

Asada K., Kameno S., Shen Z. Q., Shinji H., GabuzdaD. C., Inoue M. 2009, in Hagiwara Y., Fomalont E., Tsuboi M., Murata Y., eds, ASP Conf. Ser. Vol. 402, Approaching Micro-arcsecond Resolution with VSOP-2. Astron. Soc. Pac., San Francisco, p. 91

Atoyan, A. M., & Dermer, C. D. 2001, PRL, 87, 221102

Atoyan, A. M., & Dermer, C. D. 2003, ApJ, 586, 79

Atwood, W. B., Abdo, A. A., Ackermann, M., et al. 2009, ApJ, 697, 1071

Barkov, M. V., Bosch-Ramon, V., & Aharonian, F. A. 2012, ApJ, 755, 170

Becker, R. H., White, R. L., & Edwards, A. L. 1991, APJS, 75, 1

Becker, J. K. 2008, Phys. Rep., 458, 173

Becker Tjus, J., Eichmann, B., Halzen, F., Kheirandish, A., & Saba, S. M. 2014, Phys. Review D. 89, 123005

Bednarek, W. 2010, MNRAS, 406, 689

Begelman, M. C., Rudak, B., & Sikora, M. 1990, ApJ, 362, 38

Bell, A. R. 1978, MNRAS, 182, 147

Bell, A. R. 2013, arXiv:1311.5779

Beresnyak, A., Yan, H., & Lazarian, A. 2011, ApJ, 728, 60

Berezinskii, V. S. 1990, Astrophysics of Cosmic Rays, North-Holland, Amsterdam

Bernardi, M., Alonso, M. V., da Costa, L. N., et al. 2002, AJ, 123, 2990

Bicknell, G. V, Melrose, D. B. 1982, ApJ, 262, 511

Biretta, J. A., Stern, C. P., & Harris, D. E. 1991, AJ, 101, 1632

Biretta, J. A., Sparks, W. B., & Macchetto, F. 1999, ApJ, 520, 621

Biskamp, D., Schwarz, E., & Drake, J. F. 1997, Physics of Plasmas, 4, 1002

Blandford, R. D. 1976, MNRAS, 176, 465

Blandford, R. D., & Payne, D. G. 1982, MNRAS, 199, 883

Blandford, R., & Eichler, D. 1987, Phys. Rev, 154, 1

Blumenthal, G. M., & Gould, R. J. 1970, Rev. Mod. Phys., 42, 237

Bodaghee, A., Tomsick, J. A., Pottschmidt, K., et al. 2013, ApJ, 775, 98

Bosch-Ramon, V., Romero, G. E., & Paredes, J. M. 2005a, A& A, 429, 267

Bosch-Ramon, V., Aharonian, F. A., & Paredes, J. M. 2005b, A& A, 432, 609

Bosch-Ramon V., Khangulyan D., Aharonian F. A. 2008, A&A, 489, L21

Boyd, T. J. M. 2005, The physics of Plasmas, Cambridge

Brown, A. M. & Adams, J. 2011, MNRAS, 413, 2785

Bulgarelli, A., Pittori, C., Lucarelli, F., et al. 2010. Atel, 2512

Buttiglione, S., Capetti, A., Celotti, A., et al. 2010, A&A, 509, A6

Canning, R. E. A., Fabian, A. C., Johnstone, R. M., et al. 2010, MNRAS, 405, 115

Caprioli, D., Spitkovsky, A. 2014, ApJ, 794, 47

Čemeljić, M., Shang, H., & Chiang, T.-Y. 2013, ApJ, 768, 5

Cerutti, B., Dubus, G., Malzac, J., et al. 2011, A&A 529, A120

Cerutti, B., Werner, G. R., Uzdensky, D. A., Begelman, M. C. 2013, ApJ., 770, 147C

Cerutti, B. 2013, PhD thesis.

Cerutti, B., Werner, G. R., Uzdensky, D. A., Begelman, M. C. 2014, ApJ., 782, 104C

Chandran, B. 2003, ApJ, 599, 1426

Cherepashchuk A., Moffat A. 1994, ApJ, 424, 53

Chiaberge, M., Capetti, A., & Celotti, A. 1999, A& A, 349, 77

Cho, J. and Lazarian, A. 2014, ApJ, 780, 30

Cho, J. and Lazarian, A. 2006, ApJ, 638, 811

Condon, J. J., Cotton, W. D., & Broderick, J. J. 2002, AJ, 124, 675

de Gouveia Dal Pino, E. M. 1995, Notes of the course of Plasma Astrophysics

de Gouveia Dal Pino, E. M. & Lazarian, A. 2005, Astronomy and Astrophysics, 441, 845 (GL05)

de Gouveia Dal Pino, E. M., Piovezan, P. P. & Kadowaki, L. H. S. 2010a, Astronomy and Astrophysics, 518, A5

de Gouveia Dal Pino, E. M., Kowal, G., Kadowaki, L. H. S., Piovezan, P. P., & Lazarian, A. 2010b, International Journal of Modern Physics D, 19, 729

de Gouveia Dal Pino, E. M., Kowal, G. 2013, arXiv1302.4374D

de Gouveia Dal Pino, E. M., Kowal, G., Lazarian, A. 2014, 8th International Conference of Numerical Modeling of Space Plasma Flows (ASTRONUM 2013), 488, 8, arXiv1401.4941D

de Gouveia Dal Pino, E. M., & Kowal, G. 2015, in Magnetic Fields in Diffuse Media (eds. A. Lazarian, E. M. de Gouveia Dal Pino, C. Melioli), Astrophysics and Space Science Library, 407, 373

del Valle, M. V., Romero, G. E., Luque-Escamilla, P. L., Martí, J., & Ramón Sánchez-Sutil, J. 2011, ApJ, 738, 115 del Valle, M. V., de Gouveia Dal Pino, E. M, Kowal, G. 2016, Submitted

Deng, X. H. & Matsumoto, H. 2001, Nature 410, 557

Dermer, C. D., Miller, J. A., & Li, H. 1996, ApJ, 456, 106

Dermer, C. D., Murase, K., & Inoue, Y. 2014, Journal of High Energy Astrophysics, 3, 29

Despringre, V., Fraix-Burnet, D., & Davoust, E. 1996, A& A, 309, 375

Dexter, J., McKinney, J. C., Markoff, S., & Tchekhovskoy, A. 2014, MNRAS, 440, 218

Di Mauro, M., Calore, F., Donato, F., Ajello, M., & Latronico, L. 2014, ApJ, 780, 161

Di Salvo T., Done C., Zycki P. T., Burderi L. & Robba N. R. 2001, ApJ, 547, 1024

Douglas, J. N., Bash, F. N., Bozyan, F. A., Torrence, G. W., & Wolfe, C. 1996, AJ, 111, 1945

Drake, J. F., Swisdak, M., Che, H. and Shay, M. A. 2006, Nature, 443, 553D

Drake, J. F., Opher, M., Swisdak, M. and Chamoun, J. N. 2010, ApJ,709, 963D

Drury, L. 2012, MNRAS, 422, 2474D

Dubus, G. 2006, A&A 451,9

Dunn, R. J. H., Allen, S. W., Taylor, G. B., et al. 2010, MNRAS, 404, 180

Dyrda, M., Wierzcholska, A., Hervet, O., et al. 2015, arXiv:1509.06851

Eichler, G. 1979, ApJ, 232, 106

Eyink, G. L., Lazarian, A., & Vishniac, E. T. 2011, ApJ, 743, 51

Falceta-Gonçalves, D., Caproni, A., Abraham, Z., Teixeira, D. M., & de Gouveia Dal Pino, E. M. 2010, ApJL, 713, L74

Falceta-Gonçalves, D., Kowal, G., de Gouveia Dal Pino, E., et al. 2015, Highlights of Astronomy, 16, 406

Fanaroff, B. L., and Riley, J. M. 1974, MNRAS, 167, 31p

Fender, R. P., Pooley, G. G., Durouchoux, P., Tilanus, R. P. J.,& Brocksopp, C. 2000, MNRAS, 312, 853

Fermi, E. 1949, Phys Rev, 75,1169

Fermi, E. 1954, ApJ, 119, 1

Fraija, N. 2014a, MNRAS, 441, 1209

Fraija, N. 2014b, ApJ, 783, 44

Frank, J., King, A., & Raine, D. J. 2002, Accretion Power in Astrophysics, by Juhan Frank and Andrew King and Derek Raine, pp. 398. ISBN 0521620538. Cambridge, UK: Cambridge University Press, February 2002.,

Gaggero, D. 2011, PhD thesis.

Gaisser, T. K. 1990, Cosmic Rays and Particle Physics, Cambridge University Press

Gebhardt, K. & Thomas, J. 2009, ApJ, 700, 1690

Georganopoulos, M., Perlman, E. S., & Kazanas, D., 2005, ApJL, 634, 33

Giacalone, J. 1998, Space Sci. Rev., 83, 351

Giacalone, J., & Jokipii, J. R. 1999, ApJ, 520, 204

Giacalone, J., & Jokipii, J. R. 2006, JPhCS, 47, 160

Giannios, D. 2010, MNRAS, 408, L46

Giannios, D., Uzdensky, D. A. & Begelman, M. C. 2010, MNRAS, 402, 1649

Gies, D. R., & Bolton, C. T. 1986, ApJ, 304, 371

Gies, D. R., et al. 2008, ApJ, 678, 1237

Ginzburg, V. L., & Syrovatskii, S. I. 1995, ARA&A, 3, 297

Gordovskyy, M., Browning, P. K., & Vekstein, G. E. 2010, ApJ, 720, 1603

Gordovskyy, M., & Browning, P. K. 2011, ApJ, 729, 101

Gould R. J., & Schreder G. P. 1967, PhRv, 155, 1404

Graham, J. A. 1978, PASP, 90, 237

Gupta, N. 2008, JCAP, 06, 022

Hardcastle, M. J., Worrall, D. M., Kraft, R. P., Forman, W. R., Jones, C., & Murray, S. S. 2003, ApJ, 593, 169

Hardcastle, M. J., Cheung, C. C., Feain, I. J., & Stawarz, Ł. 2009, MNRAS, 393, 1041

Harmon, B. A., Wilson, C. A., Fishman, G. J., et al. 2004, ApJS, 154, 585

Hartman, R. C., et al. 1999, ApJS, 123, 79

Hawarden, T. G., Sandell, G., Matthews, H., E., et al. 1993, MNRAS, 260, 844

Hazlen, F. & Zas, E. 1997, ApJ, 488, 669

Hazlen, F. 2007, ApS&S, 309, 407

Hjellming R. M., Rupen M. P. 1995, Nature, 375, 464

Ho, L. C., Filippenko, A. V., & Sargent, W. L. W. 1997, ApJS, 112, 315

Ho, L. C. 2008, ARA&A, 46, 475

Ho, L. C., Filippenko, A. V., & Sargent, W. L. W. 1997, ApJS, 112, 315

Huang, C. Y., Wu, Q., & Wang, D. X. 2014, MNRAS, 440, 965

Igumenshchev, I. V. 2009, ApJL, 702, L72

Istomin, Y. N., & Sol, H. 2009, Astrophys. Space Sci., 321, 57

Johnstone, R. M., & Fabian, A. C. 1995, MNRAS, 273, 625

Jokipii, J. R. 1966, ApJ, 146, 480

Jokipii, J. R. 1982, ApJ, 255, 716

Jokipii, J. R. 1987, Apj, 313, 842

Jokipii, J. R., & Giacalone, J. 2007, Apj, 660, 336

Jourdain, E., Roques J. P., Chauvin, M.,& Clark, D. J. 2012, ApJ, 761, 21

Kadler, M., Eisenacher, D., Ros, E., et al. 2012, A& A, 538, L1

Kadowaki, L. H. S., de Gouveia Dal Pino, E. M., & Singh, C. B. 2015, ApJ, 802, 113

Kalashev, O., Semikoz, D. & Tkachev, I. 2014, arXiv:1410.8124

Kalberla, P. M. W., McClure-Griffiths, N. M., Pisano, D. J., et al. 2010, A&A, 521, A17

Kazanas, D., & Ellison, D. C. 1986, ApJ, 304, 178

Katarzynski, K., Sol,H., & Kus, A. 2001, A&A 367, 809

Kachelriess, M., Ostapchenko,S., & Tomas, R. 2009a, New J. Phys. 11, 065017

Kachelriess, M., Ostapchenko,S., & Tomas, R. 2009b, Int. J. Mod. Phys. D 18, 1591

Kachelriess, M., Ostapchenko,S., & Tomas, R. 2010, arXiv: 1002.4874

Kellermann, K. I., Lister, M. L., Homan, D. C., et al. 2004, ApJ, 609, 539

Kelner, S. R., Aharonian, F. A., & Bugayov, V. V. 2006, Phys.Rev. D, 74, 0330108

Kelner, S. R., Aharonian, F. A., & Bugayov, V. V. 2009, Phys.Rev. D, 79, 039901

Khiali, B., de Gouveia Dal Pino, E. M. & del Valle, M. V. 2015a, MNRAS, 449, 34

Khiali, B., de Gouveia Dal Pino, E. M. & Sol, H. 2015b, arXiv:1504.07592

Khiali, B. & de Gouveia Dal Pino, E. M. 2015, arXiv:1506.01063, Accepted for publication in MNRAS.

Kimura, S. S., Murase, K. & Toma, K. 2014, arXiv: 1411.3588

Kinzer, R. L., et al. 1995, ApJ, 449, 105

Kirk, J. G., Guthmann, A. W., Gallant, Y. A., & Achterberg, A. 2000, ApJ, 542, 235

Klamer, I. J., Ekers, R. D., Sadler, E. M., et al. 2005, ApJL, 621, L1

Klein, O., and Nishina, Y., The Oskar Klein Memorial Lectures, Vol. 2, World Scientific Publishing Co. Pte. Ltd., Singapore, 1994, pp. 113â139

Kotera, K., & Olinto, A. V. 2011, ARA&A, 49, 119

Kowal, G., Lazarian, A., Vishniac, E. T., Otmianowska-Mazur, K. 2009, ApJ, 700, 63

Kowal, G., de Gouveia Dal Pino, E. M., Lazarian, A. 2011, The Astrophysical Journal, 735, 102

Kowal, G., de Gouveia Dal Pino, E. M., Lazarian, A. 2012, Physical Review Letters, 108, 241102

Krimsky, G. F. 1977, Sov Phys Doklady 234, 1306

Laurent, P., Rodriguez, J., Wilms, J., Cadolle Bel, M. and Pottschmidt, K.,& Grinberg,V. 2011, Sci, 332, 438

Lazarian, A., & Vishniac, E. T. 1999, The Astrophysical Journal, 517, 700

Lazarian, A., & Opher, M. 2009, ApJ, 703, 8

Lazarian, A., & Desiati, P. 2010, ApJ, 722, 188

Lazarian, A., Vlahos, L., Kowal, G., Yan, H., Beresnyak, A. & de Gouveia Dal Pino, E. M. 2012, Space Science Reviews, 173, 557

Lazarian, A., & Yan, H. 2013, arXiv:1302.3254L

Lazarian, A., & Yan, H. 2014, ApJ, 784, 38

Lazarian, A., Eyink, G., Vishniac, E., & Kowal, G. 2015, Philosophical Transactions of the Royal Society of London Series A, 373, 40144

Lehe, R., Parrish, I. J., & Quataert, E. 2009, Astrophys .J., 707, 404

Lenain, J. P., Boisson, C., Sol, H. & Katarzynski, K. 2008 A&A, 478, 111

Levinson, A., 2000, Phys. Rev. Lett., 85, 912

Lieu, R., Mittaz, J. P. D., Bowyer, S., et al. 1996, ApJ, 458, L5

Lin, R. P., & Hudson, H. S. 1971, SoPh, 17, 412

Ling, Z., Zhang, S. N. & Tang, S. 2009, ApJ, 695, 1111

Lister, M. L., Aller, H. D., Aller, M. F. et al. 2009, AJ, 137, 3718

Liu, F. K. and Chen, X. 2007 ApJ, 671, 1272

Liu, B. F., Mineshige, S., & Shibata, K. 2002, ApJ, 572, 173

Liu, B. F., Mineshige, S., & Ohsuga , K. 2003, ApJ, 587, 571

Lorentz, E. 2004, NewAR, 48, 339

Loureiro, N. F., Schekochihin, A. A., & Cowley, S. C. 2007,Physics of Plasmas, 14, 100703

Macchetto, F., Marconi, A., Axon, D. J., Capetti, A., Sparks, W., Crane, P. 1997, ApJ, 489, 579

Malyshev, D., Zdziarski, A., & Chernyakova, M. 2013, MNRAS, 434, 2380

Malzac, J., Petrucci, P. O., & Jourdain, E. et al. 2006, A&A, 448, 1125

Mannheim, K. 1995, APh, 3, 295

Marconi, A., Pastorini, G., Pacini, F., Axon, D. J., Capetti, A., Macchetto, D., Koekemoer, A. M., & Schreier, E. J. 2006, A&A, 448, 921

Margolis, S. H., Schramm, D. N., & Silberberg, R. 1978, ApJ, 221, 990

Marinelli, A., Fraija, N., & Patricelli, B. 2014a, arXiv:1410.8549

Marinelli, A., & Fraija, N. 2014b, arXiv:1411.2695

Markowitz, A., et al. 2007, ApJ, 665, 209

Mariotti, M. 2010, ATel, 2510

Matthaeus, W. H., Qin, G., Bieber, J. W., & Zank, G. P. 2003, ApJ, 590, L53

McConnell M. L. et al. 2000, ApJ, 543, 928

McConnell M. L. et al. 2002, ApJ, 572, 984

McKinney, J. C., Tchekhovskoy, A., & Blandford, R. D. 2012, MNRAS, 423, 3083

Meier, D. L., 2012, Black Hole Astrophysics: The Engine Paradigm, Springer Verlag, Berlin Heidelberg

Melrose, D. B., 2009, arXiv:0902.1803

Merloni, A., Heinz, S., & di Matteo, T. 2003, MNRAS, 345, 1057

Meszaros, P., & Rees, M. J. 1992, MNRAS, 257, 29P

Michalak, W., Wdowczyk, J., & Wolfendale, A. W. 1990, Journal of Physics G Nuclear Physics, 16, 1917

Mirabel, I. F., & Rodriquez, L. F. 1994, Nature, 371, 46

Mirabel, I. F., Claret, A., Cesarsky, C. J., Boulade, O.,& Cesarsky, D. A. 1996, A&A, 315, L113

Mirabel, I. F., Laurent, O., Sanders, D. B., et al. 1999, A& A, 341, 667

Morganti, R., Oosterloo, T., Struve, C., & Saripalli, L. 2008, A&A, 485, L5

Mucke, A., & Protheroe, J. P. 2001, Astrop. Phys., 15, 121

Murase, K. 2007, Phys. Rev. D 76, 123001

Murase, K., Inoue, Y., & Dermer, C. D. 2014, PhRvD, 90, 023007

Nagar, N. M., Falcke, H., & Wilson, A. S. 2005, A&A, 435, 521

Neronov, A., & Semikoz, D. V. 2002, Phys. Rev. D 66,123003

Neronov, A., & Aharonian, F. A. 2007, ApJ, 671, 85

Neronov, A., Demikoz, D., & Vovk, Ie. 2010, A& A, 519, L6

Neumayer, N., Cappellari, M., Reunanen, J., Rix, H. W., van der Werf, P. P., de Zeeuw, P. T., & Davies, R. I. 2007, ApJ, 671, 1329

Orosz, A. 2011, ApJ, 742, 84

Michalek, G. & ostrowski, M. 1996, Nonlinear processes in geophysics, 3, 66

Paredes, J. M., Bosch-Ramon, V. and Romero, G. E. 2006, A& A 451, 259

Parker, E. N. 1957, Journal of Geophysical Research, 62, 509

Parker, E. N. 1979, Oxford, Clarendon Press; New York, Oxford University Press, 1979, 858 p.,

Pedlar, A., Ghataure, H. S. et al. 1990, MNRAS, 246, 477

Perlman, E. S., Sparks, W. B., Radomski, J., et al. 2001, ApJ, 561, L51

Persi, P., Ferrari-Toniolo, M., Grasdalen, G. L.,& Spada, G. 1980, A&A, 92, 238

Petschek, H. E. 1964, Magnetic Field Annihilation, in The Physics of Solar Flares, ed. by W. N. Hess, p. 425

Piano, G., et al. 2012, A & A 545, A110

Poutanen, J. & Fabian, A. C. 1999, MNRAS 306, L31

Priest, E. R. 2001, Earth Planets Space, 53, 483

Protheroe, R. J. & Kasanas, D. 1983, ApJ, 265, 620

Qin, G. & Shalchi, A. 2009, ApJ, 707, 61

Reid, M. J., McClintock, J. E., Narayan, R., Gou, L., Remillard, R. A., & Orosz, J. A. 2011, ApJ, 742, 83

Reimer, A., Protheroe, R. J. & Donea, A. C. 2004, A&A, 419, 89

Rejkuba, M. 2004, A&A, 413, 903

Remillard, R. A., McClintock, J. E. 2006, ARA&A, 44, 49R

Retinò, A., Sundkvist, D., Vaivads, A., et al. 2007, Nature Physics, 3, 236

Reynoso, M. M., Medina, M. C. and Romero, G. E. 2011, A&A 531, A30, 201

Rieger, F. M., & Aharonian, F. A. 2008b, A&A, 479, L5

Romanova, M. M., Ustyugova, G. V., Koldoba, A. V., & Lovelace, R. V. E. 2002 ApJ, 578, 420

Romanova, M. M., Ustyugova, G. V., Koldoba, A. V., & Lovelace, R. V. E. 2011, MNRAS, 416, 416

Romero, G. E., Torres, D. F., Kaufman Bernardo, M. M., & Mirable, I. F. 2003, A&A, 410,L1

Romero, G. E., Christiansen, H. R., Orellana, M. 2005, apj 632,1093, 2005

Romero, G., E., del Valle, M., V., & Orellana, M. 2010a, A&A 518, A12

Romero, G. E., Vieyro, F. L. and Villa, G. S. 2010b, A&A 519, A109

Romero, G. E., Vieyro, F. L.,& Chaty, S. 2014, A&A 562, 7

Rybicki, G. B., & Lightman, A. P. 1986, Radiative Processes in Astrophysics, by George B. Rybicki, Alan P. Lightman, pp. 400. ISBN 0-471-82759-2. Wiley-VCH , June 1986., Ryter, C. E. 1996, Ap& SS, 236, 285

Sabatini, S., Striani, E., Verrecchia, F., et al. 2010a, ATEL, 2715

Sabatini, S., Tavani, M., Striani, E., et al. 2010b, ApJL, 712, L10

Sabatini, S., Tavani, M., Coppi, P., et al. 2013, ApJ, 766, 83

Sahakyan, N., Piano, G., Tavani, M. 2013, arXiv:1310.7805

Sahu, S., Zhang, B., & Fraija, N. 2012, Physical Review Letters, 85, 043012

Sato, K., Furusho, T., Yamasaki, N. Y., et al. 2005, PASJ, 57, 743

Schlickeiser, R., & Miller, J. 1998, ApJ, 492, 352

Schmutz, W., Geballe, T. R., & Schild, H. 1996, A&A, 311, L25

Shakura, N. I., & Sunyaev, R. A. 1973, A&A, 24, 337

Shalchi, A. 2009, Astrophysics and Space Science Library, 362,

Shay, M. A., Drake, J. F., Denton, R. E., & Biskamp, D. 1998, JGR, 103, 9165

Shay, M. A., Drake, J. F., Swisdak, M., & Rogers, B. N. 2004, Physics of Plasmas, 11, 2199

Shi, Y., Rieke, G. H., Hines, D. C., Gordon, K. D., & Egami, E. 2007, ApJ, 655, 781

Shibata, K., & Tanuma, S. 2001, Earth, Planets, and Space, 53, 473

Sierpowska-Bartosik A. & Torres D. F. 2008, APh, 30, 239

Singh, C. B., de Gouveia Dal Pino, E. M., & Kadowaki, L. H. S. 2015, ApJL, 799, L20 (SGK15)

Sironi, L., & Spitkovsky, A. 2011, ApJ, 726, 75

Sironi, L., Spitkovsky, A., & Arons, J. 2013, ApJ, 771, 54

Sironi, L., & Spitkovsky, A. 2014, ApJ, 783, 21

Soker, N. 2010, ApJL, 721, L189

Sol, H., Zech, A., Boisson, C., et al. 2013, Astroparticle Physics, 43, 215

Soldi, S., Beckmann, V., Baumgartner, W. H., et al. 2014, A&A, 563, A57

Somov, B. V. 2012,*Plasma Astrophysics, Part I: Fundamentals and Practice*, Astrophysics and Space Science Library, 391

Sparks, W. B., Biretta, J. A., & Macchetto, F. 1996, ApJ, 473, 254

Spitzer, L. 1962, Physics of Fully Ionized Gases, New York: Interscience (2nd edition), 1962

Spruit, H. C. 1988, A&A, 194, 319

Spurio, M. 2015, Publications of the American Astronomical Society, page 322

Sreekumar, P., Bertsch, D. L., Hartman, R. C., Nolan, P. L., & Thompson, D. J. 1999, Astropart. Phys., 11, 221

Stawarz, Ł., Siemiginowska, A., Ostrowski, M., & Sikora, M. 2005, ApJ, 626, 120

Stawarz, Ł., Kneiske, T. M., & Kataoka, J. 2006, ApJ, 637, 693

Stecker, F. W. 1968, Phys. Rev. Lett., 21, 1016

Stecker, F. W. 1970, Ap&SS, 6, 377

Stecker, F. W. 1971, NASA Special Publication, 249, 499

Stecker, F. W. 1979, ApJ, 228, 919

Stecker, F. W., Done, C., Salamon, M. H., & Sommers, P. 1991, PhRvL, 66, 2697

Steinle, H., et al. 1998, A&A, 330, 97

Su, Y., Veronig, A. M., Holman, G. D., Dennis, B. R., Wang, T., Temmer, M., & Gan, W. 2013, NatPh, 9, 489

Sweet, P. A. 1958, Electromagnetic Phenomena in Cosmical Physics, 6, 123

Tan, J. C., Beuther, H., Walter, F., & Blackman, E. G. 2008, ApJ, 689, 775

Tautz, R. C., & Shalchi, A. 2011, ApJ, 735, 92

Tavani, M., et al. 2009, A& A, 502, 99

Tavecchio F., Ghisellini G., 2008, MNRAS, 385, L98

Tavecchio F., Ghisellini G. & Guetta D., 2014, ApJ, LL18

Tavecchio, F., & Ghisellini, G. 2014, arXiv:1411.2783

Tchekhovskoy, A., Narayan, R., & McKinney, J. C. 2011, MNRAS, 418, L79

Tingay S. J., et al. 1995, Nature, 374, 141

Tingay S. J., et al. 1998, AJ, 115, 960

Torresi, E. 2012, arXiv:1205.1691

Uzdensky, D. A. 2011, Space Science Reviews, 160, 45

Uzdensky, D. A., & Spitkovsky, A. 2014, ApJ, 780, 3

Uzdensky, D. A. 2015, arXiv:1510.05397

van Kerkwijk, M. H., et al. 1992, Nature, 355, 703

Vermeulen, R. C., Readhead, A. C. S., Backer, D. C. 1994, ApJ, 430, L41

Vila G. S. and Aharonian F. 2009, Asociaon Argentina de Astronomia- Book Series, AAABS, Vol. 1, 2009

Vila G. S. 2012, arXiv:1212.4196

Vincent, S., 2014, arXiv:1411.1957

Walker R. C., Romney J. D., Benson J. M. 1994, ApJ, 430, L45

Waxman, E. & Bahcall, J. N. 1997, Physical Review Letters, 78, 2292

White, R. L., & Becker, R. H. 1992, APJS, 79, 331

Wild, J. P., Smerd, S. F., Weiss, A. A. 1963, Solar bursts. Ann Rev Astron Astrophys 1, 291

Wilman R. J., Edge A. C., Johnstone R. M. 2005, MNRAS, 359, 755

Wilson-Hodge, C. A., Case, G. L., Cherry, M. L., et al. 2012, ApJS, 201, 33

Xu, S., & Yan, H. 2013, ApJ, 779, 140

Yamada, M., Kulsrud, R., & Ji, H. 2010, Reviews of Modern Physics, 82, 603

Yamada, M., Jongsoo, Y., Jonathan J. A., Hantao, J., Russell M. K.& Clayton E. M. 2014, Nature Communications 5, 4774

Yan, H., & Lazarian, A. 2008, ApJ, 673, 942

Yuan, Z., & Wang, J. 2012, ApJ, 744, 84

Zanni, C., & Ferreira, J. 2009, AAP, 508, 1117

Zanni, C., & Ferreira, J. 2013, AAP, 550, A99

Zdziarski, A. A. 2000, IAUS, 195, 153Z

Zdziarski, A. A., Lubinski, P.,& Sikora, M. 2012, MNRAS, 423, 663

Zdziarski, A. A., Mikolajewska, J., & Belczynski, K. 2013, MNRAS, 429, L104

Zdziarski, A. A., Stawarz, L., Pjanka, H. C., Bhatt, P.& Sikora, M. 2014, MNRAS, 440, 2238Z

Zenitani, S. and Hoshino, M. 2001, ApJ, 562L, 63Z

Zenitani, S., Hesse, M. & Klimas, A. 2009, ApJ, 696, 1385Z

Zhang L., Chen S. B. & Fang J. 2008, The astrophysical Journal, 676:1210-1217, 2008

Zharkova, V. V., Arzner, K., Benz, A. O., et al. 2011, SSR, 159, 357

Zhang, B., & Yan, H. 2011, ApJ, 726, 90

Zhang, S. 2013, Fron. Phys., 8(6), 630

Zhang, J., Xu, B. & Lu, J. 2014, ApJ, 788, 143

Ziolkowski, J. 2005, MNRAS, 358, 851

Appendix A

How to find the magnetic reconnection acceleration rate from the numerical simulations?

Here we are going to describe how we have obtained the expressions for the acceleration rate by magnetic reconnection directly from numerical simulations involving test particles.

As discussed in Chapter 2, Kowal et al. (2012) studied the first-order Fermi particle acceleration by magnetic reconnection numerically and demonstrated that in the presence of turbulence within the current sheet to make reconnection fast, the particles suffer an exponential increase in their energy with time, characteristic of the first-order Fermi process, as predicted by de Gouveia Dal Pino and Lazarian (2005) and later in several other studies of particle acceleration in magnetic reconnection domains (e.g., Drake et al. 2006, 2010; Zenitani et al. 2009; Sironi & Spitkovsky 2014).

Figure A.1 (see also Figure 2.5), shows the kinetic energy evolution of 10,000 test particles in a current sheet with embedded turbulence. In this figure colors indicate which velocity component is accelerated. Red corresponds to the parallel component to the local magnetic field, and blue to the perpendicular component. The energy is normalized by m_pc^2, while the time is expressed in units of the Alfvén time (given by the ratio between the characteristic length scale and the Alfvén speed related to the large scale mean magnetic field, $t_A = l_{acc}/v_A$, see Chapter 2). Since the proton kinetic energy is defined as $(\gamma - 1)m_pc^2$, the vertical axis in this figure is showing the values of $\gamma - 1$ where γ is the Lorentz factor. Both vertical and horizontal axes in this figure are scaled logarithmically and show the $Log(\gamma - 1)$ and $Log(t_A)$, respectively.

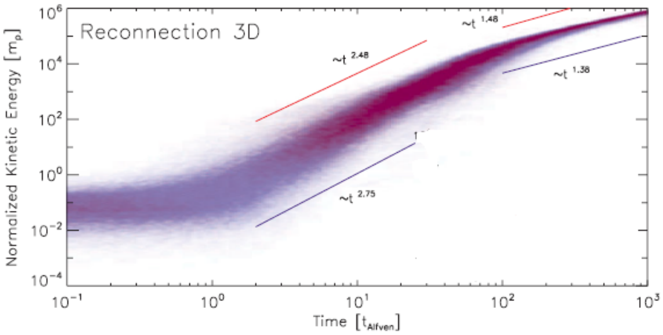

Figure A.1: Particle kinetic energy evolution for 10,000 test particles injected in a current sheet with turbulence embedded in a large scale current sheet in order to make magnetic reconnection fast (Kowal et al. 2012).

The acceleration rate is defined as:

$$t_{acc}^{-1} = \frac{dE/dt}{E}. \tag{A.1}$$

where E is the kinetic energy. In order to find t_{acc}^{-1} as a function of the particle energy due to the first-order Fermi process in the reconnection region, we consider only the region of exponential growth of the particles energy, i.e., the region between points A and B in Figure A.2, or between $t = 10^0 - 10^2 t_A$. Beyond this time interval, the accelerated particles have reached a Larmor radius that is larger than the size of the reconnection zone and then stop being accelerated by the Fermi process. From this time on, their energy continues to increase more slowly due to drift acceleration (Kowal et al. 2012).

Line **AB**, therefore, represents the particle energy growth by the magnetic reconnection acceleration mechanism with a slope ~ 2.5, so we have (see also del Valle et al. 2016):

$$\log{(\gamma - 1)} \simeq 2.5 \log{t_A}, \tag{A.2}$$

and since $E = (\gamma - 1) m_p c^2$, the equation above with time given in seconds reads:

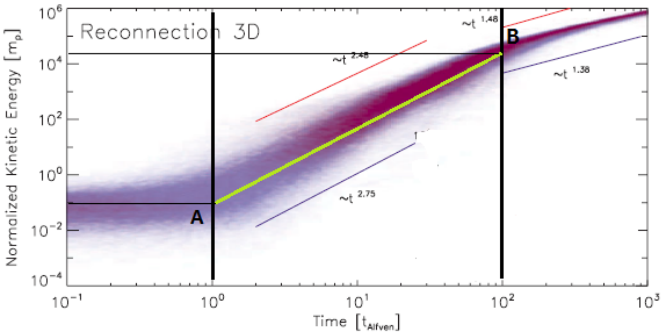

Figure A.2: Same as Fig A.1 but with vertical lines to highlight the region of exponential acceleration rate due to magnetic reconnection.

$$\log(\frac{E}{m_p c^2}) = 2.5 \log(\frac{t}{l_{acc}/v_A}), \tag{A.3}$$

and then

$$\log(E) = 2.5 \log(t) + \log(m_p c^2) - 2.5 \log(l_{acc}/v_A), \tag{A.4}$$

finally we have:

$$E = t^{2.5} m_p c^2 (l_{acc}/v_A)^{-2.5}. \tag{A.5}$$

If the quantities on the RHS of eq. A.5 are given in cgs units, obviously the energy on the LHS will be given in ergs. Nevertheless, usually the acceleration rate as function of the energy is given with the later in units of eV and the time given in seconds (see e.g., Figures 4.5 and 5.9). Thus,

$$E(eV) = t^{2.5} m_p c^2 (l_{acc}/v_A)^{-2.5} \times 6.25 \times 10^{11}, \tag{A.6}$$

then

$$dE(eV)/dt = 2.5\chi t^{1.5}, \tag{A.7}$$

where

$$\chi = m_p c^2 (l_{acc}/v_A)^{-2.5} \times 6.25 \times 10^{11}. \tag{A.8}$$

Finally, substituting Eqs. A.6-A.8 into A.1 we will have:

$$t_{acc}^{-1} = 2.5 \times E(eV)^{-0.4} \times m_p c^2 \times (\frac{l_{acc}}{v_A})^{-2.5} \times 6.25 \times 10^{11}, \tag{A.9}$$

Or substituting the constants on the RHS by their values in cgs units, we obtain:

$$t_{acc}^{-1} = 1.3 \times 10^5 (\frac{E(eV)}{E_0(eV)})^{-0.4} t_0^{-1} \ s^{-1}, \tag{A.10}$$

where E_0 and t_0 are defined in §.2.2.

This equation gives the acceleration rate by magnetic reconnection for the protons, which were used as test particles in the numerical simulations of Figure A.2 of Kowal et al. (2012). For the determination of the acceleration rate for electrons we can consider the following approach.

The 3D numerical simulations of Kowal et al. (2102) indicate that the particles are accelerated in both directions, i.e., in the parallel and perpendicular directions to the underlying magnetic field, at approximately the same rate (see also del Valle et al. 2016). So, let us take the modulus of the particle equation of motion in the non-relativistic regime $md\vec{v}/dt \simeq q\vec{\epsilon}$, where is the particle velocity and $\vec{\epsilon}$ is the strength of the effective electric field in the magnetic reconnection sheet which is

$$\vec{\epsilon} =\mid (\vec{v} - \vec{u}) \times \vec{B} \mid, \tag{A.11}$$

where $\vec{u}$ is the fluid velocity in the reconnection region and is the same for any particle of velocity $\vec{u}$ (see Kowal et al. 2011; 2012). Then in the non-relativistic regime

$$1/2 \frac{mdv^2}{dt} \simeq q\epsilon v, \tag{A.12}$$

where $v = (\frac{2E}{m})^{1/2}$ and the left hand side is the derivative of the kinetic energy

$$dE/dt \simeq q\epsilon(\frac{2E}{m})^{1/2}, \tag{A.13}$$

using Eq. A.1, the acceleration rate is

$$t_{acc}^{-1} = \frac{dE/dt}{E} \simeq \frac{q\epsilon}{\sqrt{\frac{1}{2}E}}(1/m)^{1/2} \tag{A.14}$$

and the acceleration rate for protons and electrons are

$$t_{acc-p}^{-1} = \frac{dE/dt}{E} \simeq \frac{q\epsilon}{\sqrt{\frac{1}{2}E}}(1/m_p)^{1/2} \tag{A.15}$$

and

$$t_{acc-e}^{-1} = \frac{dE/dt}{E} \simeq \frac{q\epsilon}{\sqrt{\frac{1}{2}E}}(1/m_e)^{1/2}, \tag{A.16}$$

respectively, so that:

$$t_{acc-e}^{-1}{}_{acc-p}^{-1}(m_p/m_e)^{1/2}. \tag{A.17}$$

Therefore, an approximate expression for the acceleration rate for electrons in the non-relativistic regime considering Eqs. A.17 and A.10 is given by:

$$t_{acc-e}^{-1} \simeq 1.3 \times 10^5(\frac{E}{E_0})^{-0.4}t_0^{-1}(m_p/m_e)^{1/2}. \tag{A.18}$$

In the relativistic regime, the particle motion is:

$$\frac{d(\gamma m v)}{dt} = q\epsilon \tag{A.19}$$

where the particle momentum is given by $\gamma m v = \sqrt{(E_t/c)^2 - m^2c^2}$, where $E_t = \gamma mc^2$ is the total energy. Since the kinetic energy is $E = (\gamma - 1)mc^2$, we have that $dE/dt = dE_t/dt$, thus doing a similar derivation as described above, we find the value $\frac{dE}{dt}$ and then using Eq. A.1, we obtain that

$$t_{acc}^{-1} \propto (1/m) \tag{A.20}$$

therefore

$$t_{acc-e}^{-1} \simeq t_{acc-p}^{-1} \frac{m_p}{m_e}. \tag{A.21}$$

Comparing the approximate relations Eqs. A.14 and A.20, we see that the relativistic regime predicts a dependence of the acceleration rate with ($\sim 1/m$, see also Giannios 2010), while in the non-relativistic regime this dependence goes with ($\sim 1/\sqrt{m}$), so that the inferred acceleration rate for the electrons in the non-relativistic regime would be less strong than in the relativistic regime (Eqs.A.17 and A.21).

On the other hand, a much simpler way to estimate the acceleration rate in the magnetic reconnection sheet is by setting the energy of the accelerated particle E equal to $e(V_R/c)Bz$, where V_R is the reconnection velocity (see Chapter 2) and z is the distance travelled by the particle along the current sheet (normal to the magnetic field direction) while being accelerated by the effective electric field $V_R B/c$. The acceleration time is, therefore approximately (see de Gouveia Dal Pino and Kowal 2015, Speiser 1965; Giannios 2010):

$$t_{acc}^{-1} \simeq c/z \simeq eV_R B/E \tag{A.22}$$

Which is independent of the mass of the accelerated particle.

Considering the results above, what approach should we adopt to estimate the electron acceleration rate? Eqs. A.17, A.21 or A.22?. The numerical simulations of test proton acceleration in collisional MHD domains of reconnection by Kowal et al (2012) indicate that the acceleration rate given by Eq. A.22 is achieved only for the largest energies (see also del Valle et al. 2016). This is compatible with the notion that when γ goes to infinite the momentum of the particle becomes independent of its mass. Also, collisionless PIC simulations indicate that as the particles approach the highest energies, the acceleration rate both for protons and electrons becomes essentially the same (Sironi and Spitkovsky 2014). Considering these facts, we have adopted in our calculations the electron acceleration rate with the mild mass dependence given by the non-relativistic approach. We expect that at least initially the particles should follow this trend. The electron acceleration would have nearly the same energy dependence of the proton acceleration rate (extracted from the numerical simulations), but multiplied by a constant factor $(mp/me)^{1/2}$ (Eq. A.17). As the particle is accelerated to higher energies, this dependence with mass could evolve according to Eq. A.21, and at much higher energies, to no dependence with mass. As we do not know exactly where this change in regime occurs we considered only Eq.A.17 to evaluate the rates in Chapters 4 and 5. If we had adopted the same acceleration rate both for electrons and protons (with no mass dependence), then this would imply electron energy thresholds in the acceleration versus energy loss diagrams of Chapters 4 and 5 (see Figures 4.3,4.5,4.7,4.8,5.5,5.3,5.7 and 5.9) smaller by factor of 10. Therefore, these would not affect much the results of the SEDs.

The analytical estimates above highlight the fact that there is not yet a precise determination for the electron acceleration rate (and for particle acceleration rate in general) in magnetic reconnection particle acceleration theory. This is a rather important topic which will be better explored in near future (see Chapter 7).

Appendix B

A magnetic reconnection model for explaining the multiwavelength emission of the microquasars Cyg X-1 and Cyg X-3

Apendix B

Monthly Notices
of the
ROYAL ASTRONOMICAL SOCIETY

MNRAS **449,** 34–48 (2015) doi:10.1093/mnras/stv248

A magnetic reconnection model for explaining the multiwavelength emission of the microquasars Cyg X-1 and Cyg X-3

B. Khiali,[1]★ E. M. de Gouveia Dal Pino[1] and M. V. del Valle[2]

[1] *IAG-Universidade de São Paulo, Rua do Matão 1226, São Paulo, SP, Brazil*
[2] *Instituto Argentino de Radioastronomia (IAR), CCT La Plata, C.C.5, 1894 Villa Elisa, Buenos Aires, Argentina*

Accepted 2015 February 4. Received 2015 February 2; in original form 2014 June 21

ABSTRACT

Recent studies have indicated that cosmic ray acceleration by a first-order Fermi process in magnetic reconnection current sheets can be efficient enough in the surrounds of compact sources. In this work, we discuss this acceleration mechanism operating in the core region of galactic black hole binaries (or microquasars) and show the conditions under which this can be more efficient than shock acceleration. In addition, we compare the corresponding acceleration rate with the relevant radiative loss rates obtaining the possible energy cut-off of the accelerated particles and also compute the expected spectral energy distribution (SED) for two sources of this class, namely Cygnus X-1 and Cygnus X-3, considering both leptonic and hadronic processes. The derived SEDs are comparable to the observed ones in the low- and high-energy ranges. Our results suggest that hadronic non-thermal emission due to photomeson production may produce the very high energy gamma-rays in these microquasars.

Key words: acceleration of particles – magnetic reconnection – MHD – radiation mechanisms: non-thermal.

1 INTRODUCTION

Detected non-thermal radio to gamma-ray emission from Galactic binary systems hosting stellar mass black holes (BHs), also denominated black hole binaries (BHBs), microquasars, or simply μQSOs (Mirabel & Rodriquez 1994; Hjellming & Rupen 1995; Tingay et al. 1995), provide clear evidence of the production of relativistic particles in their jets and probably also in the innermost regions very close to the BH. Currently, more than a dozen μQSOs have been detected in the Galaxy (Zhang 2013).

Generally, these sources are far from being stable and individual systems have often complex emission structure. Nevertheless, all classes of BHBs exhibit common features and show basically two major states when considering their X-ray emission (2–100 keV): a quiescent and an outburst state (e.g. Remillard & McClintock 2006). The former is characterized by low X-ray luminosities and hard non-thermal spectra. Usually, transient BHBs exhibit this state for long periods, which allows one to obtain typical physical parameters of the system. On the other hand, the outburst state corresponds to intense activity and emission, and can be sub-classified in three main active and many intermediary states. According to Remillard & McClintock (2006, see also Zhang 2013), the three main active states are the thermal state (TS), the hard state (HS) and the steep power law state (SPLS). These states are usually explained as changes in the structure of the accretion flow, as remarked before. During the TS, the soft X-ray thermal emission is believed to come from the inner region of the thin accretion disc that extends until the last stable orbits around the BH. On the other hand, during the HS the observed weak thermal component suggests that the disc has been truncated at a few hundreds/thousands gravitational radii. The hard X-ray emission measured during this state is dominated by a power-law (PL) component and is often attributed to inverse Compton (IC) scattering of soft photons from the outer disc by relativistic electrons in the hot inner region of the system (e.g. Malzak et al. 2006; Remillard & McClintock 2006). The SPLS is almost a combination of the above two states, but the PL is steeper.

The observed radio and infrared (IR) emission in μQSOs is normally interpreted as due to synchrotron radiation produced by relativistic particles in the jet outflow.

More recently a few μQSOs have been also detected in the gamma-ray range with *AGILE* (Tavani et al. 2009; Bulgarelli et al. 2010; Sabatini et al. 2010a,b, 2013), *Fermi*-LAT (Atwood et al. 2009; Bodaghee et al. 2013) and MAGIC (Lorentz 2004). For Cygnus X-1 (Cyg X-1), for instance, upper limits with 95 per cent confidence level have been obtained in the range of $\geq$150 GeV (Albert et al. 2007), while in the case of Cygnus X-3 (Cyg X-3), upper limits of integrated gamma-ray flux above 250 GeV have been inferred by Aleksic et al. (2010). Upper limits in the 0.1–10 GeV range have been also suggested for GRS 1915+105 and GX 339-4.

There is no definite mechanism yet to explain the origin of the very high energy (VHE) emission in μQSOs. The main reason for this is that the current sensitivity of the gamma-ray instruments is too poor to establish the location of this emission in the source (e.g. Bodaghee et al. 2013).

★ E-mail: bkhiali@usp.br

© 2015 The Authors
Published by Oxford University Press on behalf of the Royal Astronomical Society

Regardless of the uncertainties, several models have been proposed, especially for Cyg X-1 and Cyg X-3. Romero et al. (2003), for instance, assumed that the gamma-ray emission is produced in a hadronic jet as a result of the decay of neutral pions created in photon–ion collisions. An alternative model developed by Bosch-Ramon, Aharonian & Paredes (2005b) assumed that relativistic protons also produced in the jet may diffuse through the interstellar medium (ISM) and then interact with molecular clouds and produce gamma-rays out of pp interactions via neutral pion decay. Another model has been proposed by Piano et al. (2012) in which both, leptonic (via IC) and hadronic (via neutral pion decay) might account for the observed gamma-ray emission.

All models above postulate that the primary relativistic particles (electrons and protons) are produced behind shocks in the jet outflow.

An alternative mechanism has been explored first in the context of μQSOs (de Gouveia Dal Pino & Lazarian 2005, hereafter GL05) and later extended to the framework of active galactic nuclei (AGNs; de Gouveia Dal Pino, Piovezan & Kadowaki 2010, hereafter GPK10) in which particles are accelerated in the surrounds of the BH of these sources, near the jet basis, by a first-order Fermi process, as proposed in GL05, within magnetic reconnection current sheets produced in *fast* encounters of the field lines arising from the accretion disc and those of the BH magnestosphere.

Fast magnetic reconnection, which occurs when two magnetic fluxes of opposite polarity encounter each other and partially annihilate very efficiently at a speed V_R of the order of the local Alfvén speed (V_A), has been detected in laboratory plasma experiments (e.g. Yamada, Kulsrud & Ji 2010) as well as in space environments, like the earth magnetotail and the solar corona (see e.g. Deng & Matsumoto 2001; Su et al. 2013). Extensive numerical work has been also carried out considering collisionless (e.g. Zenitani & Hoshino 2001; Drake et al. 2006, 2010; Zenitani, Hesse & Klimas 2009; Cerutti et al. 2013, 2014; Sironi & Spitkovsky 2014) and collisional flows (e.g. Shibata & Tanuma 2001; Loureiro, Schekochihin & Cowley 2007; Kowal et al. 2009; Kowal, de Gouveia Dal Pino & Lazarian 2012). Different processes such as kinetic plasma instabilities (Shay et al. 1998, 2004; Yamada et al. 2010), anomalous resistivity (AR; e.g. Parker 1979; Biskamp, Schwarz & Drake 1997; Shay et al. 2004), or turbulence (Lazarian & Vishniac 1999, hereafter LV99; Kowal et al. 2009; Eyink, Lazarian & Vishniac 2011), can lead to fast reconnection. The latter process in particular, has been found to be very efficient because it provokes the wandering of the magnetic field lines allowing for several simultaneous events of reconnection within the current sheet (see Section 2.2).

Fast reconnection has recently gained increasing interest also in other astrophysical contexts beyond the Solar system because of its potential efficiency to explain magnetic field diffusion, dynamo process, and particle acceleration in different classes of sources and environments – from compact objects, like BHs (e.g. GL05; GPK10; Giannios 2010), pulsars (e.g. Cerutti et al. 2013, 2014; Sironi & Spitkovsky 2014), and gamma-ray bursts (e.g. Zhang & Yan 2011), to more diffuse regions like the ISM), intergalactic medium, and star-forming regions (e.g. Santos-Lima et al. 2010; Santos-Lima, de Gouveia Dal Pino & Lazarian 2012, 2013; Leão et al. 2013, see also Uzdensky 2011; de Gouveia Dal Pino, Kowal & Lazarian 2014; de Gouveia Dal Pino & Kowal 2015 and references therein for reviews).

In the mechanism proposed by GL05, particles are accelerated to relativistic velocities within the fast magnetic reconnection sheet in a similar way to the first-order Fermi process that occurs in shocks, i.e. trapped charged particles may bounce back and forth several times and gain energy due to head-on collisions with the two converging magnetic fluxes of opposite polarity (see Section 2.3). This acceleration mechanism has been also successfully tested numerically both in collisionless by means of two-dimensional (2D) PIC simulations (e.g. Zenitani & Hoshino 2001; Drake et al. 2006, 2010; Zenitani et al. 2009; Cerutti et al. 2013, 2014; Sironi & Spitkovsky 2014) and collisional magnetic reconnection sheets by means of 2D and 3D magnetohydrodynamic (MHD) simulations with test particles (Kowal, de Gouveia Dal Pino & Lazarian 2011; Kowal et al. 2012). Furthermore, this process has been explored in depth in the natural laboratories of fast reconnection provided by solar flares (e.g. Drake et al. 2006, 2010; Lazarian & Opher 2009; Gordovskyy, Browning & Vekstein 2010; Gordovskyy & Browning 2011; Zharkova et al. 2011) and the earth magnetotail. For instance, Lazarian & Opher (2009) verified that the anomalous cosmic rays (CRs) measured by Voyager seem to be indeed accelerated in the reconnection regions of the magnetopause (see also Drake et al. 2010). In another study, Lazarian & Desiati (2010) invoked the same mechanism to explain the excess of CRs in the sub-TeV and multi-TeV ranges in the wake produced as the Solar system moves through interstellar gas. Magnetic reconnection has been also invoked in the production of ultrahigh energy CRs (e.g. Kotera & Olinto 2011) and in particle acceleration in astrophysical jets and gamma-ray bursts (Giannios 2010; del Valle et al. 2011; Zhang & Yan 2011).

In the context of BHs, GPK10 found that the energy power extracted from events of fast magnetic reconnection between the magnetosphere of the BH and the lines rising from the inner accretion disc can be more than sufficient to accelerate primary particles and produce the observed core radio synchrotron radiation from μQSOs and low-luminosity AGNs (LLAGNs). Moreover, they proposed that the observed correlation between the radio emission and the BH mass of these sources, spanning 10^{10} orders of magnitude in mass (in the so called Fundamental Plane of BHs, Merloni, Heinz & di Matteo 2003), might be related to this process. More recently, Kadowaki, de Gouveia Dal Pino & Singh 2014 (Kadowaki, de Gouveia Dal Pino & Singh 2015, henceforth KGS15) revisited this model exploring different mechanisms of fast magnetic reconnection and extended the study to include also the gamma-ray emission of a much larger sample containing over two hundred sources. They found that both LLAGNs and μQSOs confirm the earlier trend found by GL05 and GPK10. Furthermore, when driven by turbulence, not only the radio but also the gamma-ray emission of these sources can be due to the magnetic power released by fast reconnection allowing for particle acceleration to relativistic velocities in the core region of these sources. In another concomitant work, Singh, de Gouveia Dal Pino & Kadowaki (2015, hereafter SGK15) have repeated the analysis above of KGS15, but instead of employing the standard accretion disc/coronal model to describe the BH surrounds, they adopted an MADAF (magnetically advected accretion flow) and obtained very similar results to those of KGS15, for the same large sample of LLAGNs and μQSOs.

In addition, it has been argued in these studies that the fast magnetic reconnection events could be directly related to the transition between the hard and the soft steep-power-law (SPLS) X-ray states seen in μQSOs, as described above.

Lately, similar mechanisms involving magnetic activity, reconnection and acceleration in the core regions of compact sources to explain their emission spectra have been also invoked by other works (e.g. Lyubarsky & Liverts 2008; Igumenshchev 2009; Soker 2010; Huang, Wu & Wang 2014; Uzdensky & Spitkovsky 2014). In particular, magnetic reconnection between the magnetospheric lines of the central source and those anchored into the accretion disc resulting in the ejection of plasmons has been detected in numerical MHD studies by (see e.g. Romanova et al. 2002, 2011; Zanni & Ferreira 2009, 2013; Čemeljić, Shang & Chiang 2013). The recent numerical relativistic MHD simulations of magnetically arrested accretion discs by (Tchekhovskoy, Narayan & McKinney 2011, McKinney, Tchekhovskoy & Blandford 2012 and Dexter et al. 2014) also evidence the development of magnetic reconnection in the magnetosphere of the BH and are consistent with our scenario above.

The results above, and especially the correlations found in the works of KGS15 and SGK15 between the magnetic reconnection power released by turbulent driven fast reconnection in the surrounds of BHs and the observed core radio and gamma-ray emission of a sample containing more than 200 sources of μQSOs and LLAGNS (see figs 7 in KGS15 and 3 in SGK15), have motivated us to perform this study, undertaking a detailed multifrequency analysis of the non-thermal emission of two well-investigated observationally μQSOs, namely Cyg X-1 and Cyg X-3 (which are also in the KGS15 and SGK15 samples), aiming at reproducing their observed spectral energy distribution (SED) from radio to gamma-rays during outburst states. As in GL05, GPK10, KGS15 and SGK15, we explore the potential effects of the interactions between the magnetosphere of the BH and the magnetic field lines that rise from the accretion disc. These magnetic fields are considered essential ingredients in most accretion disc/BH models to help to explain the variety and complexity of observed data (e.g. Neronov & Aharonian 2007; Zhang 2013), but are, in general, paradoxically neglected or avoided in the discussion of the acceleration and emission mechanisms in the nuclear regions of these compact sources.

We here compute the power released by fast magnetic reconnection between these two magnetic fluxes and then the resulting particle spectrum of accelerated particles in the magnetic reconnection site. In particular, we explore the first-order Fermi acceleration process that may occur within the current sheet as proposed in GL05.

We finally consider the relevant radiative loss mechanisms due to the interactions of the accelerated particles with the ambient matter, magnetic and radiation fields, and also assess the importance of the acceleration by magnetic reconnection in comparison to shock acceleration.

The outline of the paper is as follows. In Section 2, we describe in detail our acceleration model, while the equations employed to calculate the emission processes from radio to gamma-ray energies are presented in Section 3. In Sections 4 and 5, we show the results of the application of the acceleration and emission model to Cyg X-1 and Cyg X-3, respectively. Finally in Section 6, we summarize our results and draw our conclusions.

2 OUR PARTICLE ACCELERATION SCENARIO

We assume here that relativistic particles may be accelerated in the core of the μQSO in the surrounds of the BH, near the basis of the jet launching region, as a result of events of fast magnetic reconnection. As stressed, this acceleration model has been described in detail in GL05 and GPK10 and recently revisited in KGS15. We summarize here its main assumptions. As in these former studies, we assume that the inner region of the accretion disc/corona system alternates between two states which are controlled by changes in the global magnetic field. Right before a fast magnetic reconnection event, we assume that the system is in a state that possibly characterizes the transition from the hard to the soft state as described in the previous section, and adopt a magnetized accretion disc with a corona around the BH.

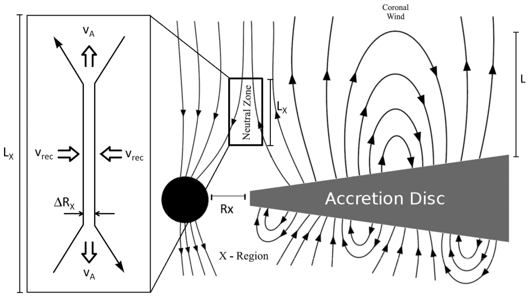

Figure 1. Scheme of magnetic reconnection between the lines rising from the accretion disc and the lines anchored into the BH horizon. Particle acceleration may occur in the magnetic reconnection site (neutral zone) by a first-order Fermi process (adapted from GL05).

2.1 The accretion disc/coronal fluid around the BH

Although there is still much speculation on what should be the strength and geometry of the magnetic fields in the surrounds of BHs, these are necessary ingredients in order to explain, e.g. the formation of narrow relativistic jets. We consider here a scenario with the simplest possible configuration by considering a magnetized standard (geometrically thin and optically thick) accretion disc around the BH as in the cartoon of Fig. 1.

A magnetosphere around the central BH can be established from the drag of magnetic field lines by the accretion disc. The large-scale poloidal magnetic field in the disc corona can in turn be formed by the action of a turbulent dynamo inside the accretion disc (see GL05, KGL14 and references therein) or dragged from the surroundings. This poloidal magnetic flux under the action of the disc differential rotation gives rise to a wind that partially removes angular momentum from the system and increases the accretion rate. This also increases the ram pressure of the accreting material that will then press the magnetic lines in the inner disc region against the lines anchored into the BH horizon allowing them to reconnect fast (see Fig. 1). Momentum flux conservation between the magnetic pressure of the BH magnetosphere and the accreting flux determines the magnetic field intensity in this inner region.

2.2 Conditions for fast reconnection in the surrounds of the BH

As discussed in Section 1 (see also GL05, GPK10, and KGS15), in the presence of kinetic plasma instabilities (Shay et al. 1998, 2004; Yamada et al. 2010), AR (e.g. Parker 1979; Biskamp et al. 1997; Shay et al. 2004), or turbulence (LV99; Kowal et al. 2009, 2012), reconnection may become very efficient and fast.

The strongly magnetized and low dense coronal fluid of the systems we are dealing with in this work satisfies the condition $L > l_{\rm mfp} > r_{\rm l}$ (where L is the typical large-scale dimension of the system, $l_{\rm mfp}$ the ion mean free path and $r_{\rm l}$ the ion Larmor radius). For such flows a weakly collisional or effectively collisional MHD description is more than appropriate (e.g. Liu, Mineshige & Ohsuga

2003) and we will employ this approach here, as in GL05, GPK10, and KGS15.[1]

In these MHD flows, a collisional turbulent fast reconnection approach is expected to be dominant (see KGL14). According to the LV99 model, the presence of even weak turbulence causes the wandering of the magnetic field lines which allows for many independent patches to reconnect simultaneously making the global reconnection rate large, $V_{\rm R} \sim v_{\rm A}(l_{\rm inj}/L)^{1/2}(v_{\rm turb}/v_{\rm A})^2$, where $V_{\rm R}$ is the reconnection speed, and $l_{\rm inj}$ and $v_{\rm turb}$ the injection scale and velocity of the turbulence, respectively. This expression indicates that the reconnection rate can be as large as $\sim V_{\rm A}$, which in the systems here considered may be near the light speed (see also KGL14). This theory has been extensively investigated (e.g. Eyink et al. 2011; Lazarian et al. 2012) and confirmed numerically by means of 3D MHD simulations (Kowal et al. 2009, 2012). In particular, it has been shown (Eyink et al. 2011) that turbulent collisional fast reconnection prevails when the thickness of the current sheet (see equation 4 below) is larger than the ion Larmor radius. As demonstrated in KGS15, for the systems we are studying this condition is naturally satisfied and we will adopt this model to derive the magnetic power released by fast reconnection.[2]

The employment of a fast magnetic reconnection model driven by turbulence as in LV99 requires fiducial sources of turbulence. The fluid in these sources, as most astrophysical fluids, has large Reynolds numbers. In fact, $R_{\rm e} = LV/\nu \sim 10^{20}$ [where V corresponds to a characteristic velocity of the fluid and ν is the kinematic viscosity which for a magnetized fluid is dominated by transverse kinetic motions to the magnetic field and is given by $\nu \sim 1.7 \times 10^{-2} n_{\rm c} \ln\Lambda/(T^{0.5}B^2)$ cm^2 s^1, being $\ln\Lambda \sim 25$ the Coulomb logarithm and $n_{\rm c}$ is the coronal particle number density given by equation 3 below]. Likewise, the magnetic Reynolds number is $R_{\rm em} = LV/\eta \sim 10^{18}$ (where the magnetic diffusion coefficient η in the regime of strong magnetic fields is given by $\eta = 1.3 \times 10^{13}{\rm cm}^2{\rm s}^1 Z \ln\Lambda T^{-3/2}$ Spitzer 1962). As argued in KGL14, such high Reynolds numbers imply that both the fluid and the magnetic field lines can be highly distorted and turbulent if there is turbulence triggering. In other words, any instability as for instance, current driven instabilities, can naturally drive turbulence with characteristic velocities around the particles thermal speed. Also, the occurrence of continuous magnetic reconnection during the building of the corona itself in the surrounds of the BH (Liu et al. 2003) will contribute to the onset of turbulence which will then be further fed by fast reconnection as in LV99 model.

Table 1. Model parameters for Cyg X-1.

B	Magnetic field (G)	2.3×10^7
$n_{\rm c}$	Coronal particle number density (cm^{-3})	4.5×10^{16}
$T_{\rm d}$	Disc temperature (K)	4.4×10^7
W	Reconnection power (erg s^{-1})	3.6×10^{36}
ΔR_X	Width of the current sheet (cm)	1.1×10^7
R_x	Inner radius of disc (cm)	2.6×10^7
L_X	Height of reconnection region (cm)	4.3×10^7
$V_{\rm vol}$	Volume of emission region (cm^3)	3.5×10^{23}
d	Distance (kpc)	2
M	Mass of BH ($M_\odot$)	14.8
p	Particle power index	1.8
$R_\star$	Stellar radius (cm)	1.5×10^{12}
$T_\star$	Stellar temperature (K)	3×10^4
$r_{\rm orb}$	Orbital radius (cm)	3.4×10^{12}
θ	Viewing angle (rad)	$\pi/6$

Numerical simulations of coronal disc accretion also indicate the formation of turbulent flow in the surrounds of the BH that may be triggered by magnetorotational instability (see e.g. Tchekhovskoy et al. 2011; McKinney et al. 2012; Dexter et al. 2014). All these processes may ensure the presence of embedded turbulence in the magnetic discontinuity described in Fig. 1.

We should also note that in the equations below which describe the accreting and coronal flow around the BH, we adopt a nearly non-relativistic approximation. In KGS15, we give quantitative arguments that indicate that this is a reasonable assumption. For instance, the evaluation of the magnetic reconnection power considering a pseudo-Newtonian gravitational potential to reproduce general relativistic effects, gives a value that is similar to the classical case. A kinematic relativistic approach for the accreting and coronal flows is not necessary either since we are dealing with characteristic ion/electron temperatures smaller than or equal $\sim 10^9$K (see KGS15). Nevertheless, with regard to reconnection, the fact that $v_{\rm A}$ may approach the light speed, may imply that relativistic effects can affect the turbulent driven fast reconnection. This question has been addressed in some detail in KGL14 as well, and we refer to this work (and the references therein). The current results indicate that one can treat both cases in a similar way. In particular, a recent study (Cho & Lazarian 2014) has demonstrated that relativistic collisional MHD turbulence behaves as in the non-relativistic case which indicates that LV99 theory can be also applicable in the nearly relativistic regime.

Considering the assumptions above, KGS15 have demonstrated that the magnetic power released by a fast magnetic reconnection event driven by turbulence in the corona around the BH, is given by

$$W \simeq 1.66 \times 10^{35} \Gamma^{-0.5} r_X^{-0.62} l^{-0.25} l_X q^{-2} \xi^{0.75} m \ {\rm erg\ s^{-1}}, \tag{1}$$

where $r_X = R_X/R_{\rm S}$ is the inner radius of the accretion disc in units of the BH Schwartzchild radius ($R_{\rm S}$) (as in KGS15, in our calculations we assume $r_X = 6$); $l = L/R_{\rm S}$ is the height of the corona in units of $R_{\rm S}$; $l_X = L_X/R_{\rm S}$ where L_X is the extension of the magnetic reconnection zone (as shown in Fig. 1; see also Tables 1 and 2); $q = [1 - (3/r_X)^{0.5}]^{0.25}$; ξ is the mass accretion disc rate in units of the Eddington rate ($\xi = \dot{M}/\dot{M}_{\rm Edd}$) which we assume to be $\xi \simeq 0.7$;[3] m is

---

[1] We should further notice that the BH of these systems is surrounded by accreting flow from the stellar companion which also favours a nearly collisional MHD approach.

[2] It should be noticed that GL05, GPK10 and KGS15 have also investigated another mechanism to induce fast magnetic reconnection based on AR. This occurs in the presence of current driven instabilities that can enhance the microscopic Ohmic resistivity and speed up reconnection to rates much larger than that probed by the latter. On the other hand, AR results rates which are much smaller than reconnection driven by turbulence as it prevails only at very small scales of the fluid. In fact, as shown in KGL14, AR predicts a much thinner reconnection region and is unable to reproduce the observed emission for most of the sources investigated. In particular, in the case of Cyg X-1 and Cyg X-3, the magnetic power released by fast reconnection driven by AR cannot accelerate particles to energies larger than 10^{12} eV (see more details in KGS15). Other instabilities, like e.g. tearing mode or Hall effect are also relevant to drive fast reconnection but only at very small scales as well, and are thus more appropriate for collisionless fluids (see Eyink et al. 2011).

[3] We note that according to the results of KGS15 (see their fig. 5), accretion rates ξ between $0.05 < \xi \leq 1$ are able to produce magnetic reconnection power values which are large enough to probe the observed luminosities from μQSOs. We here adopted $\xi \simeq 0.7$ as a fiducial value.

Table 2. Model parameters for Cyg X-3.

B	Magnetic field (G)	2.1×10^7
n_c	Coronal particle number density (cm^{-3})	3.9×10^{16}
T_d	Disc temperature (K)	4.5×10^7
W	Reconnection power (erg s^{-1})	4.5×10^{36}
ΔR_X	Width of the current sheet (cm)	1.3×10^7
R_x	Inner radius of disc (cm)	3×10^7
L_X	Height of reconnection region (cm)	5×10^7
V_vol	Volume of emission region (cm^3)	5.3×10^{23}
d	Distance (kpc)	8
M	Mass of BH ($M_\odot$)	17
p	Particle power index	2.2
$R_\star$	Stellar radius (cm)	2×10^{11}
$T_\star$	Stellar temperature (K)	9×10^4
r_orb	Orbital radius (cm)	4.5×10^{11}
θ	Viewing angle (rad)	$\pi/6$

the BH mass in units of solar mass, and $v_\mathrm{A} = v_\mathrm{A0}\Gamma$, is the relativistic form of the Alfvén velocity, with $v_\mathrm{A0} = B/(4\pi\rho)^{1/2}$, B being the local magnetic field, ρ the fluid density, and $\Gamma = [1 + (\frac{v_\mathrm{A0}}{c})^2]^{-1/2}$ (Somov 2012). In this work, $v_\mathrm{A0} \sim c$ (see below).

The ambient magnetic field in the surrounds of the BH calculated from the GL05 and KGS15 model is given by

$$B \cong 9.96 \times 10^8 r_X^{-1.25} \xi^{0.5} m^{-0.5}\ \mathrm{G}. \tag{2}$$

The particle density in the coronal region in the surrounds of the BH is

$$n_\mathrm{c} \cong 8.02 \times 10^{18} r_X^{-0.375} \Gamma^{0.5} l^{-0.75} q^{-2} \xi^{0.25} m^{-1}\ \mathrm{cm}^{-3}. \tag{3}$$

The equations above will be employed in Sections 4 and 5 to model the acceleration in the core region of the μQSOs Cyg X-1 and Cyg X-3. The acceleration region in our model is taken to be the cylindrical shell where magnetic reconnection takes place, as in Fig. 1. This shell has a length l_X, and inner and outer radii R_X and $R_X + \Delta R_X$, respectively, where ΔR_X is the width of the current sheet given by (KGS15)

$$\Delta R_X \cong 2.34 \times 10^4 \Gamma^{-0.31} r_X^{0.48} l^{-0.15} l_X q^{-0.75} \xi^{-0.15} m\ \mathrm{cm}. \tag{4}$$

In Sections 4 and 5, we will also need the accretion disc temperature in order to evaluate its blackbody radiation field

$$T_\mathrm{d} \cong 3.71 \times 10^7 \alpha^{-0.25} r_X^{-0.37} m^{0.25}\ \mathrm{K}, \tag{5}$$

where $0.05 \leq \alpha < 1$ is the Shakura–Sunyaev disc viscosity parameter which we here assume to be of the order of 0.5.

2.3 Particle acceleration due to the magnetic energy released by fast reconnection

The magnetic power released by a fast reconnection event heats the surrounding gas and may accelerate particles. We assume that approximately 50 per cent of the reconnection power is used to accelerate the particles. This is consistent with recent plasma laboratory experiments of particle acceleration in reconnection sheets (e.g. Yamada et al. 2014) and also with solar flare observations where up to 50 per cent of the released magnetic energy appears in the form of energetic electrons (e.g. Lin & Hudsun 1971).

As in shock acceleration where particles confined between the upstream and downstream flows undergo a first-order Fermi acceleration, GL05 proposed that a similar mechanism would occur when particles are trapped between the two converging magnetic flux tubes moving to each other in a magnetic reconnection current sheet with a velocity V_R. They showed that, as particles bounce back and forth due to head-on collisions with magnetic fluctuations in the current sheet, their energy after a round trip increases by $\langle \Delta E/E \rangle \sim 8V_\mathrm{R}/3c$, which implies a first-order Fermi process with an exponential energy growth after several round trips (GL05; see also de Gouveia Dal Pino & Kowal 2015). Under conditions of *fast* magnetic reconnection V_R is of the order of the local Alfvén speed V_A, at the surroundings of relativistic sources, $V_\mathrm{R} \simeq v_\mathrm{A} \simeq c$ and thus the mechanism can be rather efficient (GL05; Giannios 2010).

As remarked earlier, this mechanism has been thoroughly tested by means of 3D MHD numerical simulations in which charged thermal particles are accelerated to relativistic energies into collisional domains of fast magnetic reconnection without including kinetic effects (Kowal et al. 2011, 2012).[4]

Using the results of the 3D MHD numerical simulations of the acceleration of test particles in current sheets where reconnection was made fast by embedded turbulence (Kowal et al. 2012), we find that the acceleration rate for a proton is given by

$$t^{-1}_\mathrm{acc,rec,p} = 1.3 \times 10^5 \left(\frac{E}{E_0}\right)^{-0.4} t_0^{-1}, \tag{6}$$

where E is the energy of the accelerated proton, $E_0 = m_\mathrm{p}c^2$, m_p is the proton rest mass, $t_0 = l_\mathrm{acc}/v_\mathrm{A}$ is the Alfvén time, and l_acc is the length-scale of the acceleration region. Although this result was found from numerical simulations employing protons as test particles, we can derive a similar expression for the electrons:

$$t^{-1}_\mathrm{acc,rec,e} = 1.3 \times 10^5 \sqrt{\frac{m_\mathrm{p}}{m_\mathrm{e}}} \left(\frac{E}{E_0}\right)^{-0.4} t_0^{-1}, \tag{7}$$

where m_e is the electron rest mass.

The equations above will be used to compute the acceleration rates in our model as described in the following sections.

The accelerated particles develop a PL energy distribution (see also Appendix A):

$$Q(E) \propto E^{-p}, \tag{8}$$

we assume for the PL index $p = 1.8$ and $p = 2.2$ for Cyg X-1 and Cyg X-3, respectively, which are compatible with the predicted values in analytical and numerical studies (GL05; Drury 2012; de Gouveia Dal Pino & Kowal 2015; del Valle et al. 2015).[5]

---

[4] We note also that tests performed in collisionless fluids, by means of 2D (e.g. Zenitani & Hoshino 2001; Drake et al. 2006, 2010; Zenitani et al. 2009; Cerutti et al. 2013, 2014; Sironi & Spitkovsky 2014), and 3D PIC simulations (Sironi & Spitkovsky 2014) have generally achieved similar results to those of collisional studies with regard to acceleration rates and particle PL spectra, with the only difference that these can probe only the kinetic scales of the process, while the collisional MHD simulations probe large scales (Kowal et al. 2011, 2012). In particular, Kowal et al. (2011) have demonstrated by means of 2D and 3D collisional MHD simulations the equivalence between first-order Fermi particle acceleration involving 2D converging magnetic islands in current sheets, which arise in collisionless fluid simulations (e.g. Drake et al. 2006, 2010), and the same process in 3D reconnection sites where the islands naturally break out into loops. Kowal et al. (2011) further demonstrated the importance of the presence of guide fields in 2D simulations to ensure equivalence with the results of more realistic 3D particle acceleration simulations.

[5] We note that analytical estimates of the first-order Fermi accelerated particle PL spectrum in current sheets predict PL indices $p \sim 1$–2.5 (e.g. GL05; Giannios 2010; Drury 2012), while 3D MHD numerical simulations with test particles predict $p \sim 1$ (Kowal et al. 2012 and see also the review by de Gouveia Dal Pino & Kowal 2015), which is comparable with results obtained from 2D collisionless PIC simulations considering merging islands

As stressed in GL05, it is also possible that a diffusive shock may develop in the surrounds of the magnetic reconnection zone, at the jet launching region, due to the interaction of 'coronal mass ejections', which are released by fast reconnection along the magnetic field lines, just like, e.g. in the Sun. A similar picture has been also suggested by e.g. Romero, Vieyro & Vila (2010b). In this case, one should expect the shock velocity to be predominantly parallel to the magnetic field lines and the acceleration rate for a particle of energy E in a magnetic field B, will be approximately given by (e.g. Spruit 1988):

$$t^{-1}_{\mathrm{acc,shock}} = \frac{\eta e c B}{E}, \tag{9}$$

where $0 < \eta \ll 1$ characterizes the efficiency of the acceleration. We fix $\eta = 10^{-2}$, which is appropriate for shocks with velocity $v_{\mathrm{s}} \approx 0.1c$ commonly assumed in the Bohm regime (Romero et al. 2010b, see further discussion in Section 6).

The accelerated particles lose their energy radiatively via interactions with the surrounding magnetic field (producing synchrotron emission), the photon field (producing IC, synchrotron-self-Compton, and photomesons $p\gamma$), and with the surrounding matter (producing pp collisions and relativistic bremsstrahlung radiation).

In the following section, we discuss the relevant radiative loss processes for electrons and protons which will allow the construction of the SED of these sources for comparison with the observations.

3 EMISSION AND ABSORPTION MECHANISMS

3.1 Interactions with magnetic field

Charged particles with energy E, mass m and charge number Z spiralling in a magnetic field $\boldsymbol{B}$ emit synchrotron radiation at a rate

$$t^{-1}_{\mathrm{synch}}(E) = \frac{4}{3}\left(\frac{m_{\mathrm{e}}}{m}\right)^3 \frac{\sigma_{\mathrm{T}} B^2}{m_{\mathrm{e}} c 8\pi} \frac{E}{mc^2}, \tag{10}$$

where m_{e} is the electron mass and σ_{T} is the Thompson cross-section. The synchrotron spectrum radiated by a distribution of particles $N(E)$ (see Appendix A) as function of the scattered photon energy (E_γ) (in units of power per unit area) is

$$L_\gamma(E_\gamma) = \frac{E_\gamma V_{\mathrm{vol}}}{4\pi d^2} \frac{\sqrt{2} e^3 B}{h m c^2} \int_{E_{\mathrm{min}}}^{E_{\mathrm{max}}} \mathrm{d}E\, N(E) \frac{E_\gamma}{E_{\mathrm{c}}} \int_{\frac{E_\gamma}{E_{\mathrm{c}}}}^{\infty} K_{5/3}(\xi)\, \mathrm{d}\xi, \tag{11}$$

where V_{vol} is the volume of the emission region, d is the distance of the source from us, h is the Planck constant, $K_{5/3}(\xi)$ is the modified Bessel function of 5/3 order, and the characteristic energy E_{c} is

$$E_{\mathrm{c}} = \frac{3}{4\pi} \frac{ehB}{mc} \left(\frac{E}{mc^2}\right)^2. \tag{12}$$

In these calculations, we assumed that the particle velocity is perpendicular to the local magnetic field.

To compute equation (11), we used the approximation

$$x \int_x^\infty K_5/3(\xi)\ \mathrm{d}\xi \approx 1.85 x^{1/3} e^{-x}. \tag{13}$$

Practically, the synchrotron emission of the electrons dominates the low-energy photon background which is a proper target for both IC and $p\gamma$ interactions (see below; see also Reynoso, Medina & Romero 2011). The number density for multiwavelength synchrotron scattered photons (in units of energy per volume), has been approximated as (Zhang, Chen & Fang 2008)

$$n_{\mathrm{synch}}(\epsilon) = \frac{L_\gamma(\epsilon)}{\epsilon^2 V_{\mathrm{vol}}} \frac{r}{c} 4\pi d^2, \tag{14}$$

where r stands for the radius of the emission region and ϵ for the scattered synchrotron radiation energy. More precisely, ϵ corresponds to the photon energy of the multiwavelength target radiation field for synchrotron self-Compton (SSC) and $p\gamma$ interactions. The volume V_{vol} of the emission region in our model is taken as the spherical region that encompasses the cylindrical shell where magnetic reconnection particle acceleration takes place in Fig. 1. Considering that the cylinder extends up to L, then $r \simeq L$ and the effective emission zone in our model has an approximate volume $4\pi L^3/3$ (see Tables 1 and 2).

3.2 Interactions with matter

3.2.1 *Bremsstrahlung*

When a relativistic electron accelerates in the presence of the electrostatic field of a charged particle or a nucleus of charge Ze, bremsstrahlung radiation is produced. For a fully ionized plasma with ion number density n_{i}, the bremsstrahlung cooling rate is (Berezinskii 1990)

$$t^{-1}_{\mathrm{Br}} = 4 n_{\mathrm{i}} Z^2 r_0^2 \alpha_{\mathrm{f}} c \left[\ln\left(\frac{2E_{\mathrm{e}}}{m_{\mathrm{e}} c^2}\right) - \frac{1}{3}\right], \tag{15}$$

where r_0 is the electron classical radius and α_{f} stands for the fine structure constant. The relativistic bremsstrahlung spectrum (in units of power per unit area) is given by (Romero, del Valle & Orellana 2010a)

$$L_\gamma(E_\gamma) = \frac{E_\gamma V_{\mathrm{vol}}}{4\pi d^2} \int_{E_\gamma}^{\infty} n \sigma_B(E_{\mathrm{e}}, E_\gamma) \frac{c}{4\pi} N_{\mathrm{e}}(E_{\mathrm{e}})\, \mathrm{d}E_{\mathrm{e}}, \tag{16}$$

where

$$\sigma_B(E_{\mathrm{e}}, E_\gamma) = \frac{4\alpha_f r_0^2}{E_\gamma} \Phi(E_{\mathrm{e}}, E_\gamma), \tag{17}$$

and

$$\Phi(E_{\mathrm{e}}, E_\gamma) = \left[1 + \left(1 - \frac{E_\gamma}{E_{\mathrm{e}}}\right)^2 - \frac{2}{3}\left(1 - \frac{E_\gamma}{E_{\mathrm{e}}}\right)\right] \times \left[\ln \frac{2E_{\mathrm{e}}(E_{\mathrm{e}} - E_\gamma)}{m_{\mathrm{e}} c^2 E_\gamma} - \frac{1}{2}\right]. \tag{18}$$

3.2.2 *pp interactions*

One relevant gamma-ray production mechanism is the decay of neutral pions which can be created through inelastic collisions of the relativistic protons with nuclei of the corona that surrounds the

---

$p \sim 1.5$ (Drake et al. 2010), or X-type Petschek 2D configurations (e.g. Zenitani & Hoshino 2001), for which it has been obtained $p \sim 1$, or even with more recent 3D PIC simulations (Sironi & Spitkovsky 2014) which obtained $p < 2$. In summary, considering both analytical and numerical predictions $p \sim$ 1–2.5. However, at least in the case of the 3D MHD simulations, some caution is necessary with the derived spectral index $p \sim 1$, because in these simulations particles are allowed to re-enter in the periodic boundaries of the computational domain and be further accelerated causing some deposition of particles in the VHE tail of the spectrum after saturation of the acceleration which may induce some artificial increase in the slope (del Valle et al. 2015).

accretion disc. In this case, the cooling rate is given by (Kelner, Aharonian & Bugayov 2006)

$$t_{\rm pp}^{-1} = n_{\rm i} c \sigma_{\rm pp} k_{\rm pp}, \tag{19}$$

where $k_{\rm pp}$ is the total inelasticity of the process of value ∼0.5. The corresponding cross-section for inelastic pp interactions $\sigma_{\rm pp}$ can be approximately by (Kelner, Aharonian & Bugayov 2009)

$$\sigma_{\rm pp}(E_{\rm p}) = \left(34.3 + 1.88L + 0.25L^2\right) \left[1 - \left(\frac{E_{\rm th}}{E_p}\right)^4\right]^2 \ {\rm mb}, \tag{20}$$

where mb stands for millibarn, $L = \ln(\frac{E_{\rm p}}{1\,{\rm TeV}})$, and the proton threshold kinetic energy for neutral pion (π^0) production is $E_{\rm th} = 2m_\pi c^2(1 + \frac{m_\pi}{4m_{\rm p}}) \approx 280\,{\rm MeV}$, where $m_\pi c^2 = 134.97\,{\rm MeV}$ is the rest energy of π^0 (Vila & Aharonian 2009). This particle decays in two photons with a probability of 98.8 per cent.

The spectrum can be calculated by

$$L_\gamma(E_\gamma) = \frac{E_\gamma^2 V_{\rm vol}}{4\pi d^2} q_\gamma(E_\gamma), \tag{21}$$

where $q_\gamma(E_\gamma)({\rm erg}^{-1}\ {\rm cm}^{-3}\ {\rm s}^{-1})$ is the gamma-ray emissivity.

For proton energies less than 0.1 TeV, $q_\gamma(E_\gamma)$ is

$$q_\gamma(E_\gamma) = 2\int_{E_{\rm min}}^{\infty} \frac{q_\pi(E_\pi)}{\sqrt{E_\pi^2 - m_\pi^2 c^4}} {\rm d}E_\pi, \tag{22}$$

where $E_{\rm min} = E_\gamma + m_\pi^2 c^4/4E_\gamma$ and $q_\pi(E_\pi)$ is the pion emissivity. An approximate expression for $q_\pi(E_\pi)$ can be calculated using the δ-function (Aharonian & Atoyan 2000). For this purpose, a fraction k_π of the kinetic energy of the proton $E_{\rm kin} = E_{\rm p} - m_{\rm p}c^2$ is taken by the neutral pion (Vila & Aharonian 2009). The neutral pion emissivity is then given by

$$\begin{aligned} q_\pi(E_\pi) &= cn_i \int \delta(E_\pi - k_\pi E_{\rm kin}) \sigma{\rm pp}(Ep) N_{\rm p}(E_{\rm p})\, {\rm d}E_{\rm p} \\ &= \frac{cn_i}{k_\pi} \sigma_{\rm pp} \left(m_{\rm p}c^2 + \frac{E_\pi}{k_\pi}\right) N_{\rm p} \left(m_{\rm p}c^2 + \frac{E_\pi}{k_\pi}\right). \end{aligned} \tag{23}$$

The target ambient nuclei density is given by $n_{\rm i}$ and $N_{\rm p}(E_{\rm p})$ stands for the energy distribution of the relativistic protons.

For proton energies in the range GeV–TeV, $k_\pi \approx 0.17$ (Gaisser 1990), the total cross-section $\sigma_{\rm pp}(E_{\rm p})$ can be approximated by

$$\sigma_{\rm pp}(E_{\rm p}) \approx \begin{cases} 30\left[0.95 + 0.06\ \ln\left(\frac{E_{\rm kin}}{1\,{\rm GeV}}\right)\right] {\rm mb} & E_{\rm kin} \geq 1\,{\rm GeV}, \\ 0 & E_{\rm kin} < 1\,{\rm GeV}. \end{cases} \tag{24}$$

For proton energies greater than 0.1 TeV, the gamma-ray emissivity is

$$\begin{aligned} q_\gamma(E_\gamma) &= cn_{\rm i} \int_{E_\gamma}^{\infty} \sigma_{\rm inel}(E_{\rm p}) N_{\rm p}(E_{\rm p}) E_\gamma \left(\frac{E_\gamma}{E_{\rm p}}, E_{\rm p}\right) \frac{{\rm d}E_{\rm p}}{E_{\rm p}} \\ &= cn_{\rm i} \int_0^1 \sigma_{\rm inel}\left(\frac{E_\gamma}{x}\right) N_{\rm p}\left(\frac{E_\gamma}{x}\right) F_\gamma\left(x, \frac{E_\gamma}{x}\right) \frac{{\rm d}x}{x}. \end{aligned} \tag{25}$$

The inelastic *pp* cross-section is approximately given by

$$\sigma_{\rm inel}(E_{\rm p}) = (34.3 + 1.88L + 0.25L^2) \left[1 - \left(\frac{E_{\rm th}}{E_{\rm p}}\right)^4\right]^2 \ {\rm mb}, \tag{26}$$

Here $E_{\rm th} = m_{\rm p} + 2m_\pi + \frac{m_\pi^2}{2m_{\rm p}} = 1.22$ GeV is the threshold energy of the proton to produce neutral pions π^0 and the number of photons whose energies are in the range of $(x, x + {\rm d}x)$, where $x = E_\gamma/E_{\rm p}$, caused per pp collision can be approximated by (Vila & Aharonian 2009)

$$\begin{aligned} F_\gamma(x, E_{\rm p}) = B_\gamma \frac{\ln x}{x} &\left[\frac{1 - x^{\beta_\gamma}}{1 + k_\gamma x^{\beta_\gamma}(1 - x^{\beta_\gamma})}\right]^4 \\ &\times \left[\frac{1}{\ln x} - \frac{4\beta_\gamma x^{\beta_\gamma}}{1 - x^{\beta_\gamma}} - \frac{4k_\gamma \beta_\gamma x^{\beta_\gamma}(1 - 2x^{\beta_\gamma})}{1 + k_\gamma x^{\beta_\gamma}(1 - x^{\beta_\gamma})}\right]. \end{aligned} \tag{27}$$

The best least-squares fits to the numerical calculations yield

$$B_\gamma = 1.30 + 0.14L + 0.011L^2, \tag{28}$$

$$\beta_\gamma = (1.79 + 0.11L + 0.008L^2)^{-1}, \tag{29}$$

$$k_\gamma = (0.801 + 0.049L + 0.014L^2)^{-1}. \tag{30}$$

Where $L = \ln(E_{\rm p}/1\,{\rm TeV})$ and $0.001 \leq x \leq 0.1$ (for more details see Vila & Aharonian 2009).

3.3 Interactions with the radiation field

Energetic electrons transfer their energy to low-energy photons causing them to radiate at high energies (IC process). On the other hand, when high-energy protons interact with low-energy photons ($p\gamma$ interactions) they produce pions and gamma-ray photons with energies larger than 10^8 eV in the so called photomeson process.

3.3.1 *Inverse Compton*

The IC cooling rate for an electron in both Thomson and Klein–Nishina regimes is given by (Blumenthal & Gould 1970)

$$t_{\rm IC}^{-1}(E_{\rm e}) = \frac{1}{E_{\rm e}} \int_{\epsilon{\rm min}}^{\epsilon_{\rm max}} \int_{E_{\rm ph}}^{\frac{\Gamma E_{\rm e}}{1+\Gamma}} (E_\gamma - E_{\rm ph}) \frac{{\rm d}N}{{\rm d}t\ {\rm d}E_\gamma} {\rm d}E_\gamma. \tag{31}$$

Here $E_{\rm ph}$ and E_γ are the incident and scattered photon energies, and

$$\frac{{\rm d}N}{{\rm d}t\ {\rm d}E_\gamma} = \frac{2\pi r_0^2 m_{\rm e}^2 c^5}{E_{\rm e}^2} \frac{n_{\rm ph}(E_{\rm ph})\ {\rm d}E_{\rm ph}}{E_{\rm ph}} F(q), \tag{32}$$

where $n_{\rm ph}(E_{\rm ph})$ is the target photon density (in the units of energy^{-1} volume^{-1}) and

$$F(q) = 2q\ln q + (1 + 2q)(1 - q) + 0.5(1 - q)\frac{(\Gamma q)^2}{1 + \Gamma}, \tag{33}$$

$$\Gamma = 4E_{\rm ph}E_{\rm e}/(m_{\rm e}c^2)^2, \tag{34}$$

$$q = \frac{E_\gamma}{[\Gamma(E_{\rm e} - E_\gamma)]}. \tag{35}$$

Accelerated electrons may have interaction with photons produced by the synchrotron emission in the coronal region (equation 14), in which case the process is SSC, or by photons emitted by the surface of the accretion disc. This photon field can be represented by a blackbody radiation and is given by[6]

$$n_{\rm bb}(E_{\rm ph}) = \frac{1}{\pi^2 \lambda_{\rm c}^3 m_{\rm e}c^2} \left(\frac{E_{\rm ph}}{m_{\rm e}c^2}\right)^2 \left[\frac{1}{\exp\left(\frac{E_{\rm ph}}{\rm kt}\right) - 1}\right]. \tag{36}$$

---

[6] We note that the contribution of target photons due to the radiation field produced by the companion star is found to be irrelevant in our model (e.g. Bosch-Ramon, Romero & Paredes 2005a).

Here λ_c, t and k are the Compton wavelength, disc temperature and Boltzmann constant, respectively. We will see below that for the μQSOs, the SSC will be dominating.

Taking into account the Klein–Nishina effect on the cross-section, the total luminosity per unit area can be calculated from (Romero et al. 2010a)

$$L_{\mathrm{IC}}(E_\gamma) = \frac{E_\gamma^2 V_{\mathrm{vol}}}{4\pi d^2} \int_{E_{\min}}^{E_{\max}} \mathrm{d}E_{\mathrm{e}} N_{\mathrm{e}}(E_{\mathrm{e}}) \times \int_{E_{\mathrm{ph,min}}}^{E_{\mathrm{ph,max}}} \mathrm{d}E_{\mathrm{ph}} P_{\mathrm{IC}}(E_\gamma, E_{\mathrm{ph}}, E_{\mathrm{e}}), \tag{37}$$

where $P_{\mathrm{IC}}(E_\gamma, E_{\mathrm{ph}}, E_{\mathrm{e}})$ is the spectrum of photons scattered by an electron of energy $E_{\mathrm{e}} = \gamma_e m_{\mathrm{e}} c^2$ in a target radiation field of density $n_{\mathrm{ph}}(E_{\mathrm{ph}})$. According to Blumenthal & Gould (1970), it is given by

$$P_{\mathrm{IC}}(E_\gamma, E_{\mathrm{ph}}, E_{\mathrm{e}}) = \frac{3\sigma_{\mathrm{T}} c (m_{\mathrm{e}} c^2)^2}{4E_{\mathrm{e}}^2} \frac{n_{\mathrm{ph}}(E_{\mathrm{ph}})}{E_{\mathrm{ph}}} F(q), \tag{38}$$

and for the scattered photons there is a range which is

$$E_{\mathrm{ph}} \leq E_\gamma \leq \frac{\Gamma}{1+\Gamma} E_{\mathrm{e}}. \tag{39}$$

3.3.2 Photomeson production (pγ)

The photomeson production takes place for photon energies greater than $E_{\mathrm{th}} \approx 145$ MeV. A single pion can be produced in an interaction near the threshold and then decay giving rise to gamma-rays. In our model the appropriate photons come from the synchrotron radiation.[7] The cooling rate for this mechanism in an isotropic photon field with density $n_{\mathrm{ph}}(E_{\mathrm{ph}})$ can be calculated by Stecker (1968)

$$t_{\mathrm{p}\gamma}^{-1}(E_{\mathrm{p}}) = \frac{c}{2\gamma_{\mathrm{p}}^2} \int_{\frac{E_{\mathrm{th}}^{(\pi)}}{2\gamma_{\mathrm{p}}}}^{\infty} \mathrm{d}E_{\mathrm{ph}} \frac{n_{\mathrm{ph}}(E_{\mathrm{ph}})}{E_{\mathrm{ph}}^2} \times \int_{E_{\mathrm{th}}^{(\pi)}}^{2E_{\mathrm{ph}}\gamma_{\mathrm{p}}} \mathrm{d}\epsilon_{\mathrm{r}} \sigma_{\mathrm{p}\gamma}^{(\pi)}(\epsilon_{\mathrm{r}}) K_{\mathrm{p}\gamma}^{(\pi)}(\epsilon_{\mathrm{r}}) \epsilon_{\mathrm{r}}, \tag{40}$$

where $\gamma_{\mathrm{p}} = \frac{E_{\mathrm{p}}}{m_{\mathrm{e}} c^2}$, ϵ_{r} is the photon energy in the rest frame of the proton and $K_{\mathrm{p}\gamma}^{(\pi)}$ is the inelasticity of the interaction. Atoyan & Dermer (2003) proposed a simplified approach to calculate the cross-section and the inelasticity which are given by

$$\sigma_{\mathrm{p}\gamma}(\epsilon_{\mathrm{r}}) \approx \begin{cases} 340\ \mu\mathrm{barn} & 300\ \mathrm{MeV} \leq \epsilon_r \leq 500\ \mathrm{MeV} \\ 120\ \mu\mathrm{barn} & \epsilon_{\mathrm{r}} > 500\ \mathrm{MeV}, \end{cases} \tag{41}$$

and

$$K_{\mathrm{p}\gamma}(\epsilon_{\mathrm{r}}) \approx \begin{cases} 0.2 & 300\ \mathrm{MeV} \leq \epsilon_{\mathrm{r}} \leq 500\ \mathrm{MeV} \\ 0.6 & \epsilon_{\mathrm{r}} > 500\ \mathrm{MeV}. \end{cases} \tag{42}$$

To find the luminosity from the decay of pions, we use the analytical approach proposed by Atoyan & Dermer (2003). Taking into account that each pion decays into two photons, the $p\gamma$ luminosity is

$$\begin{aligned} L_{\mathrm{p}\gamma}(E_\gamma) &= 2\frac{E_\gamma^2 V_{\mathrm{vol}}}{4\pi d^2} \int Q_{\pi^0}^{(\mathrm{p}\gamma)}(E_\pi) \delta(E_\gamma - 0.5E_\pi)\, \mathrm{d}E_\pi \\ &= 20 \frac{E_\gamma^2 V_{\mathrm{vol}}}{4\pi d^2} N_{\mathrm{p}}(10E_\gamma) \omega_{\mathrm{p}\gamma,\pi}(10E_\gamma) n_{\pi^0}(10E_\gamma), \end{aligned} \tag{43}$$

where $Q_{\pi^0}^{(\mathrm{p}\gamma)}$ is the emissivity of the neutral pions given by

$$Q_{\pi^0}^{(\mathrm{p}\gamma)} = 5N_{\mathrm{p}}(5E_\pi) \omega_{\mathrm{p}\gamma,\pi}(5E_\pi) n_{\pi^0}(5E_\pi), \tag{44}$$

$\omega_{\mathrm{p}\gamma}$ stands for the collision rate which is

$$\omega_{\mathrm{p}\gamma}(E_{\mathrm{p}}) = \frac{m_{\mathrm{p}}^2 c^5}{2E_{\mathrm{p}}^2} \int_{\frac{E_{\mathrm{th}}}{2\gamma_{\mathrm{p}}}}^{\infty} \mathrm{d}E_{\mathrm{ph}} \frac{n_{\mathrm{ph}}(E_{\mathrm{ph}})}{E_{\mathrm{ph}}^2} \int_{E_{\mathrm{th}}}^{2E_{\mathrm{ph}}\gamma p} \mathrm{d}E_r \sigma_{\mathrm{p}\gamma}^{(\pi)}(E_{\mathrm{r}}) E_{\mathrm{r}}, \tag{45}$$

and n_{π^0} is the mean number of neutral pions produced per collision given by

$$n_{\pi^0}(E_{\mathrm{p}}) = 1 - P(E_{\mathrm{p}}) \xi_{\mathrm{pn}}. \tag{46}$$

In the single-pion production channel, the probability for the conversion of a proton to a neutron with the emission of a $\pi^+ -$ *meson* is given by $\xi_{\mathrm{pn}} \approx 0.5$. For photomeson interactions of a proton with energy E_{p}, the interaction probability is represented by $P(E_{\mathrm{p}})$, which is

$$P(E_{\mathrm{p}}) = \frac{K_2 - \bar{K}_{\mathrm{p}\gamma}(E_{\mathrm{p}})}{K_2 - K_1}. \tag{47}$$

The inelasticity in the single-pion channel is approximated as $K_1 \approx 0.2$, whereas $K_2 \approx 0.6$. For energies above 500 MeV the mean inelasticity $\bar{K}_{\mathrm{p}\gamma}$ is

$$\bar{K}_{\mathrm{p}\gamma} = \frac{1}{t_{\mathrm{p}\gamma}(\gamma_{\mathrm{p}}) \omega_{\mathrm{p}\gamma}(E_{\mathrm{p}})}. \tag{48}$$

3.4 Absorption

Gamma-rays can be annihilated by the surrounding radiation field via electron–positron pair creation: $\gamma + \gamma \rightarrow e^+ + e^-$. In μQSOs, besides the radiation field of the tight companion star, coronal and accretion disc photons can also absorb γ-rays. However, it has been shown by Cerutti et al. (2011) that the absorption due to coronal photons is negligible compared with the contribution from the disc. Adopting the same absorption model for the disc radiation field of these authors, we find that the disc contribution to gamma-ray absorption is less relevant than that of the stellar companion, generally a Wolf–Rayet star, which produces ultraviolet (UV) radiation. To evaluate the optical depth due to this component, we have adopted the model described by (Sierpowska-Bartosik & Torres 2008, see also Dubus 2006; Zdziarski, Mikolajewska & Belczynski 2013). This process is possible only above a kinematic energy threshold given by

$$E_\gamma \epsilon (1 - \cos\theta) \geq 2m_{\mathrm{e}}^2 c^4, \tag{49}$$

and

$$E_\gamma \epsilon > (m_{\mathrm{e}} c^2)^2, \tag{50}$$

in head-on collisions (Romero et al. 2010b), where E_γ and ϵ are the energies of the emitted gamma-ray and the ambient photons and θ is the collision angle in the laboratory reference frame.

The attenuated luminosity $L_\gamma(E_\gamma)$ after the γ-ray travels a distance l is (Romero, Christiansen & Orellana 2005)

$$L_\gamma(E_\gamma) = L_\gamma^0(E_\gamma)\, \mathrm{e}^{-\tau(l, E_\gamma)}, \tag{51}$$

where L_γ^0 is the intrinsic coronal gamma-ray luminosity and $\tau(l, E_\gamma)$ is the optical depth. The differential optical depth is given by

$$\mathrm{d}\tau = (1 - \mu) n_{\mathrm{ph}} \sigma_{\gamma\gamma}\, \mathrm{d}\epsilon\, \mathrm{d}\Omega\, \mathrm{d}l', \tag{52}$$

---

[7] We find that for photomeson production, the radiation from the accretion disc and from the companion star are irrelevant compared to the contribution from the synchrotron emission.

where $d\Omega$ is the solid angle of the target soft photons, μ is the cosine of the angle between the gamma-ray and the arriving soft photons, l' is the path along the gamma-ray emission and $n_{\rm ph}$ is the blackbody photon density in $\rm cm^{-3}\,erg^{-1}\,sr^{-1}$.

The $\gamma\gamma$ interaction cross-section $\sigma_{\gamma\gamma}$ is defined as (Gould & Scheder 1967)

$$\sigma_{\gamma\gamma}(\epsilon, E_\gamma) = \frac{\pi r_0^2}{2}(1-\beta^2)\left[2\beta(\beta^2-2) + (3-\beta^4)\ln\left(\frac{1+\beta}{1-\beta}\right)\right], \tag{53}$$

where r_0 is the classical radius of the electron and

$$\beta = \left[1 - \frac{(m_{\rm e}c^2)^2}{\epsilon E_\gamma}\right]^{1/2}. \tag{54}$$

The companion star with radius $R_\star$ and a blackbody surface temperature $T_\star$ produces a photon density at a distance $d_\star$ from the star

$$n_{\rm ph} = \frac{2\epsilon^2}{h^3c^3}\frac{1}{\exp(\epsilon/kT_\star)}\frac{R_{\rm star}^2}{d_\star^2}. \tag{55}$$

In the absorption models proposed by Sierpowska-Bartosik & Torres (2008) and Dubus (2006), the geometrical parameters $d_\star$, μ and l are strongly dependent on the viewing angle θ and the orbital phase $\phi_{\rm b}$. In the superior conjunction, the compact object is behind the star and the orbital phase is $\phi_{\rm b} = 0$. We here consider the same orbital phase that has been observed during the high-energy observations for Cyg X-1 and Cyg X-3. (For more details on the geometrical conditions of the binary system and the integration extremes, see Sierpowska-Bartosik & Torres 2008 and Dubus 2006.)

We note that the pairs produced by the absorbed gamma-rays may emit predominantly synchrotron emission in the surrounding magnetic fields (Bosch-Ramon, Khangulyan & Aharonian 2008), but their emission is expected to be negligible compared to the other synchrotron processes of the system. We thus neglect this effect in our treatment of pair absorption (Zdziarski et al. 2014).

4 APPLICATION TO CYGNUS X-1

Cyg X-1 is a widely studied BHB system (Malyshev, Zdziarski & Chernyakova 2013) at a distance of 1.86–2.2 kpc (Ziolkowski 2005; Reid et al. 2011) which is accreting from a high-mass companion star orbiting around the BH with a period is 5.6 d (Gies et al. 2008). The orbit inclination is between 25° and 35° (Gies & Bolton 1986) with an eccentricity of ~0.018 (Orosz 2011), so that one can assume an approximate circular orbit with a radius $r_{\rm orb}$.

The parameters of the model for Cyg X-1 are tabulated in Table 1. The values for the first five parameters in the table have been calculated from equations (1)–(5) above. We take for the accretion disc inner radius the value $R_X = 6R_S$, and for the extension L_X of the reconnection region (see Fig. 1), we consider the value $L_X \simeq 10R_S$ (GL05; GPK10). As remarked in Section 3, the volume V of the emission region in Table 1 was calculated by considering the spherical region that encompasses the reconnection region in Fig. 1.

The BH mass has been taken from Orosz (2011). Figs 2 and 3 show the cooling rates for the different energy loss processes described in Section 3 (equations 10, 15, 19, 31 and 40) for electrons and protons. These are compared with the acceleration rates due to first-order Fermi acceleration by magnetic reconnection (equations 6 and 7) and to shock acceleration (equation 9).

We notice that for both protons and electrons the acceleration is dominated by the first-order Fermi magnetic reconnection process in the core region. Besides, the main radiative cooling process for the electrons is synchrotron radiation, while for protons the photomeson production ($p\gamma$ interactions) governs the loss mechanisms (Fig. 3). In this case, the proper target radiation field are the photons from synchrotron emission. The intercept between the magnetic reconnection acceleration rate and the synchrotron rate in Fig. 2 gives the maximum energy that the electrons can attain in this acceleration process, which is ~10 GeV. Protons on the other hand, do not cool as efficiently as the electrons and can attain energies as high as ~4 × 10^{15} eV.

In order to reproduce the observed SED, we have calculated the non-thermal emission processes as described in Section 3 in the surrounds of the BH. Fig. 4 shows the computed SED for Cyg X-1 compared with observed data. As remarked, we have also considered the gamma-ray absorption due to electron–positron pair production resulting from interactions of the gamma-ray emission in the core with the surrounding radiation field. As stressed, our calculations indicate that this process is dominated by the radiation field of the companion star. As a result, the opacity depends on the phase of the orbital motion and on the viewing angle.

The parameters employed in the evaluation of this absorption are in the last four lines of Table 1, and have been taken from Romero et al. (2010a). It has been proposed from MAGIC observations

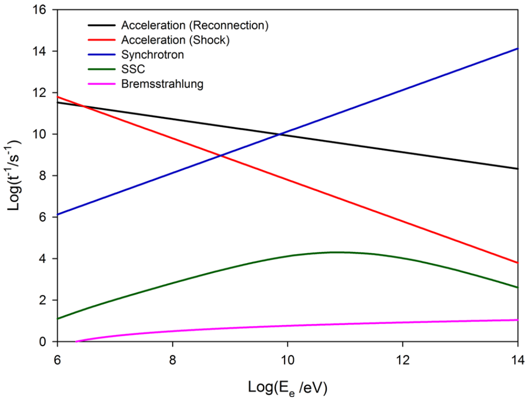

Figure 2. Acceleration and cooling rates for electrons in the nuclear region of Cyg X-1. (A colour version of this figure is available in the online version.)

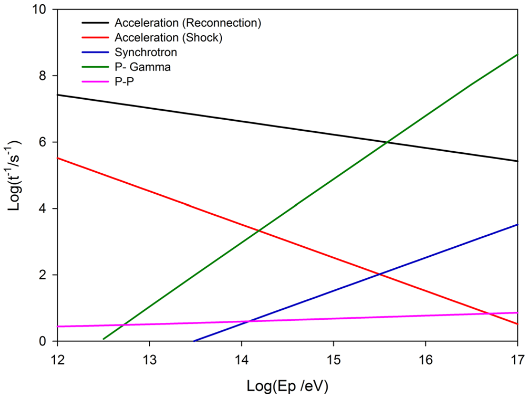

Figure 3. Acceleration and cooling rates for protons in the nuclear region of Cyg X-1. (A colour version of this figure is available in the online version.)

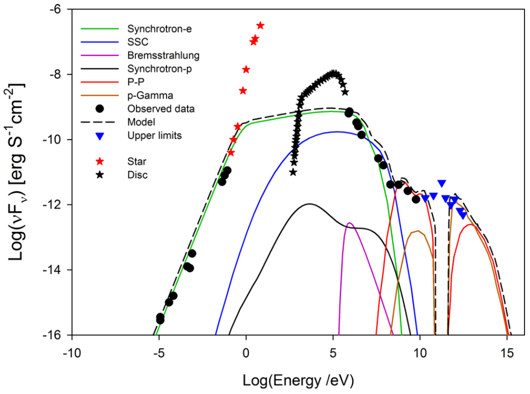

Figure 4. Calculated SED for Cyg X-1 using the magnetic reconnection acceleration model compared with observations. The data depicted in the radio range is from Fender et al. 2000, the IR fluxes are from Persi et al. 1980; Mirabel et al. 1996, the hard X-ray data above 20 keV are from *INTEGRAL* (Zdziarski, Lubinski & Sikora 2012), the soft X-ray data below 20 keV are from BeppoSAX (Di Salvo et al. 2001), the soft γ-ray data are from COMPTEL (McConnell et al. 2000, 2002), the data in the range 40 MeV–40 GeV are measurements and upper limits from the *Fermi*-LAT (Malyshev et al. 2013), and the data in the range 40 GeV–3 TeV are upper limits from MAGIC (with 95 per cent confidence level; Albert et al. 2007). The red and black stars correspond to emission from the companion star and the accretion disc, respectively, and are not investigated in the present model (see more details in the text.) (A colour version of this figure is available in the online version.)

(Albert et al. 2007) that the gamma-ray production and absorption are maximized near the superior conjunction (Bodaghee et al. 2013) at phase $\phi_b = 0.91$. In our calculations, we considered this orbital phase for Cyg X-1.

The calculated opacity according to the equations above results in a VHE gamma-ray absorption. We find that the produced gamma-rays are fully absorbed in the energy range of 50 Gev–0.5 TeV which causes the energy gap seen in the calculated SED in Fig. 4. The observed upper limits by MAGIC plotted in the diagram in this range are possibly originated outside the core, along the jet where γ-ray absorption by the stellar radiation is not important (see also Romero et al. 2010a).

We note that in Fig. 4 the observed flux in radio (10 μeV$-$0.1 eV) and soft gamma-ray (10^5–10^8 eV) are explained by leptonic synchrotron and SSC processes according to the present model. In the range 10 MeV–0.2 GeV, SSC is the main mechanism to produce the observed data as a result of interactions between the high-energy electrons with synchrotron photons. At energies in the range 0.2 GeV–3 TeV, neutral pion decays reproduce the observed gamma-rays. These neutral pions result from pp and $p\gamma$ interactions. In the range of 0.3 GeV–30 GeV, pp collisions are the dominant radiation mechanism, but in the VHE gamma-rays, interactions of relativistic hadrons (mostly protons) with scattered photons from synchrotron radiation may produce the observed flux.

The observed emission in the near-IR (0.1 eV–10 eV), represented in Fig. 4 by red stars is attributed to thermal blackbody radiation from the stellar companion, and the accretion X-ray emission (1 keV–0.1 MeV) also represented in Fig. 4 by dark stars, is believed to be due to thermal Comptonization of the disc emission by the surrounding coronal plasma of temperature $\sim 10^7$ K (Di Salvo et al. 2001; Zdziarski et al. 2012). For this reason, these observed data are not fitted by the coronal non-thermal emission model investigated here.

5 APPLICATION TO CYGNUS X-3

Cyg X-3 is also a high-mass X-ray binary that possibly hosts a BH (Zdziarski et al. 2013) and a Wolf–Rayet as a companion star (van Kerkwijk et al. 1992). The system is located at a distance of 7.2–9.3 kpc (Ling, Zhang & Tang 2009) and has an orbital period of 4.8 h and an orbital radius $\approx 3 \times 10^{11}$ cm (Piano et al. 2012). Our model parameters for Cyg X-3 are given in Table 2. As in Cyg X-1, the values for the first five parameters were calculated from equations (1)–(5) which describe the magnetic reconnection acceleration model in the core region. We have also used for the accretion disc inner radius the value $R_X = 6R_S$ and for the extension L_X of the reconnection region the value $L_X = 10R_S$ (GL05, GPK10 and KGS15). The BH mass has been taken from Schmutz, Geballe & Schild (1996).

The cooling and acceleration rates for electrons and protons are depicted in Figs 5 and 6, respectively. The maximum electron and proton energies in both diagrams are obtained from the

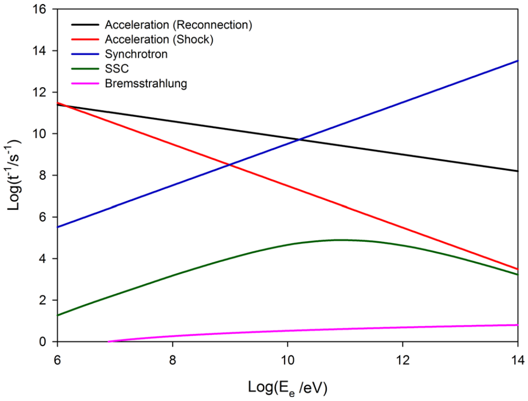

Figure 5. Acceleration and cooling rates for electrons in the core region of Cyg X-3. (A colour version of this figure is available in the online version.)

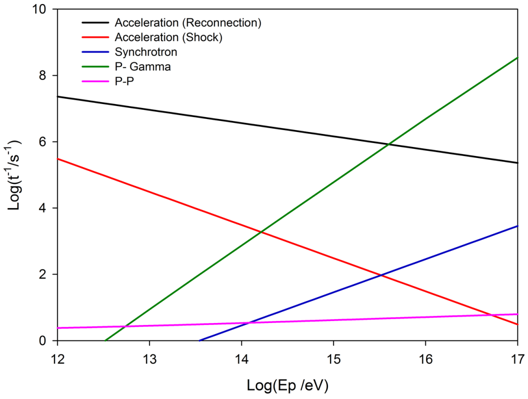

Figure 6. Acceleration and cooling rates for protons in the core region of Cyg X-3. (A colour version of this figure is available in the online version.)

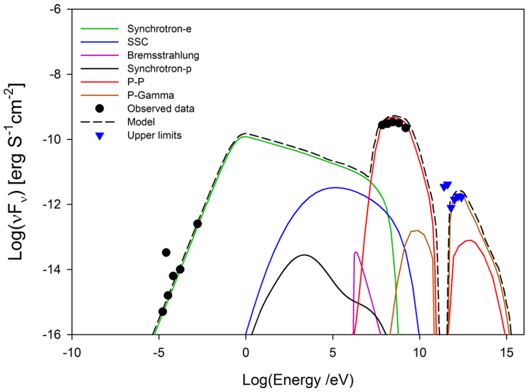

Figure 7. SED for Cyg X-3. The observed radio emission is taken from AMI-LA and RATAN (Piano et al. 2012); the data in the range 50 MeV–3 GeV are from AGILE-GRID (Piano et al. 2012); and the data in the range 0.2−3.155 TeV are from MAGIC differential flux upper limits (95 per cent C.L.). (A colour version of this figure is available in the online version.)

intercept between the acceleration rate curve and the dominant radiative loss rate curve. As in Cyg X-1, it is clear from the diagrams that acceleration by magnetic reconnection is dominating over shock acceleration in the core region. Synchrotron emission is the main mechanism to cool the electrons which may reach energies as high as ∼10 GeV, while the most important loss mechanism for protons is $p\gamma$ interactions with synchrotron photons. They can be accelerated up to $\sim 4 \times 10^{15}$ eV. In this system, the close proximity ($R_{\rm d} \approx 3 \times 10^{11}$ cm), the large stellar surface temperature ($T_\star \sim 10^5$ K), and the high stellar luminosity ($L_\star \sim 10^{39}$ erg s^{-1}) of the WolfRayet star may result a considerable attenuation of the gamma-rays via γ–γ pair production (Bednarek 2010). The detection of TeV gamma-rays in Cyg X-3, therefore, relies on the competition between the production and the attenuation process above.

Fig. 7 shows the calculated SED compared to the observed data for this source. The gamma-ray absorption was calculated from equation (52), employing the UV field of the companion star which is a more significant target than the radiation fields of the accretion disc and the corona (see the stellar parameters in the last four lines of Table 2 which were taken from Cherepashchuk & Moffat 1994). The orbital phase considered was $\phi_b = 0.9$, near the superior conjunction (Aleksic et al. 2010), as in Cyg X-1. The energy gap caused by this gamma-ray absorption is shown in Fig. 7 in the 50 GeV−0.4 TeV. The contributions of pp and $p\gamma$ interactions are the dominant ones in the high energy gamma-ray range. These processes become more relevant in the coronal region around the BH since the magnetic field there is strong and enhances the synchrotron radiation of the electrons and protons. Also the matter and photon densities are large enough in the core region, providing dense targets for pp and $p\gamma$ collisions and SSC scattering. In the energy range 10 MeV−50 Gev, the emission is dominated by the neutral pion decay resulting from pp inelastic collisions. Also, the resulting interactions between accelerated protons and scattered photons from synchrotron emission produce neutral pions and the gamma-ray emission from these pion decays results in the tail seen in the SED for energies ≥1 TeV.

6 DISCUSSION AND CONCLUSIONS

The multiwavelength detection, from radio to gamma-rays, of non-thermal energy from Galactic (BHBs or $\mu QSRs$) is clear evidence of an efficient production of relativistic particles and makes these sources excellent nearby laboratories to investigate and review particle acceleration theory in the surrounds of BH sources in general. Based on recent studies (GL05, GPK10, KGS15), we investigated here the role of magnetic reconnection in accelerating particles in the innermost regions of these sources, applying this acceleration model to reconstruct the SED of the BHBs Cyg X-1 and Cyg X-3.

According to GL05, particles can be accelerated to relativistic velocities in the surrounds of the BH, near the jet basis, by a first-order Fermi process occurring in the magnetic reconnection discontinuity formed by the encounter of the magnetic field lines rising from the accretion disc with those anchored into the BH (Fig. 1). This process becomes very efficient when these two magnetic line fluxes are squeezed together by enhanced disc accretion and the reconnection is fast driven e.g. by turbulence (LV99; Kowal et al. 2009, 2012).

This driving mechanism has been employed to compute the magnetic reconnection power released to heat and accelerate particles in this work (see KGS15). Moreover, the first-order Fermi acceleration mechanism within reconnection sites has been tested successfully by means of 2D and 3D numerical simulations (e.g. Drake et al. 2006; Zenitani et al. 2009; Kowal et al. 2011, 2012; Sironi & Spitkovsky 2014) and the resulting acceleration time-scale is proportional to $\sim E^{0.4}$ (Kowal et al. 2012; del Valle et al. 2015). This can be compared with the typical estimated acceleration time-scale in diffusive shocks for the same environment conditions $t_{\rm acc,\ shock} \propto E$ (see equation 9). We find a larger efficiency of the first mechanism in regions where magnetic discontinuities are dominant.

It should be noted that in a shock with perpendicular velocity to the magnetic field (for which particles diffuse *across* the magnetic field lines), it is predicted that the acceleration rate may be larger than that resulting from Bohm diffusion (equation 9) (Jokipii 1987; Giacalone 1998; Giacalone & Jokipii 1999, 2006; Jokipii & Giacalone 2007). As a matter of fact, if we consider the parameters in the inner coronal regions of our BHs, a perpendicular shock could lead to acceleration rates up to two or three orders of magnitude larger than that predicted by the Bohm rate, therefore, comparable to the computed magnetic reconnection acceleration rates in Figs 2, 3, 5 and 6. However, the model we explored here assumes that the surrounds of the BH is a magnetically dominated region, which makes the development of strong shocks harder in the inner nuclear regions. Nevertheless, as stressed in Section 3, fast magnetic reconnection can release coronal mass ejections along the reconnected magnetic field lines which will then induce the formation of a shock front further out, but in this case, the shock velocity will be predominantly parallel to the large-scale magnetic field lines and this explains why in Figs 2, 3, 5 and 6 we compared the magnetic reconnection acceleration rate with the Bohm shock acceleration rate which is suitable for diffusive and parallel shocks.

Even if the presence of turbulence may allow the formation of important perpendicular magnetic field components in the shock location that may affect the shock acceleration rate, it is important to remark that recent results (Lazarian & Yan 2014) have demonstrated that the divergence of the magnetic field on scales less than the injection scale of the turbulence induces superdiffusion of CRs in the direction perpendicular to the mean magnetic field. This makes the square of the perpendicular displacement to increase not with the distance x along the magnetic field, as in the case for a regular diffusion, but with x^3, for freely streaming CRs. They showed that this superdiffusion decreases the efficiency of the CR acceleration in perpendicular shocks. This superdiffusion has been also demonstrated numerically by Xu & Yan (2013) and these results suggest that perpendicular shock acceleration efficiency is still an open question that deserves further extensive numerical testing. A perpendicular shock would still be possible for particular geometries of magnetic field lines as proposed by Jokipii (1987), Giacalone & Jokipii (1999) and Giacalone & Jokipii (2006), but this is out of the scope of this work.

As remarked earlier, fast magnetic reconnection has been detected in space environments, like the earth magnetotail and the solar corona (see e.g. Deng & Matsumoto 2001; Su et al. 2013). Striking evidence of turbulent reconnection in the flares and coronal events at work on the Sun have been provided by observations from the *Yohkoh* and *SOHO* satellites (Priest 2001). Retinò et al. (2007) have also reported evidence of reconnection in the turbulent plasma of the solar wind downstream of the earth bow shock. They showed that this turbulent reconnection is fast and the released electromagnetic energy is converted into heating of the ambient plasma and acceleration of particles. These findings have significant implications for particle acceleration within turbulent reconnection sheets not only in the solar, but also in astrophysical plasmas, in general. Particle acceleration models due to fast magnetic reconnection have been widely explored in the solar framework. The Voyager spaceships completely failed to detect any observational evidence for shock acceleration. As the ultimate energy source in impulsive flares and in many other solar magnetic activities, fast reconnection naturally arose to explain the acceleration of the observed anomalous CRs throughout the heliosphere, from the solar flares and the earth magnetosphere (e.g. Drake et al. 2006) to the heliopause (Lazarian & Opher 2009; Drake et al. 2010; Oka et al. 2010).

Considering all the relevant leptonic and hadronic radiative loss mechanisms due to the interactions of the accelerated particles with the surrounding matter, magnetic and radiation fields in the core regions of the BHBs Cyg X-1 and Cyg X-3, we compared the time-scales of these losses with the acceleration time-scales above and found larger energy cut-offs for particles being accelerated by magnetic reconnection than by a diffusive shock (see Figs 2 and 3 for Cyg X-1, and Figs 5 and 6 for Cyg X-3). These cut-offs have an important role in the determination of the energy distribution of the accelerated particles and therefore, in the resulting SED, and stress the potential importance of magnetic reconnection as an acceleration mechanism in the core regions of BHBs and compact sources in general.

In most astrophysical systems, synchrotron is known as a dominant mechanism to cool the electrons and for the sources studied here, its cooling rate is also larger than that of the other loss mechanisms in all electron energy range. In Cyg X-1 and Cyg X-3, electrons gain energy up to 10 GeV (Figs 2 and 5). In both cases, the achieved maximum energy are larger than the possible values obtained with Bohm-limit shock acceleration in the nuclear region. Also, for both μQSOs we find that $p\gamma$ is the dominant mechanism to cool the accelerated relativistic protons in most of the investigated energy range. Only for energies below $\sim$2 TeV, the pp inelastic collisions are more efficient. The calculated energy cut-off for protons obtained from the comparison of the $p\gamma$ cooling time with the magnetic reconnection acceleration time is 4×10^{15}eV, for both sources. In these $p\gamma$ processes, the synchrotron radiation is the dominant target photon field that interacts with the energetic protons, this because the magnetic field in the core region of these sources is relatively large, as calculated from equation (14).

We note that the maximum energy of the accelerated particles is not constrained only by the emission losses, but also by the size of the acceleration region, i.e. the particle Larmor radius, $r_L = E/ceB$, cannot be larger than the length-scale of the acceleration zone. Considering the parameters employed in our model for both sources and ΔR_X as the length-scale of the acceleration zone, we find that the maximum energy to which the protons (and electrons) can be accelerated by magnetic reconnection is $\sim 10^{17}$ eV, which is larger than the cut-off values obtained above. This value also reassures the efficiency of this acceleration process.

We have also shown that, under fiducial conditions, the acceleration model developed here is capable of explaining the multi-wavelength non-thermal SED of both μQSOs Cyg X-1 and Cyg X-3. The radio emission may result from synchrotron process in both cases.

The observed soft gamma-rays from Cyg X-1 are due to synchrotron and IC processes. The target photons for the IC come mainly from synchrotron emission (SSC). Neutral pion decay resulting from pp inelastic collisions may produce the high-energy gamma-rays in both systems, while the VHE gamma-rays are the result of neutral pion decay due to photomeson production ($p\gamma$) in the core of these sources.

The importance of the γ–γ absorption due to interactions with the photon field of the companion star for electron–positron pair production has been also addressed in our calculations. According to our results, the observed gamma-ray emission in Cyg X-1 in the range 5×10^{10}–5×10^{11} eV (see inverted blue triangles in Fig. 4) cannot be produced in its core region (see also Romero et al. 2010a). In the case of Cyg X-3, we have found that the emission in the range of 50GeV-0.4 TeV (see inverted blue triangles in Fig. 7) is also fully absorbed in the core region by the same process. This suggests that in both sources, this emission is produced outside the core, probably along the jet, since at larger distances from the core the gamma-ray absorption by the stellar companion decreases substantially. In fact, this is what was verified by Zhang, Xu & Lu (2014) in the case of Cyg X-1.

Other authors have proposed alternative scenarios to the one discussed here. The models of Piano et al. (2012), for instance, which were based on particle acceleration near the compact object and on propagation along the jet, indicate that the observed gamma-ray $\leq$10 GeV in Cyg X-3 could be produced via leptonic (IC) and hadronic processes (pp interactions). However, they have no quantitative estimates for the origin of the VHE gamma-ray upper limits at $\geq$0.1 TeV obtained by MAGIC. Sahakyan, Piano & Tavani (2013), on the other hand, assumed that the jet of Cyg X-3 could accelerate both leptons and hadrons to high energies and the accelerated protons escaping from the jet would interact with the hadronic matter of the companion star producing γ-rays and neutrinos. However, their model does not provide proper fitting in the TeV range either.

In the case of Cyg X-1, Zhang et al. (2014) have employed a leptonic model to interpret recent *Fermi*-LAT measurements also as due to synchrotron emission but produced along the jet and to Comptonization of photons of the stellar companion. The TeV emission in their model is attributed to interactions between relativistic electrons and stellar photons via IC scattering. According to them this process could also explain the MAGIC upper limits in the range of 50 GeV–0.5 TeV, i.e. the band gap in Fig. 4. However, unlike this work where we obtained a reasonable match due to $p\gamma$ interactions, their model is unable to explain the observed upper limits by MAGIC in the VHE gamma-ray tail.

Also with regard to Cyg X-1, we should note that the detection of strong polarized signals in the high-energy range of 0.4–2 MeV by Laurent et al. (2011) and Jourdain et al. (2012) suggest that the optically thin synchrotron emission of relativistic electrons from the jet may produce soft gamma-rays. There are indeed some theoretical models that explain the emission in this range by using a jet model (Zdziarski et al. 2012, 2014; Malyshev et al. 2013; Zhang et al. 2014). Nevertheless, contrary to this view, Romero, Vieyro & Chaty (2014) argue that the MeV polarized tail may be originated in the coronal region of the core without requiring the jet. This study is therefore, consistent with the present model as it supports the coronal nuclear region for the origin of the non-thermal emission.

The results above clearly stress the current uncertainties regarding the region where the HE and VHE emission are produced in these compact sources. This work has tried to shed some light on this debate focusing on a core model with a magnetically dominated environment surrounding the BH, but a definite answer to this question should be given by much higher resolution and sensitivity observations which may be achieved in near future with the forthcoming Cherenkov Telescope Array (CTA; Actis et al. 2011; Acharya et al. 2013; Sol et al. 2013).

We should also stress that there are two possible interpretations for the lack of clear evidence of detectable TeV emission in Cyg X-1 and Cyg X-3. On one hand, there may be a strong absorption of these photons by the UV radiation of the companion star (through the photon–photon process). On the other hand, the lack of emission may be due to the limited time of observation (Sahakyan et al. 2013). In our model, we verified that neutral pion decays due to $p\gamma$ interactions at the emission region close enough to the central BH, near the jet basis, could produce TeV gamma-rays. Because of the high magnetic field near the BH, a large density synchrotron radiation field produced there could be a target photon field for the photomeson production. These results predict that a long enough observation time and higher sensitivity would allow us to capture substantial TeV γ-ray emission from these μQSOs. This may be also probed by the CTA.

A final remark is in order. To derive the SEDs of the sources investigated here, we have assumed a nearly steady-state accelerated particle energy distribution at the emission zone. This assumption is valid as long as acceleration by fast magnetic reconnection is sustained in the inner disc region, or in other words, as long as a large enough disc accretion rate is sustained in order to approach the magnetic field lines rising from the accretion disc to those anchored into the BH. In μQSOs, this should last no longer than the time the system remains in the outburst state, normally ranging from less than one day to several weeks.

ACKNOWLEDGEMENTS

This work has been partially supported by grants from the Brazilian agencies FAPESP (2006/50654-3, and 2011/53275-4), CNPq (306598/2009-4) and CAPES. The authors are also indebted to Helene Sol for her useful comments on this work. EMGDP particularly thanks her kind hospitality during her visit to the Observatoire de Paris-Meudon.

REFERENCES

Acharya B. S. et al., 2013, Astropart. Phys., 43, 3
Actis M. et al., 2011, Exp. Astron., 32, 193
Aharonian F. A., Atoyan A. M., 2000, A&A, 362, 937
Albert J. et al., 2007, ApJ, 665, L51
Aleksić J. et al., 2010, ApJ, 721, 843
Atoyan A. M., Dermer C. D., 2003, ApJ, 586, 79
Atwood W. B. et al., 2009, ApJ, 697, 1071
Bednarek W., 2010, MNRAS, 406, 689
Berezinskii V. S., 1990, Astrophysics of Cosmic Rays. North-Holland, Amsterdam
Biskamp D., Schwarz E., Drake J. F., 1997, Phys. Plasmas, 4, 1002
Blumenthal G. M., Gould R. J., 1970, Rev. Mod. Phys., 42, 237
Bodaghee A., Tomsick J. A., Pottschmidt K., Rodriguez J., Wilms J., Pooley G. G., 2013, ApJ, 775, 98
Bosch-Ramon V., Romero G. E., Paredes J. M., 2005a, A&A, 429, 267
Bosch-Ramon V., Aharonian F. A., Paredes J. M., 2005b, A&A, 432, 609
Bosch-Ramon V., Khangulyan D., Aharonian F. A., 2008, A&A, 489, L21
Bulgarelli A. et al., 2010, Astronomer's Telegram, 2512
Čemeljić M., Shang H., Chiang T. Y., 2013, ApJ, 768, 5
Cerutti B., Dubus G., Malzac J., Szostek A., Belmont R., Zdziarski A. A., Henri G., 2011, A&A, 529, A120
Cerutti B., Werner G. R., Uzdensky D. A., Begelman M. C., 2013, ApJ, 770, 147
Cerutti B., Werner G. R., Uzdensky D. A., Begelman M. C., 2014, ApJ, 782, 104
Cherepashchuk A., Moffat A., 1994, ApJ, 424, 53
Cho J., Lazarian A., 2014, ApJ, 780, 30
de Gouveia Dal Pino E. M., Kowal G., 2015, in Lazarian A., de Gouveia Dal Pino E. M., Melioli C., eds, Astrophysics and Space Science Library, Vol. 407, Magnetic Fields in Diffuse Media. Springer-Verlag, Berlin, p. 373
de Gouveia Dal Pino E. M., Lazarian A., 2005, A&A, 441, 845 (GL05)
de Gouveia Dal Pino E. M., Piovezan P. P., Kadowaki L. H. S., 2010, A&A, 518, A5 (GPK10)
de Gouveia Dal Pino E. M., Kowal G., Lazarian A., 2014, in Nikolai V., Pogorelov E. A., Gary P. Z., eds, ASP Conf. Ser. Vol. 488, 8th International Conference of Numerical Modeling of Space Plasma Flows (ASTRONUM 2013). Astron. Soc. Pac., San Francisco, p. 8
del Valle M. V., Romero G. E., Luque-Escamilla P. L., Martí J., Ramón Sánchez-Sutil J., 2011, ApJ, 738, 115
del Valle M. V., Romero G. E., de Gouveia Dal Pino E. M., Kowal G., 2015, submitted
Deng X. H., Matsumoto H., 2001, Nature, 410, 557
Dexter J., McKinney J. C., Markoff S., Tchekhovskoy A., 2014, MNRAS, 440, 218
Di Salvo T., Done C., Zycki P. T., Burderi L., Robba N. R., 2001, ApJ, 547, 1024
Drake J. F., Swisdak M., Che H., Shay M. A., 2006, Nature, 443, 553
Drake J. F., Opher M., Swisdak M., Chamoun J. N., 2010, ApJ, 709, 963
Drury L., 2012, MNRAS, 422, 2474
Dubus G., 2006, A&A, 451, 9
Eyink G. L., Lazarian A., Vishniac E. T., 2011, ApJ, 743, 51
Fender R. P., Pooley G. G., Durouchoux P., Tilanus R. P. J., Brocksopp C., 2000, MNRAS, 312, 853
Gaisser T. K., 1990, Cosmic Rays and Particle Physics. Cambridge Univ. Press, Cambridge
Giacalone J., 1998, Space Sci. Rev., 83, 351
Giacalone J., Jokipii J. R., 1999, ApJ, 520, 204
Giacalone J., Jokipii J. R., 2006, J. Phys. Conf. Ser., 47, 160
Giannios D., 2010, MNRAS, 408, L46
Gies D. R., Bolton C. T., 1986, ApJ, 304, 371
Gies D. R. et al., 2008, ApJ, 678, 1237
Ginzburg V. L., Syrovatskii S. I., 1995, ARA&A, 3, 297
Gordovskyy M., Browning P. K., 2011, ApJ, 729, 101
Gordovskyy M., Browning P. K., Vekstein G. E., 2010, ApJ, 720, 1603
Gould R. J., Schreder G. P., 1967, Phys. Rev., 155, 1404
Hjellming R. M., Rupen M. P., 1995, Nature, 375, 464
Huang C. Y., Wu Q., Wang D. X., 2014, MNRAS, 440, 965
Igumenshchev I. V., 2009, ApJ, 702, L72
Jokipii J. R., 1987, ApJ, 313, 842
Jokipii J. R., Giacalone J., 2007, ApJ, 660, 336
Jourdain E., Roques J. P., Chauvin M., Clark D. J., 2012, ApJ, 761, 21
Kadowaki L. H. S., de Gouveia Dal Pino E. M., Singh C. B., 2015, ApJ, preprint (arXiv:1410.3454) (KGS15)

Kelner S. R., Aharonian F. A., Bugayov V. V., 2006, Phys. Rev. D, 74, 034018

Kelner S. R., Aharonian F. A., Bugayov V. V., 2009, Phys. Rev. D, 79, 039901

Kotera K., Olinto A. V., 2011, ARA&A, 49, 119

Kowal G., Lazarian A., Vishniac E. T., Otmianowska-Mazur K., 2009, ApJ, 700, 63

Kowal G., de Gouveia Dal Pino E. M., Lazarian A., 2011, ApJ, 735, 102

Kowal G., de Gouveia Dal Pino E. M., Lazarian A., 2012, Phys. Rev. Lett., 108, 241102

Laurent P., Rodriguez J., Wilms J., Cadolle Bel M., Pottschmidt K., Grinberg V., 2011, Science, 332, 438

Lazarian A., Desiati P., 2010, ApJ, 722, 188

Lazarian A., Opher M., 2009, ApJ, 703, 8

Lazarian A., Vishniac E. T., 1999, ApJ, 517, 700 (LV99)

Lazarian A., Yan H., 2014, ApJ, 784, 38

Lazarian A., Vlahos L., Kowal G., Yan H., Beresnyak A., de Gouveia Dal Pino E. M., 2012, Space Sci. Rev., 173, 557

Leão M. R. M., de Gouveia Dal Pino E. M., Santos-Lima R., Lazarian A., 2013, ApJ, 777, 46

Lin R. P., Hudson H. S., 1971, Sol. Phys., 17, 412

Ling Z., Zhang S. N., Tang S., 2009, ApJ, 695, 1111

Liu B. F., Mineshige S., Ohsuga K., 2003, ApJ, 587, 571

Lorentz E., 2004, New Astron. Rev., 48, 339

Loureiro N. F., Schekochihin A. A., Cowley S. C., 2007, Phys. Plasmas, 14, 100703

Lyubarsky Y., Liverts M., 2008, ApJ, 682, 1436

McConnell M. L. et al., 2000, ApJ, 543, 928

McConnell M. L. et al., 2002, ApJ, 572, 984

McKinney J. C., Tchekhovskoy A., Blandford R. D., 2012, MNRAS, 423, 3083

Malyshev D., Zdziarski A., Chernyakova M., 2013, MNRAS, 434, 2380

Malzac J. et al., 2006, A&A, 448, 1125

Merloni A., Heinz S., di Matteo T., 2003, MNRAS, 345, 1057

Mirabel I. F., Rodriquez L. F., 1994, Nature, 371, 46

Mirabel I. F., Claret A., Cesarsky C. J., Boulade O., Cesarsky D. A., 1996, A&A, 315, L113

Neronov A., Aharonian F. A., 2007, ApJ, 671, 85

Oka M., Phan T. D., Krucker S., Fujimoto M., Shinohara I., 2010, ApJ, 714, 915

Orosz A., 2011, ApJ, 742, 84

Parker E. N., 1979, Cosmical Magnetic Fields: Their Origin and Their Activity, Vol. 1. Clarendon Press, Oxford/Oxford University Press, New York, p. 858

Persi P., Ferrari-Toniolo M., Grasdalen G. L., Spada G., 1980, A&A, 92, 238

Piano G. et al., 2012, A&A, 545, A110

Priest E. R., 2001, Earth Planets Space, 53, 483

Reid M. J., McClintock J. E., Narayan R., Gou L., Remillard R. A., Orosz J. A., 2011, ApJ, 742, 83

Remillard R. A., McClintock J. E., 2006, ARA&A, 44, 49

Retinò A., Sundkvist D., Vaivads A., Mozer F., André M., Owen C. J., 2007, Nature Phys., 3, 236

Reynoso M. M., Medina M. C., Romero G. E., 2011, A&A, 531, A30

Romanova M. M., Ustyugova G. V., Koldoba A. V., Lovelace R. V. E., 2002, ApJ, 578, 420

Romanova M. M., Ustyugova G. V., Koldoba A. V., Lovelace R. V. E., 2011, MNRAS, 416, 416

Romero G. E., Torres D. F., Kaufman Bernardo M. M., Mirable I. F., 2003, A&A, 410, L1

Romero G. E., Christiansen H. R., Orellana M., 2005, ApJ, 632, 1093

Romero G. E., del Valle M. V., Orellana M., 2010a, A&A, 518, A12

Romero G. E., Vieyro F. L., Vila G. S., 2010b, A&A, 519, A109

Romero G. E., Vieyro F. L., Chaty S., 2014, A&A, 562, 7

Sabatini S. et al., 2010a, ApJ, 712, L10

Sabatini S. et al., 2010b, Astronomer's Telegram, 2715

Sabatini S. et al., 2013, ApJ, 766, 83

Sahakyan N., Piano G., Tavani M., 2013, ApJ, 780, 29

Santos-Lima R., Lazarian A., de Gouveia Dal Pino E. M., Cho J., 2010, ApJ, 714, 442

Santos-Lima R., de Gouveia Dal Pino E. M., Lazarian A., 2012, ApJ, 747, 21

Santos-Lima R., de Gouveia Dal Pino E. M., Lazarian A., 2013, MNRAS, 429, 3371

Schmutz W., Geballe T. R., Schild H., 1996, A&A, 311, L25

Shay M. A., Drake J. F., Denton R. E., Biskamp D., 1998, J. Geophys. Res., 103, 9165

Shay M. A., Drake J. F., Swisdak M., Rogers B. N., 2004, Phys. Plasmas, 11, 2199

Shibata K., Tanuma S., 2001, Earth Planets Space, 53, 473

Sierpowska-Bartosik A., Torres D. F., 2008, Astropart. Phys., 30, 239

Singh C. B., de Gouveia Dal Pino E. M., Kadowaki L. H. S., 2015, ApJ, 799, L20 (SGK15)

Sironi L., Spitkovsky A., 2014, ApJ, 783, 21

Soker N., 2010, ApJ, 721, L189

Sol H. et al., 2013, Astropart. Phys., 43, 215

Somov B. V., 2012, Astrophysics and Space Science Library, Vol. 391, Plasma Astrophysics, Part I: Fundamentals and Practice. Springer, Berlin

Spitzer L., 1962, Physics of Fully Ionized Gases, 2nd edn. Interscience, New York

Spruit H. C., 1988, A&A, 194, 319

Stecker F. W., 1968, Phys. Rev. Lett., 21, 1016

Su Y., Veronig A. M., Holman G. D., Dennis B. R., Wang T., Temmer M., Gan W., 2013, Nature Phys., 9, 489

Tavani M. et al., 2009, A&A, 502, 99

Tchekhovskoy A., Narayan R., McKinney J. C., 2011, MNRAS, 418, L79

Tingay S. J. et al., 1995, Nature, 374, 141

Uzdensky D. A., 2011, Space Sci. Rev., 160, 45

Uzdensky D. A., Spitkovsky A., 2014, ApJ, 780, 3

van Kerkwijk M. H. et al., 1992, Nature, 355, 703

Vila G. S., Aharonian F. A., 2009, in Romero G. E., Benaglia P., eds, Compact Objects and their Emission, Asociación Argentina de Astronomía, Book Series (Editorial Paideia, La Plata, Argentina), p. 1

Xu S., Yan H., 2013, ApJ, 779, 140

Yamada M., Kulsrud R., Ji H., 2010, Rev. Mod. Phys., 82, 603

Yamada M., Jongsoo Y., Jonathan J. A., Hantao J., Russell M. K., Clayton E. M., 2014, Nature Commun., 5, 4774

Zanni C., Ferreira J., 2009, A&A, 508, 1117

Zanni C., Ferreira J., 2013, A&A, 550, A99

Zdziarski A. A., Lubinski P., Sikora M., 2012, MNRAS, 423, 663

Zdziarski A. A., Mikolajewska J., Belczynski K., 2013, MNRAS, 429, L104

Zdziarski A. A., Stawarz L., Pjanka H. C., Bhatt P., Sikora M., 2014, MNRAS, 440, 2238

Zenitani S., Hoshino M., 2001, ApJ, 562, L63

Zenitani S., Hesse M., Klimas A., 2009, ApJ, 696, 1385

Zhang S., 2013, Frontier Phys., 8, 630

Zhang B., Yan H., 2011, ApJ, 726, 90

Zhang L., Chen S. B., Fang J., 2008, ApJ, 676, 1210

Zhang J., Xu B., Lu J., 2014, ApJ, 788, 143

Zharkova V. V. et al., 2011, Space Sci. Rev., 159, 357

Ziolkowski J., 2005, MNRAS, 358, 851

APPENDIX A: PARTICLE ENERGY DISTRIBUTION FUNCTION

The relativistic particles in the core region surrounding the BH may be accelerated up to relativistic energies by a first-order Fermi process occurring within the magnetic reconnection site. The injection and cooling of the accelerated particles occurs mainly in the coronal region around the BH (see Fig. 1). We parametrize the isotropic injection function (in units of $\mathrm{erg}^{-1}\,\mathrm{cm}^{-3}\,\mathrm{s}^{-1}$) as a PL with a high-energy cut-off,

$$Q(E) = Q_0 E^{-p} \exp[-E/E_0] \tag{A1}$$

with $p > 0$ and E_0 is the cut-off energy. The normalization constant Q_0 is calculated from the total power injected in each type of particle

$$L_{(\mathrm{e,p})} = \int_{V_{\mathrm{vol}}} \mathrm{d}^3 r \int_{E^{\mathrm{min}}}^{E^{\mathrm{max}}} \mathrm{d}E\; E\; Q_{(\mathrm{e,p})}(E) \tag{A2}$$

where $L_{(\mathrm{e,\,p})}$ is the fraction of the magnetic reconnection power that accelerates the electrons and protons (see equation 1 in the text). The injection particle spectrum is modified in the emission region due to energy losses. We assume that the minimum energy of the particles is given by mc^2, where m is the rest mass of the particle[8] and the maximum energy that the primary particles can attain is fixed by the balance of acceleration and the energy losses. Particles can gain energy up to a certain value E_{max} for which the total cooling rate equals the acceleration rate.

The kinetic equation that describes the general evolution of the particle energy distribution $N(E, t)$ is the Fokker–Planck differential equation (Ginzburg & Syrovatskii 1995). We here use a simplified form of this equation. We employ the one-zone approximation to find the particle distribution, assuming that the acceleration region is spatially thin enough, so that we can ignore spatial derivatives in the transport equation. Physically, this means that we are neglecting the contributions to $N(E)$ coming from other regions than the magnetic reconnection region in the inner accretion disc zone in the surrounds of the BH. We consider a steady-state particle distribution which can be obtained by setting $\frac{\partial N}{\partial t} = 0$ in the Fokker–Planck differential equation, so that the particle distribution equation is

$$N(E) = \left|\frac{\mathrm{d}E}{\mathrm{d}t}\right|^{-1} \int_E^{\infty} Q(E)\,\mathrm{d}E. \tag{A3}$$

Here $-\frac{\mathrm{d}E}{\mathrm{d}t} \equiv E t_{\mathrm{cool}}^{-1}$. It is very interesting to note that if the energy losses are proportional to the particle energy ($\frac{\mathrm{d}E}{\mathrm{d}t} \propto E$), $N(E)$ does not change the injection spectrum and $N(E) \propto E^{-p}$, as in the *pp* inelastic collisions or bremsstrahlung cool processes. In such loss mechanisms like synchrotron and IC scattering, in the Thomson regime, the $N(E)$ is steeper because in these cases $\frac{\mathrm{d}E}{\mathrm{d}t} \propto E^2$ and $N(E) \propto E^{-(p+1)}$.

The spectrum would be harder if $\mathrm{d}E/\mathrm{d}t$ were constant as for ionization losses, $N(E) \propto E^{-(p-1)}$. In the case of IC scattering in the Klein–Nishina limit, $\frac{\mathrm{d}E}{\mathrm{d}t} \propto E^{-1}$ and so, the spectrum is even harder and $N(E) \propto E^{-(p-2)}$.

This paper has been typeset from a TEX/LATEX file prepared by the author.

---

[8] We note that the calculation of the emitted flux is little affected by the choice of the minimum energy of the particle spectrum.

Appendix C

Particle Acceleration and gamma-ray emission due to magnetic reconnection around the core region of radio galaxies

Astronomy & Astrophysics manuscript no. manuscript
September 19, 2015

©ESO 2015

Particle Acceleration and gamma-ray emission due to magnetic reconnection around the core region of radio galaxies

B. Khiali[1], E. M. de Gouveia Dal Pino[1], and H. Sol[2]

[1] IAG-Universidade de São Paulo, Rua do Matão 1226, São Paulo, SP, Brazil
e-mail: `bkhiali@usp.br`
[2] LUTH, Observatoire de Paris, CNRS, Universite Paris Diderot, 5 Place Jules Janssen, 92190 Meudon, France

Received September ??, 2015; accepted ??? ??, ????

ABSTRACT

Context. The current detectors of gamma-ray emission specially at TeV energies have too poor resolution to determine whether this emission is produced in the jet or in the core, particularly of low luminous, non-blazar AGNs (like radio galaxies). In recent works it has been found that the power released by events of turbulent fast magnetic reconnection in the core region of these sources is more than sufficient to reproduce the observed gamma-ray luminosities. Besides, 3D MHD simulations with test particles have demonstrated that a first-order Fermi process within reconnection sites with embedded turbulence results very efficient particle acceleration rates.
Aims. We computed here the spectral energy distribution (SED) from radio to gamma-rays of the radio galaxies for which energy emission up to TeVs has been detected (namely, M87, Cen A, Per A, and IC 310).
Methods. For this aim, we employed the acceleration model above and considered all the relevant leptonic and hadronic loss processes around the core region of the sources.
Results. We found that the calculated SEDs match very well specially with the VHE observations, therefore strengthening the conclusions above in favour of a core emission origin for the VHE emission of these sources. The model also naturally explains the observed very fast variability of the VHE emission.
Conclusions.

Key words. Magnetic reconnection – particle acceleration – radiation mechanisms: non-thermal

1. Introduction

The non-thermal multi wavelength emission from active galactic nuclei (AGNs) has been broadly studied. Regarding the very high energy (VHE) emission, until recently only AGNs with highly beamed jets towards the line of sight, namely blazars, were detected by gamma-ray telescopes. More than a chance coincidence, these detections are consistent with the conventional scenario that attributes the VHE emission of these sources to particle acceleration along the jet being strongly Doppler boosted and producing apparently very high fluxes.

Lately, however, a few non-blazar sources which belong to the branch of low luminosity AGNs (or simply LLAGNs) for having bolometric luminosities of only a few times the Eddington luminosity, L_{Edd} (Ho et al. 1997; Nagar et al. 2005) have been also detected at TeV energies by ground based γ-ray observatories (e.g., Sol et al. 2013 and references therein). The angular resolution and sensitivity of these detectors are still so poor that it is hard to establish exactly the location of the emission, i.e. whether it comes from the jet or the core (e.g., Kachelriess et al. 2010).

Among these sources, the radio galaxies M87, Centaurus A (Cen A or NGC 5128), Persus A (Per A or NGC 1275) and IC 310 are probably the most striking cases. These VHE detections were surprising because, besides being highly underluminous, the viewing angle of the jets of these sources is of several degrees, therefore allowing for only moderate Doppler boosting. These characteristics make it difficult explaining the VHE of these sources adopting the same standard scenario of blazars.

Furthermore, observations by *MAGIC*, *HESS* and *VERITAS* of short time scale variability in the γ-ray emission of IC 310, M87 and Per A (Aharonian et al. 2006; Abdo et al. 2009a; Ackermann et al. 2012; Aleksić et al. 2010a,b, 2012a,b, 2014a,c) indicate that it is produced in a very compact region that might be the core. In the case of Cen A, though there is no evidence of significant variability at $E >$100MeV, GeV or TeV bands by *Fermi-LAT*(Abdo et al. 2010) or *HESS* (Aharonian et al. 2009), it has been also argued that the $HESS$ data of this source would be more compatible with a point source near the core (Kachelriess et al. 2010). If the $\gamma-ray$ photons were due, for instance, to proton-proton (pp) interactions along the jet then on leaving the source they would interact with the extragalactic background light (EBL) resulting in a flatter spectrum in the TeV range which is not compatible with *HESS* measurements (Kachelriess et al. 2009b, see however, other potential explanations in §. 5).

Though a number of works have attempted to explain these observations as produced in the large scale jets of these sources (e.g., Stawarz et al. 2006), the evidences above led to the search for alternative particle acceleration scenarios involving the production of the VHE in the surrounds of the nuclear black hole (BH), for instance, in a pulsar-like cascade mechanism in the BH magnetosphere (e.g., Neronov & Aharonian 2007), or in the sub-parsec scale jet (e.g., Tavecchio & Ghisellini 2008; Abdo et al. 2009b). In particular, Tavecchio & Ghisellini (2008), invoked a two zone model with a jet with a fast spine and a slower layer to explain the TeV flares, while Lenain et al. (2008) proposed that the emission would occur while the jet is collimating, and Georganopoulos et al. (2005) while it is decelerating. Another process to explain these VHE flares has been proposed by Giannios et al. (2010) in which misaligned mini-jets driven by magnetic reconnection are moving within the jet with relativistic velocities relative to it. A two-step acceleration model to TeV energies was also proposed by Istomin & Sol (2009) in the surrounds of the BH involving initial particle acceleration within the accretion disk and then further centrifugal acceleration in the rotating magnetosphere.

In this work, we consider an alternative model in which particles are accelerated, through a first-order Fermi process, in the surrounds of the BH by the magnetic power extracted from fast magnetic reconnection events occurring between the magnetosphere of the BH and the magnetic field lines arising from the inner accretion disk (see Figure 1). Inspired by similar phenomena occurring in space environments, like the earth magnetotail and the solar corona, de Gouveia Dal Pino & Lazarian (2005) explored this process first in the framework of microquasars and then de Gouveia Dal Pino et al. (2010a) and de Gouveia Dal Pino et al. (2010b) extended it to AGNs.

In these works, de Gouveia Dal Pino & Lazarian (2005) and de Gouveia Dal Pino et al. (2010a) found that fast reconnection could be efficient enough to produce the core radio outbursts in microquasars and AGNs. More recently, Kadowaki et al. (2015) (henceforth KGS15) and Singh et al. (2015) revisited this model exploring different mechanisms of fast magnetic reconnection and accretion, and extending the study to include also the gamma-ray emission of a much larger sample containing more than 230 sources. They confirmed the earlier trend found by de Gouveia Dal Pino & Lazarian (2005) and de Gouveia Dal Pino et al. (2010a), and verified that if fast reconnection is driven by turbulence (Lazarian & Vishniac 1999) there is a correlation between the fast magnetic reconnection power and the BH mass spanning 10^{10} orders of magnitude that can explain not only the observed radio, but also the VHE luminosity from microquasars and LLAGNs (involving all the sources of the so called fundamental plane of BH activity Merloni et al. 2003).

The correlations found in the works above (specially in KGS15 and Singh et al. 2015) between the calculated power released by magnetic reconnection in the surrounds of the BH and the observed radio and gamma-ray luminosities of a very large sample of LLAGNs and microquasars, have motivated further investigation to test the validity of the model. In particular, in a recent work, we explored in detail the non-thermal emission of the microquasars Cygnus X-1 and Cygnus X-3 and found that this reconnection acceleration model is able to reproduce most of the features of their observed spectral energy distribution (SED) in outburst states up to TeV energies (Khiali et al. 2015 hereafter KGV15).

Our aim here is to extend this study to the supermassive BH sources of the KGS15 and Singh et al. (2015) sample, trying to reconstruct the observed SEDs, specially at the VHE branch, of the four radio galaxies mentioned earlier, i.e., Centaurus A, Per A, M87 and IC 310 applying the same acceleration model above.

We first compute the power released by fast magnetic reconnection in the surrounds of the BH as described, and then the resulting particle spectrum of the accelerated particles in the magnetic reconnection site. In particular, we explore the first-order Fermi acceleration process that may occur within the current sheet as proposed in de Gouveia Dal Pino & Lazarian (2005). Such acceleration mechanism has been extensively tested numerically in 3D collisional MHD simulations of magnetic current sheets employing test particles (Kowal et al. 2011, 2012; de Gouveia Dal Pino et al. 2014) and also in collisionless particle in cell simulations (e.g., Drake et al. 2006; Zenitani et al. 2009; Drake et al. 2010; Cerutti et al. 2013, 2014; see also the reviews by de Gouveia Dal Pino et al. 2014; de Gouveia Dal Pino & Kowal 2015).

In order to reconstruct the SED, we consider the relevant radiative processes due to the interactions of the accelerated particles by magnetic reconnection with the surrounding radiation, matter and magnetic fields. We then compare the rates of these radiative losses with the magnetic reconnection acceleration rate and determine the maximum energy that the electrons and protons can attain. For comparison, we also consider the acceleration rate due to shocks in the surrounds of the reconnection region, but find that this is less effective than the acceleration by magnetic reconnection.

We show for the first time that a consistent and numerically tested acceleration model by magnetic reconnection in the surrounds of BH sources can effectively reproduce the observed SEDs of the four radio galaxies up to TeVs.

The outline of the paper is as follows. In Section 2, we describe in detail our scenario presenting both the acceleration model and the emission mechanisms. In section 3, we show the results of the application of the acceleration and emission model to Cen A, Per A, M87 and IC 310. Finally, we discuss and summarize our results drawing our conclusions in Section 4.

2. Description of the acceleration and emission model

As stressed, we consider here that relativistic particles may be accelerated in the core of LLAGNs, i.e., in the coronal region around the BH near the basis of the jet launching, as a result of events of fast magnetic reconnection and examine whether this process may reproduce the observed emission specially at VHEs. This model has been described in detail by de Gouveia Dal Pino & Lazarian (2005) and de Gouveia Dal Pino et al. (2010a), and more recently by KGS15. We summarize below its main characteristics. We assume that the inner region of the accretion disk/corona system alternates between two states which are controlled by changes in the global magnetic field. Right before a fast magnetic reconnection event, we adopt the simplest possible configuration by considering a magnetized standard geometrically thin and optically thick accretion disk around the BH as in the sketch of Figure 1 (see also Singh et al. 2015 for an alternative solution considering a magnetic-ADAF accretion disk).

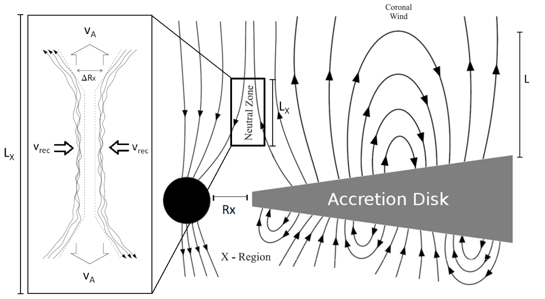

Fig. 1. Scheme of magnetic reconnection between the lines rising from the accretion disk into the corona and the lines around the BH horizon. Reconnection is made fast by the presence of embedded turbulence in the reconnection zone (as indicated in the detail). Particle acceleration may occur in the magnetic reconnection zone by a first-order Fermi process (adapted from de Gouveia Dal Pino & Lazarian 2005).

The magnetosphere around the central BH can be built from the drag of magnetic field lines by the accretion disk (e.g., MacDonald et al. 1986; Koide et al. 2002). The large-scale poloidal magnetic field in the disk corona can in turn be formed by the action of a dynamo inside the accretion disk or dragged from the surroundings. Under the action of disk differential rotation, this poloidal magnetic flux gives rise to a wind that partially removes angular momentum from the system and increases the accretion rate. This, in turn, increases the ram pressure of the accreting material that will press the magnetic lines in the inner disk region against the lines of the BH magnetosphere thus favouring the occurrence of reconnection (see Figure 1). We note that according to mean field dynamo theory, an inversion of the polarization of the magnetic lines is expected to occur every half of the dynamo cycle; when this happens a new flux of disk lines should reach the inner region with an inverted polarity with respect to the magnetic flux already sitting around the BH, therefore, favouring magnetic reconnection between the two fluxes. The advection of field lines from the outer regions also allows for periodic changes in the polarity. Also for simplicity, we assume the co-rotation between the inner disk region and the BH magnetosphere.

The magnetic field intensity in this inner region can be determined from the balance between the magnetic pressure of the BH magnetosphere and the accretion ram pressure and is given by (KGL15):

$$B \cong 9.96 \times 10^8 r_X^{-1.25} \xi^{0.5} m^{-0.5} \text{ G}, \tag{1}$$

where m is the BH mass in units of solar mass, ξ is the mass accretion disk rate in units of the Eddington rate ($\xi = \dot{M}/\dot{M}_{Edd}$, with $\dot{M}_{Edd} = 1.45 \times 10^{18} m$ g s^{-1}), and $r_X = R_X/R_S$ is the inner radius of the accretion disk in units of the BH Schwarzchild radius ($R_S = \frac{2GM}{c^2}$). As KGS15, we adopt here $r_X = 6$.

2.1. Conditions for fast reconnection in the surrounds of the BH

As discussed in KGS15, the presence of embedded turbulence in the nearly collisional MHD coronal flow of the core region of the AGNs can make reconnection very fast (e.g., Lazarian & Vishniac 1999) and cause the release of large amounts of magnetic energy power in the scenario described in Figure 1. [1]

According to the model proposed by Lazarian & Vishniac (1999), even weak embedded turbulence causes the wandering of the magnetic field lines which allows for many independent patches to reconnect simultaneously making the global reconnection rate large, $V_R \sim v_A (l_{inj}/L)^{1/2} (v_{turb}/v_A)^2$, where V_R is the reconnection speed, v_A is the Alfvén speed, and l_{inj} and v_{turb} the injection scale and velocity of the turbulence, respectively. This expression indicates that the reconnection rate can be as large as $\sim V_A$.

This theory has been deeply investigated (e.g. Eyink et al. 2011; Lazarian et al. 2012) and confirmed numerically (Kowal et al. 2009, 2012). In particular, it has been shown (Eyink et al. 2011) that turbulent collisional fast reconnection prevails when the thickness of the magnetic discontinuity layer (see Eq. 3 below, and Figure 1) is larger than the ion Larmor radius. As demonstrated in KGS15, for the systems we are studying this condition is naturally satisfied and we will adopt this process to derive the magnetic power released by fast reconnection. We should also notice that there has been direct evidences of turbulent reconnection in solar coronal events (e.g., Priest 2001) and also in the Earth magnetotail (Retinò et al. 2007).

The fluids we are investigating here have large hydrodynamical and magnetic Reynolds numbers (KGS15) implying that they can be easily distorted and become turbulent. For instance, current driven instabilities, can naturally drive turbulence with characteristic velocities around the particles thermal speed. Also, the occurrence of continuous slow magnetic reconnection during the building of the corona itself in the surrounds of the BH (Liu et al. 2003) will contribute to the onset of turbulence which will then be further fed by fast reconnection as in the Lazarian & Vishniac (1999) model (see Oishi et al. 2015; Lazarian et al. 2015). Numerical simulations of coronal disk accretion also indicate the formation of turbulent flow in the surrounds of the BH (see e.g, Dexter et al. 2014). All these processes may ensure the presence of embedded weak turbulence in the magnetic discontinuity described in Figure 1. [2]

The magnetic reconnection power released by turbulent driven fast reconnection in the magnetic discontinuity region (as schemed in Figure 1), has been derived in KGS15 and is given by:

---

[1] We note that the strongly magnetized and low dense coronal fluid of the systems we are considering in this work satisfies the condition $L > l_{mfp} > r_l$ (where L is a typical large scale dimension of the system, l_{mfp} the ion mean free path and r_l the ion Larmor radius). For such flows a weakly collisional or effectively collisional MHD description is more than appropriate and we will employ this approach here (see more details in KGS15).

[2] We note that in the model described here, the turbulence is in general sub-Alfvénic due to the strong magnetic fields implied and nearly tran-sonic (since the turbulent velocity is of the order of the sound speed and smaller than the Alfvén speed) and therefore, incompressible. This regime of turbulence has been extensively investigated in the literature (see e.g., Lazarian & Vishniac 1999; Lazarian et al. 2012) and the acceleration formulae employed here have been obtained directly from numerical MHD simulations with particle tests injected in current sheets with embedded turbulence also implying this regime (Kowal, de Gouveia Dal Pino, Lazarian 2012).

$$W \simeq 1.66 \times 10^{35} \psi^{-0.5} r_X^{-0.62} l^{-0.25} l_X q^{-2} \xi^{0.75} m \ \text{erg s}^{-1}, \quad (2)$$

where $l = L/R_S$ is the height of the corona in units of R_S; $l_X = L_X/R_S$, $L_X \leq L$ is the extension of the magnetic reconnection zone (as shown in Figure 1; see also Table 1), $q = [1-(3/r_X)^{0.5}]^{0.25}$ and $v_A = v_{A0}\psi$ is the relativistic form of the Alfvén velocity, with $v_{A0} = B/(4\pi\rho)^{1/2}$, B being the local magnetic field, $\rho \simeq n_c m_p$ the fluid density in the corona, n_c the coronal number density, m_p the proton mass, and $\psi = [1 + (\frac{v_{A0}}{c})^2]^{-1/2}$, in this work, $v_{A0} \sim c$. The results of KGS15 (Figure 5 in KGS15) have shown that accretion rates ξ between $0.05 < \xi \leq 1$ are able to produce magnetic reconnection power values which are larger than the observed luminosities of LLAGNs. We adopt here $\xi \simeq 0.7$, but we should notice that the results are not very much sensitive to the choice of this parameter. As demonstrated in KGS15 and SKG15 studies, one can match the observations by taking alternative fiducial combinations of the free parameters in the equation above, particularly by constraining the size of the height of the corona, L.

We will employ the equations above in Section 3 to model the acceleration of particles in the core of Cen A, Per A, M87 and IC 310. The acceleration region in our model corresponds to the cylindrical shell around the BH where magnetic reconnection takes place (see Figure 1). This shell has a length l_X, with inner and outer radii given by R_X and $R_X + \Delta R_X$ respectively, where ΔR_X is the width of the current sheet given by (KGS15):

$$\Delta R_X \cong 2.34 \times 10^4 \psi^{-0.31} r_X^{0.48} l^{-0.15} l_X q^{-0.75} \xi^{-0.15} m \ \text{cm}. \quad (3)$$

In §. 3, we will also need the accretion disk temperature in order to evaluate the black body radiation field:

$$T_d \cong 3.71 \times 10^7 \alpha^{-0.25} r_X^{-0.37} m^{0.25} \ \text{K}, \quad (4)$$

where $0.05 \leq \alpha < 1$ is the Shakura-Sunyaev disk viscosity parameter which we here assume to be of the order of 0.5.

In addition, we will need the coronal number density to compute the radiative losses of accelerated particles which is (KGS15)

$$n_c \cong 8.02 \times 10^{18} r_X^{-0.375} \psi^{0.5} l^{-0.75} q^{-2} \xi^{0.25} m^{-1} \ \text{cm}^{-3}, \quad (5)$$

while the coronal temperature is given by

$$T_c \cong 2.73 \times 10^9 r_X^{-0.187} \psi^{0.25} l^{0.125} q^{-1} \xi^{0.125} \ \text{K}. \quad (6)$$

The magnetic power in Eq. 2 heats the surrounding gas and accelerates particles. As in KGV15, we assume that approximately 50% of the reconnection power is used to accelerate the particles. This is consistent with plasma laboratory experiments of particle acceleration in reconnection sheets (e.g., Yamada et al. 2014) and also with the observations of flares in the Sun (e.g., Lin & Hudsun 1971).

2.2. Particle acceleration due to magnetic energy released by fast reconnection

A first-order Fermi acceleration may occur when particles of the fluid are trapped between the two converging magnetic flux tubes moving to each other in the magnetic reconnection discontinuity with a velocity V_R. de Gouveia Dal Pino & Lazarian (2005) first investigated this process analytically and showed that, as the particles bounce back and forth undergoing head-on collisions with magnetic fluctuations in the current sheet, their energy increases by $< \Delta E/E > \sim 8V_R/3c$ after each round trip, which leads to an exponential energy growth after several round trips. If magnetic reconnection is fast, V_R is of the order of the local Alfvén speed V_A and, at the surroundings of relativistic sources $V_R \simeq v_A \simeq c$ and thus the mechanism can be rather efficient.

From the results of 3D MHD numerical simulations of this process (Kowal et al. 2012), we find that the acceleration rate for a proton is given by (KGV15):

$$t_{acc,rec,p}^{-1} = 1.3 \times 10^5 \left(\frac{E}{E_0}\right)^{-0.4} t_0^{-1}, \quad (7)$$

where E is the energy of the accelerated proton, $E_0 = m_p c^2$, m_p is the proton rest mass, $t_0 = l_{acc}/v_A$ is the Alfvén time, and l_{acc} is the length scale of the acceleration region.

Similarly, for the electrons one can get:

$$t_{acc,rec,e}^{-1} = 1.3 \times 10^5 \sqrt{\frac{m_p}{m_e}} \left(\frac{E}{E_0}\right)^{-0.4} t_0^{-1}, \quad (8)$$

where m_e is the electron rest mass.

The two equations above do not take into account the effects of radiative losses upon the accelerated particles. They will be used to compute the acceleration rates in our model.

As stressed in de Gouveia Dal Pino & Lazarian (2005), it is also possible that a diffusive shock may develop in the surrounds of the magnetic reconnection zone at the jet launching region caused by plasmons or coronal mass ejections. As in solar flares, these can be produced in the reconnection layer and released along the magnetic field lines. In this case, we expect the shock velocity to be predominantly parallel to the magnetic lines. and the acceleration rate for a particle of energy E will be approximately given by (e.g., Spruit 1988):

$$t_{acc,shock}^{-1} = \frac{\eta e c B}{E}, \quad (9)$$

where $0 < \eta \ll 1$ characterizes the efficiency of the acceleration. We fix $\eta = 10^{-1}$, which is appropriate for shocks with velocity $v_s \approx 0.1c$ commonly assumed in the Bohm regime.

In §. 3 we compare both the magnetic reconnection acceleration time (Eqs. 7 & 8) and the shock acceleration time (Eq. 9) with the relevant radiative cooling process that cause the loss of energy of the accelerated particles and constrain their maximum energy. These particles may lose energy via interactions with the surrounding magnetic field (producing synchrotron emission), the photon field (producing inverse Compton, synchrotron-self-Compton, and photo-meson interactions), and with the surrounding matter (producing pp collisions and relativistic Bremsstrahlung radiation). In §. 2.4, we discuss the relevant radiative loss processes for electrons and protons which will allow the construction of the SED of the sources M87, Cen A, Per A and IC 310 for comparison with the observations.

2.3. Particle energy distribution

The accelerated particles are expected to develop a power law spectrum. Their injection and cooling will occur mainly in the coronal region around the black hole (see Figure 1). The isotropic injection function (in units of $\mathrm{erg}^{-1}\mathrm{cm}^{-3}\mathrm{s}^{-1}$) is given by (see e.g. KGV15):

$$Q(E) = Q_0 E^{-p} exp[-E/E_{max}] \tag{10}$$

with $p > 0$ and E_{max} the cut-off energy which can be calculated by the balance of acceleration and the energy losses. Particles can gain energy up to a certain value E_{max} for which the total cooling rate equals the acceleration rate.

We assume for the power law index p values between 1 and 2.5 for the sources here investigated (see §. 3), which are compatible with the analytical and numerical studies of particle acceleration within magnetic reconnection sheets (e.g., Drury 2012; Kowal et al. 2012).

The normalization constant Q_0 is calculated from the total power injected in each type of particle

$$L_{(e,p)} = \int_V d^3r \int_{E_{min}}^{E_{max}} dE\ E\ Q_{(e,p)}(E) \tag{11}$$

where V is the emission volume in the surrounds of the magnetic reconnection acceleration region in Figure 1 (see §. 2.5) and $L_{(e,p)}$ is the fraction of the magnetic reconnection power that accelerates the electrons and protons calculated from Eq. 2. This injected power is equally shared between protons and electrons.

The kinetic equation that describes the general evolution of the particle energy distribution $N(E,t)$ is the Fokker-Planck differential equation (Ginzburg & Syrovatskii 1995). We here use a simplified form of this equation. We employ the one-zone approximation to find the particle distribution, assuming that the acceleration region is spatially thin enough, so that we can ignore spatial derivatives in the transport equation. Physically, this means that we are neglecting the contributions to $N(E)$ coming from other regions than the magnetic reconnection region in the inner accretion disk/corona zone in the surrounds of the BH. We consider a steady-state particle distribution which can be obtained by setting $\frac{\partial N}{\partial t} = 0$ in the Fokker-Planck differential equation, so that the particle distribution equation is

$$N(E) = |\frac{dE}{dt}|^{-1} \int_E^{\infty} Q(E) dE. \tag{12}$$

Here $-\frac{dE}{dt} \equiv E t_{cool}^{-1}$, where t_{cool}^{-1} is the total cooling rate that can be calculated assuming all the cooling mechanisms (we describe them in the following section briefly).

2.4. Photon Absorption

We consider two main absorption processes of the photons produced by the accelerated particles in the nuclear region of the sources: the gamma-ray photon absorption due to e^-e^+ pair creation, and the absorption of optical and X-ray photons due to external interstellar neutral gas and dust (photon-neutral) absorption.

2.4.1. Photon-photon ($\gamma\gamma$) annihilation

The produced γ-rays can be annihilated by the surrounding radiation field via electron-positron pair production, i.e., $\gamma + \gamma \rightarrow e^+ + e^-$. In our model the dominant radiation field for this process in the coronal region is due to the scattered photons from the accretion disk (see Figure 2). [3]

To evaluate the optical depth due to this process, we have adopted the model described in Cerutti et al. (2011), assuming that the γ-rays are produced within a spherical region around the disk with radius extending up to $L \simeq 20R_S$. The attenuated $\gamma-$ray luminosity $L_\gamma(E_\gamma)$ at a distance z above the disk is given by (Romero & Christiansen 2005)

$$L_\gamma(E_\gamma) = L_\gamma^0(E_\gamma) e^{-\tau(z,E_\gamma)} \tag{13}$$

where L_γ^0 is the intrinsic coronal gamma-ray luminosity and $\tau(z, E_\gamma)$ is the optical depth. The calculated optical depth depends on the γ-ray energy and the distance above the disk z.

Figure 2 depicts the gamma-ray absorption spectrum for the sources investigated here, for different heights z. We see that in all cases at distances larger than $\sim 0.1R_S$ from the disk surface, the absorption of γ-rays becomes negligible. Since we are adopting here an emission region with an extension $\simeq 0.3R_S$ to $\simeq 20R_S$, it is reasonable to exclude the absorption effect above in our calculations of the SEDs (see §. 3).

2.4.2. Photon-neutral (γN) interactions

The low energy photons produced in the nuclear emission region will propagate in the surrounding interstellar medium of the host galaxy filled mainly by hydrogen and helium gas. Photons with energies larger than the hydrogen Lyman threshold (13.6 eV) will be able to photo-ionize the neutral gas.

The optical depth resulting from these interactions is approximately given by

$$\tau_{\gamma H}(E_\gamma) = N_H \sigma_{\gamma N}(E_\gamma) \tag{14}$$

where N_H is the neutral hydrogen column density, and $\sigma_{\gamma N}$ is the absorption cross section. As in Reynoso et al. 2011, we take this from Ryter (1996) for $E_\gamma < 1$ keV considering that atomic hydrogen and galactic dust are the dominant components of the environment. The values of N_H for each source investigated here are taken from the observations and are listed in Table 1.

This γN absorption has been considered in the reconstruction of the SEDs of the four LLAGNs in §. 3. As we will see there, the photons produced in the optical-soft X-ray range are fully absorbed by these interactions.

2.5. Radiative cooling processes

In this section we discuss briefly the relevant radiative loss processes for electrons and protons.

We take into account both leptonic and hadronic radiative loss mechanisms in the emission region. This corresponds to the torus with volume V that encompasses the

---

[3] We should remark that we found the contribution due to the coronal radiation field itself to be much smaller than that of the accretion disk.

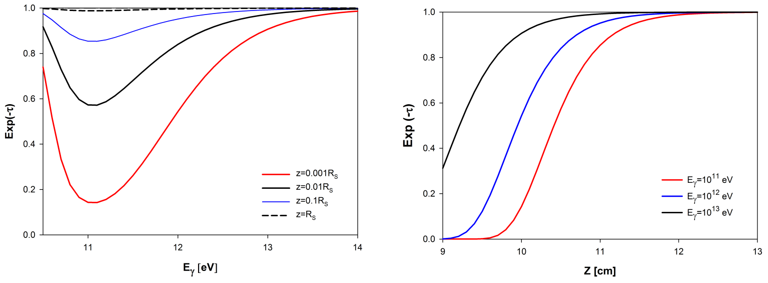

(a) Cen A (b) Cen A

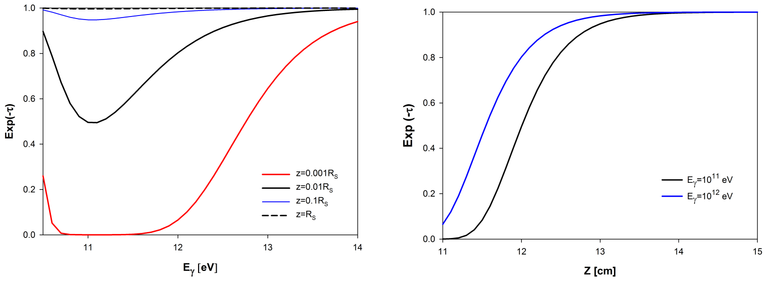

(c) Per A (d) Per A

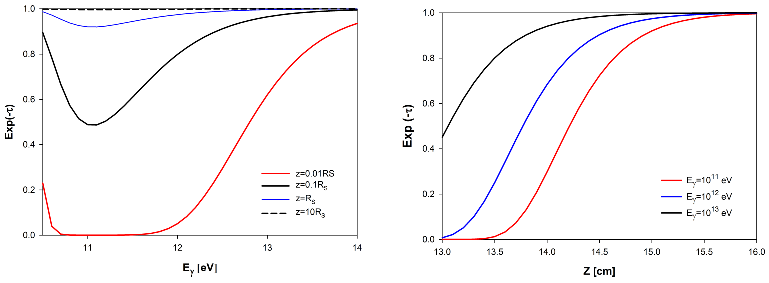

(e) M87 (f) M87

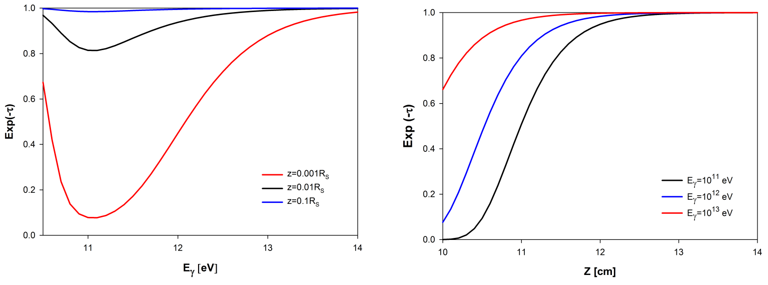

(g) IC 310 (h) IC 310

Fig. 2. Left panels: Spectrum of γ-ray absorption at selected heights z above the plane of the disk in Cen A, Per A, M87, and IC 310 (a, c, e, and g panels, respectively). Rigt panels: The transmitted flux $exp(-\tau)$ for different γ-ray energies as function of the height z above the disk in Cen A, Per A, M87, and IC 310 (b, d, f, and h panels, respectively).

Table 1. Model parameters for Cen A, Per A, M87 and IC 310.

	Parameters	Cen A	Per A	M 87	IC 310
B	Magnetic field (G)	1.25×10^4	4812	1620	8874
W	Magnetic reconnection power (erg/s)	1.2×10^{43}	8.2×10^{43}	5.25×10^{44}	4.5×10^{43}
ΔR_X	Width of the current sheet (cm)	3.6×10^{13}	2.4×10^{14}	1.35×10^{15}	3.2×10^{12}
n_c	Coronal particle number density (cm^{-3})	7.1×10^9	10^9	3.3×10^8	10^{11}
T_d	Temperature of the disk (K)	1.9×10^8	3×10^8	5.2×10^8	2.25×10^8
R_x	Inner radius of disk (cm)	8.8×10^{13}	6×10^{14}	5.3×10^{15}	1.7×10^{14}
L_X	Extension of the reconnection region (cm)	1.5×10^{14}	10^{15}	4.4×10^{15}	8.8×10^{12}
L	Extension of the corona (cm)	3×10^{14}	2×10^{15}	4.4×10^{15}	8.8×10^{12}
V	Volume of emission region (cm^3)	7.8×10^{43}	2.3×10^{46}	10^{48}	1.36×10^{41}
d	Distance of the source(Mpc)	3.8	75	16.7	78
m	Mass of BH ($M_\odot$)	5×10^7	3.4×10^8	3×10^9	10^8
p	Injection spectral index	2.4	2.15	2.4	1.7
γ_{min}	Particle minimum Lorentz factor	6	2	4	2
N_H*	Dust/neutral gas column density (cm^{-2})	10^{23}	4×10^{20}	2×10^{20}	1.2×10^{21}

* The observed values for N_H of Cen A, Per A, M87 and IC310 are taken from Morganti et al. (2008); Canning et al. (2010); Lieu et al. (1996) and Kalberla et al. (2010), respectively.

cylindrical shell where magnetic reconnection particle acceleration takes place in Figure 1. Considering that the cylinder extends up to L in both hemispheres, then the small radius of the torus is $r = L/2$ and the large radius is R_X, so that the effective emission zone in our model has an approximate volume $V = \pi^2 L^2 R_X$.

For leptonic processes, we consider the interactions of relativistic electrons with the surrounding magnetic, charged matter, and photon fields.

Accelerated electrons spiralling in the magnetic field emit synchrotron radiation. We calculate the synchrotron loss rate for the sources considered here and the radiated synchrotron spectrum as functions of the scattered photon energy (see Eqs. 10 and 11 in KGV15). Electron interactions with the electrostatic field of nuclei of charge Ze allow for the production of bremsstrahlung radiation. Finally, relativistic electron interactions with photons may produce inverse Compton (IC) radiation. We considered different photon fields in the surrounds of BH, namely, the scattered photons from accretion disk and core black-body radiation (Eq. 36 in KGV15) and the electron synchrotron emission (which allows for SSC; Eq. 14 in KGV15) and found that the latter, i.e., the SSC mechanism is dominant in the inner coronal/accretion disk region we are interested in this work.

Accelerated protons produce hadronic emission from interactions with the magnetic field (synchrotron), and also through the decay of neutral pions. These are produced either by inelastic collisions with nuclei of the corona (pp interactions; Eqs. 19 & 21 of KGV15), or via interactions with photons, in photo-meson production ($p\gamma$ mechanism; Eqs. 40 & 43 in KGV15). The latter mechanism takes place for photon energies greater than $E_{th} \approx 145$ MeV in the reference frame of the relativistic proton. A single pion can be produced in an interaction near the threshold and then decay giving rise to gamma-rays. In our model the dominating photon field comes from the synchrotron radiation.[4]

The cooling rates due to these leptonic and hadronic mechanisms are plotted as functions of the particle energy for the sources here studied in Figures 3a, 5a, 7a and 9a, and Figures 3b, 5b, 7b and 9b, respectively, where they are also compared with the acceleration rates due to shock and magnetic reconnection.

The radiative losses considered above are used to calculate the SEDs of the sources in §3.

3. application to radio galaxies

We describe here the results of the application of the model described above to Cen A, Per A, M87 and IC 310 which are classified as radio galaxies. As remarked in §. 1, these radio galaxies have been observed at VHE by *FERMI-LAT, VERITAS* and *HESS* (e. g., Abdo et al. 2009c, 2010; Abramowski et al. 2012; Aleksić et al. 2014b).

In general lines, in all cases, the procedure to calculate the SED begins with the determination of the total power released by fast magnetic reconnection within the acceleration region (Eq. 2), that is, in the cylindrical shell of height L_X and thickness ΔR_X (Eq. 3) (see Figure 1). This power is then employed to compute the spectrum of accelerated electrons and protons (Eq. 12) that will be injected into the emission volume V, i.e., the torus that surrounds the acceleration region (as described in §. 2.5). The parameters employed for each source are given in Table 1. We note that our model has actually only 7 free parameters (i.e., R_x, L_X, $L \leq L$, p, γ_{min}, ξ and α). The remaining quantities of Table 1 are obtained directly from these parameters through Eqs. 1 to 5 (i.e, B, W, ΔR_X, n_c and T_d), or from the observations (i.e, d and m). The maximum energy that each particle spectrum can attain is obtained from the comparison of the acceleration rates, for both electrons and protons, with the relevant radiative loss processes (seen §. 2). As remarked, the accelerated electrons will loose energy by synchrotron, IC and Bremsstrahlung mechanisms, with a dominance of the synchrotron process shaping their spectrum. The fluxes of these emission processes are then calculated and also the number density of the synchrotron photons that are partially self-scattered by the electrons (leading to SSC emission) and by protons (in $p\gamma$ interactions). Likewise, the energy distribution of the protons is also calculated taking into account the radiative cooling mechanisms due to synchrotron, *pp* and $p\gamma$ interactions (see §2.3) that will shape the very high energy part of the SED.

---

[4] We find that for photo-meson production, the radiation from the accretion disk and from the corona are irrelevant compared to the contribution from the synchrotron emission.

3.1. Application to Cen A

The Prominent radio galaxy Cen A (or NGC 5128) is the nearest FR I active radio galaxy to Earth (z=0.0018, Graham 1978), at a distance of $\simeq$ 3.8 Mpc (Rejkuba 2004), making it uniquely observable among this class of objects and an excellent source for studying the physics of relativistic outflows as well as of the core region. Cen A is one of the best well known extragalactic objects over a wide range of frequencies and the photon emission from the nuclear region of the galaxy has been detected from the radio to the γ-rays band. Cen A has been proposed as a possible source of UHE cosmic rays (with energies $\leq 6 \times 10^{19}$eV; Abraham et al. 2007) by the Pierre Auger collaboration. The SMBH mass inferred from kinematics of stars, as well as H_2 and ionized gas is estimated to be in the range of $\sim 10^7 - 10^8\ M_\odot$ (Marconi et al. 2006; Neumayer et al. 2007), and here we adopted the value $5 \times 10^7 M_\odot$. The viewing angle of the jet (θ) is still debatable, for instance at parsec scales it is $\theta \sim 50^\circ - 80^\circ$ (Tingay et al. 1995), whereas at the 100 pc scale $\theta \sim 15^\circ$ (Hardcastle et al. 2003).

In this section we show the results for Cen A obtained by applying the model described in §. 2 around the nuclear region, employing the set of parameters listed in Table 1.

The values for the first five parameters in Table 1 have been calculated from Eqs. 1-4 and 5. We take for the accretion disk inner radius the value $R_X = 6R_S$, for the extension L_X of the reconnection region (see Figure 1), we consider the value $L_X \simeq 10R_S$, and for the extension of the corona $L \simeq 20R_S$. As remarked earlier, the volume V of the emission region in Table 1 was calculated by considering the torus that encompasses the reconnection region in Figure 1. The magnetic reconnection power W is evaluated from Eq. 2.

Figure 3 shows the radiative cooling rates for the different energy loss processes for electrons and protons as described in Section 2.4. These are compared with the acceleration rates due to first-order Fermi acceleration both within the magnetic reconnection site (Eqs. 7 & 8) and behind a shock (Eq. 9). We notice that at high energies for both protons and electrons the acceleration is dominated by the first-order Fermi magnetic reconnection process in the core region. Besides, the main radiative cooling process for the electrons is synchrotron radiation (Figure 3a), while for protons the photo-meson production ($p\gamma$ interactions) governs the loss mechanisms (Figure 3b). For the $p\gamma$ interactions, we have found that the proper target radiation field is that of the photons from the electron synchrotron emission.

The intercept between the magnetic reconnection acceleration rate and the synchrotron rate in Figure 3a gives the maximum energy that the electrons can attain in this acceleration process, which is $\sim 3 \times 10^{11}$eV. Protons on the other hand, do not cool as efficiently as the electrons and can attain energies as high as $\sim 2.5 \times 10^{17}$eV.

We have constructed the SED of Cen A using a lepton-hadronic model where particles are accelerated close to the central BH by magnetic reconnection and interact with the surrounding fields radiating in a spherical region of radius L (see section 2.4). The SED is depicted in (Figure 4) where it is compared with the observations.

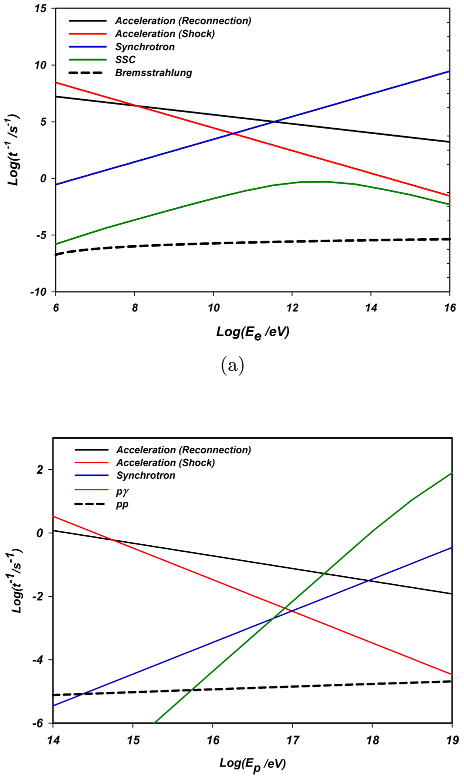

(a)

(b)

Fig. 3. Acceleration and cooling rates for electrons (a) and protons (b) in the nuclear region of Cen A.

We note that the data presented in this figure in the low and intermediate energy ranges come mostly from archival data and represent typical average emission and activity. The emission in the high energy range obtained by *Fermi-LAT* and *HESS* at the same epoch correspond to non-variable and moderate activity too.

As described in section 2.3, we have adopted a particle energy injection power law function:

$$Q(E) \propto E^{-p}. \tag{15}$$

In Figure 4, we considered injected primary particles with $p = 2.4$ which is consistent with theoretical predictions of particle acceleration within magnetic reconnection sites (see §. 2.3). Our calculations show that synchrotron radiation explains the observed emission in the radio to visible band, while SSC is the dominant mechanism to produce the observed hard $X-$rays and low energy γ-rays as a result of interactions between energetic electrons with scattered synchrotron photons. Also in the Figure, neutral pion (π^0) decays can explain the observed γ-rays at TeV energies, via *pp* and $p\gamma$ interactions which are the two main processes producing π^0.

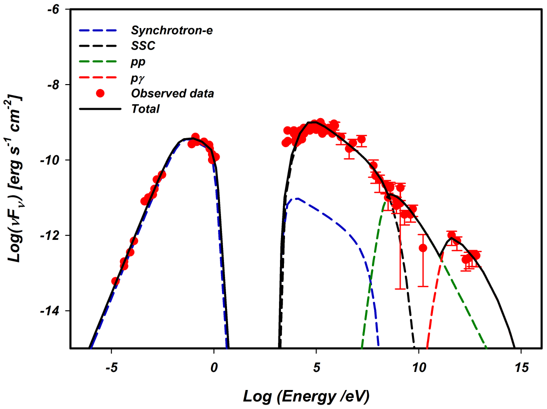

Fig. 4. Calculated spectral energy distribution (SED) for Cen A using the magnetic reconnection acceleration model in a lepton-hadronic scenario compared with observations. The data depicted in the radio to optical energy range (10^{-5}eV $-$ 1eV) is from SCUBA at 800 μm (Hawarden et al. 1993), ISO & SCUBA at 450 μm and 850 μm (Mirabel et al. 1999); the data in the hard x-rays range is from *Swift-BAT* (Ajello et al. 2009) and *Suzaku* (Markowitz et al. 2006). We also include data from *OSSE* (Kinzer et al. 1995) and *COMPTEL* (Steinle et al. 1998) in the range of $5 \times 10^5 - 10^7$eV. The data observed in the energies $10^8 - 10^{10}$eV are taken by *EGRET* (Sreekumar et al. 1999; Hartman et al. 1999) and in the energies $10^8 - 10^{10}$eV by *Fermi-LAT* (Abdo et al. 2009b, 2010). The TeV data are taken by *HESS* (Aharonian et al. 2009).

We note that in order to fit the observed data in the radio to optical range, we had to assume a minimum energy for the injected electrons in the acceleration zone (Eq. 11 in KGV15), $E_{min} = (\gamma_{min} - 1)m_e c^2$, with $\gamma_{min} = 6$. Though this injected value has no influence on the VHE tail of the SED, it is determinant in the match of the low energy branch. We have found that values of $\gamma_{min} < 6$ do not lead to the synchrotron match in the low energy range (see also §4).

As remarked in §. 2.4, the γ-ray absorption due to pair production occurs according to Figures 2a and 2b very near the accretion disk at heights smaller than $\sim 0.001 R_S$, thus much smaller than the emission region that extends up to $\sim 20 R_S$ in our model, so that $exp(-\tau) \simeq 1$ and the absorption effect is not effective at the heights of interest. On the other hand, due to the high dust and neutral gas column density in Cen A ($N_H = 10^{23}$cm^{-2}, see e.g., Morganti et al. 2008) we find that the optical to soft X-ray emission is fully absorbed via γN absorption (see figure 4, Eq. 14).

3.2. Application to Per A

Perseus A (also known as NGC 1275 and 3C 84), is a nearby active galaxy located at the centre of the Perseus cluster and hosts a central SMBH mass of $\sim 3.4 \times 10^8 \mathrm{M}_\odot$ (Wilman et al. 1994). In fact, Per A is one of the closest γ-ray emitting AGNs. Its distance to the Earth is 75 Mpc (Brown & Adams 2011) and is also of great interest, specially due to its proximity, also providing an excellent opportunity to study the physics of relativistic outflows. Per A also seems to exhibit jet precession with an orientation angle $\approx 30° - 55°$ (Walker et al. 1994; see also Falceta-Gonçalves et al. 2010), which may be an indication that Per A is the result of a merger between two galaxies (Liu and Chen 2007). It is a very bright radio galaxy showing an extended jet with FR I morphology (e.g., Vermeulen et al. 1994; Buttiglione et al. 2010) with asymmetric jets at both kpc (Pedlar et al. 1990) and pc scales (Asada et al. 2006).

The parameters of our model for producing the SED of Per A are tabulated in Table 1. The first five parameters are calculated from Eqs. 1- 4 and 5. As for Cen A, we have also used for the accretion disk inner radius the value $R_X = 6R_S$ and for the extension L_X of the reconnection region the values $L_X = 10R_S$ and $L \simeq 20R_S$.

The radiative loss and acceleration rates for electrons and protons are compared in Figure 5. As in Cen A, magnetic reconnection is the dominant acceleration mechanism over shock acceleration at the high energy branch for both electrons and protons and determines the maximum energy that the particles can achieve before losing part of it radiatively. Electrons may be accelerated up to 3×10^{11}eV and the main process to cool them is synchrotron. While the maximum energy the protons can achieve is 10^{17}eV and *photo-meson* production ($p\gamma$) is the dominant mechanism to cool them. Similarly to Cen A, the dominant photon field interacting with the accelerated protons is the synchrotron radiation.

We have constructed the SED for this source employing a leptonic scenario (Figure 6). In this case, the primary particles were injected with a power law spectral index $p = 2.15$ (Eq. 10). The radio spectrum is matched by electron synchrotron emission, with particles injected into the acceleration zone with rest mass energy (i.e., with $\gamma_{min} = 2$). The observed X-ray and γ-ray emission is nearly reproduced by SSC occurring in the nuclear region in a spherical region of radius $L \sim 20R_S$, as described in §. 2.4. However, it should be noticed that there is a high intensity BATSE data point in the $\sim 10^5$ eV that is not matched by the model. Given the fact that this source is highly variable, this feature probably corresponds to a more active state superposed to the less active one (represented by the less intense data points in the same energy range).

The observations also indicate that there is a high energy cut-off around $\sim 3 \times 10^{11}$eV in this source. In our scenario this is due to leptonic emission produced by interactions of high energy electrons with the radiation field produced by themselves and this cut-off is compatible with the maximum energy calculated from the comparison of the reconnection acceleration rate with the synchrotron loss rate in Fig. 5a.

As stressed in §. 2.5, the optical depth for the produced γ-rays was also calculated in this case and is shown if Figures 2c and 2d). We note that the 100 GeV γ-rays may be fully absorbed due to pair production but only very near to disk ($z < 0.001R_s$). However, these vertical distances from the disk, comparing to the length scale of the emission region is very small and reasonably, we can ignore the absorption effect at the heights larger than $\sim R_s$ which is compatible with extension of emission region in our model.

Similarly to Cen A, the neutral gas and dust of the interstellar medium of the host galaxy in this source also causes the extinction of the emission in the range of $10 - 10^2$eV (Fig. 6; see also §. 2.4.2).

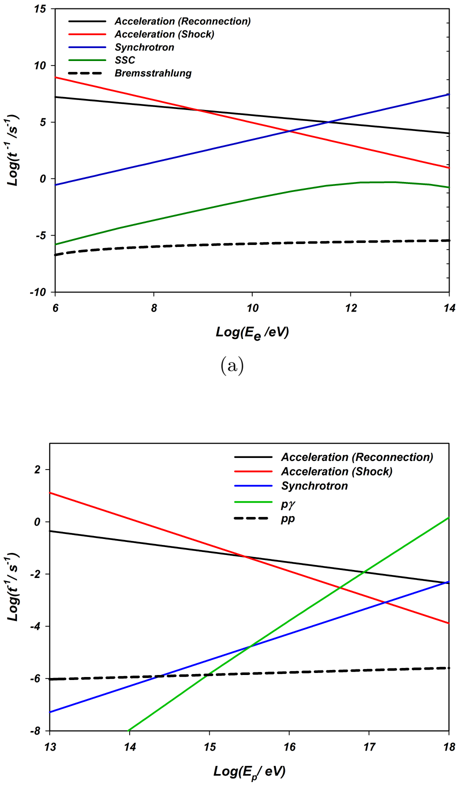

(a)

(b)

Fig. 5. Acceleration and cooling rates for electrons (a) and for protons (b) in the nuclear region of Per A (NGC 1275).

3.3. Application to M87

The FR I giant radiogalaxy M87 is another well-known nearby AGN located at 16.7 Mpc within the Virgo cluster which harbours a SMBH with a mass of $M_{BH} \sim 6 \times 10^9\ M_\odot$ (e. g., Gebhardt & Thomas 2009) which, along with Cen A and Per A, has been known as a peculiar extragalactic laboratory to study high energy astrophysics and investigate the nonthermal mechanisms of VHE emission in AGNs. The observations indicate that its jet is oriented within 20° of the line of sight (Biretta et al. 1999), so that as in the other cases, no significant Doppler boosting is expected for the γ-ray flux.

The TeV γ-ray signal from M87 was first reported by *HEGRA* (Aharonian et al. 2003) and then confirmed by *HESS* (Aharonian et al. 2006). The latter also revealed that this emission is strongly variable with time scales of 1-2 days and thus produced in a very compact region, as pointed out before.

Table 1 shows the parameters that we used to calculate the acceleration and cooling rates and also to reconstruct the SED of this source.

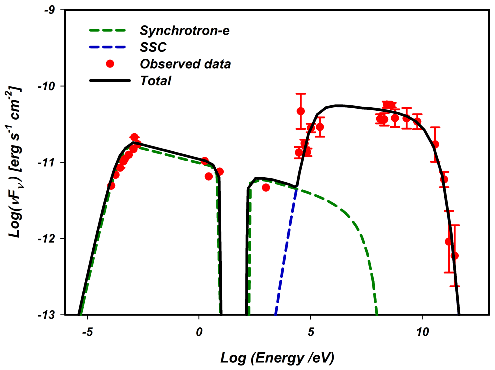

Fig. 6. A leptonic model to reproduce the SED of Per A (NGC 1275) using the magnetic reconnection acceleration model. Data include *MOJAVE* (Lister et al. 2009), *Planck* (Ade et al. 2011), HST (Chiaberge et al. 1999), and HST FOS (Johnstone & Fabian 1995) for the radio to optical spectrum; data depicted in X-rays is from the XMM (Torresi 2012), *Swift*-BAT (Ajello et al. 2009), and BATSE (Harmon et al. 2004); and data depicted in the gamma-ray band is from *Fermi-LAT* (Abdo et al. 2009a; Ackermann et al. 2012) in the 100 MeV-100GeV energy range, and from *MAGIC* (Aleksić et al. 2010a,b, 2012a,b) in the VHE tail. We note that the error bars for the BATSE data (in the 10^5 eV range) were evaluated using Harmon et al. (2004); Soldi et al. (2014) and Wilson et al. (2012).

In Figures 7, we compare the rates of the radiative cooling processes with the rates of the acceleration mechanisms for electrons and protons. As in the other two sources, we find that the dominant energy loss mechanisms are the synchrotron and the $p\gamma$ interactions for electrons and protons, respectively, and the acceleration is dominated by the magnetic reconnection process which defines the energy cut off for both electrons and protons. Figure 7a indicates that this maximum energy is $\sim 4 \times 10^{10}$eV for electrons and $\sim 5 \times 10^{16}$eV for protons.

Figure 8 shows the calculated SED for M87 compared to the observations. It is also reproduced by a lepton-hadronic model in the core region as described in §. 2, where we assumed an injected particle energy distribution $\propto E^{-p}$ with a power index $p = 2.4$.

With an electron minimum energy $E_{min} = 4 m_e c^2$, we can fit the observed core radio to visible spectrum by synchrotron emission.

As in Cen A, the low and intermediate energy data in Figure 8 come from archive and represent typical average emission. The data obtained by *Fermi-LAT* ($10^8 - 10^{11}$eV) and by *HESS* (the TeV tail) correspond both to more quiescent states and have been taken in different epochs. They are reproduced in our model by different mechanisms. While *Fermi-LAT* data are fitted by SSC and *pp* collisions, *HESS* data are fitted by the decay of neutral pions from $p\gamma$ interactions with photons coming from the synchrotron radiation. We note that an observed flare state by *HESS* (Aharonian et al. 2006; not shown in Fig. 8) can be also reproduced by our model assuming a flatter injection particle spectrum with a spectral index = 2.1).

Figures 2e and 2f show the absorbed $\gamma-$ray flux for M87. As in the other cases, this absorption is significant only at heights smaller than R_S and therefore, its effect can

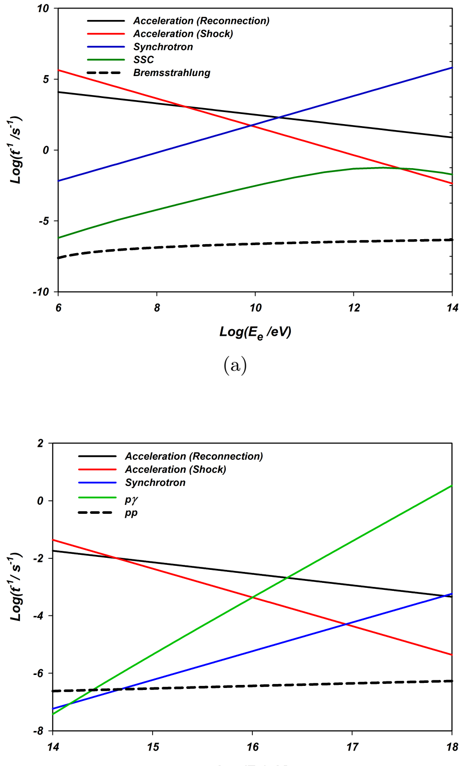

(a)

(b)

Fig. 7. Acceleration and cooling rates for electrons (a) and for protons (b) in the nuclear region of M87.

be neglected at the much larger emission scales considered here.

The absorption of low energy photons by interstellar neutral gas and dust in this source is also important (Fig. 8).

We note that our model and the chosen parametrization is also consistent with the observed TeV rapid variability of M87 which is $\sim 1-2$ days (Abramowski et al. 2012) implying an extremely compact emission region (corresponding to scales of only a few R_S). As remarked in §2.4, the emission region in our model corresponds to the torus region that encompasses the cylindrical shell where magnetic reconnection particle acceleration takes place in Figure 1, i.e., the effective emission zone in our model has a thickness $\simeq L$. For this source $L \simeq 5R_S$ (see Table 1), which is of the order of the inferred scale from the observed variability.

3.4. Application to IC 310

The peculiar galaxy IC 310 (also named B0313+411 and J0316+4119 in observational reports) is one of the brightest objects which, as Per A, is also located in the Perseus galaxy cluster at a distance of 78 Mpc from Earth (Aleksić et al. 2014c) and harbours a supermassive BH with a mass of $\sim 10^8 M_\odot$ (Aleksić et al. 2014c). The redshift of this source is z=0.0189 (Bernardi et al. 2002) which has made it the fourth nearest AGN at VHE gamma-rays (Kadler et al. 2012), after Cen A with z=0.00183, M 87 with z=0.004 and Per A with z=0.017559.

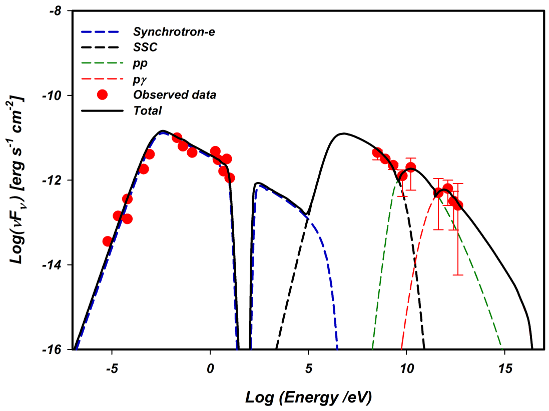

Fig. 8. A lepton-hadronic model of the SED of M 87 compared with observations. The core radio data are obtained from MOJAVE VLBA (Kellermann et al. 2004) at 15 GHz, from (Biretta et al. 1991) at 1.5, 5 and 15 GHz, from IRAM (Despringre et al. 1996) at 89 GHz, from SMA at 230 GHz (Tan et al. 2008), from Spitzer at 21 and 7.2 GHz (Shi et al. 2007) and from Gemini (Perlman et al. 2001) at 3.2 GHz. Optical-UV emission from HST (Sparks et al. 1996). MeV/GeV γ-ray data are from *Fermi-LAT* (Abdo et al. 2009c), and the low-state TeV spectrum (Aharonian et al. 2006) from *HESS*.

IC 310 has been observed at energies E>100 GeV by MAGIC (Mariotti et al. 2010) and Fermi-LAT collaboration also reported the detection of photons above 30 GeV (Neronov et al. 2010). However the origin of the gamma-ray emission is not clear yet and both the jet and the core have been considered as possible emission regions.

Recently, MAGIC collaboration has reported fast time variability for IC 310 on the VHE γ-ray with time scales $\sim$4.8 min (Aleksić et al. 2014a,c) which constrains the size of the emission zone to 20% of its R_S.

The parameters we used to calculate the acceleration and cooling time scales and also to reconstruct the SED of this source are shown in Table 1.

The comparison between the acceleration and cooling rates are depicted in Figures 9a and 9b for electrons and protons, respectively. As in the other cases, we see that the calculated maximum energy for both electrons and protons reaches larger values for magnetic reconnection than for shock acceleration, so that magnetic reconnection should be the dominating mechanism to accelerate particles in the nuclear region of this source as well. The diagrams indicate that electrons can accelerate up to 8×10^{10} eV, while the protons up to 2×10^{17} eV. Also in this source synchrotron emission is the dominant loss mechanism for electrons and $p\gamma$ radiation is the dominant one for protons for energies larger than $\sim 10^{15}$ eV.

Figure 10 shows the calculated SED for IC 310. As in the other sources, the observed radio emission can be explained

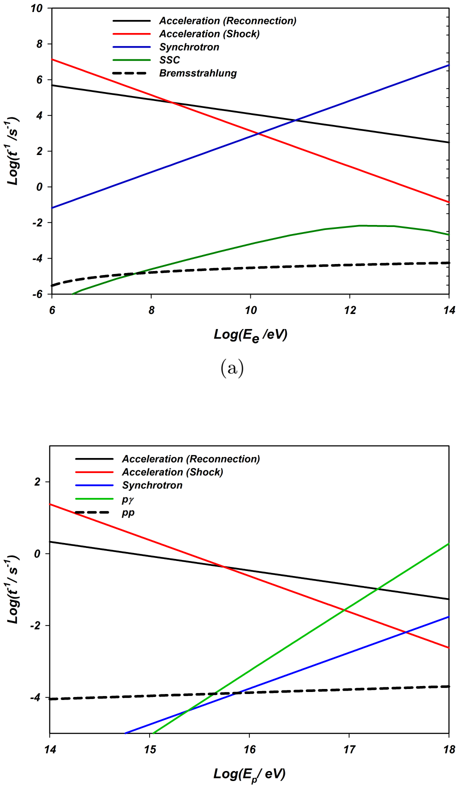

(b)

Fig. 9. Acceleration and cooling rates for electrons (a) and for protons (b) in the nuclear region of IC 310.

by synchrotron and the TeV γ-rays by the pp and $p\gamma$ processes due to particles injected with a power law spectral index p=1.7. The core opacity to this emission has been also calculated for IC 310 in figure 2 which indicates that the γ-ray absorption is negligible in the emission length scales here considered which are above $0.3R_S$.

Also in this case the radiation in low energy range ($10-10^2$eV) is fully absorbed due to photon-neutral interactions (Figure 10).

As for M87, our model and the adopted parametrization can also naturally explain the fast variability of the VHE γ-rays in 3C 310. The effective emission zone for this source is $L \simeq 0.3R_S$ according to our model (see Table 1), which is compatible with the scale inferred from the observed high variability in the γ-ray emission, ~ 4.8 min.

4. Discussion and Conclusions

Our main purpose here was to explore an alternative mechanism to explain the spectral energy distribution (SED) and, particularly, the VHE emission in non-blazar AGNs, i.e., those for which the jet probably does not point to the line of sight and therefore, do not have their emission enhanced by Doppler boosting in the relativistic jet. Instead, we have examined an acceleration mechanism occurring in the innermost region of the AGN. Based on recent results by de Gouveia Dal Pino et al. (2010a), KGS15, and Singh et al. (2015) we investigated the role of fast magnetic reconnection events in accelerating particles in the nuclear regions of low luminosity AGNs, applying this acceleration model to reconstruct the SED of Cen A, Per A, M87 and IC 310.

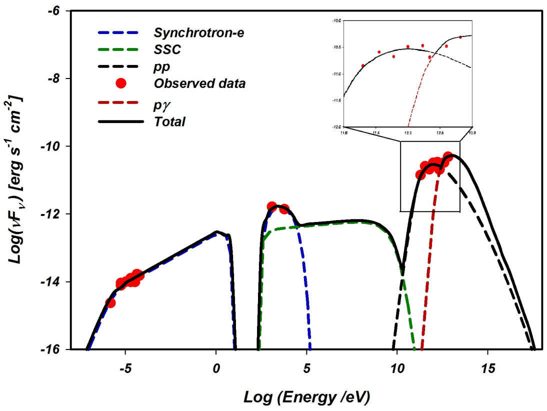

Fig. 10. A lepton-hadronic model of the SED of IC 310 compared with observations. The core radio data are obtained from Kadler et al. 2012; Dunn et al. 2010; Becker et al. 1991; White & Becker 1992; Condon et al. 2002; Douglas et al. 1996. The X-ray data are from XMM-Newton (Sato et al. 2005) and the VHE γ-ray data are from *MAGIC* (Aleksić et al. 2014c). In the upper right side of the diagram it is depicted the detail of the modeling of the VHE branch.

According to this model, trapped particles within the magnetic reconnection discontinuity formed by the encounter of the magnetic field lines arising from the accretion disk with those of the BH magnetosphere (Figure 1), can be accelerated to relativistic velocities by a first-order Fermi process in the surrounds of the BH, as described in de Gouveia Dal Pino & Lazarian (2005). Magnetic reconnection events will occur specially when there is substantial increase in the disk accretion rate which helps to press the two magnetic fluxes together. Since turbulence is expected to be present in these systems (see §. 2.1), the reconnection can be made naturally fast by it (Lazarian & Vishniac 1999 and Kowal et al. 2009)

KGS15 and Singh et al. (2015) used this model to compute the magnetic power released by reconnection in the surrounds of the BHs and compared it with the core radio and $\gamma-$ray luminosities of outbursts of a sample with more than 230 sources including the microquasars and LLAGNs of the fundamental plane of BH activity (Merloni et al. 2003) and also hundreds of blazars and GRBs. They have found that the reconnection power is large enough and is correlated with the observed luminosities of the microquasars and LLAGNs, following the observed trend for more than 10^{10} orders of magnitude in luminosity and mass of these sources. [5]

---

[5] We note that this power is generally not enough to reproduce the radio or gamma-ray luminosities of the blazars and GRBs,

These correlations found with the emission of microquasars and LLAGNs are very important, because they connect the non-thermal emission, specially the VHE one, with the core of these sources, offering a reliable, self-consistent mechanism for their origin. However, in order to determine the real effectiveness of this mechanism, it is necessary to reproduce the SEDs of these sources based on this model. This has been done recently for two microquasars Cyg X1 and Cyg X3, for which the observed SEDs have been successfully reproduced by the model above (KGV15). In this work we have extended this analysis applying the reconnection model to the four radio galaxies with detection of VHE emission up to TeV.

Considering all relevant leptonic and hadronic radiative loss times due to the interactions of the accelerated particles with matter, radiation and magnetic field in the core regions of Cen A, Per A, M87 and IC 310, we compared these times with the acceleration times and found larger energy cut-offs for particles being accelerated by magnetic reconnection than by diffusive shock (see Figures 3, 5, 7, and 9). This result stresses the importance of magnetic reconnection as a potential acceleration mechanism in the core regions around BHs and compact sources in general.

Moreover, we note that the maximum energies for the electrons and protons obtained from these comparisons, are actually much smaller than the maximum possible energy that the particles can attain within the acceleration region in the reconnection sheet. The latter is constrained by the thickness of the acceleration region, i.e., ΔR_X (given by Eq. 3) which must be larger than or equal to the particle Larmor radius, $r_L = E/ceB$. This implies that the maximum energy to which the particles can be accelerated by magnetic reconnection is $\sim 10^{20}$ eV, so that the reconnection layer is large enough to accelerate the particles to UHEs. This value reassures the efficiency of this acceleration process and suggests that if the surrounds of the BHs in AGNs were not so full of interacting matter and radiation fields they might be excellent sites for the production of UHECRs.

The cut-off values above were employed in the determination of the accelerated particle fluxes in the construction of the SED of the sources. The electron synchrotron cooling rate is found to be larger than any other loss mechanism in all leptonic energy range (Figures 3a, 5a, 7a, and 9a). Also, it is the dominant process providing the radiation field that produces the SSC and the photo-meson ($p\gamma$) radiation in the SEDs of the four sources. We have also found that the $p\gamma$ process is the dominant mechanism to cool the accelerated relativistic protons in the high energy branch. This is shown in Figure 3b for Cen A for proton energies $\geqslant 6 \times 10^{16}$eV, and in Figure 5b for Per A for proton energies $\geqslant 2 \times 10^{15}$eV, while in figures 7b and 9b for M87 and IC 310, we see that synchrotron radiation can cool the protons for energies $\leqslant 2 \times 10^{15}$eV, but for larger energies it is overcome by the $p\gamma$ mechanism.

In summary, we have shown that, employing fiducial parameters, our acceleration model is capable of explaining the non-thermal low and high energy emission of the SED of the four investigated LLAGNs Cen A (Figure 4), Per A (Figure 6), M87 (Fiugre 8) and IC 310 (Figure 10).

An interesting advantage of the model presented here is the relatively small number of free parameters used to construct the SED (seven). In particular, we adopted an one-zone approximation in order to avoid the introduction of more free-parameters. Furthermore, this work is a first attempt to test the acceleration model by magnetic reconnection in the surrounds of these BH sources whose physics and distribution of the photon, density and magnetic fields are still poorly known making the use of multi-zone models even more challenging or artificial. Unlike other models (e.g. Kachelriess et al. 2009b), our acceleration mechanism was used to constrain the characteristics of the acceleration region. While most of the models take the maximum energy of the particles as a free parameter to fit the SED (e.g. Abdo et al. 2009a,b,c, 2010; Kachelriess et al. 2010), our model determines this directly from the acceleration model, as described.

4.1. Cen A

According to our results for Cen A, the observed hard X-rays and $Femi - LAT$ γ-ray data can be interpreted as due to SSC and pp interactions, respectively, with accelerated particles injected in the nuclear region (at distances $\sim 20R_S$) driven by magnetic reconnection with a distribution with power law index $p = 2.4$. The TeV radiation observed by $HESS$, on the other hand, is explained by neutral pion decays resulting from $p\gamma$ interactions.

In Sahu et al. 2012, the authors also showed that the TeV γ-rays in Cen A could be explicated by $p\gamma$ interactions, but between relativistic protons accelerated by Fermi process in shocks along the jet with the monochromatic photons observed at 170keV. Another model (Reynoso et al. 2011 also proposed particle acceleration at the jet basis with the production of the hard X-rays by synchrotron emission, and the $Fermi - LAT$ and $HESS$ data by IC and pp mechanisms, respectively, along the jet. Kachelriess et al. 2010, on the other hand, have argued against the production of the $\gamma - rays$ in Cen A by pp interactions along the jet because on leaving the source they would interact with the EBL resulting in a flatter spectrum in the TeV range than the observed one by HESS (see also §. 1).

All these studies demonstrate that the origin of the VHE emission in this source is still highly debatable. A core origin, as the one suggested in this work arises as an interesting possibility as long as magnetic activity is significant in the surrounds of BHs, and it might be considered as well. To disentangle this puzzle we will need substantially improved observations, specially in the $\gamma-$ray range. It is possible that with the much larger resolution and sensitivity of the forthcoming CTA observatory (Actis et al. 2011;Acharya et al. 2013; Sol et al. 2013), and with longer times of exposure of this nearby source (and also of M87, Per A and IC 310), we may collect higher resolution data, and more significant information on variability that may help to determine the location of the emission region.

4.2. Per A

In the case of Per A, there is no relevant data yet in TeV energies, but our core model can nearly explain the observed $Fermi - LAT$ and $MAGIC$ data in the 0.1 GeV $-$ 650 GeV range with a leptonic scenario dominated by SSC. The

---

but this is compatible with the notion that the emission in these cases is produced outside the core, at the jet that points to the line of sight and screens any deep nuclear emission.

synchrotron photons that are absorbed in SSC are produced by accelerated electrons by magnetic reconnection in the coronal nuclear region around the BH (within distances $\sim 20R_S$) having a distribution with a power law index $p = 2.15$.

An SSC model has been also proposed by Aleksić et al. (2014b), but they assumed that the Per A core could be a BL Lac blazar with the jet bending strongly at larger scales and the high energy non-thermal radiation could be originated in a sub-structure of the jet near the core pointing towards our line of sight. This bending still requires observational support and any evidence of jet precession (e.g., Walker et al. 1994; Falceta-Gonçalves et al. 2010) may favour this model. But our proposed model dismisses the necessity of such a strong bending and besides, is supported by the correlations with the observations found in KGS15 and Singh et al. (2015).

4.3. M87

In the case of M87, we have applied the same magnetic reconnection model in the nuclear region around the BH (within a region of 20 R_S) considering the injection of the accelerated particles with a power law index $p = 2.4$. This has resulted a lepton-hadronic scenario for the SED with SSC emission and neutral pion decays from *pp* collisions explaining the $Fermi - LAT$ data. We also found that the decay of the neutral pions due $p\gamma$ interactions can explain the observed data by $HESS$ in the TeV range.

The suggested sites of TeV emission for this source in former works range from large scale structures of the kpc jet (Stawarz et al. 2005) to a compact peculiar hot spot (the so-called HST-1 knot) at a distance 100 pc along the jet (Stawarz et al. 2006) and inner (sub-parsec) parts of the sources. Reynoso et al. (2011) for instance, considered that this emission is produced in the jet, but reconstructed all the emission features, which are highly variable and possibly non-simultaneous, with a single *pp* mechanism.

Giannios et al. (2010), on the other hand, proposed that compact minijets induced by magnetic reconnection moving relativistically within the jet in different directions, some of which pointing to our line of sight, might explain the short-time variable TeV flares observed in M87. This model bears several similarities with ours as it proposes that the minijets are generated by reconnection events in the core region, and then move out with the jet flow up to scales of $\sim 100R_S$. Our model also predicts the development of outbursts with the formation of reconnected features (plasmons) that may be carried out with the jet and might explain e.g., observed superluminal features near the jet basis (de Gouveia Dal Pino & Lazarian 2005, de Gouveia Dal Pino et al. 2010a). However, Giannios et al. (2010) study provides no predictions for the SED structure of M87.

In addition, there is an extensive list of models that propose that the variable VHE emission of M87 can be originated in the inner jet. These span from leptonic models, such as the decelerating flow (Georganopoulos et al. 2005), the spine-shear (Tavecchio & Ghisellini 2008), and the mini/multi-blob model (Lenain et al. 2008), to hadronic models with the emission due to proton synchrotron-$p\gamma$ interactions (Reimer et al. 2004), or *pp* interactions in a cloud-jet scenario (Barkov et al. 2012). However, the location of the emission region is still an unsolved problem.

Neronov & Aharonian (2007) also proposed a nuclear origin for the TeV emission of M87 coming directly from the magnetosphere of the black hole (see also Levinson 2000). They showed that accelerated electrons in the strong rotation-induced electric fields in vacuum gaps in the BH magnetosphere, similar to a pulsar magnetosphere, could lead to the observed TeV emission. Since the acceleration and emission mechanisms occurs in a very compact region close to the event horizon of the BH, it potentially can explain the observed variability of TeV γ-ray emission from M87. Besides, as in our model, they also explain this emission as due to $p\gamma$ interactions with an IR compact target photon field produced by synchrotron emission. However, as stressed in §. 3, the attenuation of γ-ray emission due to electron-positron pair production may be significant in distances smaller than or equal to $\sim R_S$ (Figure 2), which may affect their results. In our model, the emission scales are larger ($\sim 5R_S$) making these attenuation effects negligible.

4.4. IC310

In the case of IC 310, also a lepton-hadronic model in the nuclear region is able to explain the observed SED features with protons and electrons accelerated by magnetic reconnection and injected in the emission region with a power law distribution with index p = 1.7. As remarked, the observed radio emission is well fitted by synchrotron and the VHE emission detected by $MAGIC$ can be explained by decays of neutral pions resulting from *pp* and $p\gamma$ interactions.

Our model with an appropriate choice of parameters is also able to explain naturally the time variability detected in the sources here investigated. In particular, the very fast variability reported for the IC 310 $\gamma-$ray emission of about ~ 4.8 min (Aleksić et al. 2014c) implies an emission region scale of $\simeq 0.3R_S$. To explain this variability and compactness of the emission region, Aleksić et al. 2014c suggested that the particles could be accelerated by electric fields in the BH magnetosphere, as in pulsar models. Nevertheless, as demonstrated, the model described here reproduces the observed SED with an emission region with a similar size as above.

In conclusion, in the construction of the SEDs for the sources discussed here (Cen A, Per A, M87 and IC 310) based on our magnetic reconnection model in the core region, the observed emission at low energies (radio to optical) can be explained by synchrotron emission. SSC with target photons coming from electron synchrotron emission is the dominant (leptonic) mechanism to produce the observed hard X-rays and low energy $\gamma-$rays, while neutral pion decays resulting from *pp* inelastic collisions is the dominant hadronic process to produce the high energy $\gamma-$rays, and neutral pion decays resulting from photo-meson interaction ($p\gamma$) the dominant one to produce the very high energy (VHE) $\gamma-$rays. Interestingly, in the case of the microquasars Cyg X1 and Cyg X3, KGV15 have also found that the core model could reproduce the full observed SED including the low and high energy branches. [6]

---

[6] We should remark that the observed emission at low energies (radio to optical) from the core regions in the case of Cen A and M87 is fitted by the core model described here only if we assume that the minimum electron energy injected in the acceleration region is a few times the particle rest mass. If one considers

4.5. Conclusions

- We have presented a reconnection acceleration model in the core region around the BH of the low luminous radio galaxies Cen A, Per A, M87 and IC 310 and showed that it is able to reproduce very well their SEDs, from radio to gamma-rays up to TeV energies.
- This is complementary to a recent study where we have performed similar analysis for the galactic black hole binaries, i.e., the microquasars Cyg X1 and X3 (Khiali et al. 2015). Together, these two works strengthen the conclusions of the previous works of Kadowaki et al. (2015) and Singh et al. (2015) in favour of a core emission specially for the observed gamma-ray radiation of microquasars and LLAGNs (which belong to the so called fundamental plane of BH activity).
- Magnetic reconnection acceleration seems to provide a better efficiency in regions where magnetic activity is dominant in comparison with diffusive shock acceleration as the cores of LLAGNs. Particles can gain energy up to a few times $\sim$100 TeV due to magnetic reconnection acceleration.
- The observed TeV γ-ray emission may be originated in these cores via neutral pion decays in hadronic processes.
- The fast magnetic reconnection acceleration model occurring in the core of these sources can naturally explain the observed short time variability, specially of the high energy γ-ray.

Finally, we note that it is possible that a neutrino spectrum may be also produced in the nuclear region of LLAGNs considering the same model here investigated, as due to charged pion decays via pp and $p\gamma$ interactions. In a concomitant work, this possibility has been investigated to explain the recently observed extragalactic neutrino flux by the IceCube experiment (Khiali & de Gouveia Dal Pino 2015).

Acknowledgements

This work has been partially supported by grants from the Brazilian agencies FAPESP (2013/10559-5), CNPq (306598/2009-4), and CAPES. We also acknowledge useful discussions with Paola Grandi in the selection of data for the construction of the SEDs.

References

Abdo, A. A., et al. 2009a, ApJ, 699, 31
Abdo, A. A., et al. 2009b, ApJ, 700, 597
Abdo, A. A., et al. 2009c, ApJ, 707, 55
Abdo, A. A., et al. 2010, ApJ, 719, 1433
Abraham, J., et al. 2007, Science, 318, 938
Abramowski, A., et al. 2012, ApJ, 746, 151
Ackermann, M., et al. 2012, ApJS, 203, 4
Ade, P. A. R. et al. 2011, A& A, 536, 7
Aharonian, F. A., Akhperjanian, A., Beilicke, M., et al. 2003, A&A, 403, L1
Aharonian, F. A., et al. 2006, Science, 314, 1424
Aharonian, F. A., et al. 2009, ApJL, 695, L40
Ajello, M., et al. 2009, ApJ, 690, 367
Aleksić, J., et al. ApJ, 723, L207
Aleksić, J., et al. ApJ, 710, 634
Aleksić, J., et al. A&A, 539, L2
Aleksić, J., et al. A&A, 541, 99
Aleksić, J., Antonelli, L. A., et al. 2014a, A& A, 563, A91
Aleksić, J., Ansoldi, S., Antonelli, L. A., et al. 2014b, A& A, 564, AA5
Aleksić, J., Ansoldi, S., Antonelli, L. A., et al. 2014c, Science, 346, 1080
Asada, K., Kameno, S., Shen, Z. Q. et al. 2006, Publ. Astron. Soc. Japan, 58, 261
Barkov, M. V., Bosch-Ramon, V., & Aharonian, F. A. 2012, ApJ, 755, 170
Becker, R. H., White, R. L., & Edwards, A. L. 1991, APJS, 75, 1
Bernardi, M., Alonso, M. V., da Costa, L. N., et al. 2002, AJ, 123, 2990
Biretta, J. A., Stern, C. P., & Harris, D. E. 1991, AJ, 101, 1632
Biretta, J. A., Sparks, W. B., & Macchetto, F. 1999, ApJ, 520, 621
Brown, A. M. & Adams, J. 2011, MNRAS, 413, 2785
Buttiglione, S., Capetti, A., Celotti, A., et al. 2010, A&A, 509, A6
Canning, R. E. A., Fabian, A. C., Johnstone, R. M., et al. 2010, MNRAS, 405, 115
Cerutti, B., Dubus, G., Malzac, J., et al. 2011, A&A 529, A120
Cerutti, B., Werner, G. R., Uzdensky, D. A., Begelman, M. C. 2013, ApJ., 770, 147C
Cerutti, B., Werner, G. R., Uzdensky, D. A., Begelman, M. C. 2014, ApJ., 782, 104C
Chiaberge, M., Capetti, A., & Celotti, A. 1999, A& A, 349, 77
Condon, J. J., Cotton, W. D., & Broderick, J. J. 2002, AJ, 124, 675
de Gouveia Dal Pino, E. M. & Lazarian, A. 2005, Astronomy and Astrophysics, 441, 845
de Gouveia Dal Pino, E. M., Piovezan, P. P. & Kadowaki, L. H. S. 2010a, Astronomy and Astrophysics, 518, A5
de Gouveia Dal Pino, E. M., Kowal, G., Kadowaki, L. H. S., Piovezan, P. P., & Lazarian, A. 2010b, International Journal of Modern Physics D, 19, 729
de Gouveia Dal Pino, E. M., Kowal, G., Lazarian, A. 2014, 8th International Conference of Numerical Modeling of Space Plasma Flows (ASTRONUM 2013), 488, 8, arXiv1401.4941D
de Gouveia Dal Pino, E. M., & Kowal, G. 2015, in Magnetic Fields in Diffuse Media (eds. A. Lazarian, E. M. de Gouveia Dal Pino, C. Melioli), Astrophysics and Space Science Library, 407, 373
Despringre, V., Fraix-Burnet, D., & Davoust, E. 1996, A& A, 309, 375
Dexter, J., McKinney, J. C., Markoff, S., & Tchekhovskoy, A. 2014, MNRAS, 440, 218
Douglas, J. N., Bash, F. N., Bozyan, F. A., Torrence, G. W., & Wolfe, C. 1996, AJ, 111, 1945
Drake, J. F., Swisdak, M., Che, H. and Shay, M. A. 2006, Nature, 443, 553D
Drake, J. F., Opher, M., Swisdak, M. and Chamoun, J. N. 2010, ApJ,709, 963D
Drury, L. 2012, MNRAS, 422, 2474D
Dunn, R. J. H., Allen, S. W., Taylor, G. B., et al. 2010, MNRAS, 404, 180
Eyink, G. L., Lazarian, A., & Vishniac, E. T. 2011, ApJ, 743, 51
Falceta-Gonçalves, D., Caproni, A., Abraham, Z., Teixeira, D. M., & de Gouveia Dal Pino, E. M. 2010, ApJL, 713, L74
Gebhardt, K. & Thomas, J. 2009, ApJ, 700, 1690
Georganopoulos, M., Perlman, E. S., & Kazanas, D., 2005, ApJL, 634, 33
Giannios, D., Uzdensky, D. A. & Begelman, M. C. 2010, MNRAS, 402, 1649
Ginzburg, V. L., & Syrovatskii, S. I. 1995, ARA&A, 3, 297
Graham, J. A. 1978, PASP, 90, 237
Hardcastle, M. J., Worrall, D. M., Kraft, R. P., Forman, W. R., Jones, C., & Murray, S. S. 2003, ApJ, 593, 169
Hardcastle, M. J., Cheung, C. C., Feain, I. J., & Stawarz, Ł. 2009, MNRAS, 393, 1041
Harmon, B. A., Wilson, C. A., Fishman, G. J., et al. 2004, ApJS, 154, 585
Hartman, R. C., et al. 1999, ApJS, 123, 79
Hawarden, T. G., Sandell, G., Matthews, H., E., et al. 1993, MNRAS, 260, 844
Ho, L. C., Filippenko, A. V., & Sargent, W. L. W. 1997, ApJS, 112, 315

---

instead, $\gamma_{min} = 2$ in the computation of the SEDs of these sources, the calculated synchrotron spectrum produced inside the core, mostly in the IR band, is fully absorbed by the energetic electrons and protons in order to produce the SSC and $p\gamma$ emissions, respectively, at the higher energies. Thus if this were the case, the observed radio to optical spectrum in these sources would be probably due to more evolved synchrotron radiation produced beyond the VHE emission region, probably in the jet basis, which would be compatible with jet-like models for the low energy range (e.g., Reynoso et al. 2011).

Istomin, Y. N., & Sol, H. 2009, Astrophys. Space Sci., 321, 57

Johnstone, R. M., & Fabian, A. C. 1995, MNRAS, 273, 625

Kachelriess, M., Ostapchenko,S., & Tomas, R. 2009b, Int. J. Mod. Phys. D 18, 1591

Kachelriess, M., Ostapchenko,S., & Tomas, R. 2010, arXiv: 1002.4874

Kadler, M., Eisenacher, D., Ros, E., et al. 2012, A& A, 538, L1

Kadowaki, L. H. S., de Gouveia Dal Pino, E. M., & Singh, C. B. 2015, ApJ, 802, 113 (KGS15)

Kalberla, P. M. W., McClure-Griffiths, N. M., Pisano, D. J., et al. 2010, A&A, 521, A17

Kellermann, K. I., Lister, M. L., Homan, D. C., et al. 2004, ApJ, 609, 539

Khiali, B., de Gouveia Dal Pino, E. M. & del Valle, M. V. 2015, MNRAS, 449, 34 (KGV15)

Khiali, B., & de Gouveia Dal Pino, E. M. 2015, arXiv:1506.01063

Kinzer, R. L., et al. 1995, ApJ, 449, 105

Koide, S., Shibata, K., Kudoh, T., & Meier, D. L. 2002, Science, 295, 1688

Kowal, G., Lazarian, A., Vishniac, E. T., Otmianowska-Mazur, K. 2009, ApJ, 700, 63

Kowal, G., de Gouveia Dal Pino, E. M., Lazarian, A. 2011, The Astrophysical Journal, 735, 102

Kowal, G., de Gouveia Dal Pino, E. M., Lazarian, A. 2012, Physical Review Letters, 108, 241102

Lazarian, A., & Vishniac, E. T. 1999, The Astrophysical Journal, 517, 700

Lazarian, A., Vlahos, L., Kowal, G., Yan, H., Beresnyak, A. & de Gouveia Dal Pino, E. M. 2012, Space Science Reviews, 173, 557

Lazarian, A., Takamoto, M., de Gouveia Dal Pino, E., Cho, J. 2015, in press.

Lenain, J. P., Boisson, C., Sol, H. & Katarzynski, K. 2008 A&A, 478, 111

Levinson, A., 2000, Phys. Rev. Lett., 85, 912

Lieu, R., Mittaz, J. P. D., Bowyer, S., et al. 1996, ApJ, 458, L5

Lin, R. P., & Hudson, H. S. 1971, SoPh, 17, 412

Lister, M. L., Aller, H. D., Aller, M. F. et al. 2009, AJ, 137, 3718

Liu, F. K. and Chen, X. 2007 ApJ, 671, 1272

Liu, B. F., Mineshige, S., & Ohsuga , K. 2003, ApJ, 587, 571

MacDonald, D. A., Thorne, K. S., Zhang, X.-H., & Price, R. H. 1986, Black Holes: The Membrane Paradigm, 121

Marconi, A., Pastorini, G., Pacini, F., Axon, D. J., Capetti, A., Macchetto, D., Koekemoer, A. M., & Schreier, E. J. 2006, A&A, 448, 921

Markowitz, A., et al. 2007, ApJ, 665, 209

Mariotti, M. 2010, ATel, 2510

Merloni, A., Heinz, S., & di Matteo, T. 2003, MNRAS, 345, 1057

Mirabel, I. F., Laurent, O., Sanders, D. B., et al. 1999, A& A, 341, 667

Morganti, R., Oosterloo, T., Struve, C., & Saripalli, L. 2008, A&A, 485, L5

Nagar, N. M., Falcke, H., & Wilson, A. S. 2005, A&A, 435, 521

Neronov, A., & Aharonian, F. A. 2007, ApJ, 671, 85

Neronov, A., Demikoz, D., & Vovk, Ie. 2010, A& A, 519, L6

Neumayer, N., Cappellari, M., Reunanen, J., Rix, H. W., van der Werf, P. P., de Zeeuw, P. T., & Davies, R. I. 2007, ApJ, 671, 1329

Oishi, J. S., Mac Low, M.-M., Collins, D. C., & Tamura, M. 2015, ApJL, 806, L12

Pedlar, A., Ghataure, H. S. et al. 1990, MNRAS, 246, 477

Perlman, E. S., Sparks, W. B., Radomski, J., et al. 2001, ApJ, 561, L51

Priest, E. R. 2001, Earth Planets Space, 53, 483

Reimer, A., Protheroe, R. J. & Donea, A. C. 2004, A&A, 419, 89

Rejkuba, M. 2004, A&A, 413, 903

Retinò, A., Sundkvist, D., Vaivads, A., et al. 2007, Nature Physics, 3, 236

Reynoso, M. M., Medina, M. C. and Romero, G. E. 2011, A&A 531, A30, 201

Romero, G. E., Christiansen, H. R., Orellana, M. 2005, apj 632,1093, 2005

Ryter, C. E. 1996, Ap& SS, 236, 285

Sahu, S., Zhang, B., & Fraija, N. 2012, Physical Review Letters, 85, 043012

Sato, K., Furusho, T., Yamasaki, N. Y., et al. 2005, PASJ, 57, 743

Shi, Y., Rieke, G. H., Hines, D. C., Gordon, K. D., & Egami, E. 2007, ApJ, 655, 781

Singh, C. B., de Gouveia Dal Pino, E. M. & Kadowaki, L. H. S. 2015, ApJ, 799, L20

Sol, H., Zech, A., Boisson, C., et al. 2013, Astroparticle Physics, 43, 215

Soldi, S., Beckmann, V., Baumgartner, W. H., et al. 2014, A&A, 563, A57

Sparks, W. B., Biretta, J. A., & Macchetto, F. 1996, ApJ, 473, 254

Spruit, H. C. 1988, A&A, 194, 319

Sreekumar, P., Bertsch, D. L., Hartman, R. C., Nolan, P. L., & Thompson, D. J. 1999, Astropart. Phys., 11, 221

Stawarz, Ł., Siemiginowska, A., Ostrowski, M., & Sikora, M. 2005, ApJ, 626, 120

Stawarz, Ł., Kneiske, T. M., & Kataoka, J. 2006, ApJ, 637, 693

Steinle, H., et al. 1998, A&A, 330, 97

Tan, J. C., Beuther, H., Walter, F., & Blackman, E. G. 2008, ApJ, 689, 775

Tavecchio F., Ghisellini G., 2008, MNRAS, 385, L98

Tingay S. J., et al. 1998, AJ, 115, 960

Torresi, E. 2012, arXiv:1205.1691

Vermeulen, R. C., Readhead, A. C. S., Backer, D. C. 1994, ApJ, 430, L41

Vincent, S., 2014, arXiv:1411.1957

Walker R. C., Romney J. D., Benson J. M. 1994, ApJ, 430, L45

White, R. L., & Becker, R. H. 1992, APJS, 79, 331

Wilman R. J., Edge A. C., Johnstone R. M. 2005, MNRAS, 359, 755

Wilson-Hodge, C. A., Case, G. L., Cherry, M. L., et al. 2012, ApJS, 201, 33

Yamada, M., Jongsoo, Y., Jonathan J. A., Hantao, J., Russell M. K.

Zenitani, S., Hesse, M. & Klimas, A. 2009, ApJ, 696, 1385Z

Appendix D

High energy neutrino emission from the core of low luminosity AGNs triggered by magnetic reconnection acceleration

Mon. Not. R. Astron. Soc. **000**, 1–9 (2015) Printed 7 October 2015 (MN LaTeX style file v2.2)

High energy neutrino emission from the core of low luminosity AGNs triggered by magnetic reconnection acceleration

B. Khiali^{1*} and E. M. de Gouveia Dal Pino^{1}
^{1}*IAG-Universidade de São Paulo, Rua do Matão 1226, São Paulo, SP, Brazil*

Accepted 2015 October 6. Received 2015 September 21; in original form 2015 June 02

ABSTRACT

The detection of astrophysical very high energy (VHE) neutrinos in the range of TeV-PeV energies by the IceCube observatory has opened a new season in high energy astrophysics. Energies ∼PeV imply that the neutrinos are originated from sources where cosmic rays (CRs) can be accelerated up to $\sim 10^{17}$eV. Recently, we have shown that the observed TeV gamma-rays from radio-galaxies may have a hadronic origin in their nuclear region and in such a case this could lead to neutrino production. In this paper we show that relativistic protons accelerated by magnetic reconnection in the core region of these sources may produce HE neutrinos via the decay of charged pions produced by photo-meson process. We have also calculated the diffuse flux of HE neutrinos and found that it can be associated to the IceCube data.

Key words: Low luminosity AGNs- very high energy neutrinos- cosmic ray acceleration: magnetic reconnection- radiation mechanisms: non-thermal.

1 INTRODUCTION

Neutrino observations can provide unique information to understand their origin and can even lead to the discovery of new classes of astrophysical sources. The inherent isotropic nature of the detected neutrino flux by IceCube is compatible with an extragalactic origin and is supported by diffuse high energy γ-ray data (Ahlers & Murase 2014). The observed neutrinos with energies $\sim PeV$ suggest that they are originated from a source where cosmic rays (CRs) can be accelerated up to $\sim 10^{17}$eV.

A potential mechanism to produce VHE neutrinos in the TeV-PeV range is through the decay of charged pions created in proton-proton (*pp*) or proton-photon ($p\gamma$) collisions in a variety of astrophysical sources which, in the framework of the IceCube observations, may include active galactic nuclei (AGNs) (Kasanas & Ellison 1986; Stecker et al. 1991; Atoyan & Dermer 2001; Neronov & Semikoz 2002) and gamma-ray bursts (GRBs) (Waxman & Bahcall 1997).

Hadronic mechanisms producing VHE neutrinos via the acceleration of cosmic rays (CRs) in AGNs have been suggested for more than three decades (Eichler 1979; Protheroe & Kasanas 1983; Mannheim 1995; Hazlen & Zas 1997; Mucke & Protheroe 2001; Kalashev et al. 2014; Marinelli & Fraija 2014b; Atoyan & Dermer 2003; Becker 2008). Currently, the detection of gamma-ray emission at TeV energies in AGNs, not only in high luminous blazars, but also in less luminous radio-galaxies, has strengthened the notion that they may be excellent cosmic ray accelerators and therefore, important potential neutrino emission candidates.

Several recent models have tried to describe the detected TeV neutrino emission as due to AGNs. For instance, Marinelli & Fraija (2014b) employed two different hadronic scenarios involving the interaction of accelerated protons at the AGN jet either with photons produced via synchrotron self-Compton (SSC) or with thermal particles in the giant lobes. They then derived the expected neutrino flux for low luminous AGNs (LLAGNs) [1], or more specifically, for radio galaxies for which they examined the origin of the observed TeV gamma-ray spectra as due to hadronic processes.

Earlier work by Gupta (2008) had already introduced hadronic scenarios to explain the TeV emission in LLAGNs (e.g., Cen A). Also, Fraija (2014a,b) suggested neutral pion decays from *pp* and $p\gamma$ interactions in these sources as probable candidates to explain the high energy neutrinos. In another model, Kalashev et al. (2014) attempt to reproduce the

---

[1] By LLAGNs we mean non-blazar sources with $L_{H_\alpha} \leq 10^{40}\mathrm{ergs}^{-1}$ (see Ho et al. 1997; Nagar et al. 2005), where L_{H_α} is the H_α luminosity. These typically consist of liners and seyfert galaxies which are also FR I or FR II radio sources. For more details see Kadowaki et al. (2015).

⋆ E-mail: bkhiali@usp.br

© 2015 RAS

IceCube data using the $p\gamma$ mechanism considering the radiation field produced by the accretion disk around the AGN central black hole (assuming a standard Shakura-Sunyaev accretion disk model). Alternatively, Kimura et al. (2014) calculated the neutrino spectra using the radiatively inefficient accretion flows (RIAF) model in the nuclei of LLAGNs considering both pp and $p\gamma$ mechanisms and stochastic proton acceleration in the RIAF turbulence.

The possibility of producing VHE neutrino emission has been also extensively explored in blazars - AGNs for which the relativistic jet points to the line of sight (e.g., Atoyan & Dermer 2003; Becker 2008; Murase et al. 2014; Dermer et al. 2014). Dermer et al. (2014), in particular, revisited the previous studies assuming that the observed neutrinos could be produced in the inner jet of blazars and concluded that neither the flux nor the spectral shape suggested by the IceCube data could be reproduced by this scenario which predicts a rapid decline of the emission below 1 PeV. Tavecchio et al. 2014 and Tavecchio & Ghisellini 2014, on the other hand, considered the distribution of lower-power blazars, namely, BL Lac objects and, by employing a two-zone spine-sheath jet model to these sources concluded that they might be suitable for the production of the observed PeV neutrinos revealed by the IceCube.

Presently, it is very hard to define what should be the dominant process or the real sources that are producing the observed neutrino flux mainly due to the lack of more precise measurements. But while waiting for better measurements, we can explore further mechanisms and try to make reliable predictions in order to constrain the candidates.

The big challenge in models that rely on hadronic processes in the AGN nuclei is how to produce the relativistic protons that may lead to γ-ray emission and the accompanying neutrino flux. Diffusive shock acceleration at the jet launching base was discussed by Begelman et al. (1990). Levinson (2000) and more recently, Vincent (2014) proposed that TeV gamma-ray emission might be produced in the BH magnetosphere by pulsar-like mechanisms, i.e., with particles being accelerated by the electric potential difference settled by non uniform magnetic field. As remarked above, Kimura et al. (2014) discussed stochastic acceleration in an accreting RIAF turbulent scenario, but currently none of these models can be regarded as dominant or disclaimed given the uncertainties from the observations regarding the location of the gamma-ray emission (see §. 5).

In this work, we consider an alternative acceleration model that may occur in the vicinity of BHs which was explored first in the framework of microquasars by de Gouveia Dal Pino & Lazarian 2005 (hereafter GL05) and then extended to AGNs by de Gouveia Dal Pino, Piovezan & Kadowaki 2010 (hereafter GPK10). In this model, particles can be accelerated in the surrounds of the BH by the magnetic power extracted from events of fast magnetic reconnection occurring between the magnetosphere of the BH and the lines rising from the inner accretion disk into the corona (Figure 1).

More recently, Kadowaki, de Gouveia Dal Pino & Singh (2015) revisited this model exploring different mechanisms of fast magnetic reconnection and extending the study to include also the gamma-ray emission of a large sample of sources (more than 200 sources involving blazars, non-blazars or LLAGNs, and galactic black hole binaries). They confirmed the earlier trend found by GL05 and GPK10, verifying that the fast magnetic reconnection power calculated as a function of the black hole (BH) mass can explain the observed radio and gamma-ray luminosity from nuclear outbursts of all LLAGNs and galactic black hole binaries of their sample, spanning 10^{10} orders of magnitude in mass (see Fig. 5 in Kadowaki et al. 2015). [2]

In the works above, a standard accretion disk model was employed, but in an accompanying work (Singh et al. 2015), the authors adopted a magnetically dominated advective flow (MDAF) for the accretion and obtained very similar results to those above, which demonstrated that the details of the accretion physics are not relevant in the development of the magnetic reconnection process and the particle acceleration occurring in the corona.

The magnetic reconnection acceleration model above (see Kadowaki et al. 2015) has been also employed to reproduce the observed multi-wavelength spectral energy distribution (SED) of a few microquasars (Cygnus X-1 and Cygnus X-3) (Khiali, de Gouveia Dal Pino & del Valle (2015), henceforth KGV15) and LLAGNs (Cen A, NGC 1275, M87 and IC310) (Khiali, de Gouveia Dal Pino & Sol (2015), hereafter KGS15), and the results indicate that hadronic mechanisms (pp and $p\gamma$) are the main radiative processes producing the observed GeV to TeV γ-rays.

The results of the works above and in particular, the reproduction of the observed SEDs and the TeV gamma-ray) emission of the radio-galaxies by hadronic processes involving particles accelerated by magnetic reconnection in the surrounds of the BH (KGS15), have motivated the present study. We aim here to calculate the spectrum of neutrinos arising from the interactions of accelerated protons by the mechanism above with the radiation and thermal-particle fields around the BH. According to our previous results (KGV15 and KGS15), these interactions produce weakly decaying π^0 and $\pi^{\pm}$ pions. The latter may generate high energy neutrinos. We will then evaluate the diffuse neutrino intensity and compare with the IceCube data in the context of LLAGNs.

For completeness, we will also compare the particle acceleration by magnetic reconnection with shock acceleration in the surrounds of the BH.

The outline of the paper is as follows. In Section 2, we describe in detail our scenario. In Section 3, we describe the hadronic interactions and calculate the acceleration and radiative cooling rates. The calculation of the spectrum of neutrinos and their diffuse intensity for comparison with the IceCube data is presented in Section 4. We discuss and summarize our results and conclusions in Section 5.

---

[2] We note that the calculated reconnection power in this core model though large enough to explain the luminosity of galactic black hole binaries and LLAGNs (or non-blazars), is insufficient for reproducing the luminosity of most of the blazars and GRBs, which is compatible with the notion that the observed emission in these cases is produced outside the core, at the jet that points to the line of sight and screens any deep nuclear emission (Kadowaki et al. 2015).

2 DESCRIPTION OF THE MODEL

In this section we summarize the main characteristics of our fast magnetic reconnection model in the surrounds of the BH and how particles can be accelerated in the magnetic reconnection layer. For a more detailed description we refer to Kadowaki et al. 2015.

2.1 Fast magnetic reconnection in the surrounds of the BH

We assume that the gamma-ray emission from low-luminous AGNs is produced in the core region and the particles responsible for this emission are accelerated in the corona around the BH and accretion disk as sketched in Figure 1.

Turbulent dynamo inside the accretion disk or plasma dragging from the surrounds can build the large-scale poloidal magnetic fields that arise into the corona. This poloidal magnetic flux under the action of disk differential rotation gives rise to a wind that partially removes angular momentum from the system increasing the accretion rate and the ram pressure of the accreting material that will then press the magnetic lines in the inner disk region against the lines anchored into the BH horizon allowing them to reconnect (see Fig. 1). The magnetic field intensity in the inner region of the accretion disk corona is approximately given by the balance between the magnetic pressure of the BH magnetosphere and the accretion ram pressure (Kadowaki et al. 2015):

$$B \cong 9.96 \times 10^{8} r_X^{-1.25} \xi^{0.5} m^{-0.5} \text{ G}. \tag{1}$$

Where $r_X = R_X/R_S$ is the inner radius of the accretion disk in units of the BH Schwartzchild radius (R_S) (in our calculations we assume $r_X = 6$); ξ is the mass accretion disk rate in units of the Eddington rate ($\xi = \dot{M}/\dot{M}_{Edd}$), with $\dot{M}_{Edd} = 1.45 \times 10^{18} m \text{ g s}^{-1}$), which we assume to be $\xi \simeq 0.7$[3]; m is the BH mass in units of solar mass.

The presence of embedded turbulence in the nearly collisional MHD coronal flow of the core region of the AGNs can make reconnection very fast with a rate $V_R \simeq v_A (l_{inj}/L)^{1/2} (v_{turb}/v_A)^2$, where l_{inj} and v_{turb} are the injection scale and velocity of the turbulence, respectively (e.g., Lazarian & Vishniac 1999, hereafter LV99[4]. This relation shows that the reconnection rate is of the order of the Alfvén speed v_A, which in the systems here considered may be near the light speed.

The magnetic reconnection power released by turbulent driven fast reconnection in the magnetic discontinuity region (Figure 1) is given by (Kadowaki et al. 2015):

$$W \simeq 1.66 \times 10^{35} \psi^{-0.5} r_X^{-0.62} l^{-0.25} l_X q^{-2} \xi^{0.75} m \quad \text{erg s}^{-1}, \tag{2}$$

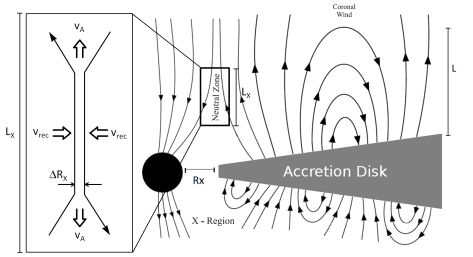

Figure 1. Scheme of magnetic reconnection between the lines arising from the accretion disk and the lines anchored into the BH horizon. Reconnection is made fast by the presence of embedded turbulence in the reconnection (neutral) zone (see text for more details). Particle acceleration may occur in the magnetic reconnection zone by a first-order Fermi process (adapted from GL05).

where $l = L/R_S$ is the height of the corona in units of R_S; $l_X = L_X/R_S$, L_X is the extension of the magnetic reconnection zone (as shown in Figure 1), $q = [1 - (3/r_X)^{0.5}]^{0.25}$ and $v_A = v_{A0}\psi$ is the relativistic form of the Alfvén velocity, with $v_{A0} = B/(4\pi\rho)^{1/2}$, B being the local magnetic field, $\rho \simeq n_c m_p$ the fluid density, and $\psi = [1 + (\frac{v_{A0}}{c})^2]^{-1/2}$, in this work, we find that $v_{A0} \sim c$.

The acceleration region in our model corresponds to the cylindrical shell around the BH where magnetic reconnection takes place, as shown in Figure 1. This shell has a length l_X, with inner and outer radii given by R_X and $R_X + \Delta R_X$ respectively, where ΔR_X is the width of the current sheet given by (Kadowaki et al. 2015):

$$\Delta R_X \cong 2.34 \times 10^{4} \psi^{-0.31} r_X^{0.48} l^{-0.15} l_X q^{-0.75} \xi^{-0.15} m \text{ cm}. \tag{3}$$

This magnetic reconnection power (Eq. 2) will both heat the surrounding gas and accelerate particles. As in Kadowaki et al. (2015), we assume that approximately 50% of the reconnection power goes to accelerate the particles (see §. 2.2.). This is consistent with plasma laboratory experiments of reconnection acceleration (Yamada et al. 2014) and also with the observations of solar flares (e.g., Lin & Hudsun 1971). We further assume that this power is equally shared between the protons and electrons/positrons, so that the proton luminosity will be 25% of the calculated value by Eq. 2.

The particle density in the coronal region in the surrounds of the BH is (Kadowaki et al. 2015):

$$n_c \cong 8.02 \times 10^{18} r_X^{-0.375} \psi^{0.5} l^{-0.75} q^{-2} \xi^{0.25} m^{-1} \text{ cm}^{-3}. \tag{4}$$

2.2 Particle acceleration due to the magnetic power released by fast reconnection

In the magnetic reconnection layer (or current sheet; see Figure 1) where the two converging magnetic flux tubes move to each other with a velocity V_R, trapped particles may bounce back and forth due to head-on collisions with magnetic fluctuations in the current sheet. As a consequence, their energy after a round trip may increase by $< \Delta E/E > \sim V_R/c$, implying an exponential energy increase after several round trips. This first-order Fermi acceleration process within reconnection layers was first studied by GL05 and successfully tested through 3D MHD simulations with test particles injected in current sheets with fast reconnection driven by turbulence (Kowal et al. 2011, 2012; see also (de Gouveia Dal Pino, Kowal & Lazarian 2014; de Gouveia Dal Pino & Kowal 2015 for reviews)[5].

---

[3] See Fig. 5 in Kadowaki et al. (2015). Accretion rates ξ between $0.05 < \xi \leq 1$ are able to produce magnetic reconnection power values which are enough to probe the observed gamma-ray luminosities from LLAGNs.

[4] According to the LV99 model, even weak embedded turbulence causes the wandering of the magnetic field lines which allows for many independent patches to reconnect simultaneously making the global reconnection rate large (for more details see Kadowaki et al. 2015). This theory has been confirmed numerically by means of 3D MHD simulations (Kowal et al. 2009, 2012).

From the results of the 3D MHD numerical simulations (Kowal et al. 2012), we find that the acceleration rate for a proton is given by (see also KGV15):

$$t^{-1}_{acc,M.R.,p} = 1.3 \times 10^{5} \left(\frac{E}{E_0}\right)^{-0.4} t_0^{-1}, \tag{5}$$

where E is the energy of the accelerated proton, $E_0 = m_p c^2$, m_p is the proton rest mass, $t_0 = l_{acc}/v_A$ is the Alfvén time, and l_{acc} is the length scale of the acceleration region and for electrons this rate is (KGV15):

$$t^{-1}_{acc,M.R.,e} = 1.3 \times 10^{5} \sqrt{\frac{m_p}{m_e}} \left(\frac{E}{E_0}\right)^{-0.4} t_0^{-1}, \tag{6}$$

where m_e is the electron rest mass.

As stressed in GL05 (see also KGV15 and KGS15), it is also possible that a diffusive shock may develop in the surrounds of the magnetic reconnection zone due to coronal mass ejections released by fast reconnection along the magnetic field lines, as observed in solar flares. A similar picture has been also suggested by e.g., Romero et al. (2010b). In this case, the shock velocity will be predominantly parallel to the magnetic field lines and the acceleration rate for a particle of energy E in a magnetic field B, will be approximately given by (e.g., Spruit 1988):

$$t^{-1}_{acc,shock} = \frac{\eta e c B}{E}, \tag{7}$$

where $0 < \eta \ll 1$ characterizes the efficiency of the acceleration. We fix $\eta = 10^{-2}$, which is appropriate for shocks with velocity $v_s \approx 0.1c$, which are commonly assumed in the Bohm regime (Romero et al. 2010b).

3 HADRONIC INTERACTIONS

In KGS15, we have demonstrated that the core region of LLAGNs is able to accelerate protons up to energies of a few 10^{17}eV through the first-order Fermi magnetic reconnection mechanism described in the previous section. This indicates that these sources could be powerful CR accelerators. We show below that these protons can cool very efficiently via synchrotron, $p\gamma$ and pp interactions in the region that surrounds the BH of these sources (Figure 2). As remarked, these hadronic interactions lead to the production of HE γ-rays and HE neutrinos via decays of neutral and charged pions, respectively. In KGS15, we have calculated the spectral energy distribution of the HE γ-ray emission for the LLAGNs for which this emission has been detected. Below, we calculate the HE neutrino emission from the nuclear region of these sources.

Table 1. Three sets of model parameters for LLAGNs.

	Parameters	Model 1	Model 2	Model 3
m	BH mass ($M_\odot$)	10^7	10^8	10^9
p	Injection spectral index	1.9	1.7	2.2

3.1 *pp* collisions

The charged pions can be created through inelastic collisions of the relativistic protons with nuclei of the corona that surrounds the BH and the accretion disk by means of the following reactions (Atoyan & Dermer 2003; Becker 2008)

$$p + p \rightarrow n_1(\pi^+ + \pi^-) + n_2\pi^0 + p + p \tag{8}$$

where n_1 and n_2 are multiplicities, $\pi^0 \rightarrow \gamma + \gamma$ (Stecker 1970, 1971), carrying 33% of the accelerated proton's energy. The charged pions $\pi^\pm$ then decay and produce neutrinos via $\pi^+ \rightarrow \nu_\mu + \bar{\nu}_\mu + \nu_e + e^+$ and $\pi^- \rightarrow \nu_\mu + \bar{\nu}_\mu + \bar{\nu}_e + e^-$, where ν_μ, $\bar{\nu}_\mu$, and ν_e are the muon neutrino, muon antineutrino, and electron neutrino, respectively (Margolis et al. 1978; Stecker 1979; Michalak et al. 1990). The pp cooling rate is almost independent of the proton energy and is given by (Kelner 2006)

$$t^{-1}_{pp} = n_i c \sigma_{pp} k_{pp}, \tag{9}$$

where, n_i is the coronal number density of protons which can be calculated by eq. 4, and k_{pp} is the total inelasticity of the process of value ~ 0.5. The corresponding cross section for inelastic pp interactions σ_{pp} can be approximately by (Kelner et al. 2009)

$$\sigma_{pp}(E_p) = \left(34.3 + 1.88Q + 0.25Q^2\right)\left[1 - \left(\frac{E_{th}}{E_p}\right)^4\right]^2 \text{mb}, \tag{10}$$

where mb stands for milli-barn, $Q = \ln\left(\frac{E_p}{1TeV}\right)$, and the proton threshold kinetic energy for neutral pion (π^0) production is $E_{th} = 2m_\pi c^2 (1 + \frac{m_\pi}{4m_p}) \approx 280$ MeV, where $m_\pi c^2 = 134.97$ MeV is the rest energy of π^0 (Villa & Aharonian 2009). This particle decays in two photons with a probability of 98.8%.

3.2 *p*γ interactions

The photomeson ($p\gamma$) production takes place for photon energies greater than $E_{th} \approx 145$MeV. Pions are also obtained from the $p\gamma$ interaction near the threshold via the channels (Atoyan & Dermer 2003)

$$p + \gamma \rightarrow p + \pi^0, \tag{11}$$

with $\pi^0 \rightarrow \gamma + \gamma$ carrying 20% of accelerated protons energy and

$$p + \gamma \rightarrow p + \pi^+ + \pi^-, \tag{12}$$

and the charged pions will also decay producing neutrinos as described in §. 3.1.

The radiative cooling rate for this mechanism in an isotropic photon field with density $n_{ph}(E_{ph})$ can be calculated by (Stecker 1968):

$$\begin{aligned} t^{-1}_{p\gamma}(E_p) = \frac{c}{2\gamma_p^2} & \int_{\frac{E_{th}^{(\pi)}}{2\gamma_p}}^{\infty} dE_{ph} \frac{n_{ph}(E_{ph})}{E_{ph}^2} \\ & \times \int_{E_{th}^{(\pi)}}^{2E_{ph}\gamma_p} d\epsilon_r \sigma_{p\gamma}^{(\pi)}(\epsilon_r) K_{p\gamma}^{(\pi)}(\epsilon_r)\epsilon_r, \end{aligned} \tag{13}$$

---

[5] Particle acceleration within reconnection sheets has been also extensively tested numerically in collisionless fluids by means of 2D (e.g., Zenitani & Hoshino 2001; Drake et al. 2006, 2010; Cerutti et al. 2013) and 3D particle in cell simulations (Sironi & Spitkovsky 2014).

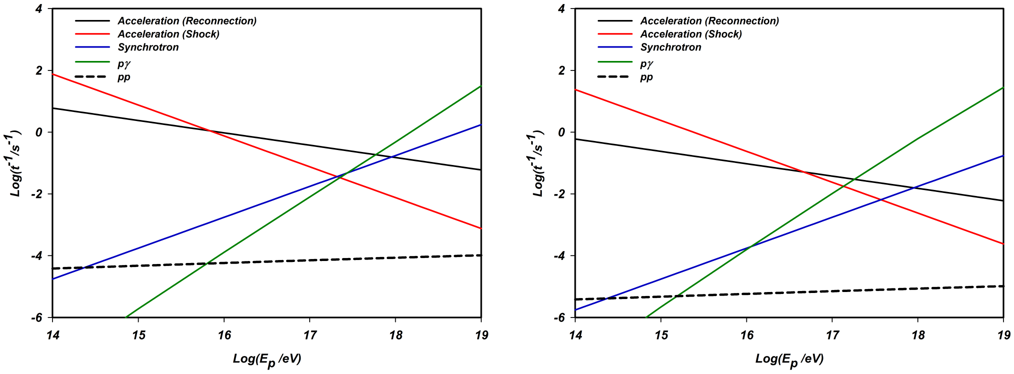

(a) *Model* 1

(b) *Model* 2

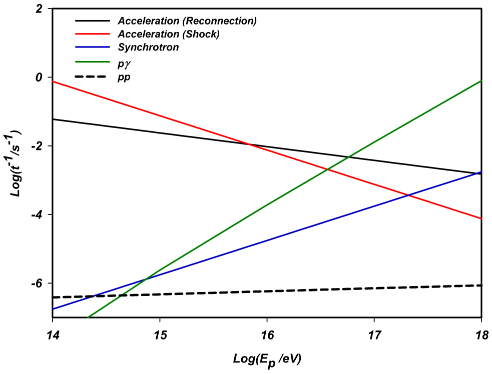

(c) *Model* 3

Figure 2. Acceleration and cooling rates for protons in the core regions of LLAGNs with a central black hole mass (*a*) $M = 10^7 M_\odot$ (Model 1), (*b*) $M = 10^8 M_\odot$ (Model 2), and (*c*) $M = 10^9 M_\odot$ (Model 3).

where in our model the appropriate photons come from the synchrotron radiation [6], $n_{ph}(E_{ph}) = n_{synch}(\epsilon)$, $\gamma_p = \frac{E_p}{m_e c^2}$, ϵ_r is the photon energy in the rest frame of the proton, and $K^{(\pi)}_{p\gamma}$ is the inelasticity of the interaction. Atoyan & Dermer (2003) proposed a simplified approach to calculate the cross-section and the inelasticity which are given by

$$\sigma_{p\gamma}(\epsilon_r) \approx \begin{cases} 340\ \mu barn & 300\text{MeV} \le \epsilon_r \le 500\text{MeV} \\ 120\ \mu barn & \epsilon_r > 500\text{MeV}, \end{cases} \tag{14}$$

and

$$K_{p\gamma}(\epsilon_r) \approx \begin{cases} 0.2 & 300\text{MeV} \le \epsilon_r \le 500\text{MeV} \\ 0.6 & \epsilon_r > 500\text{MeV}. \end{cases} \tag{15}$$

4 NEUTRINO EMISSION AND DIFFUSE INTENSITY

To calculate the neutrino emission from the nuclear region of an LLAGN, we consider a population of protons accelerated by magnetic reconnection in the surrounds of the BH according to the model described in Section 2.

We assume for these accelerated particles an isotropic power law spectrum (in units of $\text{erg}^{-1}\text{cm}^{-3}\text{s}^{-1}$) (see e.g. KGV15 and references there in):

$$Q(E) = Q_0 E^{-p} exp[-E/E_{max}] \tag{16}$$

where $p > 0$ and E_{max} is the cut-off energy.

The normalization constant Q_0 above is calculated from the total power injected to accelerate the protons according to the relation:

$$L_p = \int_V d^3r \int_{E_{min}}^{E_{max}} dE\ E\ Q(E) \tag{17}$$

where V is the volume of the emission region around the magnetic reconnection zone and L_p corresponds to the magnetic reconnection power W given by Eq. 2. To calculate W we have adopted the following suitable set of parameters $\xi = 0.7$, $R_X = 6R_S$, $L_X = 10R_S$, and $L = 20R_S$.

---

[6] We find that for photomeson production, the radiation from the accretion disk is irrelevant compared to the contribution from the coronal synchrotron emission above the disk (see KGV15 and KGS15 for a detailed derivation of the synchrotron rate and its radiation field density).

The maximum energy of the accelerated particles E_{max} is derived from the balance between the magnetic reconnection acceleration rate (Eq. 5) and the radiative loss rates as given in Section 3. Figure 2 compares these rates for protons considering LLAGNs with three different BH masses 10^7, 10^8 and $10^9 M_\odot$. We have also considered different power-law indices (p) for the injected particle spectrum in each of these models (see Table 1) which are compatible with the values derived from analytical and numerical studies of first-order Fermi acceleration by magnetic reconnection and also with values inferred from the observations (e.g., KGS15). The calculated values of B, W, ΔR_X and n_c from Eqs. 1-4 for these three representative source models are listed in Table 2. For simplicity, we consider the derived proton luminosities (which are $\sim 1/4W$) and the emission properties of these three models to characterize the whole range of LLAGNs in the calculation of the HE neutrino flux below. The adoption of this approach, rather than accounting for a whole range of BH mass sources allows us to avoid the introduction of further free parameters in the modelling.

In Fig. 2, for comparison we have also calculated the proton acceleration rate due to a shock formed in the surrounds of the reconnection region (Eq. 7) for the same set of parameters as above. As in KGV15 and KGS15, we find that the maximum energy attained from magnetic reconnection acceleration is higher than that from the shock . It should be also remarked that protons with these calculated maximum energies have Larmor radii smaller than the thickness of the reconnection layer ΔR_X (eq. 3), as required.

The neutrinos that are produced from pion decay will escape from the emission region without any absorption and their spectrum is given by (Tavecchio et al. 2014; Kimura et al. 2014):

$$E_\nu L_\nu(E_\nu) \simeq (0.5 t_{pp}^{-1} + \frac{3}{8} t_{p\gamma}^{-1}) \frac{L_X}{c} E_p L_p, \qquad (18)$$

where E_ν is the neutrino energy and E_p the proton energy. Since Figure 2 demonstrates that the $p\gamma$ emission cools the protons faster than pp collisions, the dominant hadronic process in our model is the $p\gamma$ emission. Therefore, this mechanism will prevail in the production of the neutrinos and the first term of eq. 18 can be neglected. In $p\gamma$ interactions, E_ν is related with the parent proton energy through the equation $E_\nu = 0.05E_p$ (Spurio 2015), because the average energy of the pion is ~ 0.2 of the parent proton energy and in the decay of the π^+ chain four leptons are produced (including one electron neutrino as remarked), each of which has roughly 1/4 of the pion energy. It has been also demonstrated in Spurio (2015) that the ratio of the neutrino luminosity to the photon luminosity from $p\gamma$ interactions is $\sim 1/3$.

In consistency with the statement above, the maximum energy of the produced neutrinos can be calculated from $E_{\nu,max} = 0.05E_{p,max}$ (Becker 2008; Hazlen 2007), which according to our model is $\sim 3 \times 10^{16}$eV for a source with a black hole mass $M_{BH} = 10^7 M_\odot$, $\sim 5 \times 10^{15}$eV for a source with $M_{BH} = 10^8 M_\odot$, and $\sim 2 \times 10^{15}$eV for a source with $M_{BH} = 10^9 M_\odot$.

The total diffuse neutrino intensity from the extragalactic sources we are considering here, i.e., LLAGNs may have contributions from different redshifts. Neglecting evolutionary effects in the core region of these sources, we can estimate the total intensity as (Murase et al. 2014)

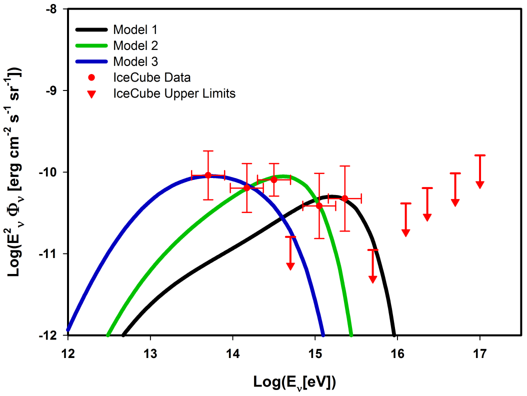

Figure 3. Calculated diffuse intensity of neutrinos from the cores of LLAGNs considering our magnetic reconnection acceleration model to produce the protons and gamma-ray photons for three different BH masses. The data are taken from IceCube measurements (Aartsen et al. 2014).

$$\Phi_\nu = \frac{c}{4\pi H_0} \int_0^{z_{max}} dz \frac{1}{\sqrt{(1+z)^3 \Omega_m + \Omega_\Lambda}} \times \int_{L_{min}}^{L_{max}} dL_\gamma \;\; \rho_\gamma(L_\gamma, z) \frac{L_\nu(E_\nu)}{E_\nu}, \qquad (19)$$

where L_γ is the γ-ray luminosity, and $\rho_\gamma(L_\gamma, z)$ is the γ-ray luminosity function (GLF) of the core of the sources, defined as the number density of sources per unit comoving volume, per unit logarithmic luminosity between the redshifts $z = 0$ to $z = z_{max}$, being the latter the maximum observed redshift for radiogalaxies, $z_{max} \simeq 5.2$ (Klamer et al. 2005). GLF is integrated from L_{min} to L_{max} which are obtained from *Fermi*-LAT observations and are given by 10^{41} and 10^{44} erg/s, respectively (Di Mauro et al. 2014). The values for the cosmological parameters are assumed as: $H_0 = 70$ km s^{-1}Mpc^{-1}, $\Omega_M = 0.3$ and $\Omega_\Lambda = 0.7$.

We evaluate the GLF, $\rho_\gamma(L_\gamma, z)$ as in Di Mauro et al. (2014), from the estimated radio luminosity function (RLF) which for non-blazars is given by

$$\rho_\gamma(L_\gamma, z) = \rho_{r,tot}(L_{r,tot}^{5\mathrm{GHz}}(L_{r,core}^{5\mathrm{GHz}}(L_\gamma)), z) \times \frac{d\log L_{r,core}^{5\mathrm{GHz}}}{d\log L_\gamma} \; \frac{d\log L_{r,tot}^{5\mathrm{GHz}}}{d\log L_{r,core}^{5\mathrm{GHz}}}. \qquad (20)$$

$d\log L_{r,core}^{5\mathrm{GHz}}/d\log L_\gamma$ and $d\log L_{r,tot}^{5\mathrm{GHz}}/d\log L_{r,core}^{5\mathrm{GHz}}$ can be calculated by (Di Mauro et al. 2014)

$$\log L_\gamma = 2.00 \pm 0.98 + (1.008 \pm 0.025) \log (L_{r,core}^{5\mathrm{GHz}}), \qquad (21)$$

and

$$\log L_{r,core}^{5\mathrm{GHz}} = 4.2 \pm 2.1 + (0.77 \pm 0.08) \log (L_{r,tot}^{5\mathrm{GHz}}), \qquad (22)$$

where $L_{r,tot}^{5\mathrm{GHz}}$ and $L_{r,core}^{5\mathrm{GHz}}$ are the radio total and core luminosities, respectively. The total RLF,

Table 2. Physical conditions around the LLAGNs represented by models 1, 2 and 3, obtained from Eqs. 1 to 4, using $r_x = 6$, $l = 20$, $l_X = 10$ and $\xi = 0.7$.

	Parameters	Model 1	Model 2	Model 3
B	Magnetic field (G)	2.8×10^4	8874	2806
W	Magnetic reconnection power (erg/s)	2.4×10^{42}	2.4×10^{43}	2.4×10^{44}
ΔR_X	Width of the current sheet (cm)	7.2×10^{12}	7.2×10^{13}	7.2×10^{14}
n_c	Coronal particle number density (cm^{-3})	3.6×10^{10}	3.6×10^{9}	3.6×10^{8}

$\rho_{r,tot}(L^{5\mathrm{GHz}}_{r,tot}(L^{5\mathrm{GHz}}_{r,core}(L_\gamma)), z)$, is found from interpolation of the observed data for radio-galaxies provided by Yuan & Wang (2012):

$$\begin{aligned}\rho_{r,tot}(L^{5\mathrm{GHz}}_{r,core}(L_\gamma), z) = {} & (-1.1526 \pm 0.0411) \log L^{5\mathrm{GHz}}_{r,core} \\ & + (0.5947 \pm 0.1224) z + 23.2943 \\ & \pm 1.0558\ \mathrm{Mpc}^{-3} (\log \mathrm{L}^{5\mathrm{GHz}}_{\mathrm{r,core}})^{-1}.\end{aligned} \tag{23}$$

The resulting neutrino flux is shown in Figure 3. It was calculated using eq. 19 above, considering the maximum neutrino energies obtained for sources with the three different BH masses (as in Figure 2).

Sources with $M_{BH} = 10^7 M_\odot$ result a spectrum that matches better with the observed most energetic part of the neutrino flux by the IceCube, at $\sim 3 \times 10^{15}$ to 10^{16} eV, while sources with BH masses of the order of $10^8 M_\odot$ produce a spectrum that nearly fits the observed neutrinos flux in the range of $10^{14} - 10^{15}$eV, and sources with mass $\sim 10^9 M_\odot$ the narrow energy band $5 \times 10^{13}\mathrm{eV} - 10^{14}\mathrm{eV}$ as well as the upper limit at 5×10^{14}eV.

5 DISCUSSION AND CONCLUSIONS

In this work we have explored a model to describe the observed flux of extragalactic very high energy (VHE) neutrinos by the IceCube (Aartsen et al. 2014) in the framework of low luminosity AGNs (LLAGNs), or more specifically, of radio-galaxies. The recent detection of gamma-ray emission in the TeV range in these sources makes them also potential candidates of VHE neutrino emission via the decay of charged pions which can be produced by the interaction of accelerated relativistic protons with ambient lower energy photons and protons.

We have examined here a fast magnetic reconnection mechanism in the surrounds of the central BH occurring between the lines lifting from the accretion disk into the corona and those of the BH magnetosphere to accelerate particles to relativistic energies through a first-order Fermi process in the reconnection layer (GL05, Kowal et al. 2012). Recently, it has been demonstrated that this model successfully reproduces the observed gamma-ray luminosity of hundreds of LLAGNs (Kadowaki et al. 2015 and SGK15) and also shapes the SEDs of several radio-galaxies, particularly reproducing their TeV gamma-ray energies mainly via photomeson ($p\gamma$) interactions (KGS15).

Applying the same acceleration model as above (see Section 2), considering three different BH masses, we have shown that also the observed VHE neutrino Icecube flux (Aartsen et al. 2014) can be obtained from the decay of charged pions produced in photomeson interactions involving the accelerated protons and Synchrotron photons in the core region of these sources (Figs. 2 and 3).

Specifically, in Fig. 2, we compared the magnetic reconnection acceleration rate (derived from the numerical simulations of Kowal et al. (2012) and calculated for the source parameters) with the relevant hadronic cooling processes and obtained the maximum energy for the accelerated protons mainly constrained by the $p\gamma$ interactions. In Fig. 2, we also compared the magnetic reconnection with the shock acceleration rate in the surrounds of the BH for the same parametric space and demonstrated the higher efficiency of the first process in this region. According to our results in Fig. 2, protons are able to accelerate up to energies of the order of $\sim 10^{17}$eV and therefore, are suitable to produce 0.1-1 PeV neutrinos.

Fig. 3 indicates that the observed neutrino flux in the few PeV range can be matched by sources with $M_{BH} \sim 10^7 M_\odot$ (Model 1), while the flux in the energy range of 0.1PeV< E_ν <1PeV can be matched by sources with $M_{BH} \sim 10^8 M_\odot$ (model 2), and that in the range $\leq$ 0.1PeV can be fitted by sources with $M_{BH} \sim 10^9$eV (model 3).

We note that, although the calculated neutrino flux was obtained from the integration of the contributions of LLAGNs over the redshifts between z=0 and 5.2 (eq. 19) considering, for simplicity, sources with only three characteristic values of BH masses, one may naturally expect that a continuous integration considering the sources with all possible BH masses within the range $10^7 - 10^9 M_\odot$ should provide a similar fitting to the observed data. We also note that our model is unable to explain the IceCube upper limits at the $\sim$ 10PeV range (also depicted in Fig. 3), which are probably due to other astrophysical compact source population.

Furthermore, we expect that with the 10-fold increased sensitivity at TeV energies, and the larger field of view and improved angular resolution of the forthcoming gamma-ray observatory CTA (Actis et al. 2011; Acharya et al. 2013), the list of LLAGNs with confirmed detection of gamma-ray emission at TeV energies (which currently has only four sources: Cen A, Per A, M87 an IC310), will increase substantially, allowing for a more precise evaluation of the contribution of individual sources for the IceCube neutrino flux.

As remarked in §. 1, other models have been proposed in the literature to explain the IceCube neutrino flux which cannot be discarded or confirmed, considering the current poorness of the data available.

Tavecchio et al. (2014) and Tavecchio & Ghisellini (2014), for instance, have proposed that the lower power blazar class of BL Lac objects could be promising candidates to produce the observed neutrino flux. In their two-zone jet model, the neutrinos are produced by photomeson interactions involving photons emitted in the slower, outer layer that envelopes the faster inner jet component. A limitation of this model is that the high-energy cut-off of the accelerated protons, as well as their injected power are free parameters, unlike in our model where both quantities are directly obtained from the magnetic reconnection acceleration mechanism. Besides, since the BL Lacs are a subclass of the blazars, another difficulty with this model is that it is not clear whether the remaining more powerful blazars, which are also TeV gamma-ray emitters, can or cannot produce neutrinos. According to the recent studies of Dermer et al. (2014) and Murase et al. (2014), which employed a single zone jet model, the powerful blazars would not be suitable candidates to explain the IceCube data. These analyses and the relatively large number of free parameters employed in the evaluation of the neutrino flux leave the question on whether or not blazars do contribute to the IceCube data opened.

Another model to explain the observed neutrino flux has been proposed by Kalashev et al. (2014) who studied photo-pion production on the anisotropic photon field of a Shakura-Sunyaev accretion disk in the vicinity of the BH in AGNs. But this model does not provide an acceleration mechanism either and therefore, the proton high energy cut-off is also a free parameter.

Recently, radio galaxies have been also discussed as possible sources of the observed HE neutrinos by Becker et al. (2014). They demonstrated that FR I radio galaxies would be more probable sources of this emission than FR II radio galaxies. In this work, as we considered the global diffuse contribution from LLAGNs spread over a range of z values, we cannot distinguish the relative contributions from both classes.

Finally, another recent study (Kimura et al. 2014) speculates that the protons responsible for the neutrino emission could be accelerated stochastically by the turbulence induced in a RIAF accretion disk in the core region of LLAGNs. This acceleration process should be essentially a second-order Fermi process and therefore, less efficient than a first-order Fermi process. Nevertheless, their analytically estimated acceleration rate $t_{acc}^{-1} \propto E^{-0.35}$ seems to be too large when compared to that predicted for first-order Fermi processes, as for instance in the present study where the acceleration rate has been extracted directly from 3D MHD simulations with test particles ($t_{acc}^{-1} \propto E^{-0.4}$; Kowal et al. 2012, KGV15), or in shock acceleration (for which analytic predictions give $t_{acc}^{-1} \propto E^{-1}$ (Spruit 1988)). Furthermore, since the candidates to produce PeV neutrinos in this case are radio-galaxies, which are the observed γ-ray emitters, it seems that the employment of the gamma-ray luminosity function (GLF; Di Mauro et al. 2014) to calculate the diffuse neutrino intensity as we did here seems to be more appropriate than the employment of the luminosity function in X-rays, as these authors considered.

In summary, in spite of its simplicity, the numerically tested acceleration model applied to the core region of LLAGNs here presented indicates that LLAGNs are very promising candidates to explain the IceCube VHE neutrinos.

ACKNOWLEDGEMENTS

This work has been partially supported by grants of the Brazilian agencies FAPESP (2013-10559-5, and 2011/53275-4), CNPq (306598/2009-4) and CAPES. We are also indebted to the referee for his/her useful comments.

REFERENCES

Aartsen, M. G., Ackermann, M., Adams, J., et al. 2014, Physical Review Letters, 113, 101101

Acharya, B. S., Actis, M., Aghajani, T., et al. 2013, Astroparticle Physics, 43, 3

Actis, M., Agnetta, G., Aharonian, F., et al. 2011, Experimental Astronomy, 32, 193

Ahlers, M., & Murase, K. 2014, Phys. Rev. D, 90, 023010

Atoyan, A. M., & Dermer, C. D. 2001, PRL, 87, 221102

Atoyan, A. M., & Dermer, C. D. 2003, ApJ, 586, 79

Becker, J. K. 2008, Phys. Rep., 458, 173

Becker Tjus, J., Eichmann, B., Halzen, F., Kheirandish, A., & Saba, S. M. 2014, Phys. Review D. 89, 123005

Begelman, M. C., Rudak, B., & Sikora, M. 1990, ApJ, 362, 38

Cerutti, B., Werner, G. R., Uzdensky, D. A., Begelman, M. C. 2013, ApJ., 770, 147C

de Gouveia Dal Pino, E. M. & Lazarian, A. 2005, Astronomy and Astrophysics, 441, 845 (GL05)

de Gouveia Dal Pino, E. M., Piovezan, P. P. & Kadowaki, L. H. S. 2010a, Astronomy and Astrophysics, 518, A5

de Gouveia Dal Pino, E. M., Kowal, G., Lazarian, A. 2014, 8th International Conference of Numerical Modeling of Space Plasma Flows (ASTRONUM 2013), 488, 8, arXiv1401.4941D

de Gouveia Dal Pino, E. M., & Kowal, G. 2015, in Magnetic Fields in Diffuse Media (eds. A. Lazarian, E. M. de Gouveia Dal Pino, C. Melioli), Astrophysics and Space Science Library, 407, 373

Dermer, C. D., Murase, K., & Inoue, Y. 2014, Journal of High Energy Astrophysics, 3, 29

Di Mauro, M., Calore, F., Donato, F., Ajello, M., & Latronico, L. 2014, ApJ, 780, 161

Drake, J. F., Swisdak, M., Che, H. and Shay, M. A. 2006, Nature, 443, 553D

Drake, J. F., Opher, M., Swisdak, M. and Chamoun, J. N. 2010, ApJ,709, 963D

Eichler, G. 1979, ApJ, 232, 106

Fraija, N. 2014a, MNRAS, 441, 1209

Fraija, N. 2014b, ApJ, 783, 44

Gupta, N. 2008, JCAP, 06, 022

Hazlen, F. & Zas, E. 1997, ApJ, 488, 669

Hazlen, F. 2007, ApS&S, 309, 407

Ho, L. C., Filippenko, A. V., & Sargent, W. L. W. 1997, ApJS, 112, 315

Kadowaki, L. H. S., de Gouveia Dal Pino, E. M., & Singh, C. B. 2015, ApJ, 802, 113

Kalashev, O., Semikoz, D. & Tkachev, I. 2014, arXiv:1410.8124

Kazanas, D., & Ellison, D. C. 1986, ApJ, 304, 178

Kelner, S. R., Aharonian, F. A., & Bugayov, V. V. 2006, Phys.Rev. D, 74, 0330108

Kelner, S. R., Aharonian, F. A., & Bugayov, V. V. 2009, Phys.Rev. D, 79, 039901

Khiali, B., de Gouveia Dal Pino, E. M. & del Valle, M. V. 2015a, MNRAS, 449, 34 (KGV15)

Khiali, B., de Gouveia Dal Pino, E. M. & Sol, H. 2015b, arXiv:1504.07592 (KGS15)

Kimura, S. S., Murase, K. & Toma, K. 2014, arXiv: 1411.3588

Klamer, I. J., Ekers, R. D., Sadler, E. M., et al. 2005, ApJL,

621, L1
Kowal, G., Lazarian, A., Vishniac, E. T., Otmianowska-Mazur, K. 2009, ApJ, 700, 63
Kowal, G., de Gouveia Dal Pino, E. M., Lazarian, A. 2011, The Astrophysical Journal, 735, 102
Kowal, G., de Gouveia Dal Pino, E. M., Lazarian, A. 2012, Physical Review Letters, 108, 241102
Lazarian, A., & Vishniac, E. T. 1999, The Astrophysical Journal, 517, 700
Lazarian, A., & Yan, H. 2014, ApJ, 784, 38
Levinson, A., 2000, Phys. Rev. Lett., 85, 912
Lin, R. P., & Hudson, H. S. 1971, SoPh, 17, 412
Mannheim, K. 1995, APh, 3, 295
Margolis, S. H., Schramm, D. N., & Silberberg, R. 1978, ApJ, 221, 990
Marinelli, A., Fraija, N., & Patricelli, B. 2014a, arXiv:1410.8549
Marinelli, A., & Fraija, N. 2014b, arXiv:1411.2695
Meier, D. L., 2012, Black Hole Astrophysics: The Engine Paradigm, Springer Verlag, Berlin Heidelberg
Merloni, A., Heinz, S., & di Matteo, T. 2003, MNRAS, 345, 1057
Michalak, W., Wdowczyk, J., & Wolfendale, A. W. 1990, Journal of Physics G Nuclear Physics, 16, 1917
Mucke, A., & Protheroe, J. P. 2001, Astrop. Phys., 15, 121
Murase, K. 2007, Phys. Rev. D 76, 123001
Murase, K., Inoue, Y., & Dermer, C. D. 2014, PhRvD, 90, 023007
Nagar, N. M., Falcke, H., & Wilson, A. S. 2005, A&A, 435, 521
Neronov, A., & Semikoz, D. V. 2002, Phys. Rev. D 66,123003
Protheroe, R. J. & Kasanas, D. 1983, ApJ, 265, 620
Romero, G. E., Vieyro, F. L. and Villa, G. S. 2010b, A&A 519, A109
Singh, C. B., de Gouveia Dal Pino, E. M., & Kadowaki, L. H. S. 2015, ApJL, 799, L20 (SGK15)
Sironi, L., & Spitkovsky, A. 2014, ApJ, 783, 21
Somov, B. V. 2012,*Plasma Astrophysics, Part I: Fundamentals and Practice*, Astrophysics and Space Science Library, 391
Spruit, H. C. 1988, A&A, 194, 319
Spurio, M. 2015, Publications of the American Astronomical Society, page 322
Stecker, F. W. 1968, Phys. Rev. Lett., 21, 1016
Stecker, F. W. 1970, Ap&SS, 6, 377
Stecker, F. W. 1971, NASA Special Publication, 249, 499
Stecker, F. W. 1979, ApJ, 228, 919
Stecker, F. W., Done, C., Salamon, M. H., & Sommers, P. 1991, PhRvL, 66, 2697
Tavecchio F., Ghisellini G. & Guetta D., 2014, ApJ, LL18
Tavecchio, F., & Ghisellini, G. 2014, arXiv:1411.2783
Vila G. S. and Aharonian F. 2009, Asociaon Argentina de Astronomia- Book Series, AAABS, Vol. 1, 2009
Vincent, S., 2014, arXiv:1411.1957
Waxman, E. & Bahcall, J. N. 1997, Physical Review Letters, 78, 2292
Yamada, M., Jongsoo, Y., Jonathan J. A., Hantao, J., Russell M. K.& Clayton E. M. 2014, Nature Communications 5, 4774
Yuan, Z., & Wang, J. 2012, ApJ, 744, 84
Zenitani, S. and Hoshino, M. 2001, ApJ, 562L, 63Z

This paper has been typeset from a TEX/ LATEX file prepared by the author.